

**STRUCTURAL, OPTICAL AND THERMAL STUDIES  
OF RARE EARTH *Sm* DOPED *Ge<sub>2</sub>Sb<sub>2</sub>Te<sub>5</sub>* PHASE  
CHANGE MATERIAL**

*Thesis submitted in fulfillment for the requirement of the Degree of*

**DOCTOR OF PHILOSOPHY**

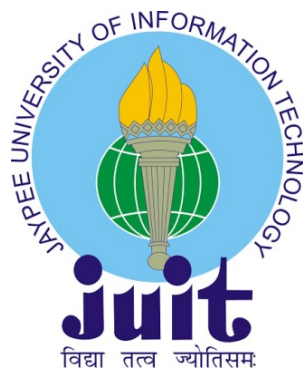
**IN**

**PHYSICS**

**BY**

**SANJAY KUMAR**

[Enrollment No. 186901]



DEPARTMENT OF PHYSICS AND MATERIALS SCIENCE

JAYPEE UNIVERSITY OF INFORMATION TECHNOLOGY

WAKNAGHAT, SOLAN, H.P. INDIA-173234

MAY 2022

Copyright

@

JAYPEE UNIVERSITY OF INFORMATION TECHNOLOGY

WAKNAGHAT

MAY 2022

ALL RIGHTS RESERVED

## **SUPERVISOR'S CERTIFICATE**

This is to certify that the work reported in the Ph.D. thesis entitled “**STRUCTURAL, OPTICAL AND THERMAL STUDIES OF RARE EARTH *Sm* DOPED *Ge<sub>2</sub>Sb<sub>2</sub>Te<sub>5</sub>* PHASE CHANGE MATERIAL**” submitted by **Mr. Sanjay Kumar** at **Jaypee University of Information Technology, Wagnaghat, Solan (HP), India** is a bonafide record of his original work carried out under my supervision. This work has not been submitted elsewhere for any other degree or diploma.

**Prof. (Dr.) Vineet Sharma**

Department of Physics and Materials Science

Jaypee University of Information Technology, Wagnaghat, Solan

(HP), India

**Email:** vineet.sharma@juit.ac.in

**Phone:** +91 94182 33083

**Date:**



## **DECLARATION BY THE SCHOLAR**

I hereby declare that the work reported in the Ph.D. thesis entitled “**STRUCTURAL, OPTICAL AND THERMAL STUDIES OF RARE EARTH *Sm* DOPED *Ge<sub>2</sub>Sb<sub>2</sub>Te<sub>5</sub>* PHASE CHANGE MATERIAL**” submitted at **Jaypee University of Information Technology, Wagnaghat, Solan (HP), India** is an authentic record of my work carried out under the supervision of **Prof. (Dr.) Vineet Sharma**. I have not submitted this thesis elsewhere for any other degree or diploma. I am fully responsible for the contents of my Ph.D. thesis.

**Sanjay Kumar**

Enrollment No. 186901

Department of Physics and Materials Science

Jaypee University of Information Technology

Wagnaghat, Solan, H.P. India-173234

**Date:**



Dedicated to my parents



## ACKNOWLEDGEMENT

I am grateful for the grace of God and blessings of my tutelary deity Bhairava for giving me strength to complete my thesis work and for everything that he has provided to me in my life.

I would like to express my deepest gratitude to my Ph.D. supervisor **Prof. Vineet Sharma, Department of Physics and Materials Science, Jaypee University of Information Technology, Wagnaghat, Solan** for giving me opportunity of doing Ph.D. under his supervision and for continuous support and valuable guidance throughout my research work.

I am grateful to acknowledge the financial assistance of **Science and Engineering Research Board (SERB) Department of Science and Technology (DST), New Delhi, India** as **Junior Research Fellow (JRF)** under the research project.

I would also like to convey my special thanks to **Prof. Pankaj Sharma, Professor and Head, Department of Applied Sciences, National Institute of Technical Teachers Training and Research, Chandigarh** for valuable suggestions and fruitful discussion about my research.

My sincere thanks to **Prof. P. B. Barman, HOD, Department of Physics and Materials Science, Jaypee University of Information Technology, Wagnaghat, Solan, India**, for his valuable suggestion, guidelines and continuous support throughout my Ph.D. work. I would like to express my sincere thanks to **Prof Sunil Kumar Khah, Dr. Ragini Raj Singh, Dr. Surajit Kumar Hazra, Dr. S. K. Tiwari, Dr. R. S. Raja Durai and Dr. Santu Vaidya** for their support, valuable comments and suggestions.

I would like to extend my special thanks to **Prof. Nagesh Thakur, Department of Physics, Himachal Pradesh University Summerhill Shimla, H.P. India** for the endless support, guidance and motivations.

I am thankful to my seniors: Dr. Rohit Sharma, Dr. Prashant Thakur, Dr. Jonny Dhiman, Dr. Neha Kondal, Dr. Subhash Chand, Dr. Asha and Dr. Pooja for their motivations, support and guidance. I would like to extend my thank to my lab members and friends: Dipti Rawat, Ekta Sharma, Kalpana Sharma, Rahul Singh, Neha Luhakhra and my all the

colleagues Sweta, Priyanka, Anuradha, Sikha, Raj Kumar sir, Shiv Kumar sir, Achyut sir and Rajan.

I would like to express my deepest gratitude to my parents and my younger brother Minay for supporting me in my tough time. I cannot express my thanks in words to my parents for the sacrifice of their own happiness for the fulfillment of my dreams and giving the priority to educate me despite of financial constraints. This work is impossible without their support.

Finally, I express my gratitude to all those who provided me the research support in the course of my investigation.

Sanjay Kumar

## Contents

Abstract	<i>xv-xvii</i>
List of Publications	<i>xix</i>
National and International Conferences/Workshops / Short-Term Courses Attended	<i>xxi</i>
List of Figures	<i>xxiii-xxvii</i>
List of Tables	<i>xxviii-xxix</i>
List of Acronyms and Abbreviations	<i>xxx-xxxiv</i>

1. Introduction.....	1
1.1. Amorphous Semiconductors.....	5
1.1.1. Tetrahedrally Coordinated Semiconductors.....	9
1.1.2. Chalcogenide Glasses.....	9
1.1.2.1. Bandgap and Electrical Properties.....	10
1.1.2.2. Defect States.....	12
1.1.2.3. Optical Properties.....	13
1.2. Phase Change Materials.....	15
1.2.1. Classifications.....	16
1.2.1.1. <i>Ge-Sb-Te</i> Alloys.....	17
1.2.1.2. <i>Ag-In-Sb-Te</i> Alloys.....	18
1.2.2. Applications.....	19
1.2.2.1. Optical Data Storage.....	19
1.2.2.2. Phase Change Memories.....	20
1.2.2.3. Neuro-inspired Computing.....	21
1.2.2.4. Thermoelectric Applications.....	23
1.2.2.5. NIR Windows.....	23
1.3. <i>Ge<sub>2</sub>Sb<sub>2</sub>Te<sub>5</sub></i> Phase Change Material.....	24
1.3.1. Switching Mechanism.....	26
1.3.2. Challenges.....	28

1.3.2.1. Aging and Resistance Drift of Amorphous $Ge_2Sb_2Te_5$ .....	28
1.3.2.2. Fast Switching Speed.....	29
1.3.2.3. Enhanced Thermal Stability.....	29
1.4. Doping of $Ge_2Sb_2Te_5$ .....	30
1.5. Current Status and Future Scope.....	32
1.6. Motivations.....	33
1.7. Thesis Outlines .....	37
References.....	39
2. Physical Properties of <i>Sm</i> doped $Ge_2Sb_2Te_5$ .....	53
2.1. Introduction.....	55
2.2. Results and Discussion.....	57
2.2.1. Bonding Constraints and Structural Rigidity.....	57
2.2.2. Kinetics of Supercooled Liquid.....	60
2.2.3. Average Heat of Atomization, Cohesive Energy and Band Gap.....	62
2.2.4. Electronegativity and Degree of Covalency.....	63
2.2.5. Conduction and Valence Band Edge Energies.....	65
2.2.6. Glass Transition Temperature.....	66
2.2.7. Bond Switching Mechanism.....	69
2.2.8. Metallicity and Lone Pair Electrons.....	72
2.2.9. Structural Modification Efficiency.....	73
2.2.10. Threshold Switching Voltage.....	75
2.3. Conclusion.....	76
References.....	78
3. Experimental Techniques.....	85
3.1. Introduction.....	87
3.2. Preparation of Chalcogenide Glass.....	88
3.2.1. Melt Quenching.....	88
3.2.2. Sol-Gel Method.....	89
3.2.3. Thermal Evaporation .....	90
3.2.4. Electron-Beam Deposition.....	91
3.2.5. Flash Evaporation.....	92
3.2.6. Pulsed Laser Deposition.....	92
3.2.7. Sputtering.....	93

3.2.8. Chemical Vapor Deposition.....	94
3.2.9. Spin Coating.....	95
3.3. Methods for Characterization .....	95
3.3.1. X-Ray Diffraction ( <i>XRD</i> ).....	95
3.3.2. Energy Dispersive X-Ray spectroscopy ( <i>EDS</i> ).....	97
3.3.3. Field Emission Scanning Electron Microscopy ( <i>FESEM</i> ).....	99
3.3.4. X-Ray Photoelectron Spectroscopy ( <i>XPS</i> ).....	100
3.3.5. Raman Spectroscopy.....	101
3.3.6. Fourier-Transform Infrared spectroscopy ( <i>FTIR</i> ).....	103
3.3.7. <i>UV-Vis-NIR</i> Spectroscopy.....	103
3.3.8. Differential Scanning Calorimetry ( <i>DSC</i> ).....	107
3.3.9. Electrical Measurements.....	108
References.....	110
4. Structural Investigation of $(Ge_2Sb_2Te_5)_{100-x}Sm_x$ Bulk Alloys and Thin films.....	113
4.1. Introduction.....	115
4.2. Experimental Details.....	116
4.2.1. Sample Preparation.....	116
4.2.2. Characterization Details.....	117
4.3. Results and Discussion.....	117
4.3.1. Characterization of $(Ge_2Sb_2Te_5)_{100-x}Sm_x$ Bulk Alloys.....	117
4.3.1.1. X-Ray Diffraction ( <i>XRD</i> ) and Rietveld Refinement Analysis.....	118
4.3.1.2. Raman Analysis.....	125
4.3.1.3. <i>FTIR</i> Measurements.....	131
4.3.2. Characterization of $(Ge_2Sb_2Te_5)_{100-x}Sm_x$ Thin Films.....	133
4.3.2.1. Thin Film <i>XRD</i> .....	133
4.3.2.2. X-Ray Photoelectron Spectroscopy ( <i>XPS</i> ).....	134
4.4. Conclusion.....	138
References.....	140
5. Optical Properties of $(Ge_2Sb_2Te_5)_{100-x}Sm_x$ Thin Films.....	145
5.1. Introduction.....	147
5.2. Experimental Details.....	148
5.3. Results and Discussion.....	149
5.3.1. Compositional Analysis.....	149

5.3.2. Linear Refractive Index ( $n$ ) and Optical Absorption Coefficient ( $\alpha$ ).....	152
5.3.3. Optical gap ( $E_g$ ) and Optical Dispersion.....	156
5.3.4. Real and Imaginary Dielectric Constants, Energy Loss functions and Optical conductivity.....	160
5.3.5. Optical Non-Linear Parameters.....	163
5.4. Conclusion.....	165
References.....	166
6. Thermal and Electrical Properties of $(Ge_2Sb_2Te_5)_{100-x}Sm_x$ Thin Films.....	171
6.1. Introduction.....	173
6.2. Experimental Section.....	174
6.3. Results and Discussion.....	175
6.3.1. DSC Analysis.....	175
6.3.2. Crystallization.....	176
6.3.2.1. Henderson's Method.....	177
6.3.2.2. Matusita's Method.....	182
6.4. Current Voltage ( $I-V$ ) Characteristics.....	183
6.5. Temperature-Resistance ( $R-T$ ) Measurements.....	184
6.6. Temperature Dependent XRD Studies .....	185
6.7. Conclusions.....	188
References.....	189
7. Summary and Conclusions.....	193

## Abstract

The advancements in memory devices for achieving efficient computing performance is one of the recent areas in research and development. Phase change (PC) memories are among the leading next generation memory technology. The basic principle behind the working of PC memories is based upon the repeated reversible phase transformation of chalcogenide PC materials which are induced thermally. The unique features of  $Ge_2Sb_2Te_5$  (GST) such as higher crystallization temperature ( $\sim 160^\circ C$ ), faster switching speed ( $\sim 60ns$ ) and better contrast in the amorphous and crystalline phases for electrical resistivity and optical reflectivity makes it a novel material for such purpose. The GST exhibits the amorphous, rocksalt cubic (fcc) and hexagonal crystal structure at different temperatures. The addition of impurity element to GST is an effective method for the improvement of switching performance by inducing the change in chemical bonding nature and local structural network which alters the optical, electrical and thermal characteristics. In the current work the outcome of Sm doping on the local structure, optical behavior, crystallization kinetics and electrical properties has been studied.

The bulk alloys of  $(Ge_2Sb_2Te_5)_{100-x}Sm_x$  PC material have been prepared by means of the melt-quenching process. The thin film deposition for Sm added GST samples have been carried out by employing thermal evaporation. The crystal structure of powder material of  $(Ge_2Sb_2Te_5)_{100-x}Sm_x$  bulk alloys has been studied by employing the X-ray diffraction (XRD) analysis and rietveld refinement by Fullprof software for phase quantification thereafter. The local structures of these samples have been probed employing the Raman spectroscopy analysis using 785 nm laser excitation and the FTIR measurements in  $30\text{ cm}^{-1}$  to  $300\text{ cm}^{-1}$  range. The XRD analysis of  $(Ge_2Sb_2Te_5)_{100-x}Sm_x$  thin films show amorphous nature. The elemental analysis of the thin films has been done using the FESEM mapping and EDX investigations. The chemical bonding nature and compositional analysis of these films have been studied using XPS measurements employing Al  $K\alpha$  X-ray source. UV-Vis-NIR spectroscopy has been utilized for investigation of optical behavior of  $(Ge_2Sb_2Te_5)_{100-x}Sm_x$  thin films. Non-isothermal crystallization kinetics of  $(Ge_2Sb_2Te_5)_{100-x}Sm_x$  thin films has been studied using the differential scanning calorimetry (DSC) at  $10^\circ C/min$  from  $30-700^\circ C$  in Ar environment. The current voltage characteristics of  $(Ge_2Sb_2Te_5)_{100-x}Sm_x$  thin films with temperature have been probed in coplanar geometry. The  $(Ge_2Sb_2Te_5)_{100-x}Sm_x$  thin films

annealed in vacuum at 50°C, 160°C and 250°C have been investigated for structural analysis using *XRD*.

The physical parameters *viz.* mean coordination number (*Z*), bond bending and bond stretching constraints, density, cohesive energy, energies of conduction as well as valence band edge and the glass transition temperature for  $(Ge_2Sb_2Te_5)_{100-x}Sm_x$  samples have been computed for calculating the glass forming ability and rigidity of structural networks. The degree of cross-linking with increase in *Sm* concentration has been theoretically examined. The structural modification efficiency for amorphous  $(Ge_2Sb_2Te_5)_{100-x}Sm_x$  system has been theoretically estimated. The stability of threshold switching voltage has been analyzed theoretically through the evaluation of metallicity and lone pair electrons which causes the bond switching and creation of valence alternation pairs and leads to the change in threshold switching voltage. The crystalline nature of  $(Ge_2Sb_2Te_5)_{100-x}Sm_x$  alloys formed after melt quenching has been analyzed from the *XRD* analysis. The rietveld refinement of the *XRD* data of these samples has been carried out for the phase quantification and lattice parameter evaluation which reveals the presence of mixed amorphous, *fcc* and hexagonal phases. The Raman analysis of the samples shows change in local structure of *Sb* on incorporation of *Sm*. The signature of *Sm—Te*, *Ge—Ge*, *Sb—Sb*, *Ge—Te*, and *Sb—Te* bond vibrations has been observed through the *FTIR* investigation. The *XPS* measurements of  $(Ge_2Sb_2Te_5)_{100-x}Sm_x$  thin films indicates creation of *Sm—Ge*, *Sm—Sb* and *Sm—Te* bonds. These also *Sm* occurrence together in oxidation states +2 as well as +3. The elemental fraction of constituent elements of  $(Ge_2Sb_2Te_5)_{100-x}Sm_x$  thin films has been observed to be in close agreement with the stoichiometric composition. The uniformity of as-deposited thin films and homogeneous elemental distribution along the thin film's surface has been observed using the *FESEM* elemental mapping and imaging measurements.

The optical behavior of thin films of  $(Ge_2Sb_2Te_5)_{100-x}Sm_x$  has been examined employing *UV-Vis-NIR* transmittance spectra from 600-2700 nm. The linear refractive index, optical absorption coefficient have been analyzed to study the effect of *Sm* addition to *GST*. The optical band gap ( $E_g$ ) evaluated through the Tauc method displays the decrease in  $E_g$  value with *Sm* content. The change in Tauc order parameter ( $B^{1/2}$ ) and urbach energy ( $E_u$ ) for the thin films of  $(Ge_2Sb_2Te_5)_{100-x}Sm_x$  indicates the the impact of incorporation of *Sm* on the degree of disorder and band tailing width. The optical dispersion behavior of these thin films has been investigated using *WDD* method to examine the ratio of free carrier concentration to effective mass ( $N/m^*$ ) and dielectric constant ( $\epsilon_\infty$ ) at high frequencies which decreases with

*Sm* content in thin films of  $(Ge_2Sb_2Te_5)_{100-x}Sm_x$ . Real and imaginary dielectric constants, dielectric-loss function along with surface and bulk energy loss functions decreases with increase in wavelength for  $(Ge_2Sb_2Te_5)_{100-x}Sm_x$  thin films. Optical non-linear parameters such as third-order non-linear optical susceptibility( $\chi^{(3)}$ ), non-linear refractive index and optical electronegativity show maximum incase of thin film  $x = 0.4$ .

The thin films of  $(Ge_2Sb_2Te_5)_{100-x}Sm_x$  have been studied for the kinetics of crystallization by utilizing the *DSC* analysis. The crystallization of  $(Ge_2Sb_2Te_5)_{100-x}Sm_x$  has been estimated by utilizing the thermal parameters crystallization onset ( $T_c$ ), melting temperature ( $T_m$ ) and peak crystallization temperature ( $T_p$ ). The non-isothermal crystallization kinetics have been analyzed employing methods proposed by Matusita and Henderson. The crystallization of  $(Ge_2Sb_2Te_5)_{100-x}Sm_x$  in both *fcc* and hexagonal phases has been observed through the appearance of separate exothermic peaks in *DSC* thermograms. The reduction of activation energy to minimum for *fcc* crystallization has been observed for addition of  $x = 0.4\%$  *Sm*. The activation energy for hexagonal crystallization has been found to rise on increasing *Sm* in  $(Ge_2Sb_2Te_5)_{100-x}Sm_x$ . The current voltage measurements of  $(Ge_2Sb_2Te_5)_{100-x}Sm_x$  thin films have been performed in coplanar geometry and show minimum resistivity for thin film sample having addition of  $x = 0.4\%$  *Sm* to *GST*. The resistance-temperature (*R-T*) analysis shows the drop in resistance on crystallization in  $(Ge_2Sb_2Te_5)_{100-x}Sm_x$  thin films. The amorphous to *fcc* and *fcc* to hexagonal phase transitions have been observed from the *XRD* patterns of  $(Ge_2Sb_2Te_5)_{100-x}Sm_x$  thin films annealed at different temperatures.



### List of Publications

1. **Sanjay Kumar** and Vineet Sharma, “Improvement in stability of *GST PCMs* on *Sm* addition for memory devices,” *Journal of Non-Crystalline Solids*, vol. 532, p. 119887, Mar. 2020.
2. **Sanjay Kumar**, Pankaj Sharma, and Vineet Sharma, “Dependence of structural cross-linking, system energy and transition temperature on coordination number for *Sm* doped *GST*,” *Results in Physics*, vol. 13, p. 102276, Jun. 2019.
3. **Sanjay Kumar** and Vineet Sharma, “Enhancing the surface morphology for improved phase change mechanism by *Sm* doping in *Ge<sub>2</sub>Sb<sub>2</sub>Te<sub>5</sub>* thin films,” *Applied Physics A: Materials Science and Processing*, vol. 127, no. 3, p. 213, Mar. 2021.
4. **Sanjay Kumar** and Vineet Sharma, “Effect of local structure on the optical and dielectric behaviour of *Sm* doped *GeSbTe* phase change material,” *Optical Materials*, vol. 115, p. 111057, May 2021.
5. **Sanjay Kumar** and Vineet Sharma, “Structural transition on doping rare earth *Sm* to *Ge<sub>2</sub>Sb<sub>2</sub>Te<sub>5</sub>* phase change material,” *Journal of Alloys and Compounds*, vol. 877, p. 160246, May 2021.
6. **Sanjay Kumar** and Vineet Sharma, “Improvement in thermal stability and crystallization mechanism of *Sm* doped *Ge<sub>2</sub>Sb<sub>2</sub>Te<sub>5</sub>* thin films for phase change memory applications” *Journal of Alloys and Compounds*, p. 162316 October 2021.



### **National and International Conferences/Workshops / Short-Term Courses Attended**

1. Presented a paper entitled “Study of morphology of  $(Ge_2Sb_2Te_5)_{98.8}Sm_{1.2}$  thin film” in the international conference “Advanced Materials and Nanotechnology (*AMN-2020*)” at Jaypee Institute of Information Technology, Noida, India From 20<sup>th</sup> to 22<sup>nd</sup> February 2020.
2. Presented a poster entitled “Analysis of thermal stability on addition of rare earth elements to *Ge-Sb-Te* compounds” in 3<sup>rd</sup> Himachal Pradesh science congress jointly organized by *H.P.* council for science, technology and environment (*HIMCOSTE*), Shimla and Indian Institute of Technology (*IIT*), Mandi, from 22<sup>nd</sup> to 23<sup>rd</sup> October 2018 .
3. Attended the international virtual conference on “Frontiers in Manufacturing Technology (*FMT-2020*)” from 13<sup>th</sup> to 14<sup>th</sup> October 2020 organized by Department of Physics, School of Applied Sciences, Kalinga Institute of Industrial Technology (*KIIT*), Deemed to be University, Bhubaneswar, Odisha India.
4. Participated in the online *AICTE* recognized faculty development program on “Nanomaterials and Devices” from 25/05/2020 to 29/05/2020 organized by applied science department *NITTTR*, Chandigarh.
5. Participated in the short term course on “Materials Characterization Techniques” from 17<sup>th</sup> to 21<sup>st</sup> June 2019, sponsored by TEQIP-III and jointly organized by department of physics and department of mechanical engineering, Dr. B. R. Ambedkar National Institute of Technology, Jalandhar, Punjab, India.



<b>List of Figures</b>		
<b>Figure No.</b>	<b>Figure Captions</b>	<b>Page No.</b>
Figure 1.1	Schematic illustration of data shuffling in physically separated <i>CPU</i> and memory units.	4
Figure 1.2	(a) Cross-sectional view of mushroom type <i>PC</i> memory storage cell. (b) Read, write ( <i>SET</i> ) and erase ( <i>RESET</i> ) operation of a phase-change memory cell. Image reprinted with permission from ref. [2] copyright © 2010 IEEE.	5
Figure 1.3	The density of states as a function of energy according to the Cohen-Fritzsche-Ovshinsky model.	7
Figure 1.4	Davis and Mott model for the energy density of states.	8
Figure 1.5	Marshall and Owen model.	9
Figure 1.6	Phase diagram of <i>Ge-Sb-Te</i> alloys and a tie line between <i>Sb<sub>2</sub>Te<sub>3</sub></i> and <i>GeTe</i> .	17
Figure 1.7	Schematic representation of rewritable digital versatile disc ( <i>DVD</i> ). Adapted with permission from [63]. Copyright © 2010 American Chemical Society.	19
Figure 1.8	Device design of Phase-change Memory. “Reprinted with permission from [67]. Copyright © 2010, American Vacuum Society”.	20
Figure 1.9	<i>I-V</i> curve of phase change memory cell with amorphous and crystalline <i>Ge<sub>2</sub>Sb<sub>2</sub>Te<sub>5</sub></i> . Figure reprinted with permission from ref. [68] copyright © 2004 IEEE.	21
Figure 1.10	Reversible synaptic potentiation and depression induced in a phase change memory by an electrical pulse. The image has been reprinted with permission from ref. [47]. copyright © 2021 John Wiley and Sons.	22
Figure 1.11	Schematic representation for <i>GST</i> based <i>NIR</i> windows.	24

Figure 1.12	<i>GeTe</i> tetrahedral, 3-, 4-, 5- fold coordinated defective octahedral and octahedral structures.	25
Figure 1.13	(a) <i>GST</i> unit cell with Rocksalt <i>fcc</i> structure. (b) Hexagonal unit cell of <i>GST</i> .	26
Figure 1.14	Alternation in local structure of <i>Ge</i> from tetrahedral to octahedral on crystallization of amorphous <i>GST</i> .	27
Figure 1.15	Memory hierarchy in terms of device cost and performance.	34
Figure 2.1	Plot for the crosslinking density ( $D_{CL}$ ) value and fraction of zero frequency modes ( $M_f$ ) with increasing <i>Sm</i> concentration.	58
Figure 2.2	The substitution of few of the <i>Sb</i> atoms by the <i>Sm</i> atoms in the unit cell of <i>GST</i> is displayed.	59
Figure 2.3	Degree of covalency ( $C_c$ ) and electronegativity of $(Ge_2Sb_2Te_5)_{100-x}Sm_x$ as a function of <i>Sm</i> content.	64
Figure 2.4	Variation of band edge energy values for <i>Sm</i> added <i>GST</i> .	66
Figure 2.5	Some possible reactions of bond switching for $(GST)_{100-x}Sm_x$ and their corresponding barrier energies.	70-71
Figure 2.6	The variation of $\Delta V_{th}$ and $CSME$ with <i>Sm</i> content and the inset showing the linear dependence of obtained values of $\Delta V_{th}$ with $CSME$ for $(Ge_2Sb_2Te_5)_{100-x}Sm_x$ .	76
Figure 3.1	Temperature dependence of volume and enthalpy for crystalline and glassy solids.	87
Figure 3.2	(a) Quartz Ampoule. (b) Vacuum Sealing of Ampoule. (c) Sealed Ampoule.	89
Figure 3.3	(a) Process of thermal evaporation. (b) Thermal Evaporation unit.	91
Figure 3.4	(a) Electron beam evaporation process. (b) DC power supply for high voltage electron gun.	92

Figure 3.5	(a) Diagrammatic representation of <i>XRD</i> working principle. (b) X-ray diffractometer model PANalytical, X'Pert Pro exploited for <i>XRD</i> analysis.	96
Figure 3.6	Working principle of <i>EDS</i> with X-ray emission.	98
Figure 3.7	Schematic representation of interaction of primary electron beam with matter	99
Figure 3.8	(a) Schematic illustration of <i>XPS</i> . (b) Thermo Scientific <i>NEXSA XPS</i> setup.	101
Figure 3.9	Energy transition in Rayleigh scattering and Raman scattering	102
Figure 3.10	Raman spectrometer model Horiba Jobin-Yvon LabRAM HR evolution ( <i>IIT Mandi</i> ) used for analysis.	102
Figure 3.11	Block diagram of <i>UV-Vis-NIR</i> spectrophotometer.	104
Figure 3.12	<i>UV-Vis-NIR</i> spectrophotometer (model Perkin Elmer Lambda 750) used to measure optical transmission.	105
Figure 3.13	Transmittance spectra of thin films with upper envelope ( $T_M$ ) and lower envelope ( $T_m$ ) and transmittance of a glass substrate.	105
Figure 3.14	Keithley 6487 electrometer used for the electrical measurements of prepared samples.	109
Figure 3.15	Schematic representation of co-planar geometry for the measurements of electrical properties of thin films.	109
Figure 4.1	<i>XRD</i> spectra of $(Ge_2Sb_2Te_5)_{100-x}Sm_x$ alloys.	119
Figure 4.2	Plot of $d_{103}$ -spacing of $(Ge_2Sb_2Te_5)_{100-x}Sm_x$ alloys with <i>Sm</i> content.	119
Figure 4.3(a-g)	$(Ge_2Sb_2Te_5)_{100-x}Sm_x$ ( $x = 0, 0.2, 0.4, 0.6, 0.8, 1.0, 1.2$ ) rietveld refinement for <i>XRD</i> patterns.	121-124
Figure 4.4	Raman spectra of $(Ge_2Sb_2Te_5)_{100-x}Sm_x$ alloys.	127

Figure 4.5(a-g)	Raman active modes Gaussian peak fitting for <i>Sm</i> added <i>GST</i> .	129-131
Figure 4.6	$(Ge_2Sb_2Te_5)_{100-x}Sm_x$ ( $x = 0, 0.2, 0.4, 0.6, 0.8, 1.0, 1.2$ ) FTIR transmittance spectra in <i>Far-IR</i> wavelength range.	132
Figure 4.7	The <i>XRD</i> spectra for $(Ge_2Sb_2Te_5)_{100-x}Sm_x$ thin films.	133
Figure 4.8 (a)	<i>Te 3d XPS</i> spectra for thin films of $(Ge_2Sb_2Te_5)_{100-x}Sm_x$ .	134
Figure 4.8(b)	<i>Sb 3d XPS</i> spectra of $(Ge_2Sb_2Te_5)_{100-x}Sm_x$ thin films.	135
Figure 4.9(a)	<i>XPS</i> spectra for <i>Ge 3d</i> , <i>Sb 4d</i> along with <i>Te 4d</i> in thin films of $(Ge_2Sb_2Te_5)_{100-x}Sm_x$ .	136
Figure 4.9(b)	<i>XPS</i> spectra of <i>Sm 3d</i> core-level in thin films of $(Ge_2Sb_2Te_5)_{100-x}Sm_x$ .	137
Figure 5.1	<i>EDX</i> spectra of $(Ge_2Sb_2Te_5)_{100-x}Sm_x$ thin films.	149-150
Figure 5.2	(a) <i>FESEM</i> top-view image of $(Ge_2Sb_2Te_5)_{100-x}Sm_x$ ( $x = 1.2$ ) thin film and inset shows the histogram of particle size. (b) Thickness of $(Ge_2Sb_2Te_5)_{100-x}Sm_x$ ( $x = 1.2$ ) thin film measured using <i>FESEM</i> cross section image.	151
Figure 5.3	<i>FESEM</i> mapping of thin film of $(Ge_2Sb_2Te_5)_{100-x}Sm_x$ ( $x = 1.2$ ).	151-152
Figure 5.4	The transmittance spectra of $(Ge_2Sb_2Te_5)_{100-x}Sm_x$ thin films.	153
Figure 5.5	The linear index of refraction for $(Ge_2Sb_2Te_5)_{100-x}Sm_x$ thin films.	153
Figure 5.6	The plot of optical absorption coefficient ( $\alpha$ ) against photon energy ( $h\nu$ ) for $(Ge_2Sb_2Te_5)_{100-x}Sm_x$ thin films.	154
Figure 5.7	Tauc plots for $(Ge_2Sb_2Te_5)_{100-x}Sm_x$ thin films.	156
Figure 5.8	$(n^2-1)^{-1}$ vs $(h\nu)^2$ plot for $(Ge_2Sb_2Te_5)_{100-x}Sm_x$ thin films.	157
Figure 5.9	$n^2$ vs $\lambda^2$ plot for $(Ge_2Sb_2Te_5)_{100-x}Sm_x$ thin films.	159

Figure 5.10	(a) The plots of wavelength versus $\varepsilon_1$ (b) and $\varepsilon_2$ for $(Ge_2Sb_2Te_5)_{100-x}Sm_x$ thin films.	160
Figure 5.11	Wavelength dependence of dielectric loss of $(Ge_2Sb_2Te_5)_{100-x}Sm_x$ thin films.	161
Figure 5.12	(a) <i>SELF</i> , Surface energy loss function. (b) <i>BELF</i> , Bulk energy loss function for thin films of $(Ge_2Sb_2Te_5)_{100-x}Sm_x$ .	162
Figure 5.13	A plot of $\sigma$ vs $\lambda$ for $(Ge_2Sb_2Te_5)_{100-x}Sm_x$ thin films.	163
Figure 6.1	<i>DSC</i> thermogram of $(Ge_2Sb_2Te_5)_{100-x}Sm_x$ thin films obtained at <i>10K/min</i> linear heating rate.	176
Figure 6.2	The crystallization fraction ( $\chi$ ) of <i>fcc</i> phase of $(Ge_2Sb_2Te_5)_{100-x}Sm_x$ phase change materials.	178
Figure 6.3	The $\ln(\ln(1-\chi)^{-1})$ vs $1000/T$ plots of $(Ge_2Sb_2Te_5)_{100-x}Sm_x$ for <i>fcc</i> crystallization.	179-180
Figure 6.4	The $\ln(d\chi/dt)$ vs. $1000/T$ plots of $(Ge_2Sb_2Te_5)_{100-x}Sm_x$ for <i>fcc</i> crystallization.	181
Figure 6.5	<i>I-V</i> characteristics of $(Ge_2Sb_2Te_5)_{100-x}Sm_x$ thin films.	183
Figure 6.6	Electrical resistivity of $(Ge_2Sb_2Te_5)_{100-x}Sm_x$ thin films.	184
Figure 6.7	Temperature dependent electrical resistance of $(Ge_2Sb_2Te_5)_{100-x}Sm_x$ thin films.	185
Figure 6.8	<i>XRD</i> patterns of $(Ge_2Sb_2Te_5)_{100-x}Sm_x$ thin films annealed at $50^\circ C$ , $160^\circ C$ and $250^\circ C$ temperature.	186-188

<b>List of Tables</b>		
<b>Table No.</b>	<b>Table Captions</b>	<b>Page No.</b>
Table 1.1	The comparison of device performance of Phase change memory, Flash memories and <i>DRAM</i> . Tabulated data reprinted with permission from ref. [2] copyright © 2010 IEEE.	35
Table 2.1	The computed values of physical parameters of $(Ge_2Sb_2Te_5)_{100-x}Sm_x$ as a function of <i>Sm</i> content.	59
Table 2.2	Calculated values of density ( $\rho$ <i>cal.</i> ), theoretical volume ( $V_t$ ), molar volume ( $V_m$ ), compactness ( $\delta$ ), molar mass ( $M$ ), free volume ratio ( <i>FVR</i> ) and number of bonds per unit volume ( $N$ ) and experimentally obtained values of density ( $\rho$ <i>exp.</i> ) for $(Ge_2Sb_2Te_5)_{100-x}Sm_x$ .	62
Table 2.3	Theoretical band gap ( $E_g$ ), cohesive energy ( <i>C.E.</i> ), $H_S$ and $H_S/Z$ values of $(Ge_2Sb_2Te_5)_{100-x}Sm_x$ system.	65
Table 2.4	The values of chalcogen content ( $R$ ), heteropolar and homopolar bond energies $E_c$ , $E_{rm}$ and mean bond energy $\langle E \rangle$ , glass transition temperature ( $T_g$ ) of $(Ge_2Sb_2Te_5)_{100-x}Sm_x$ evaluated by adopting the Tanaka [26], Gibbs [45], Tichy [44] and Rockstad [46] approaches.	69
Table 2.5	Average valence shell electrons ( $\bar{Z}$ ), metallicity ( $M$ ), covalent coupling of structural networks ( $C_N$ ), <i>CSME</i> and change in threshold switching voltage ( $\Delta V_{th}$ ) of $(Ge_2Sb_2Te_5)_{100-x}Sm_x$ ( $x = 0, 0.2, 0.4, 0.6, 0.8, 1.0, 1.2$ ).	73
Table 2.6	The fractions of bonds formed in <i>Sm</i> doped <i>GST</i> phase change materials and coefficient of ionicity ( $I_c$ ).	74
Table 4.1	The values of $d_{106}$ -spacing, $D_{hkl}$ and $\varepsilon$ for $(Ge_2Sb_2Te_5)_{100-x}Sm_x$ alloys.	120
Table 4.2	The lattice parameters along with phase fractions of <i>fcc</i> and hexagonal phases for $(Ge_2Sb_2Te_5)_{100-x}Sm_x$ alloys.	125

Table 4.3	The ratios of peak area and Raman shift of $(Ge_2Sb_2Te_5)_{100-x}Sm_x$ alloys.	128
Table 4.4	$(Ge_2Sb_2Te_5)_{100-x}Sm_x$ thin films compositions observed employing <i>XPS</i> measurements and corresponding stoichiometric compositions.	138
Table 5.1	$(Ge_2Sb_2Te_5)_{100-x}Sm_x$ ( $x = 0, 0.8$ ) thin film's compositional analysis.	149
Table 5.2	Thickness of thin film ( $d$ ), optical band gap ( $E_g$ ) evaluated employing the Tauc and <i>WDD</i> methods, Urbach energy or tailing width ( $E_u$ ), dispersion energy ( $E_d$ ), single oscillator energy ( $E_o$ ), ordered parameter ( $B^{1/2}$ ) and cation coordination ( $N_c$ ) for $(Ge_2Sb_2Te_5)_{100-x}Sm_x$ thin films.	155
Table 5.3	The value of parameters <i>viz.</i> high-frequency dielectric constant ( $\epsilon_\infty$ ), $N/m^*$ ratio, $M_{-3}$ and $M_{-1}$ negative momentum coefficients, static refractive index ( $n_0$ ), static dielectric constant ( $\epsilon_L$ ) and plasma frequency ( $\omega_{plasma}^2$ ) for <i>Sm</i> doped <i>GST</i> .	159
Table 5.4	Linear optical susceptibility ( $\chi^{(1)}$ ), non-linear refractive index ( $n_2$ ), 3 <sup>rd</sup> order non-linear susceptibility ( $\chi^{(3)}$ ), as well as optical electronegativity ( $\eta_{opt}$ ) for $(Ge_2Sb_2Te_5)_{100-x}Sm_x$ thin films.	164
Table 6.1	Onset and peak crystallization temperature and $T_m$ values for $(Ge_2Sb_2Te_5)_{100-x}Sm_x$ thin films.	175
Table 6.2	The activation energy for <i>fcc</i> crystallization in $(Ge_2Sb_2Te_5)_{100-x}Sm_x$ samples.	177
Table 6.3	The evaluated values of parameters of $(Ge_2Sb_2Te_5)_{100-x}Sm_x$ for the estimation of hexagonal phase crystallization kinetics.	179

## List of Acronym and Abbreviations

$\chi^{(3)}$	3 <sup>rd</sup> Order Non-Linear Optical Susceptibility
<i>ACI</i>	Acoustic Impedance
<i>AIST</i>	<i>AgInSbTe</i>
<i>AI</i>	Artificial Intelligence
$n_1$	Avrami Exponent for <i>fcc</i> Crystallization
$n_2$	Avrami Exponent for Hexagonal Crystallization
$N_\alpha$	Bond Bending Constraints
$N_\beta$	Bond Stretching Constraints
<i>BELF</i>	Bulk Energy Loss Function
<i>CPU</i>	Central Processing Unit
$\Delta V_{th}$	Change in Threshold Switching Voltage
<i>CCD</i>	Charge-Coupled Device
<i>CBA</i>	Chemical Bond Approach
<i>CVD</i>	Chemical Vapor Deposition
$I_c$	Coefficient of Ionicity
<i>C.E.</i>	Cohesive Energy
<i>CD</i>	Compact Disc
$\delta$	Compactness
$E^0_{CB}$	Conduction Band Edge Energy
$C_N$	Covalent Coupling of Structural Network
<i>CSME</i>	Criterion for Structural Modification Efficiency

$D_{CL}$	Cross-linking Density
$D_{hkl}$	Crystallite Size
$E_c$	Crystallization Activation Energy
$\chi$	Crystallization fraction
$T_c$	Crystallization Onset
$I-V$	Current Voltage
$\sigma_{dc}$	DC Electrical Conductivity
$C_c$	Degree of Covalency
$\rho$	Density
$DFT$	Density Functional Theory
$DSC$	Differential Scanning Calorimetry
$DTM$	Digital Thickness Monitor
$DVD$	Digital Video Disc
$E_d$	Dispersion Energy
$DRAM$	Dynamic Random Access Memory
$\Delta\phi$	Efficiency of Structural modification
$\rho_e$	Electrical Resistivity
$ESCA$	Electron Spectroscopy for Chemical Analysis
$EDX$	Energy Dispersive X-Ray
$EDS$	Energy-Dispersive X-Ray Spectroscopy
$k$	Extinction Coefficient
$fcc$	Face Centered Cubic

$T_{p1}$	<i>fcc</i> Peak Crystallization Temperature
$E_{c1}$	<i>fcc</i> Phase Crystallization Activation Energy
<i>FESEM</i>	Field Emission Scanning Electron Microscopy
<i>ZT</i>	Figure of Merit
<i>FTIR</i>	Fourier Transform Infrared Spectroscopy
$M_f$	Fraction of Zero Frequency Modes
$N/m^*$	Free Carrier Concentration to Effective Mass Ratio
<i>FVR</i>	Free Volume Ratio
<i>GST</i>	$Ge_2Sb_2Te_5$
<i>GFA</i>	Glass Forming Ability
$T_g$	Glass Transition Temperature
<i>HDD</i>	Hard Disc Drive
$\Delta C_p$	Heat Capacity Change
$H_s$	Heat of Atomization
$E_{c2}$	Hexagonal Phase Crystallization Activation Energy
$T_{p2}$	Hexagonal Phase Peak Crystallization Temperature
$\epsilon_\infty$	High Frequency Dielectric Constant
$\epsilon_2$	Imaginary Dielectric Constant
$h\nu$	Incident Photon Energy
<i>JMA</i>	Johnson-Mehl-Avrami
<i>LED</i>	Light Emitting Diode
<i>L</i>	Lone Pair Electrons

$Z$	Mean coordination Number
$T_m$	Melting Temperature
$M$	Metallicity
$V_m$	Molar Volume
$NIR$	Near Infrared
$N_{con}$	Net Constraints
$n_2$	Non-linear Refractive Index
$\alpha$	Optical Absorption coefficient
$E_g$	Optical Band Gap
$\sigma$	Optical Conductivity
$\eta_{opt}$	Optical Electronegativity
$T_p$	Peak Crystallization Temperature
$PC$	Phase Change
$PCM$	Phase Change Materials
$PVD$	Physical Vapor Deposition
$\omega_{Plasma}$	Plasma Frequency
$P$	Polarizability
$PLD$	Pulsed Laser Deposition
$\epsilon_l$	Real Dielectric Constant
$T_{rg}$	Reduced Glass Transition Temperature
$n$	Refractive Index
$E_0$	Single Oscillator Energy

<i>SSD</i>	Solid State Drive
$C_p$	Specific Heat Capacity
$\epsilon_L$	Static Dielectric constant
<i>SRAM</i>	Static Random Access Memory
$n_0$	Static Refractive Index
<i>SEM</i>	Surface Electron Microscopy
<i>SELF</i>	Surface Energy Loss Function
$B^{1/2}$	Tauc Order Parameter
<i>R-T</i>	Temperature-Resistance
$V_i$	Theoretical Molar Volume
<i>d</i>	Thin Film Thickness
$V_{th}$	Threshold Voltage
<i>TFC</i>	Tooling Factor
<i>TEM</i>	Transmission Electron Microscopy
$E_u$	Urbach Energy
<i>VAP</i>	Valence Alternation Pair
$E_{VB}^0$	Valence Band Edge Energy
<i>WDD</i>	Wemple –DiDomenico
<i>XRD</i>	X –Ray Diffraction
<i>XPS</i>	X-Ray Photoelectron Spectroscopy

**Chapter 1**  
**Introduction**



The information technology today has gained the huge attention of each individual for the digitalization in every sector. Most of the tasks are today driven by computer systems. Human civilization has been largely influenced by digitalization and has played a major role in the development of society. Today the advancement in information technology has made it possible to communicate with in a fraction of a second not only to the person in a distant part of the earth but also to the space. Due to an increasing demand for information technology the global data size is increasing at a very fast rate day by day and will soon go beyond the capacities of existing storage devices. The requirement of devices for huge data storage has also increased with the increasing demands of Artificial Intelligence (*AI*) based applications and establishment of 5G technology. The global data size has reached 64 zettabytes by the end of 2020 and is expected to reach 180 zettabytes within the next five years. Our conventional memory technology is lacking in many aspects to reach the goals of increasing global data size.

The conventional computer systems are based upon the traditional von Neumann computing architecture. The central processing unit (*CPU*) and memory units such as dynamic random access memory (*DRAM*) are physically separated in computer systems as shown in figure 1.1. One of the main bottlenecks of von Neumann's computing architecture is the several times back and forth data shuffling between *CPU* and *DRAM* which limits the computing performance. With the increasing demand for data storage and processing the development of a new class of next-generation non-volatile memories are under active research in the past few decades. In view of this, the phase change memory technology has been considered as one of the potential candidates for the next-generation non-volatile memory technology because of its ability to unify the performances of *DRAM* and cache memory. Phase change memory can bridge the performance gap between cache memory and *DRAM* in terms of programming speed, data storage density, persistent data storage capability. Among all the next-generation non-volatile memory technologies, the chalcogenide phase change materials (*PCM*) based memories have attained the potential interest and are the most mature memory technology. The use of *DRAM* based main memory in high performance computer systems has also limitations in terms of the device cost and power consumption. Over 40% of the total system energy is consumed by the main memory unit. The use of phase change memories is also advantageous in view of low cost and reduced power consumption for the high performance computing. However there are several challenges which must be addressed for the replacement of *DRAM* by the phase change

memory. The improvement in operating speed of phase change memories is required for the commercialization of this technology.

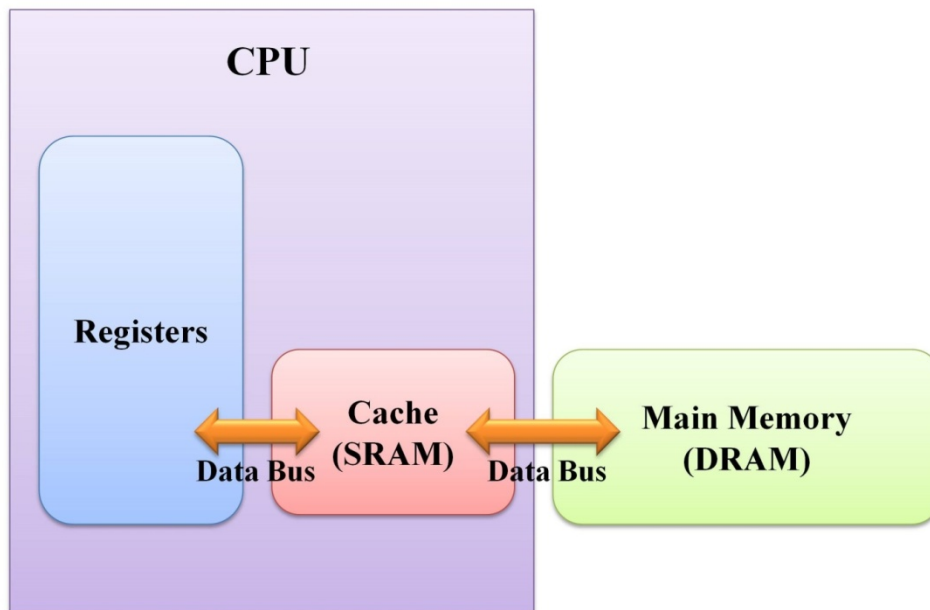


**Figure 1.1.** Schematic illustration of data shuffling in physically separated *CPU* and memory units.

Phase change memory utilizes the amorphous (high resistance) to crystalline (low resistance) switching of the material for data storage applications. Figure 1.2(a) shows the cross-sectional view of mushroom type *PC* memory one-bit storage cell. The read, write (*SET*) and erase (*RESET*) operations of the phase change memory cell are implemented by applying the sufficient electric current between the top and bottom electrodes. The *RESET* operation is implemented by applying the large current for a shorter time ( $< 50$  ns) leading to the melting of programmable material and the subsequent quenching leaves it behind with the high resistance state [1]. Similarly, the *SET* operation is implemented in a *PC* memory cell by applying the medium electric pulse to anneal the programming region above the crystallization temperature for a longer time enough for crystallization (typically  $100$  ns- $10\mu$ s) [1]. A comparatively lower electric pulse is applied between the top and bottom electrodes to read the state of *PC* memory cell as has been shown in figure 1.2(b). The resistive switching in *PCMs* is the result of the change in the local atomic structure of the amorphous phase on heating. The change in local structure on phase transition results in the alteration in the electrical and optical properties of *PCMs*.

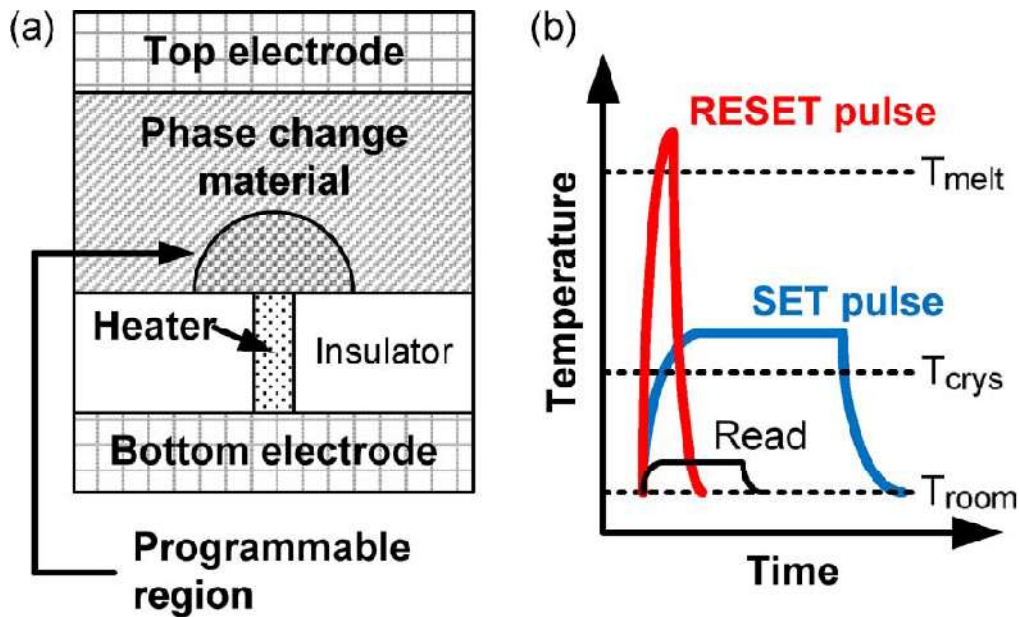


**Figure 1.2 (a).** Cross-sectional view of mushroom type *PC* memory storage cell. **(b)** Read, write (*SET*) and erase (*RESET*) operation of a phase-change memory cell. Image reprinted with permission from ref. [2] copyright © 2010 IEEE.

The crystallization kinetics of amorphous structures describes the long term data stability and switching speed of memory device. Understanding the underlying mechanism of phase transition necessitates the in-depth knowledge of involvement of atomic structures in switching and concept of electron localization, electron transport properties and the lack of long-range ordering in amorphous semiconductors.

### 1.1 Amorphous Semiconductors

Solids are broadly classified into two categories, crystalline solids and amorphous solids. The crystalline solids comprise of the regular long-range three-dimensional periodic array of atoms, ions, or molecules with a well-defined crystal structure. Whereas amorphous solids lack the long-range translational symmetry of atomic arrangements, however, the short-range order is preserved in the amorphous solids. The properties of amorphous solids are described by the nature of chemical bonding between the neighboring atoms. Due to the absence of periodic ordering of atoms in amorphous solids the electron wave function cannot be expressed by Bloch function similar to the crystalline solids. The lack of periodicity and the presence of short-range ordering and medium-range ordering of atoms in amorphous solids define their optical and electronic properties. Amorphous solids can be prepared in two ways, either by the condensation of the vapor such as vacuum evaporation, glow discharge

decomposition, sputtering or by melt quenching. Among all these methods the first type of method is used for thin-film depositions and the second type is for the synthesis of bulk materials.

According to the type of bonding, amorphous solids possess different electrical properties based on which they are categorized as conductors, semiconductors, or insulators. Among them, amorphous semiconductors show a wide range of applications in transistors, amorphous *Si*-based p-n junction diode, photovoltaic devices, non-volatile memories, solar cells, night vision *IR* glasses, *etc.* The semiconducting nature of amorphous solids was first studied by Kolomiets and Goryunova [3], [4]. Amorphous semiconductors find immense applications in the large area of electronics because of low free carrier mobility. On the basis of the difference between the types of bonding in amorphous semiconductors, they can be broadly classified as tetrahedrally bonded amorphous semiconductors such as *a-Si*, *a-Si:H*, *a-Ge*, *etc.* and chalcogenide glasses. The absence of long-range order and the presence of defects in amorphous semiconductors lead to tailing of the conduction band edge and valence band edge and results in the appearance of localized states.

The electronic properties of amorphous semiconductors can be better explained with the help of an energy band diagram illustrated in figure 1.3. The origin of sharp conduction band edge and valence band edge separated by forbidden energy gap in the crystalline solids is due to the presence of periodic potential wells and long-range order of atomic arrangements. The amorphous solids exhibit a high degree of disorder and the presence of non-periodic potentials induces the tailing of band edges resulting in the finite density of states in the middle of the energy gap. The mobility of electrons falls drastically in the tailing states and the electron wave functions are localized for these states. The edges at the density of states where the mobility of electrons falls drastically are called the mobility edges. The mobility edge on the conduction band is known as the conduction band edge and the mobility edge on the valence band side is called the valence band edge and the gap separating them is referred to as the mobility gap.

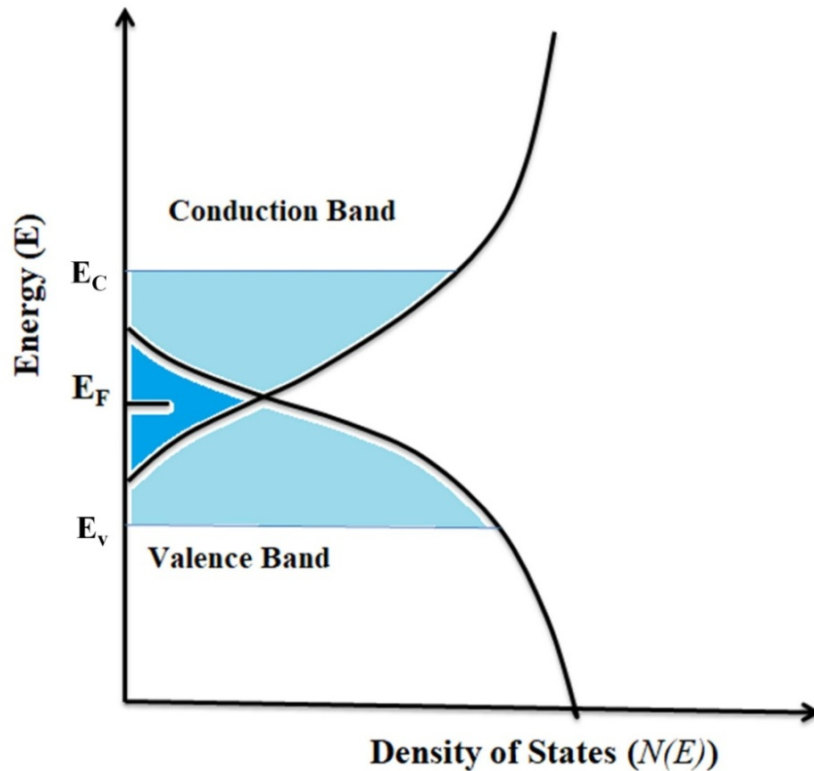


**Figure 1.3.** The density of states as a function of energy according to the Cohen-Fritzsche-Ovshinsky model.

Various band models have been developed to understand the electrical properties of amorphous solids. Cohen, Fritzsche and Ovshinsky in 1969 has developed a model for the chemical inertness of covalently bonded amorphous semiconductors and assumed that the overlapping of localized tailing states arise due to the compositional and topological disorder resulting in finite density of states in the middle of energy gap [5]. The redistribution of charges takes place in the middle of the gap and few of the electrons or negatively charged defects occupy the states near the conduction band edge and the positively charged defects occupy states near the valence band edge below the Fermi level as has been displayed in figure 1.3. This model successfully explains the pinning of the Fermi level near the middle of the energy gap resulting in the intrinsic nature of amorphous semiconductors.

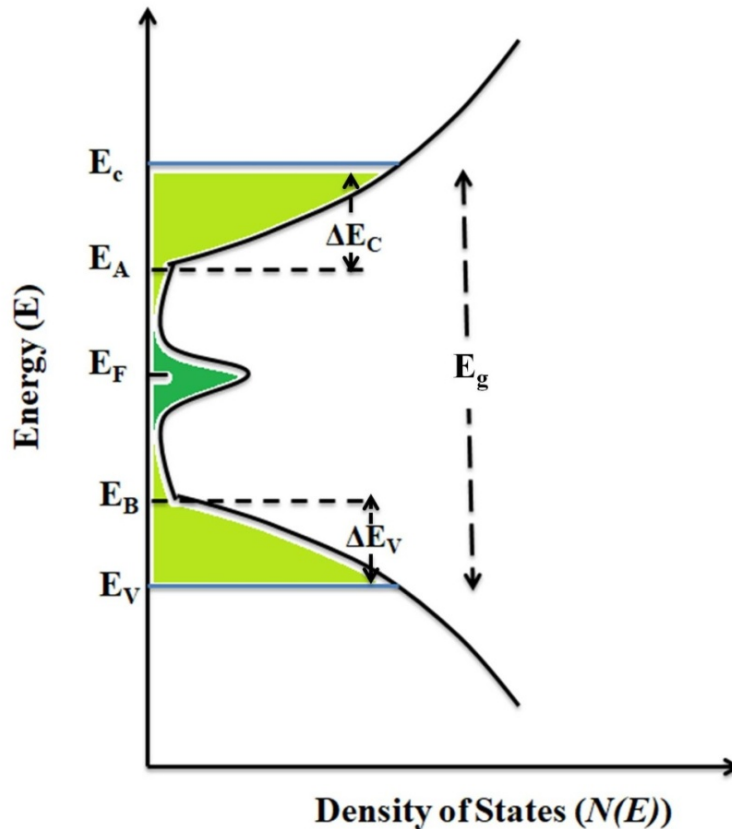


**Figure 1.4.** Davis and Mott model for the energy density of states.

Later on, Davis and Mott also proposed a model to explain the pinning of the Fermi level near the middle of the energy gap [6]. Based on this model the tailing states extend within few tens of  $eV$  and suggests the existence of donor and acceptor levels near the Fermi level which causes the pinning of Fermi level (Figure 1.4). According to this model, the presence of vacancy defects, dangling bonds and non-bonding lone pair electrons in amorphous materials results in the appearance of states near the center of the energy band which results in the pinning of the Fermi level near the middle of the energy gap with variation in compositions. Marshall and Owen in 1971 proposed a model with the concept of a self-compensating mechanism of fixing the Fermi level near the middle of the energy gap [7]. Figure 1.5 displays the energy band diagram presented by Marshall and Owen. The pinning of the Fermi level of amorphous semiconductors displays their intrinsic nature on variation in composition. Amorphous semiconductors also exhibit a wide variety of photo induced phenomena because of the relaxation of metastable structure on the exposure of light with a wavelength of the order of band gap of materials. Amorphous semiconductors are categorized into different following categories.

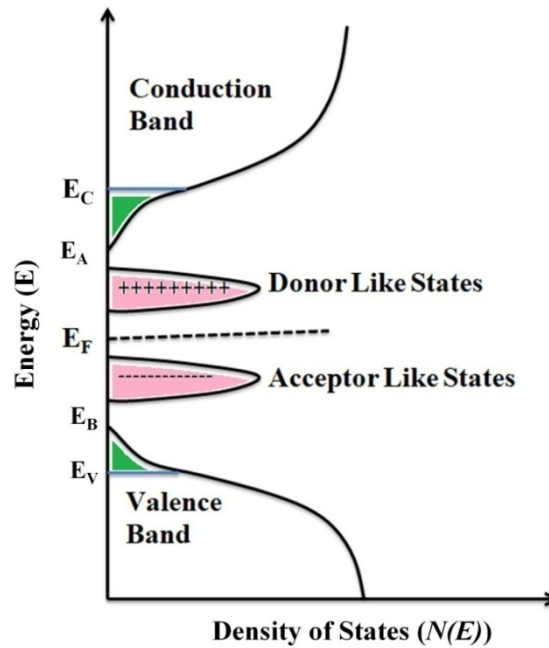


Figure 1.5. Marshall and Owen model.

### 1.1.1 Tetrahedrally Coordinated Semiconductors

The compounds of group III-V such as *GaAs*, *GaSb*, *etc.* and wide bandgap semiconductors of group II-VI such as *CdTe*, *ZnS*, *etc.*, and the compounds of group IV amorphous semiconductors such as amorphous *Si*, *Ge*, *SiC*, *etc.* constitute this class of semiconductors. The atoms in this class of semiconductors are bonded covalently. These types of semiconductors cover a wide range of applications in solar cells, sensors, transistors, optoelectronic devices, *LEDs*, *etc.*

### 1.1.2 Chalcogenide Glasses

The alloys of group VI elements *S*, *Se*, and *Te* such as *As<sub>2</sub>Se<sub>3</sub>*, *Ge-Sb-Se*, *Ge-Sb-Te*, *Ag-In-Sb-Te*, *etc.* are referred to as chalcogenides. Chalcogenides find a wide range of applications in memory storage, optoelectronic devices, biomedical applications, optical fibers, optical switching, *etc.* because of their inherent structural, optical, electrical, and thermal properties. Chalcogenides form covalent bonds and follow the 8-N rule in the amorphous phase. Sulfur-based chalcogenide alloys exhibit high refractive index and large optical nonlinearity and good transparency in the *IR* region and hence, find applications in optoelectronic devices. Selenium-based alloys are mostly used for the practical applications in solar cells, xerography, photovoltaic devices and biomedical applications. Tellurium-based

alloys are used in data storage applications such as phase-change memory and infrared detectors.

The bandgap of chalcogenide alloys ranges from  $0.3 \text{ eV}$  to  $3 \text{ eV}$ . Most of the chalcogenides exhibit the phenomenon of glass transition. Glass transition is achieved by rapidly cooling the liquid melt below its melting temperature ( $T_m$ ) which results in the increase in viscosity of the supercooled liquid and subsequently attaining the glassy state when the viscosity reaches  $\sim 10^{14.5}$  poise. The chalcogenides exhibiting the glass transition temperature are referred to as chalcogenides glass. Below the glass transition temperature, the glassy materials undergo structural relaxation with aging and the specific heat capacity increases drastically. The glass-forming ability of any material depends largely on the presence of lone pair electrons and coordination numbers. Semiconducting chalcogenide glasses are further divided into two categories, *viz.*, elemental lone pair semiconductors and crosslinked semiconductors. The bonding between molecular complexes of lone pair semiconductors is weak van der Waal type whereas crosslinked semiconductors constitute the rigid three-dimensional structural networks. Based upon the inherent bonding and structural features, the chalcogenide glasses possess the following unique properties.

### 1.1.2.1 Bandgap and Electrical Properties

Chalcogenide glasses exhibit the intrinsic semiconducting behaviour, *i.e.*, the position of Fermi level is unchanged with the doping and has been well explained by Kolomiets [3], [4] and Mott [6] on account of the presence of charged defects states.

The chalcogenide glasses show semiconducting nature at room temperature. The magnitude of the band gap of chalcogenide glasses is dependent on several factors such as material compositions, temperature, method of preparation *etc.* The chalcogenide glasses display p-type semiconducting characteristics with holes as the free carriers for electrical conduction. The glasses rich in *Te* content show the metallic character with a bandgap of the order of  $\sim 1 \text{ eV}$  and the bandgap decreases with *Te* content. The mobility of free carriers in chalcogenide glasses increases many folds with the temperature which is due to the crystallization induced on heat treatment. The annealing of chalcogenide glasses results in the removal of mid-gap defect states and shows decrease in band tailing width. The chalcogenide glasses exhibit crystallization on annealing causing an increase in conductivity and a decrease in bandgap and midgap states. The conductivity of chalcogenide glasses is comparatively smaller in the amorphous phase than the corresponding crystalline phase because of the lower

mobility of free carriers in the amorphous phase. The hole mobility of *Se* at room temperature is  $0.1 \text{ cm}^2 (\text{Vs})^{-1}$ . The electrical transport mechanism in chalcogenide glasses is based upon the hopping of holes between the states in the gap. The position of Fermi level in chalcogenide glasses is unchanged on doping and is maintained at the center of the bandgap because of the presence of deep donor and deep acceptors levels which displays the intrinsic nature of chalcogenide semiconductors.

The dc electrical conductivity of chalcogenide glasses is dependent on the temperature through the relation

$$\sigma_{dc} = \sigma_0 \exp \left[ \frac{-\Delta E}{kT} \right]$$

where  $\Delta E$  represents the activation energy,  $k$  denotes the Boltzmann constant and  $\sigma_0$  is the pre-exponential factor. The conduction mechanism in chalcogenide glasses can be due to the band conduction and or hopping conduction. The band conduction in chalcogenide glasses above the electric field of  $10^4 \text{ V/cm}$  can be explained using the Poole-Frenkel mechanism which describes the excitation of free carriers that occurs between the valance band and conduction band tailing states above the mobility edges at low temperature and by the hopping conduction mechanism causing the excitation near the band edges [8]. Hopping is the process of conduction where charge carriers are excited within the trap centers. The total conductivity of chalcogenide glasses is the sum of intrinsic conductivity due to band conduction and hopping conductivity.

The temperature dependent dc conductivity of thin films of *S* doped  $\text{In}_4\text{Se}_{96}$  from  $300 \text{ K}$  to  $370 \text{ K}$  has been reported by Ganaie *et al.* and observed the conduction in thin films by the thermally activated process [9]. The dc conductivity of *S* doped  $\text{In}_4\text{Se}_{96}$  has been observed to decrease with the *S* content from  $2.8 \times 10^{-8} \Omega^{-1}\text{cm}^{-1}$  to  $5.3 \times 10^{-9} \Omega^{-1}\text{cm}^{-1}$  and increase with the temperature. Alvi *et al.* reported the effect of illumination of  $1500 \text{ W}$  tungsten lamp white light on the dc conductivity of  $\text{Ga}_{15}\text{Se}_{81}\text{Ag}_4$  at  $358 \text{ K}$  temperature and suggested the hopping conduction mechanism for charge carriers in the tailing states [10]. The dc conductivity of thermally deposited  $\text{Ga}_{15}\text{Se}_{81}\text{Ag}_4$  thin films has been observed to increase with the increase in illumination time of tungsten lamp white light. Al-Agel reported the conduction due to thermally assisted tunneling of carriers in the localized states for  $\text{Ga}_{15}\text{Se}_{77}\text{In}_8$  thin films and found the activation energy to decrease and dc conductivity to increase in  $\text{Ga}_{15}\text{Se}_{77}\text{In}_8$  thin films on increasing the annealing temperature from  $333 \text{ K}$  to  $363 \text{ K}$  [11]. Behera *et al.*

reported an increase in the electrical conductivity of thermally evaporated thin films of  $As_{40}Se_{60-x}Bi_x$  ( $x = 2, 7, 10$  and  $15\%$ ) with  $Bi$  content [12]. Sharma *et al.* observed rise in dark conductivity on  $In$  doping due to rise in hopping conduction and found the activation energy of  $Se_{58-x}Te_{15}In_x$  ( $x = 0, 2, 4, 6$  and  $10$  at%) to decrease with  $In$  concentration [13]. Poole-Frenkel conduction mechanism of multi-component  $Se-Te-In-Pb$  thin films has been observed by Anjali *et al.* [14]. Ojha *et al.* studied the nature of conduction mechanism in  $Cu-S-Te$  system and observed an increase in the dc conductivity with temperature due to its semiconducting nature [15]. The conduction due to variable range hopping of charge carriers near Fermi level at a low temperature and thermally assisted charge carrier tunnelling process in the extended states at a higher temperature has been observed in the similar study [15]. Electrical measurements of  $Ge_{50}In_4Ga_{13}Se_{33}$  thin films has been carried out by Assim and Elmetwally and observed the dc electrical conductivity due to thermally activated process in  $293\text{ K}-413\text{ K}$  temperature range [16].

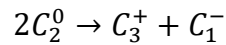
### 1.1.2.2. Defect States

The ideal glasses are those where all the atoms satisfy the valence requirements and obey the  $8-N$  rule. The deviation in stoichiometry leads to the deviation from the  $8-N$  rule leading to the origin of defects in chalcogenide glasses due to the unsatisfied bonds also known as dangling bonds. Ovshinsky suggested that the interaction between the lone pair electrons in chalcogenides with the local environment results in the formation of localized gap states [5]. The defect states due to the dangling bonds lie near the middle of the mobility gap. The presence of gap states in chalcogenide glasses plays a significant role in the electrical conduction and optical absorption processes [17]. Ideally, glasses must possess only the energetically favorable heteropolar bonds, but, the real glasses exhibit the large fraction of energetically less favorable homopolar wrong bonds and unsatisfied bonds or dangling bonds [18]. Anderson postulated the strong coupling between the electron and phonon resulting in the electron pairing of unsatisfied dangling bonds with negative correlation energy for pairing [19].

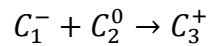


where  $D^0$  denotes the neutral dangling bond with one electron,  $D^-$  and  $D^+$  denote the negatively and positively charged dangling bonds respectively.

Street and Mott proposed the existence of a large density of dangling bonds ( $\sim 10^{18} \text{ cm}^{-3}$ ) in lone pair chalcogenide semiconductors which can act as acceptors and donors [20]. Kastner put forward the valence alternation pair model for the formation of charged defects in over-coordinated chalcogenide glasses [17]. Based on this model the chalcogen atom in the ground state is two-fold coordinated ( $C_2^0$ ) which forms one positively charged 3 fold coordinated chalcogen atom ( $C_3^+$ ) and one negatively charged singly coordinated chalcogen atom ( $C_1^-$ ).



The pair of positively and negatively charged chalcogen atoms formed in this process is referred to as valence alternation pair (*VAP*). The density of *VAPs* is very high in most of the chalcogenide glasses due to the low formation energy of *VAPs*.  $C_2^0$  and  $C_1^-$  further forms the  $C_3^+$  with the following process.



The presence of *VAPs* in chalcogenide glasses accounts for their unusual properties and plays an important role in photoinduced diffusion and crystallization processes.

### 1.1.2.3. Optical Properties

The optical properties of chalcogenide glasses are dependent largely upon the presence of lone pair electrons, bandgap, atomic structure and materials composition. The high refractive index values and third-order optical nonlinearity of chalcogenide glasses find them ideal materials for telecommunication and optical fiber applications [21]. Chalcogenide glasses display low phonon energy and are transparent in long wavelength regions ranging from infrared to visible [22]. The values of the refractive index show the normal dispersion behavior in chalcogenide glasses.

The chalcogenide glasses also exhibit high value of optical absorption coefficient ( $\alpha$ ) in the range  $10^4 - 10^5 \text{ cm}^{-1}$  and are the materials of choice for photonic applications. The optical absorption in chalcogenide glasses is divided into three main regions, the high absorption region ( $\alpha \geq 10^4 \text{ cm}^{-1}$ ), exponential tail region ( $1 \text{ cm}^{-1} < \alpha < 10^4 \text{ cm}^{-1}$ ) and low absorption region ( $\alpha \leq 1 \text{ cm}^{-1}$ ). The transition from extended to extended or tail states occur in high absorption region and follow the frequency dependence as predicted by the well known Tauc relation  $\alpha h\nu = A (h\nu - E_g)^r$  where  $A$  is the constant and  $r = 1/2, 2, 3/2$  and 3

for direct allowed, indirect allowed, direct forbidden and indirect forbidden band gap respectively. The exponential tail region in chalcogenide glasses arises due to the transition between the localized tailing states. The origin of low absorption region is the result of transition between defects and impurity states. The charge carrier transport mechanism in chalcogenide glasses is described by the frequency dependence of optical absorption coefficient ( $\alpha$ ). The transition of charge carriers between the valence band maxima and conduction band minima give rise to the optical band gap. The transition of charge carriers between the valence band and conduction band at the same momentum value for a semiconductor corresponds to the release of photon with an energy equal to the difference of energy for the two bands is referred to as direct band gap semiconductors. However, the transitions in the indirect bandgap semiconductors occur at different momentum values. The charge carrier transport behavior of chalcogenides can be explored by the estimation of disorder effects for the opto-electronic applications.

Sharma and Hassanien studied the optical properties of *Pb-Se-Ge* alloys in bulk and thin films and obtained an optical band gap of  $\sim 1.6$  eV and refractive index of  $\sim 2.8$  [23]. Singh *et al.* reported the linear and non-linear optical properties of thin films of *Ge<sub>2</sub>Sb<sub>2</sub>Te<sub>5</sub>* phase change materials [24]. Raj *et al.* reported the transparency of *GeS<sub>2</sub>-Sb<sub>2</sub>S<sub>3</sub>* in the wavelength region  $2.5\mu\text{m}$  to  $25\mu\text{m}$  for the mid-infrared device applications [25]. Bahishti *et al.* reported the laser irradiation effect on the optical properties of *Se<sub>100-x</sub>Te<sub>x</sub>* ( $x = 8, 12, 16$ ) thin films [22]. The outcome of doping *Ag* in thin films of *Se<sub>70</sub>Te<sub>30</sub>* for optical properties in  $0.3\mu\text{m}$  -  $2.5\mu\text{m}$  wavelength range has been reported by El-Denglawey *et al.* and has observed the decrease in optical band gap with *Ag* concentration [26]. The thin films of *SnS* display the narrow bandgap and have been suggested as a candidate material for solar cell applications [27]. The decrease in indirect optical bandgap of thermally evaporated *Bi*-doped *Se<sub>80</sub>Te<sub>20</sub>* thin films from  $1.55$  eV to  $1.34$  eV and rise in refractive index from  $3.12$  to  $3.40$  with *Bi* content has been reported [28]. Good optical non-linearity in *Ge-Sn-Se* chalcogenides has been reported and proposed for the mid-infrared window applications [29].

Sharma *et al.* have studied the normal dispersion behavior of linear refractive index of *(As<sub>2</sub>Se<sub>3</sub>)<sub>90</sub>Ge<sub>10</sub>* thin films in the wavelength range of  $400-1500\text{nm}$  and analyzed the dispersion parameters using the Wemple-DiDomenico single oscillator model [30]. El-Hagary *et al.* obtained the absorption coefficient and refractive index from the transmittance and reflectance spectra of *Se<sub>70</sub>S<sub>30-x</sub>Sb<sub>x</sub>* ( $x = 0, 12, 18$  and  $30$  at%) thin films [31]. Anshu and Sharma evaluated the optical extinction coefficient of *Se-Pb-(Bi, Te)* thin films [32]. The

optical band gap and Urbach tailing energy of  $Ge_{20}Se_{80-x}S_x$  ( $x = 0, 15$  and  $30$ ) thin films have been evaluated by Dongol *et al.* and reported an increase in bandgap and decrease in Urbach tailing with  $S$  content [33].

## 1.2. Phase Change Materials

Phase change materials (*PCMs*) have been studied immensely in the past few decades and have been considered as potential candidates for optical as well as electrical data storage applications. The fascinating structural, electrical, optical and thermal properties of chalcogenide *PCMs* make them ideal material for *RF* switches, data storage devices, neuromorphic computing, thermoelectric devices rewritable compact discs (*CD*) and digital video discs (*DVD*) [34]–[36]. The *PCMs* exhibit the reversible phase change among amorphous and crystalline phases on local heating of the materials either by laser irradiation or electrical joule heating. The idea of reversible switching of chalcogenide *PCMs* was first put forward by Ovshinsky in 1968 [37]. *PCMs* exploit the large contrast in the electrical resistance and optical reflectivity between the amorphous and crystalline phases. The amorphous phase exhibits high electrical resistivity along with low optical reflectivity, whereas, the crystalline phase of *PCMs* display low electrical resistivity along with high optical reflectivity. This large contrast in the optical and electrical properties between the amorphous and crystalline phases of *PCMs* opens up the opportunity for application of these materials in optical data storage and non-volatile memories.

The chalcogenide *PCMs* crystallize in nanosecond time scale through the mechanism of nucleation and subsequent growth process. The crystallization of melt-quenched amorphous phase of chalcogenide *PCMs* can be induced on heat treatment above its glass transition temperature. The slower or faster crystallization time and the thermal stability of the amorphous phase determine its applicability for device applications. The crystallization time of chalcogenide *PCMs* has an inverse relation with its thermal stability. The faster crystallization rate and higher thermal stability of the *PCMs* are desired in memory device applications for better device performance. At higher glass transition temperature ( $T_g$ ) value the amorphous phase of *PCMs* is retained at the higher temperature resulting in the enhanced thermal stability.

Efforts have been made by many researchers to estimate the thermal stability and crystallization process of *PCMs* using differential scanning calorimetry (*DSC*), electrical sheet resistance measurements, temperature-dependent crystal growth velocity measurements

and laser irradiation studies on thin films. Several *PCMs* have been reported in the literature [37]–[42]. The reversible switching between high resistance state and conducting state induced by applied voltage was first time reported by Ovshinsky in 1968 [37]. Smith and co-workers also reported the phase change characteristics of *Te-As-Ge* thin films on *GaAs* laser injection and demonstrated the direct bit storage capability of *Te-As-Ge* chalcogenide thin films in 1974 [38]. Chen *et al.* studied the reflectivity measurements of  $Te_{87}Ge_8Sn_5$  thin films in 1986 and observed a change in reflectivity from 40 % to 60 % on phase transition from amorphous to the crystalline state. They also reported the crystallization temperature of  $\sim 75^\circ C$  and observed it to increase with an increase in *Ge* concentration [39]. In 1987, the optical fast reversible switching in *GeTeSb* thin films on laser irradiation was studied by Yamada *et al.* and suggested the application of *GeTeSb* in overwritable optical phase-change storage discs [40]. Iwasaki and co-workers analyzed the *Sb-Te PCM* incorporated with *Ag* and *In* for optical storage with improved writing and erasing power and enhanced signal-to-noise ratio [41]. Dimitrov *et al.* studied the crystallization kinetics of *PCM Sb-Se* thin films using both isothermal and non-isothermal crystallization methods [42]. Electrical switching behavior of  $Se_{78-x}Te_{20}Sn_2Cd_x$  ( $x = 0, 2, 4$  and  $6$ ) thin films has been investigated by Fouad *et al.* and reported the decrease in thermal stability with *Cd* content [43]. Recently chalcogenide *PCMs* have attained immense attention in data storage applications [44], [45], neuromorphic computing [36] and thermoelectric devices. Hu *et al.* have fabricated a *PCM* device utilizing the *GeTe/Sb<sub>2</sub>Te<sub>3</sub>* superlattice structures to mimic the activity of the biological synapses for artificial neural networks [46]. The highly efficient synaptic characteristics, low power consumption and high density integration of *GeTe/Sb<sub>2</sub>Te<sub>3</sub>* superlattice structure based *PCM* devices have attracted huge attention for futuristic “brain-inspired computing” applications. The recent progress in neuro-inspired computing for artificial “biological neural networks” based on chalcogenide *PCMs* have been reviewed by Wang *et al.* [47]. The *GeTe* based *PCMs* have also been explored recently for thermoelectric applications because of their high figure of merit (*ZT*), low thermal conductivity and high Seebeck coefficient [48].

### 1.2.1 Classifications

This section reviews the classification of various chalcogenide *PCMs* and their corresponding thermal properties for their compatibility in phase-change memory applications. The different crystallization behavior of these *PCMs* comprises distinct nucleation and growth rates and acquires different phase transformation mechanisms that decide the performance of storage devices. *PCMs* have been categorized into two broad

classes, one major class contains the alloys based upon *Ge-Sb-Te* e.g.  $Ge_2Sb_2Te_5$  (*GST*) and the other class includes *Sb* rich  $Sb_2Te_3$  alloys e.g. *AgInSbTe* (*AIST*) etc. These *PCMs* are being used in the storage device application. *GST* crystallizes through the nucleation-dominated crystallization mechanism in two different phases viz. Rocksalt and hexagonal.

### 1.2.1.1. *Ge-Sb-Te* Alloys

Germanium, Antimony and Tellurium (*Ge-Sb-Te*) based chalcogenide alloys have been prominently utilized in optical rewritable data storage as well as non-volatile memory applications [47]. Figure 1.6 shows the phase diagram of *Ge-Sb-Te* alloys and the tie line connecting the *GeTe* and  $Sb_2Te_3$  [49]. The phase change alloys based upon  $Ge_xTe_{1-x}$  were the first to be chosen for the data storage applications [50]. The ternary alloys lying in the tie line between *GeTe* and  $Sb_2Te_3$  were the most focused materials of choice for phase change memory applications [49]. Several materials belonging to the tie line, such as,  $Ge_1Sb_4Te_7$ ,  $Ge_1Sb_2Te_4$ ,  $Ge_2Sb_2Te_5$ ,  $Ge_3Sb_2Te_6$ ,  $Ge_4Sb_2Te_7$ ,  $Ge_6Sb_2Te_9$  and  $Ge_8Sb_2Te_{11}$  and the material lying close to the tie line  $Ge_4Sb_1Te_5$ ,  $Ge_1Sb_6Te_{10}$ ,  $Ge_1Sb_8Te_{13}$ ,  $Ge_2Sb_1Te_4$ ,  $Ge_{1.5}Sb_2Te_4$  and  $Ge_2Sb_2Te_4$  have been reported in literature for the phase change memory applications [49]. The nature of  $Ge_2Sb_2Te_4$  has been reported to be unstable due to which it decomposes into  $Ge_1Sb_2Te_4$  and  $Ge_2Sb_1Te_4$  [51]. The alloys lying near the end of  $Sb_2Te_3$  crystallizes rapidly compared to the alloys rich in *GeTe*, but, show lower electrical and optical contrast between the amorphous and crystalline states and in addition to this, possess lower thermal stability [52].

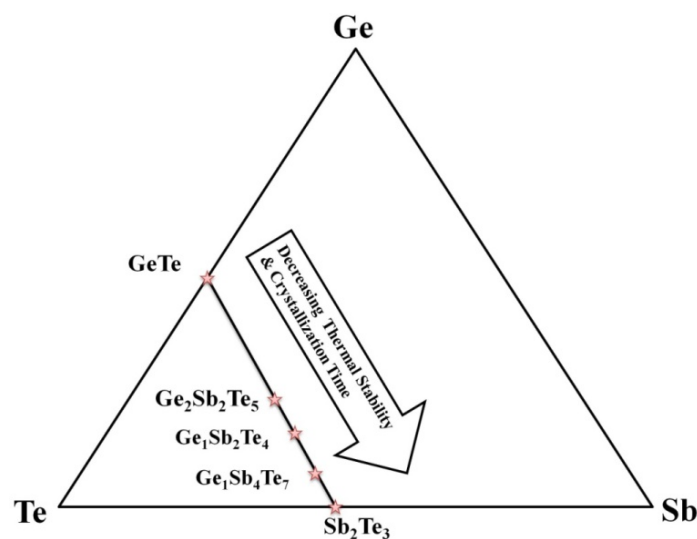


**Figure 1.6.** Phase diagram of *Ge-Sb-Te* alloys and a tie line between  $Sb_2Te_3$  and *GeTe*.

Among *Ge-Sb-Te* alloys,  $Ge_2Sb_2Te_5$  has attained immense attention and has been chosen as the material of choice for the *PC* memory applications because of the best combination of crystallization speed and thermal stability in it [51]. The bandgap energy of alloys lying along the  $GeTe-Sb_2Te_3$  tie line shows a decrease with *Sb* content and increase with *Ge* content [53].  $GeTe$ ,  $Ge_1Sb_2Te_4$  and  $Ge_2Sb_2Te_5$  possess indirect bandgap whereas  $Ge_1Sb_4Te_7$  and  $Sb_2Te_3$  show the direct bandgap [54]. Xu *et al.* [53] carried out a comparative study of electrical properties in  $Ge_1Sb_2Te_4$  and  $Ge_2Sb_2Te_5$  and obtained the optical bandgap of  $0.7\text{ eV}$  and  $0.9\text{ eV}$  and activation energy  $0.42\text{ eV}$  and  $0.45\text{ eV}$  respectively. This study reports the smaller mobility of  $Ge_1Sb_2Te_4$  in comparison to  $Ge_2Sb_2Te_5$  which suggests the presence of comparatively more number of vacancies in  $Ge_1Sb_2Te_4$  [53]. The mechanism of isothermal crystallization and thermal stability for  $Ge_1Sb_2Te_4$  and  $Ge_2Sb_2Te_5$  have been studied by Liu *et al.* and found the crystallization temperature to be  $149\text{ }^\circ\text{C}$  and  $161\text{ }^\circ\text{C}$  respectively [51]. Therefore,  $Ge_1Sb_2Te_4$  phase change material is observed to be thermally less stable with comparatively large carrier concentration than  $Ge_2Sb_2Te_5$ .

#### 1.2.1.2. *Ag-In-Sb-Te* Alloys

In addition to *Ge-Sb-Te* phase change material, *In* and *Ag* doped  $Sb_2Te$  has also been recognized as a candidate with potential for data storage application. The *In* and *Ag* doped  $Sb_2Te$  have the crystallization temperature of  $\sim 165\text{ }^\circ\text{C}$  [55]. *Ag-In-Sb-Te* (*AIST*) alloys have been widely used for rewritable compact discs (*RW-CD*) and digital versatile discs (*DVD*). The crystallization mechanism of *Ag-In-Sb-Te* alloys is different from those of the *Ge-Sb-Te* alloys. In contrast to the nucleation-dominated crystallization of *Ge-Sb-Te*, *AIST* exhibits the growth-dominated crystallization mechanism. Matsunaga *et al.* reported the comparative study of local structure and crystallization mechanism in  $Ag_{3.5}In_{3.8}Sb_{75}Te_{17.7}$  and  $Ge_2Sb_2Te_5$  phase change materials [56]. The *Ag* and *In* doping to  $SbTe$  increases the crystallization temperature from  $125\text{ }^\circ\text{C}$  to  $175\text{ }^\circ\text{C}$  [57]. The addition of *Ag* and *In* leads to the change in the local structure around *Te* and there is no change in the local structure of *Sb*. The doping of *Ag* and *In* resulted an increase in the viscosity at room temperature and increases the stability of the amorphous phase. Pries *et al.* examined the glass transition temperature of *AIST* at  $182.5\text{ }^\circ\text{C}$  using ultrafast calorimetry [55]. The crystalline *AIST* alloys showed no vacancies in the lattice. The origin of growth dominated crystallization mechanism of *AIST* alloys has been explained using the bond interchange model. The bandgap of amorphous and crystalline *AIST* has been reported to be  $1.12\text{ eV}$  and  $0.52\text{ eV}$  respectively.

Maeda *et al.* [58] in 1988 have reported the reversible transformation from amorphous to the crystalline state in  $In_3SbTe_2$  thin film using the diode laser pulse for crystallization of spot and observed the crystallization temperature to be  $250\text{ }^\circ\text{C}$  and the activation energy to be  $1.8\text{ eV}$ . The reported higher crystallization temperature in  $In_3SbTe_2$  thin films shows the potential for reversible optical data storage media. The crystallization temperature of  $In_3SbTe_2$  has been reported by Y. T. Kim and S. Kim at  $293.9\text{ }^\circ\text{C}$ ,  $290.4\text{ }^\circ\text{C}$  and  $286.7\text{ }^\circ\text{C}$  using the differential scanning calorimetry (DSC) measurements at the heating rates of  $20\text{ K/min}$ ,  $10\text{ K/min}$  and  $5\text{ K/min}$  respectively [59]. Pandey *et al.* [60] reported the switching characteristics of  $In_3SbTe_2$  phase change material with a threshold switching voltage of  $1.9\text{ V}$ . The local atomic structure of  $Ag_5In_5Sb_{60}Te_{30}$  and  $In_3SbTe_2$  phase change materials have been studied by Sahu and co-workers and reported the identical local environment of  $In$  in both the materials forming the  $In-Sb$  and  $In-Te$  bonds [61]. Deringer *et al.* [62] studied the similarities in the chemical bonding nature of  $Ge-Sb-Te$  and  $In_3SbTe_2$  phase change materials and reported the intrinsic nature in both materials.

## 1.2.2. Applications

### 1.2.2.1. Optical Data Storage

Optical data storage devices utilize the optical reflectivity difference between the amorphous and crystalline states of *PCMs*. The optical reflectivity of the crystalline phase is much higher than the amorphous phase. The commercially available optical data storage devices *viz.* digital versatile discs (*DVDs*), rewritable compact discs (*CDs*) and Blu-ray discs utilize  $GeTe-Sb_2Te_3$  pseudobinary phase change material and  $Ag$  and  $In$  doped  $Sb_2Te$  as programmable material. The multilayer of rewritable *DVDs* has been illustrated in figure 1.7 containing the top protective layer for the prevention of disc from mechanical damage. The *PC* layer is sandwiched between two  $ZnS-SiO_2$  dielectric layers to prevent the *PC* layer from oxidation and segregation. The recording is done in rewritable *DVDs* by writing the amorphous bit using the laser beam.

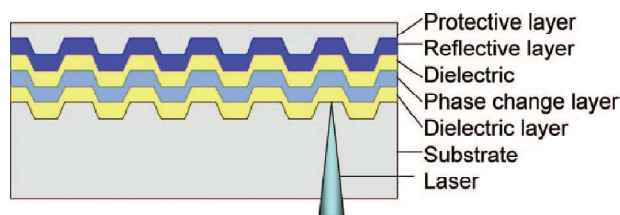


**Figure 1.7.** Schematic representation of rewritable digital versatile disc (*DVD*). Adapted with permission from [63]. Copyright © 2010 American Chemical Society.

The increase in storage density requires a decrease in the wavelength of the laser beam used for reading, writing and erasing the bit. However, decreasing the wavelength beyond blue light is very challenging and requires a different approach in the next-generation optical storage media. The solid immersion lenses have been used to focus the laser beam, which result in an increase in the numerical aperture from  $0.85$  to  $1.9$  for Blu-ray and enhances the resolution [64]. The read and write operation in smaller size bits can be performed with the increased numerical aperture and results in an increased storage density [64]. Another technology for increasing the storage density is based on the super-resolution near-field structure [65] Based on this technology, the non-linear  $Sb$  layer is deposited over the  $PC$  layer which acts as a mask layer for the laser beam. The mask layer allows the reading and writing over the  $PC$  layer by the laser beam with a reduced wavelength.

### 1.2.2.2. Phase Change Memories

Phase change memory is a non-volatile memory technology based upon the switching property of chalcogenide phase change materials between high and low resistance states on heat treatment. The amorphous phase of chalcogenide  $PCMs$  constitutes the high resistivity of the order of  $\sim 10^3 - 10^6 \Omega\text{-cm}$  and the crystalline phase constitutes the  $\sim 10^{-1} - 10^{-3} \Omega\text{-cm}$  order of resistivity. The large difference of resistivity ( $\sim 10^5 \Omega\text{-cm}$ ) between the crystalline and amorphous state is utilized as the two binary logic states for data storage applications. The fast switching speed and higher thermal stability of  $PCMs$  are beneficial for the device applications which can be achieved by choosing the material with higher crystallization temperature and lower crystallization time. The commercial phase-change memory devices utilize  $Ge_2Sb_2Te_5$  and  $Ag, In$  doped  $Sb_2Te$  phase change materials as programmable layer and have been chosen as materials of choice due to their less than  $100ns$  crystallization time and enhanced thermal stability [66].

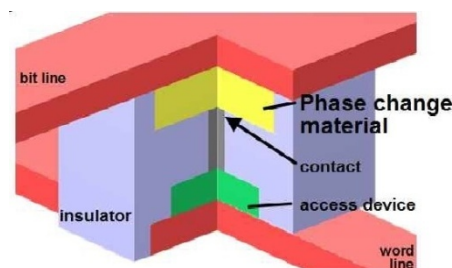


**Figure 1.8.** Device design of Phase-change Memory. “Reprinted with permission from [67] Copyright © 2010, American Vacuum Society”.

Figure 1.8 illustrates the schematic representation of the phase change memory device showing the top and bottom electrodes, heating element and the dielectric materials to prevent excessive heating of the device. The phase change material has been placed between the top and bottom electrodes in the memory device. The phase change material switches to a crystalline state on heating above the crystallization temperature for a time long enough to crystallize. The heat treatment for *PCM* is done by placing the heating element below it and above the bottom electrode. The crystallization so induced in the phase change material is called the *SET* operation. To reset the device back into the amorphous phase, high current pulse is passed through the top and bottom electrodes for a shorter duration resulting in the melt quenching of the material and is referred to as *RESET* operation. The *RESET* and *SET* operations can be performed repeatedly in the phase change memory devices. Figure 1.9 shows the *I-V* characteristics of  $Ge_2Sb_2Te_5$  phase change material with *SET* and *RESET* operations. The *I-V* curves display the large resistance contrast between the amorphous and crystalline phases below the threshold voltage ( $V_{th}$ ).

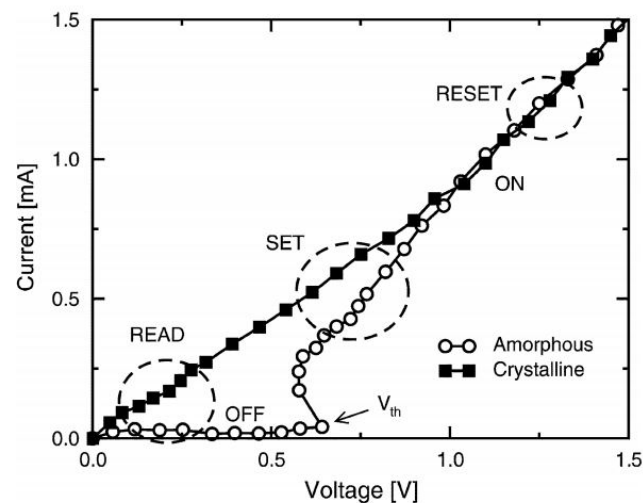


**Figure 1.9.** *I-V* curve of phase change memory cell with amorphous and crystalline  $Ge_2Sb_2Te_5$ . Figure reprinted with permission from ref. [68] copyright © 2004 IEEE.

### 1.2.2.3. Neuro-inspired Computing

Neuro-inspired or neuromorphic computing is one of the potential applications of phase change materials. Neuromorphic computing refers to the brain-like hardware architecture for extremely efficient computing efficiency. Neuromorphic computing is beneficial for artificial intelligence (*AI*) based advanced computing applications. The human brain consists of  $10^{11}$  neurons and  $10^{15}$  neuron interconnects also known as synapses. The main aim of neuro-

inspired computing is to overcome the bottleneck of von Neumann computing. The limitation of the von Neumann computing algorithm is the separated storage (*DRAM*) and data processing devices (*CPU*) causing the data shuffling between these separated units, which limits the data processing speed. Neuron-inspired computing is beneficial for the rapid development of *AI* applications for performing complex tasks such as image and pattern recognition, language translations and automatic driving *etc.* [47], [69].

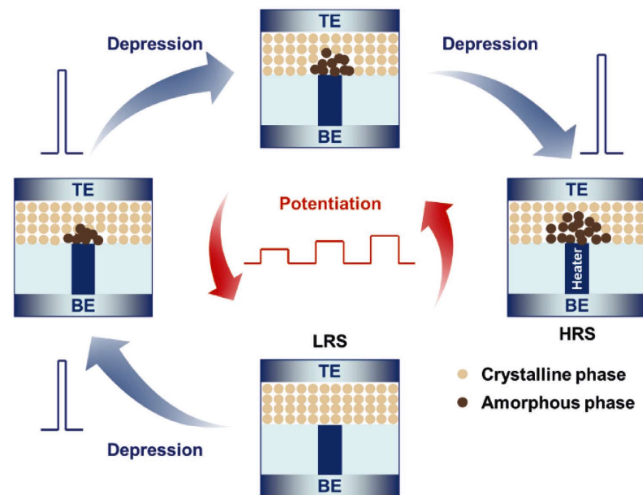


**Figure 1.10.** Reversible synaptic potentiation and depression induced in a phase change memory by an electrical pulse. The image has been reprinted with permission from ref. [47]. copyright © 2021 John Wiley and Sons.

Kuzum *et al.* demonstrated a nanodevice based upon the *PCMs* which shows close resemblance with biological synapses activity [70]. Synapses activity of *PCMs* utilizes their reversible amorphization and crystallization ability which are induced by applying the electrical pulse with variable pulse width. The shorter duration electrical pulse with higher amplitude is applied for the amorphization process, whereas, comparatively lower amplitude current pulse for a time long enough to crystallize the *PCM* is applied for the crystallization process. In terms of the biological neural system, the process of amorphization is referred to as synaptic depression, whereas, the crystallization process of phase change materials is called synaptic potentiation. The potentiation and depression pulse of appropriate width and amplitude is required to imitate the synapses neural network. Suri *et al.* characterized the synaptic potentiation and synaptic depression behavior of  $Ge_2Sb_2Te_5$  and  $GeTe$  chalcogenide phase change materials [71]. The  $Ge_2Sb_2Te_5$  synapsis has been observed to be superior to the  $GeTe$  synapsis in terms of the storage capacity in this study. Figure 1.10 shows the reversible synaptic potentiation and synaptic depression process of the phase change memory cell which

is induced by rapid crystallization and amorphization using the lower current pulse with a wider width and higher current pulse having narrow width respectively.

#### 1.2.2.4. Thermoelectric Applications

The alloys based on lead-free *GeTe* phase change materials also exhibit the thermoelectric behavior with a high figure of merit  $zT = \left(\frac{S^2\sigma}{\kappa}\right)T$ , where  $T$  is the absolute temperature,  $S$  is the Seebeck coefficient,  $\sigma$  and  $\kappa$  are electrical and thermal conductivity respectively. It has been reported that the alloys based on *GeTe* exhibit low thermal conductivity and high electrical conductivity and display p-type semiconducting behavior [35]. The figure of merit  $zT$  describes the thermoelectric performance of materials. The thermoelectric performance of materials varies directly with their electrical conductivity as well as Seebeck coefficient and inversely with the thermal conductivity. The high free carrier concentration ( $\sim 10^{21} \text{ cm}^{-3}$ ) and low Seebeck coefficient ( $\sim 18\text{-}30 \mu\text{V/K}$ ) limit the performance of *GeTe* thermoelectric materials [35]. However, doping of *GeTe* has been recognized as an effective approach to reduce the free carrier concentration and enhance the Seebeck coefficient. Hu *et al.* optimized the thermoelectric performance of  $\text{Ge}_2\text{Sb}_2\text{Te}_5$  by doping with *In* element in *Ge* sites which results in the enhancement of Seebeck coefficient and reduction of free carrier concentration with *In* concentration [72]. The enhanced electrical performance and reduced thermal conductivity with a maximum value of the figure of merit  $zT$  at 0.78 have been observed for the composition  $\text{Ge}_{1.85}\text{In}_{0.15}\text{Sb}_2\text{Te}_5$  [72]. The improved thermoelectric performance of *Cu* doped  $\text{Ge}_{1-x-y}\text{Cu}_{2x}\text{Sb}_y\text{Te}$  with varying *Sb* concentration and free carrier mobility of the order of  $\sim 100 \text{ cm}^2 \text{ V}^{-1} \text{ s}^{-1}$  and lowest thermal conductivity of  $0.38 \text{ W m}^{-1} \text{ K}^{-1}$  have been observed [73]. The *Cu* doping has been observed to cause the occupation of the *Ge* vacancy sites resulting in the reduction in *Ge* vacancy concentration leading to an enhanced  $zT$  value of the order of 2 at the temperature of 750K.

#### 1.2.2.5. NIR Windows

The phase change material  $\text{Ge}_2\text{Sb}_2\text{Te}_5$  (*GST*) has been also recognized as the potential candidate for the near-infrared (*NIR*) window applications because of its tendency to show the reversible phase transition between amorphous to the crystalline phase. *GST* exhibits optical contrast between the different phases *viz.* amorphous, face-centered cubic (*fcc*) and hexagonal in the *NIR* wavelength region. The high transmission of amorphous *GST* of 92% and comparatively less transmission of  $\sim 46\%$  in the *fcc* phase and negligible transmission in

the hexagonal phase at the wavelength of  $2740\text{ nm}$  has been reported [74]. The amorphous *GST* is nearly transparent in the *NIR* region. Conversely, *GST* shows very high optical reflectivity in crystalline phase in comparison to amorphous phase. Approximately  $\sim 25\%$  reflectivity contrast between the amorphous and crystalline phases of *GST* thin films on laser irradiation has been reported [75].

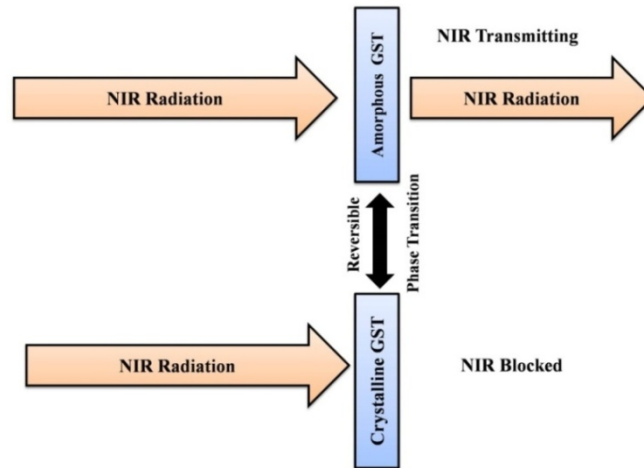


**Figure 1.11.** Schematic representation for *GST* based *NIR* windows.

The transformation of *GST* phase from the amorphous to crystalline state blocks the *NIR* radiations and hence, can be used for *NIR* window applications. Figure 1.11 displays the schematic representation of *NIR* windows based on reversible amorphous-crystalline transformation of *GST*. Singh *et al.* reported the phase transition of *Ag*-doped *GST* thin films and have observed the higher optical contrast at a lower temperature [76].

### 1.3. $\text{Ge}_2\text{Sb}_2\text{Te}_5$ Phase Change Material

$\text{Ge}_2\text{Sb}_2\text{Te}_5$  (*GST*) is a phase-change material focused most on applications in optical data storage as well as non-volatile memories [77]. *GST* exists in three solid phases *viz.* amorphous, metastable face-centered cubic rocksalt phase and the stable hexagonal phase. The amorphous *GST* can be prepared by melt quenching process, whereas, the crystalline phase can be achieved by annealing the amorphous phase. The non-volatile phase-change memories and the optical data storage applications utilize the reversible switching between these phases of *GST* which is thermally induced. *GST* can be repeatedly transformed between the amorphous, rocksalt cubic and hexagonal phases as a function of temperature which can be stimulated either by the application of electric pulse or irradiation using laser. The *GST* amorphous phase is attributed to local ordering of constituents up to short-range order and medium range order.

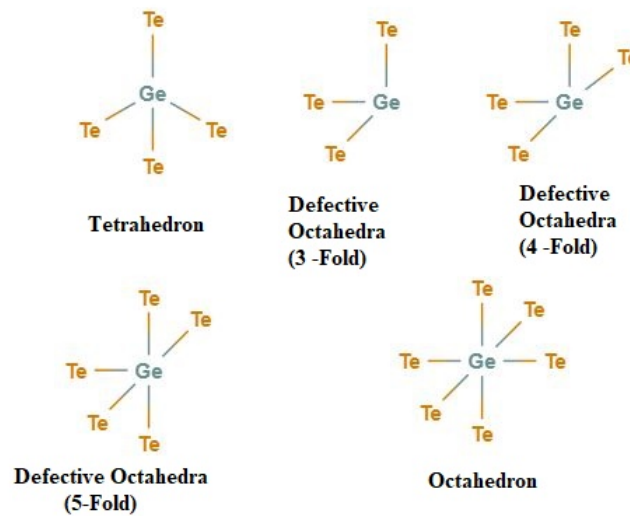


**Figure 1.12.** *GeTe* tetrahedral, 3-, 4-, 5- fold coordinated defective octahedral and octahedral structures.

The short-range order of amorphous *GST* constitutes the *GeTe* tetrahedral structures, defective octahedral and octahedral structures as displayed in figure 1.12. The average coordination number in amorphous *GST* for *Te*, *Sb* and *Ge* are  $2.4 \pm 0.8$ ,  $2.8 \pm 0.5$  and  $3.9 \pm 0.8$  respectively which are in close agreement with the  $8-N$  rule [78]. The amorphous *GST* consists of heteropolar *Sb—Te* and *Ge—Te* bonds which are shorter than in their crystalline counterparts and the *Sb—Sb*, *Ge—Sb* and *Ge—Ge* homopolar wrong bonds. The *Ge* and *Sb* atoms tend to bond with *Te* atoms in the  $-Ge-Te-Sb-Te$  square ring structure in the amorphous phase of *GST*, which acts as the initiating clusters for crystallization [79].

The annealing of amorphous *GST* up to the temperature of  $150\text{ }^{\circ}\text{C}$  results in the crystallization into the rocksalt *fcc* structure. The rocksalt *fcc* crystal structure of *GST* is composed of  $4a$  anionic sites which are inhabited by *Te* atoms and  $4b$  cationic sites inhabited by *Ge*, *Sb* atoms along with vacancies. The presence of vacancies in the *GST fcc* structure has been reported as highly ordered instead of random [80]. The stacking of the  $Te - Ge - Te - Sb - Te - v - Te - Sb - Te - Ge$  layer in  $[111]$  direction results in the formation *fcc* structure of *GST*. Figure 1.13 (a) illustrates the rocksalt *fcc* unit cell structure of *GST*. The rocksalt structure of *GST* transforms into hexagonal at a higher temperature  $\sim 235\text{ }^{\circ}\text{C}$ . The presence of vacancies in the rocksalt structure of *GST* plays main part in the transformation to hexagonal phase. The hexagonal *GST* constitutes the 9 layered unit cell with the space group  $P-3m1$  [81]. Many models have been suggested in the literature to discuss the stacking

sequence in the hexagonal phase of *GST*. Petrov *et al.* suggested the possible 9 layers staking sequence  $Te - Sb - Te - Ge - Te - Te - Ge - Te - Sb -$  in the hexagonal phase along [0001] direction [82]. Kooi *et al.* later on in 2002 proposed  $Te - Ge - Te - Sb - Te - Te - Sb - Te - Ge -$  stacking sequence [83]. Matsunaga *et al.* put forward the stacking sequence  $Te - Ge / Sb - Te - Sb / Ge - Te - Te - Ge / Sb - Te - Sb / Ge -$  with *Sb* and *Ge* atoms randomly occupying the position in layers [84]. Sun *et al.* have carried out the *ab initio* total energy calculation by means of density functional theory and observed the Kooi stacking sequence as the most stable with the lowest total energy and also in good agreement with the experimental results [82].

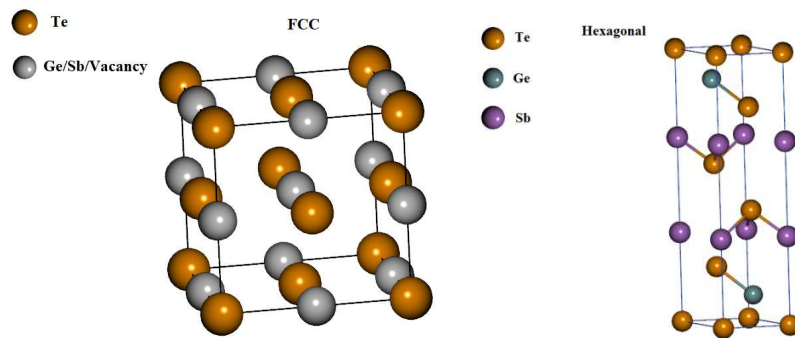


**Figure 1.13** (a). *GST* unit cell with Rocksalt fcc structure (b) Hexagonal unit cell of *GST*.

The lattice parameters  $a = 6.096 \text{ \AA}$  for rocksalt cubic phase of *GST* with  $Fm-3m$  space group symmetry and  $a = 4.22 \text{ \AA}$ ,  $c = 17.37 \text{ \AA}$  for hexagonal phase with space group  $P-3m1$  have been figured out [81]. Figure 1.13 (b) shows the hexagonal unit cell of *GST* phase change materials. The presence of vacancies in the *fcc* structure of *GST* disappears with the transformation to the hexagonal phase.

### 1.3.1. Switching Mechanism

The mechanism of phase change of *GST* alloy has been extensively studied and has been much debated in the past few decades. *GST* exhibits the two-step phase transition, *i.e.*, amorphous to rocksalt *fcc* structure and then to the hexagonal phase at higher temperature. The phase transition of *GST* from amorphous to the rocksalt cubic phase has been analyzed in terms of the bonding environment alteration of *Ge* atom. Kolobov and co-workers proposed the umbrella flip model for local bonding alteration of *Ge* from tetrahedral to defective octahedral structure with the transition from amorphous to rocksalt cubic structure [85]. The transition from tetrahedral to defective octahedral structure on phase transformation from amorphous to *fcc* crystal structure results in the change in bond lengths of *Ge-Te* and *Sb-*

*Te* bonds. The *Ge—Te* bond length increases from  $2.61 \text{ \AA}$  to  $2.83 \text{ \AA}$  on *fcc* crystallization and *Sb—Te* bond lengths also increase from  $2.85 \text{ \AA}$  to  $2.91 \text{ \AA}$  [85]. Figure 1.14 displays the local structure alteration of *Ge* atom in *GST* as a result of phase transition from amorphous to rocksalt *fcc* crystal structure. The square rings of *Ge-Te-Sb-Te* act as nuclei for the *GST fcc* phase. The *fcc* phase emerges as a result of the spread of square rings *Ge-Te-Sb-Te* in the [200] direction.



**Figure 1.14.** Alteration in *Ge* local structure from tetrahedral to octahedral on crystallization of amorphous *GST*.

The transition from *fcc* to hexagonal phase of *GST* is still under active discussion. It has been widely accepted that the *fcc* to the hexagonal transformation of *GST* is due to the diffusionless movement of *Sb* and *Ge* atoms along  $\langle 111 \rangle$  direction resulting in ordering of vacancies [81]. Zheng *et al.* discussed the cationic migration behavior of *Ge* and *Sb* atoms to the neighboring vacant sites [81]. The cationic sites in the *fcc* phase are randomly inhabited by *Ge* and *Sb* atoms and vacancies. With increase in the annealing temperature above  $200^\circ\text{C}$ , *Ge* and *Sb* atoms start migrating to the vacant sites in the neighboring layer in  $\langle 111 \rangle$  direction. Because of the lower migration energy of the *Sb* element of the order of  $-0.026 \text{ eV}$  in comparison to that of  $0.035 \text{ eV}$  for *Ge* migration energy, the movement of *Sb* atom is faster than the *Ge* atom [81]. The cationic migration on *fcc* to hexagonal phase transition results in the vacancy ordering. The increase in the temperature above  $200^\circ\text{C}$  results in the formation of ordered vacancy layers in (111) plane and subsequently the sliding of one of the building blocks towards  $\langle 210 \rangle$  direction leading to the collapse of vacancy layer resulting in the formation of the final hexagonal phase [81].

The early migration of *Sb* atoms in comparison to the *Ge* atoms leads to the occupation of *Ge* and *Sb* atoms in the outer and inner cationic layers respectively. The nine layered atomic stacking sequence in final hexagonal phase is suggested alike the Matsunaga stacking

sequence:  $Te - Sb_x / Ge_y - Te - Sb_y / Ge_x - Te - Sb_y / Ge_x - Te - Sb_x / Ge_y - Te - (x > y)$  [81]. The small energy difference of the order of  $5eV$  between the most stable Kooi stacking sequence and Matsunaga indicates that both the models are energetically favourable [81]. Exploring the atomic scale microscopic properties of *GST* facilitates the further advances in phase change memory applications. The doping of the appropriate element at the cationic sites can prevent the transformation to hexagonal phase because of the reduction in vacancies and consequently the restraining of cationic migrational behavior.

### 1.3.2. Challenges

#### 1.3.2.1. Aging and Resistance Drift of Amorphous $Ge_2Sb_2Te_5$

The aging of amorphous materials results in the structural relaxation of metastable structural units. Amorphous *GST* shows the  $\beta$ -relaxation of structural units with the prolonged *PCM* device performance resulting in the resistance drift [86]. The resistance drift refers to the continuous increase in electrical resistance of the amorphous phase of *GST* with time. The resistance contrast among the amorphous and crystalline phases of *GST* gets enlarged as a result of the resistance drift in the amorphous phase, which leads to the slowdown of crystallization speed with device aging and affects the multilevel storage. The resistance drift can be expressed as  $R(t) = R(t_0) \left(\frac{t}{t_0}\right)^\nu$  where  $\nu$  is the resistance drift exponent and its value for *GST* is  $\sim 0.1$ ,  $R(t_0)$  is the resistance of unit cell at time  $t_0$  and  $R(t)$  is the resistance at time  $t$  greater than the  $t_0$  [87]. The  $Ge-Ge$ ,  $Sb-Ge$  and  $Te-Te$  homopolar wrong bonds associated with the tetrahedral  $Ge$  of amorphous *GST* phase have been suggested behind the origin of resistance drift [86], [87]. The relaxation of metastable structural unit results in the removal of  $Ge-Ge$ ,  $Sb-Ge$  and  $Te-Te$  homopolar wrong bonds in the amorphous *GST* phase. The structural defects in the amorphous materials give rise to the formation of electronic trap states lying in the middle of the mobility gap. The resistance drift causes the disappearance of mid-gap defect states in the energy band resulting in the widening of the mobility gap. The resistance drift in amorphous *GST* hampers multilevel *PCM* data storage device performance. The annealing of amorphous materials below the crystallization temperature accelerates the aging process. The compositional and device engineering approaches can be employed for the reduction of resistance drift issue of the phase-change memory. The substitution of any suitable element to the *GST* that can reduce the fraction of homopolar bonds can suppress the resistance drift of amorphous materials. The design of phase change heterostructure has also been observed to be an approach to reduce

the resistance drift over the mushroom-like memory cell [88]. One of the reasons for the resistance drift in the melt-quenched phase is the relaxation of internal mechanical stress which is induced during the process of quenching [89]. Mitra *et al.* utilized the phase change nanowires with the enhanced surface to volume ratio and observed drastic decrease in the drift coefficient [89].

### 1.3.2.2. Fast Switching Speed

Fast crystallization and amorphization speed are crucial for the rapid write and erase process of *PCM* devices. The amorphization of *GST* is much faster than the crystallization speed which is of the order of few nanoseconds [90]. Crystallization speed decreases with the increase in the glass transition temperature. The enhanced data transfer rate of the phase change memory device relies on the faster crystallization speed. The crystallization speed of *GST* is one of the limiting factors for achieving the efficient data transfer rate of phase-change memory. The crystallization process of *GST* proceeds with the nucleation and subsequent growth. Crystallization of the phase change materials is accompanied by a change in bonding mechanism. Optimization of the underlying mechanism of crystallization necessitates understanding of the change in bonding network for enhanced performance of phase change memory storage devices. The crystallization speed—strongly depends on the composition of the *PCM*. The increased crystallization speed is achieved on accelerating the nucleation and growth processes by doping with the suitable element. *GST* is nucleation-dominated phase change material with a crystallization time of  $\sim 60ns$  and exhibits a higher rate of nucleation in comparison to the crystal growth rate [91]. Alloying *GST* with a suitable element is an effective method for optimizing the crystallization speed for efficient storage device performance. Numerous efforts have been devoted to improve the crystallization kinetics of *GST* by alloying with metallic, semiconducting or insulating impurities [46]–[49].

### 1.3.2.3. Enhanced Thermal Stability

Thermal stability refers to the long-term data retention and the stability of the amorphous state of *PCM* at a higher temperature. The data is stored in *PCM* devices in the form of optical reflectivity or electrical resistivity which largely differs in magnitude for the amorphous and the crystalline phases. The materials with higher crystallization temperature and glass transition temperature are considered thermally more stable. *GST* exhibits the glass transition temperature of  $\sim 110^\circ C$  and crystallization temperature of  $\sim 155^\circ C$  which is not adequate to meet the long-term data retention of the phase change memory device at elevated

temperatures [96], [97]. The higher thermal stability of *PCMs* is also related to the activation energy for crystallization which is of the order of  $\sim 2.23$  eV for the *fcc* crystallization of *GST* [96]. The thermal stability of *PCMs* is dependent upon the nature of atomic bonding of constituent elements in the amorphous state. The effective way to improve the thermal stability is the alloying with a suitable element that can create stronger heteropolar bonds. The addition of suitable element that results in an increase in the average coordination and the formation of stronger bonds constrain the atomic movement in the amorphous state for phase change materials. This increases the crystallization temperature providing advantage for the better thermal stability of the amorphous state. The higher crystallization temperature also hinders the switching speed of the phase change materials. Therefore, the improved phase change memory device performance can be attained by achieving both the higher crystallization temperature and higher switching speed.

#### 1.4. Doping of $Ge_2Sb_2Te_5$

The challenges posed by undoped *GST* constrain its use in commercial storage devices and stress upon the requirement for the improvement in the switching mechanism of *GST* by incorporating the suitable element for the enhanced device performance. Numerous efforts have been made to improve the switching mechanism of *GST* by doping with metallic, non-metallic and semiconducting impurities [98]–[101]. Han *et al.* studied the change in bonding arrangement of *GST* on *Ag* incorporation and reported a decrease in the crystallization temperature by  $20^\circ C$  on *Ag* doping with the weakening of bond length and bond strength of *Ge—Te* bond [98]. Prasai *et al.* investigated the effect of *Ag* incorporated *GST* using the *ab-initio* molecular dynamics simulations and observed reduction in the fraction of tetrahedral *Ge* atoms and increase in the four-membered rings resulting in the enhanced crystallization speed of *GST* [99]. Song and co-workers investigated the crystallization mechanism of  $Ag_{0.1}(Ge_2Sb_2Te_5)_{0.9}$  thin films using nanobeam laser illumination [100]. The change in two-step phase transition (amorphous to *fcc* to hexagonal) of *GST* into one-step phase transition from amorphous to *fcc* with the suppression of hexagonal phase on *Ag* incorporation has been reported. Nitrogen doping has been studied resulting in change of *Ge* coordination and increase in the optical band gap of *GST* with *N* concentration [101]. The effect of nitrogen addition has also been studied by Liu *et al.* and they investigated the suppression of *fcc* to hexagonal transition on account of the grain refinement mechanism induced by *N* doping [102]. Nitrogen doping has been observed to act as a center of suppression for *fcc* to hexagonal phase transition due to the substitution of *N* atoms in the tetrahedral interstitial

sites resulting in the distortion in the crystal structure and also causes the reduction in the grain size for the improved device performance [92]. Carbon doping has been reported to suppress the grain size due to the aggregation of *C* atoms on the grain boundaries and this has been observed to increase the thermal stability of *GST*. Zhou and co-workers studied the impact of *C* doping on *GST* and observed the modification of local environment of *Ge* tetrahedral with the formation of covalent *C—C* chains [79]. Carbon doping has been observed to reduce the number of four-membered rings with the formation of *C—C* chains resulting in the enhanced amorphous phase stability and lower *RESET* power. Song *et al.* fabricated the *128MB* phase change memory test chip with *C* doped *GST* material in *40nm* node and examined the data retention and endurance characteristics and observed the *10*-year data retention using the Arrhenius extrapolation at the highest temperature of *128 °C* [103]. The power consumption and improved performance of phase change memory by *C* doping in *GST* have been also investigated by Song and co-workers and they explained the grain refinement mechanism of *GST* by *C* incorporation [104].

Arsenic doping has also been observed to be advantageous for the improvement in the crystallization mechanism of *GST* alloy [105]. Vinod and co-workers studied the dependence of *GST* thin film optical and electrical properties *w.r.t.* *As* content and reported an increase in the threshold switching voltage of *GST* from *4.0 V* to *5.2 V* for  $(Ge_2Sb_2Te_5)_{0.85}As_{0.15}$  thin films with *As* content [105]. Vinod *et al.* reported the direct hexagonal transition of amorphous *GST* on *Se* substitution in a separate study and observed the crystallization temperature of *200 °C* for  $(Ge_2Sb_2Te_5)_{0.9}Se_{0.1}$  thin film and found the optical band gap energy to increase from *0.63 eV* to *0.66 eV* on *Se* addition [106]. The improvement in thermal stability of amorphous *GST* has been also observed using the *Hf* doping with an increase in crystallization temperature to *220 °C* and the highest temperature of *10* years data retention at *169 °C* on *Hf* doping [93]. The *Hf* doped *GST* thin films displayed the suppression of grain size of rocksalt *fcc* phase and crystallization speed of *GST* phase change material has not been affected. The density functional theory (*DFT*) based first principle calculation of *Al* and *Ga* doped *GST* has been observed to give similar results and shows the formation of bonds mostly with tetrahedral *Te* atom resulting in the higher thermal stability [107]. The improvement in the electrical properties of *GST* thin films on *SiC* doping has been reported and found to be suitable for phase change memory applications [108]. *Zn* has also been considered as the optimal candidate for doping in *GST* phase change material for memory storage applications showing an enhanced crystallization temperature of *272 °C* and wide bandgap [109]. The rare

earth elements have also been chosen as the suitable dopants for *GST* because of their unique properties. In situ temperature-dependent sheet resistance measurements of *GST* on rare earth *Er* doping has been reported by Gu *et al.* and reported an increase in crystallization temperature from 168 °C to 181 °C on 0.7 at% *Er* doping because of the formation of stronger *Er—Sb* heteropolar bonds [110]. The transition of the second *fcc* phase to *GST* hexagonal phase has not been observed on *Er* doping. The reduction in melting temperature of *GST* from 630°C to 564°C and increase in crystallization activation energy from 2.25 eV to 2.54 eV on doping *Sn* have been reported [111]. Chen *et al.* studied the rare earth *Gd* doped *GST* for phase change memory applications and investigated the electrical properties of *GST* and observed an enhancement in resistance of the crystalline phase on *Gd* doping [112]. Rare earth doping is an effective approach to improve the performance of *PCMs* because of their comparatively lower electronegativity and higher coordination number. Doping *GST* with rare earth elements can induce changes in the local structure of *Te*, *Sb* and *Ge* and subsequently may lead to the modification of crystallization behavior of *GST*. The improvement in the thermal stability of *GST* on the addition of rare earths because of the formation of strong bonds can enhance the structural rigidity of *GST* on rare earth doping [112]. It has been also noted that the rare earth doping also modifies the phase transition behavior of *GST* with the suppression of two-step crystallization behavior in undoped *GST* to single-step crystallization [110].

## 1.5. Current Status and Future Scope

Several research groups have studied the phase change memory which has been considered to be the future non-volatile memory technology. Phase change memory has already entered the market as a storage class memory of optane 3D *X*-point memories marketed by Intel and Micron [113]. The first persistent memory device announced by Intel in 2018 displays the feature of non-volatile nature and large storage capacity of 512 GB, but, shows a comparatively slower operation than the *DRAMs* [114]. This product has proved its capabilities for the next generation of memory and can replace *DRAMs* and *SSDs*. The phase-change memory devices have also shown the strong capability and potential for brain-inspired neuromorphic computing devices [36], [47]. Phase change memory can emulate the behavior of biological neurons and synapses, *i.e.*, the neuron interconnections, by utilizing the crystallization kinetics of *GST* induced by the applied electric pulse. The phase-change memory device fabricated to mimic the human brain-behavior is referred to as memristor.

Currently, the development of this technology requires the focus on reduction in power consumption of *PCM* storage cell, multi-bit operation for large scale integration, cycling capability and *PCM* contact resistance [1]. The programming current of *GST* is larger than  $1mA$  on  $180nm$  lithography [115]. For the applications of the practical device, it is desirable to reduce the current to few hundred  $\mu A$ . The scaling down of device size is the key to minimize power consumption. Another approach that has been adopted to reduce the power consumption is based upon *GST* superlattice materials also called the interfacial phase change materials [116]. *GST* superlattice has been prepared by fabricating the ultrathin layers (of the order of  $1 nm$  to  $8 nm$ ) of *GeTe* and *Sb<sub>2</sub>Te<sub>3</sub>* separated by van der Waal gap utilizing the synthesis techniques *MBE* or *PLD* demonstrating ultra-low power consumption and enhanced switching speed [117], [118]. The nanowires and nanodots of *GST* have also been fabricated which have shown the outstanding performance with respect to the power consumption and the switching speed of *PCM* devices compared to bulk *GST* [89], [119]. The scaling down of device size to  $< 30 nm$  has been also found to improve the cycling endurance of *GST* to  $10^{11}$ - $10^{12}$  cycles [114].

The requirement of a faster switching speed of phase change material impacts the thermal stability of the amorphous phase, so it becomes difficult to combine the feature of fast operation and data retention of phase change memory in long-term to match the universal memory requirements. The enhancement of amorphous phase stability in phase change materials without affecting the crystallization speed has been also discussed in recent reports by introducing the capping layer over it [120]. The strategies have been adopted to improve the data storage capacity by introducing the *3D* vertical stacking of memory sheets over the conventional *2D* structures [1]. However, the limitation of leakage current in *3D* stacking needs to be explored. Improving the chalcogenide *PCM*'s performance by substituting the impurity element has currently received the enormous attention in order to model the storage capacity because of the compositional dependence of switching properties chalcogenide *PCMs* [93].

## 1.6. Motivation

The switching of chalcogenide *PCMs* have been studied first time in *1968* and has attained huge attention since *2000*. Various aspects of *PCMs* for memory storage have been investigated and are the most mature memory technology. One of the advantages of *PC* memories is their non-volatile nature and also can unify the performance gap between the

solid-state drives (*SSDs*) and dynamic random access memories (*DRAMs*) due to the best combination of persistent storage capacity and operation speed. *DRAMs* exhibit the fastest access time of less than  $10ns$  with a very small retention time of  $\sim 64ms$ . Because of the volatile nature of *DRAMs*, they cannot be utilized for long-term data storage. *SSDs* display a slower operation with an access time of the order of  $100\mu s$  and cannot be utilized for data processing. Because of this reason separate processing unit and storage unit is utilized in the conventional computer system.

Phase change memory is the best substitute for conventional non-volatile memories and has proven the capabilities of next-generation universal memory technology exhibiting both faster operation and large storage capacity. Figure 1.15 shows the memory hierarchy in terms of device cost and performance and the comparison of phase change memory with the existing conventional memories. *SRAMs* and *DRAMs* are the most expensive and have very small data retention time and access time whereas the hard disc drives (*HDD*) are the most cost-effective with large storage capacity and poor performance. Phase change memory exhibits the best combination of device cost-effectiveness and performance.

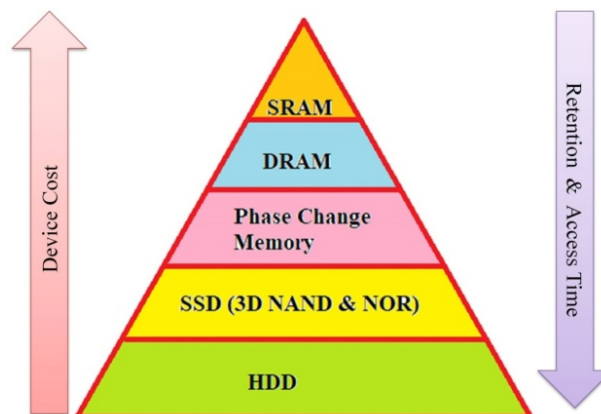


**Figure 1.15.** Memory hierarchy in terms of device cost and performance.

The Phase-change (*PC*) memories have been launched with *3D X-point* storage class memories already into the market having a low cost ( $< \$1/GB$ ) and access time of  $< 10\mu s$  [1]. Table 1.1 summarizes the device characteristics of *PC* memory in comparison to the flash memories and *DRAMs*. For the commercialization of this memory technology, a few critical issues regarding the performance of *PC* memories need to be addressed such as lower power consumption, improved thermal stability, rapid crystallization and drift resistance for the replacement of existing memory technology.

	Cell Area	Read Time	Write / Erase Time	Retention Time	Write Cycles	Operating Voltage	Ref.
<b>DRAM</b>	$6F^2$	$<10\text{ ns}$	$<10\text{ ns}$	$64\text{ ms}$	$>10^{16}$	$2.5\text{ V}$	[2]
<b>NOR Flash</b>	$10F^2$	$10\text{ ns}$	$1\mu\text{s}/10\text{ms}$	$>10\text{ years}$	$10^5$	$12\text{ V}$	[2]
<b>NAND Flash</b>	$5F^2$	$50\text{ ns}$	$1\text{ms}/0.1\text{ ms}$	$>10\text{ years}$	$10^5$	$15\text{ V}$	[2]
<b>Phase Change Memory</b>	$7-16F^2$	$60\text{ ns}$	$50\text{ ns}$	$>10\text{ years}$ <i>at 128 °C</i>	$10^8$	$3.3\text{ V}$	[2], [103]

**Table 1.1.** The comparison of device performance of Phase change memory, Flash memories and DRAM. Tabulated data reprinted with permission from ref. [2] copyright © 2010 IEEE.

Chalcogenide *Ge-Sb-Te* ternary alloys have proven their superior capabilities to be compatible with future high-performance computing requirements and to overcome existing memory hierarchy [121]. The *Ge-Sb-Te* alloys show high contrast of resistivity between amorphous and crystalline states which offers the better signal-to-noise ratio of *PC* memory. The pseudo-binary *Ge-Sb-Te* alloys also display lower melting temperature which is advantageous for lower power consumption of memory. The optimization of material properties for improving the device performance is better explored by modifying stoichiometry. The *Ge-Sb-Te* alloys containing larger content of *GeTe* display enhanced thermal stability because of the higher crystallization activation energy of *GeTe*. The increase in thermal stability at a higher crystallization temperature simultaneously slows down the crystallization rate. On the other hand, *SbTe* rich systems display a comparatively faster rate of transformation, but, show lower thermal stability. *Ge<sub>2</sub>Sb<sub>2</sub>Te<sub>5</sub>* (*GST*) constitutes both *SbTe* and *GeTe* in a suitable proportion which counterbalances the shortcoming of each other for the utilization in *PC*-memory device applications. *GST* has recently attained huge attention for storage applications due to its higher thermal stability and crystallization speed [121]. The crystallization in *GST* initiates with the formation of small crystal nuclei and their subsequent growth. The mechanism of crystallization in *GST* is nucleation dominated which means a comparatively higher rate of nucleation than the crystal growth in *GST*. The tens of

nanosecond crystallization speed of *GST* leads to the slower data transfer rate of *PC*-memory devices which limits its use for commercialization [103]. The improvement in *PC*-memory device performance by opting for the substitution of a suitable impurity element to *GST* may be useful in accomplishing the goals of next-generation universal memory. Doping impurities into the cationic vacancy sites of *GST* has been proven as a milestone to boost the thermal stability of *GST* without affecting the crystallization speed [98]. Reducing the grain growth by choosing the suitable dopants that can occupy the position at the grain boundaries is beneficial to bring down the power consumption of the device [79]. Substituting the suitable impurities in *GST* has been also advantageous to improve the issue of resistance drift in the amorphous phase which causes the slowdown of device performance with aging due to the relaxations of covalently bonded amorphous structures [87]. The addition of non-metallic impurities such as *N*, *O* and *C* into *GST* has been observed useful in lowering the power consumption of memory device as these impurities induce the grain refinement in *GST* [79]. These impurities either create the extra phase at grain boundaries or occupy the cationic vacancy sites because of their smaller atomic radii. The aggregation of impurity elements at the boundaries of grains restricts the atomic migration because of the formation of interlocked long atomic chains. But, the addition of these impurity elements results in the slowdown of crystallization speed of *GST* [79]. The substitution of metallic impurity elements increases the rigidity of amorphous *GST* leading to the enhancement in thermal stability. Rare earth doping has recently gained attention for modeling the *GST* performance as it offers control over the electrical properties and can lower the melting temperature of *GST* [110], [112]. Rare earth doping is also advantageous to enhance *GST* thermal stability due to lower electronegativity and availability of vacant *f*-orbital for bond formation in rare earths. Rare earths exist in a positively charged ionic state and are chemically active and can form the stronger heteropolar bonds and rigid 3-dimensional structural networks in *GST*. For the current work, *Sm* has been chosen as a dopant for *GST* because of its ability to form both monochalcogenide and dichalcogenide compounds which may be beneficial to model the switching mechanism of *GST* by modifying the local structure of the amorphous phase.

The objective of the current work is aimed to investigate the effect of *Sm* addition on the crystallization kinetics, chemical bonding nature along with optical properties of *GST* *PCMs*.  $(Ge_2Sb_2Te_5)_{100-x}Sm_x$  ( $x = 0, 0.2, 0.4, 0.6, 0.8, 1.0, 1.2$ ) *PCMs* have been probed and effect of *Sm* on the structural, optical, thermal and electrical behavior of *GST* has been investigated. The physical properties of  $(Ge_2Sb_2Te_5)_{100-x}Sm_x$  have been analyzed to

understand the impact of *Sm* on average coordination number, covalent bonding nature and the rigidity of the structural network. The bulk alloys of  $(Ge_2Sb_2Te_5)_{100-x}Sm_x$  have been prepared using melt quenching and the deposition of thin films has been carried out using the thermal evaporation method. The outcome of *Sm* addition on the nature of chemical bonding in thin films and bulk alloys of *GST* has been analysed by means of *X*-ray diffraction, Raman spectroscopy, *X*-ray photoelectron spectroscopy (*XPS*) and *FTIR* spectroscopy measurements. The optical properties of thin films of  $(Ge_2Sb_2Te_5)_{100-x}Sm_x$  have been studied using *UV-Vis-NIR* spectroscopy. The *Sm* incorporation effect on *GST* thin film thermal behavior including crystallization kinetics and thermal stability for thin films of  $(Ge_2Sb_2Te_5)_{100-x}Sm_x$  have been studied by utilizing the measurements of differential scanning calorimetry.

## 1.7. Thesis Outlines

**Chapter 1** briefly introduces amorphous semiconductors and their classifications. Properties of chalcogenide glasses and phase change materials have been discussed. The current status and future scope of *GST PCM* in view of non-volatile memory application have been reviewed. The aim and motivation of this current thesis work has been highlighted.

**Chapter 2** presents the theoretical study of physical parameters of  $(Ge_2Sb_2Te_5)_{100-x}Sm_x$  system to understand the structural modification efficiency of *Sm* in *GST* for its improved thermal stability. The physical parameters *viz.* mean coordination number, net bonding constraints per atom, average number of lone pair electron, mean bond energy and cohesive energy has been calculated to understand the glass forming ability of alloys. The empirical correlation has been utilized for predicting the glass transition temperature of alloys.

**Chapter 3** describes the synthesis techniques of bulk alloys of *Sm* doped *GST* and methods of deposition of thin films. The detail about the characterization techniques such as *XRD*, *EDAX*, *XPS*, *FTIR*, Raman spectroscopy, *UV-Vis-NIR* spectroscopy, *DSC* and electrical measurement method utilized for investigation of samples has been discussed.

**Chapter 4** describes the structural investigation of  $(Ge_2Sb_2Te_5)_{100-x}Sm_x$  bulk alloys and thin films and analyzes the impact of *Sm* incorporation in *GST* on the structural properties using different structural studies like *XRD*, *XPS*, *FTIR* and Raman spectroscopy. The chapter correlates the content of *Sm* with structural transition in *GST*.

**Chapter 5** discusses the non-linear as well as linear optical properties of  $(Ge_2Sb_2Te_5)_{100-x}Sm_x$  thin films by utilizing the *UV-Vis-NIR* spectroscopy. The result of rare earth element *Sm* addition to  $(Ge_2Sb_2Te_5)_{100-x}Sm_x$  thin films on the optical behavior has been investigated.

**Chapter 6** includes the differential scanning calorimetry (*DSC*) analysis for the mechanism of crystallization for  $(Ge_2Sb_2Te_5)_{100-x}Sm_x$  samples and the investigation of electrical properties as a function of temperature of *Sm* doped *GST* thin films for analysis of resistivity change on crystallization. The *Sm* doped *GST* thin films have been annealed in vacuum at temperatures  $50\text{ }^\circ\text{C}$ ,  $160\text{ }^\circ\text{C}$  and  $250\text{ }^\circ\text{C}$  and have been subsequently analysed using *XRD* to study the phase change.

**Chapter 7** contains the summary and conclusion of the current work.

---

**References**

- [1] S. W. Fong, C. M. Neumann, and H.-S. P. Wong, "Phase-Change Memory—Towards a Storage-Class Memory," *IEEE Trans. Electron Devices*, vol. 64, no. 11, pp. 4374–4385, Nov. 2017.
- [2] H.-S. P. Wong, S. Raoux, S. B. Kim, J. Liang, J. P. Reifenberg, B. Rajendran, M. Asheghi, and K. E. Goodson, "Phase Change Memory," *Proc. IEEE*, vol. 98, no. 12, pp. 2201–2227, Dec. 2010.
- [3] B. T. Kolomiets, "Vitreous Semiconductors (I)," *Phys. status solidi*, vol. 7, no. 2, pp. 359–372, Feb. 1964.
- [4] B. T. Kolomiets, "Vitreous Semiconductors (II)," *Phys. status solidi*, vol. 7, no. 3, pp. 713–731, 1964.
- [5] M. H. Cohen, H. Fritzsche, and S. R. Ovshinsky, "Simple Band Model for Amorphous Semiconducting Alloys," *Phys. Rev. Lett.*, vol. 22, no. 20, pp. 1065–1068, May 1969.
- [6] N. F. Mott, E. A. Davis, and R. A. Street, "States in the gap and recombination in amorphous semiconductors," *Philos. Mag.*, vol. 32, no. 5, pp. 961–996, Nov. 1975.
- [7] J. M. Marshall and A. E. Owen, "Drift mobility studies in vitreous arsenic triselenide," *Philos. Mag.*, vol. 24, no. 192, pp. 1281–1305, Dec. 1971.
- [8] R. M. Hill, "Poole-Frenkel conduction in amorphous solids," *Philos. Mag.*, vol. 23, no. 181, pp. 59–86, Jan. 1971.
- [9] M. Ganaie and M. Zulfequar, "Optical and electrical properties of  $\text{In}_4\text{Se}_{96-x}\text{S}_x$  chalcogenide thin films," *J. Alloys Compd.*, vol. 687, pp. 643–651, 2016.
- [10] M. A. Alvi, S. A. Khan, and A. A. Al-Ghamdi, "Photo-induced effects on electrical properties of  $\text{Ga}_{15}\text{Se}_{81}\text{Ag}_4$  chalcogenide thin films," *Mater. Lett.*, vol. 66, no. 1, pp. 273–275, 2012.
- [11] F. A. Al-Agel, "Effects of annealing temperatures on optical and electrical properties of vacuum evaporated  $\text{Ga}_{15}\text{Se}_{77}\text{In}_8$  chalcogenide thin films," *Vacuum*, vol. 85, no. 9, pp. 892–897, 2011.
- [12] M. Behera, N. C. Mishra, R. Naik, C. Sripan, and R. Ganesan, "Thermal annealing

- induced structural, optical and electrical properties change in  $\text{As}_{40}\text{Se}_{60-x}\text{Bi}_x$  chalcogenide thin films,” *AIP Adv.*, vol. 9, no. 9, p. 095065, 2019.
- [13] V. Sharma, A. Thakur, N. Goyal, G. S. S. Saini, and S. K. Tripathi, “Effect of in additive on the electrical properties of Se-Te alloy,” *Semicond. Sci. Technol.*, vol. 20, no. 1, pp. 103–107, 2005.
- [14] Anjali, B. S. Patial, S. Chand, and N. Thakur, “On high-field conduction and I–V measurements in quaternary Se–Te–In–Pb nano-chalcogenide thin films,” *J. Mater. Sci. Mater. Electron.*, vol. 31, no. 4, pp. 2741–2756, Feb. 2020.
- [15] S. Ojha, M. Roy, A. Chamuah, K. Bhattacharya, and S. Bhattacharya, “Transport phenomena of Cu–S–Te chalcogenide nanocomposites: frequency response and AC conductivity,” *Phys. Chem. Chem. Phys.*, vol. 22, no. 42, pp. 24600–24613, 2020.
- [16] E. M. Assim and E. G. El-Metwally, “A study on electrical (dc/ac) conductivity and dielectric characteristics of quaternary  $\text{Ge}_{50}\text{In}_4\text{Ga}_{13}\text{Se}_{33}$  chalcogenide thin films,” *J. Non. Cryst. Solids*, vol. 566, no. January, p. 120892, Aug. 2021.
- [17] M. Kastner, D. Adler, and H. Fritzsche, “Valence-Alternation Model for Localized Gap States in Lone-Pair Semiconductors,” *Phys. Rev. Lett.*, vol. 37, no. 22, pp. 1504–1507, Nov. 1976.
- [18] E. Cho, J. Im, C. Park, W. J. Son, D. H. Kim, H. Horii, J. Ihm and S. Han, “Atomic and electronic structures of amorphous  $\text{Ge}_2\text{Sb}_2\text{Te}_5$ ; melt-quenched versus ideal glasses,” *J. Phys. Condens. Matter*, vol. 22, no. 20, p. 205504, May 2010.
- [19] P. W. Anderson, “Model for the Electronic Structure of Amorphous Semiconductors,” *Phys. Rev. Lett.*, vol. 34, no. 15, pp. 953–955, Apr. 1975.
- [20] R. A. Street and N. F. Mott, “States in the gap in glassy semiconductors,” *Phys. Rev. Lett.*, vol. 35, no. 19, pp. 1293–1296, 1975.
- [21] I. Sharma, S. K. Tripathi, and P. B. Barman, “Effect of deposition parameters and semi-empirical relations between non-linear refractive index with linear refractive index and third order susceptibility for a  $-\text{Ge}_{20}\text{Se}_{70-x}\text{In}_{10}\text{Bi}_x$  thin films,” *J. Appl. Phys.*, vol. 110, no. 4, p. 043108, Aug. 2011.
- [22] A. A. Bahishti, M. Husain, and M. Zulfequar, “Effects of laser irradiation on optical

- properties of a- $\text{Se}_{100-x}\text{Te}_x$  thin films,” *Radiat. Eff. Defects Solids*, vol. 166, no. 7, pp. 529–536, Jul. 2011.
- [23] I. Sharma and A. S. Hassanien, “Effect of Ge-addition on physical and optical properties of chalcogenide  $\text{Pb}_{10}\text{Se}_{90-x}\text{Ge}_x$  bulk glasses and thin films,” *J. Non. Cryst. Solids*, vol. 548, no. May, p. 120326, Nov. 2020.
- [24] P. Singh, P. Sharma, V. Sharma, and A. Thakur, “Linear and non-linear optical properties of Ag-doped  $\text{Ge}_2\text{Sb}_2\text{Te}_5$  thin films estimated by single transmission spectra,” *Semicond. Sci. Technol.*, vol. 32, no. 4, p. 045015, Apr. 2017.
- [25] R. Raj, P. Lohia, and D. K. Dwivedi, “Investigation of structural and optical properties of  $(\text{GeS}_2)_{100-x}(\text{Sb}_2\text{S}_3)_x$  ( $x = 15, 30, 45, 60$ ) chalcogenide glasses for mid infrared applications,” *Optik (Stuttg.)*, vol. 218, p. 165041, Sep. 2020.
- [26] A. El-Denglawey, V. Sharma, E. Sharma, K. A. Aly, A. Dahshan, and P. Sharma, “Optical and mechanical properties of Ag doped thermally evaporated  $\text{SeTe}$  thin films for optoelectronic applications,” *J. Phys. Chem. Solids*, vol. 159, no. June, p. 110291, Dec. 2021.
- [27] R. Mariappan, T. Mahalingam, and V. Ponnuswamy, “Preparation and characterization of electrodeposited SnS thin films,” *Optik (Stuttg.)*, vol. 122, no. 24, pp. 2216–2219, Dec. 2011.
- [28] F. M. Abdel-Rahim, “Synthesis and characterization of  $\text{Bi}_x(\text{Se}_{80}\text{Te}_{20})_{100-x}$  amorphous thin films,” *Indian J. Phys.*, vol. 90, no. 5, pp. 529–537, 2016.
- [29] B. Qiao, S. Dai, Y. Xu, P. Zhang, X. Shen, T. Xu, Q. Nie, W. Ji and F. Chen, “Third-order optical nonlinearities of chalcogenide glasses within  $\text{Ge-Sn-Se}$  ternary system at a mid-infrared window,” *Opt. Mater. Express*, vol. 5, no. 10, p. 2359, Oct. 2015.
- [30] P. Sharma and S. C. Katyal, “Effect of Cd and Pb impurities on the optical properties of fresh evaporated amorphous  $(\text{As}_2\text{Se}_3)_{90}\text{Ge}_{10}$  thin films,” *Appl. Phys. B*, vol. 95, no. 2, pp. 367–373, May 2009.
- [31] M. El-Hagary, M. Emam-Ismail, E. R. Shaaban, and A. El-Taher, “Effect of  $\gamma$ -irradiation exposure on optical properties of chalcogenide glasses  $\text{Se}_{70}\text{S}_{30-x}\text{Sb}_x$  thin films,” *Radiat. Phys. Chem.*, vol. 81, no. 10, pp. 1572–1577, Oct. 2012.

- [32] K. Anshu and A. Sharma, "Study of Se based quaternary *Se Pb (Bi,Te)* chalcogenide thin films for their linear and nonlinear optical properties," *Optik (Stuttg.)*, vol. 127, no. 1, pp. 48–54, Jan. 2016.
- [33] M. Dongol, A. F. Elhady, M. S. Ebied, and A. A. Abuelwafa, "Impact of sulfur content on structural and optical properties of  $Ge_{20}Se_{80-x}S_x$  chalcogenide glasses thin films," *Opt. Mater. (Amst.)*, vol. 78, pp. 266–272, Apr. 2018.
- [34] T. Cao and M. Cen, "Fundamentals and Applications of Chalcogenide Phase-Change Material Photonics," *Adv. Theory Simulations*, vol. 2, no. 8, p. 1900094, Aug. 2019.
- [35] Y. Jin, Y. Xiao, D. Wang, Z. Huang, Y. Qiu, and L. D. Zhao, "Realizing High Thermoelectric Performance in GeTe through Optimizing Ge Vacancies and Manipulating Ge Precipitates," *ACS Appl. Energy Mater.*, vol. 2, no. 10, pp. 7594–7601, Oct. 2019.
- [36] F. Brückerohoff-Plückelmann, J. Feldmann, C. D. Wright, H. Bhaskaran, and W. H. P. Pernice, "Chalcogenide phase-change devices for neuromorphic photonic computing," *J. Appl. Phys.*, vol. 129, no. 15, p. 151103, Apr. 2021.
- [37] S. R. Ovshinsky, "Reversible Electrical Switching Phenomena in Disordered Structures," *Phys. Rev. Lett.*, vol. 21, no. 20, pp. 1450–1453, Nov. 1968.
- [38] A. W. Smith, "Injection Laser Writing on Chalcogenide Films," *Appl. Opt.*, vol. 13, no. 4, p. 795, Apr. 1974.
- [39] M. Chen, K. A. Rubin, V. Marrello, U. G. Gerber, and V. B. Jipson, "Reversibility and stability of tellurium alloys for optical data storage applications," *Appl. Phys. Lett.*, vol. 46, no. 8, pp. 734–736, Apr. 1985.
- [40] N. Yamada, E. Ohno, N. Akahira, K. Nishiuchi, K. Nagata, and M. Takao, "High Speed Overwritable Phase Change Optical Disk Material," *Jpn. J. Appl. Phys.*, vol. 26, no. S4, p. 61, Jan. 1987.
- [41] H. Iwasaki, Y. Ide, M. Harigaya, Y. Kageyama, and I. Fujimura, "Completely Erasable Phase Change Optical Disk," *Jpn. J. Appl. Phys.*, vol. 31, no. Part 1, No. 2B, pp. 461–465, Feb. 1992.
- [42] D. Dimitrov, M. A. Ollacarizqueta, C. N. Afonso, and N. Starbov, "Crystallization

- kinetics of  $Sb_xSe_{100-x}$  thin films,” *Thin Solid Films*, vol. 280, no. 1–2, pp. 278–283, Jul. 1996.
- [43] S. S. Fouad, H. E. Atyia, A. E. Bekheet, A. Kumar, and N. Mehta, “Phenomenology of electrical switching behavior of  $SeTeSnCd$  thin films for memory applications,” *J. Non. Cryst. Solids*, vol. 571, no. June, p. 121025, Nov. 2021.
- [44] C. Chen, J. Lin, X. Mai, C. Qiao, H. Tong, X. Cheng, S. Wang, C. -Z. Wang, K. -M. Ho, M. Xu and X. Miao, “Characterizations of electronic and optical properties of Sb-based phase-change material stabilized by alloying Cr,” *Appl. Phys. Lett.*, vol. 118, no. 4, p. 042104, Jan. 2021.
- [45] S. Lepeshov and A. Krasnok, “Tunable phase-change metasurfaces,” *Nat. Nanotechnol.*, no. April, pp. 6–8, Apr. 2021.
- [46] Q. Hu, B. Dong, L. Wang, E. Huang, H. Tong, Y. He, M. Xu and X. Miao, “An artificial synapse by superlattice-like phase-change material for low-power brain-inspired computing,” *Chinese Phys. B*, vol. 29, no. 7, p. 070701, Jun. 2020.
- [47] Q. Wang, G. Niu, W. Ren, R. Wang, X. Chen, X. Li, Z. -G. Ye, Y. -H. Xie, S. Song and Z. Song, “Phase Change Random Access Memory for Neuro-Inspired Computing,” *Adv. Electron. Mater.*, vol. 7, no. 6, p. 2001241, Jun. 2021.
- [48] D. Wu, L. D. Zhao, S. Hao, Q. Jiang, F. Zheng, J. W. Doak, H. Wu, H. Chi, Y. Gelbstein, C. Uher, C. Wolverton, M. Kanatzidis and J. He, “Origin of the High Performance in GeTe-Based Thermoelectric Materials upon Bi 2 Te 3 Doping,” *J. Am. Chem. Soc.*, vol. 136, no. 32, pp. 11412–11419, Aug. 2014.
- [49] M. Agati, M. Vallet, S. Joulié, D. Benoit, and A. Claverie, “Chemical phase segregation during the crystallization of Ge-rich  $GeSbTe$  alloys,” *J. Mater. Chem. C*, vol. 7, no. 28, pp. 8720–8729, 2019.
- [50] J. Feinleib, J. DeNeufville, S. C. Moss, and S. R. Ovshinsky, “Rapid reversible light-induced crystallization of amorphous semiconductors,” *Appl. Phys. Lett.*, vol. 18, no. 6, pp. 254–257, Mar. 1971.
- [51] D. Liu, L. Xu, Y. Liao, M. Dai, L. Zhao, J. Xu, L. Wu, Z. Ma and K. Chen, “Comparison of Thermal Stability and Electrical Characterization between  $Ge_2Sb_2Te_5$

- and  $Ge_1Sb_2Te_4$  Phase-Change Materials,” *Jpn. J. Appl. Phys.*, vol. 48, no. 12, p. 121104, Dec. 2009.
- [52] P. Guo, A. Sarangan, and I. Agha, “A Review of Germanium-Antimony-Telluride Phase Change Materials for Non-Volatile Memories and Optical Modulators,” *Appl. Sci.*, vol. 9, no. 3, p. 530, Feb. 2019.
- [53] L. Xu, L. Tong, L. Geng, F. Yang, J. Xu, W. Su, D. Liu, Z. Ma and K. Chen, “A comparative study on electrical transport properties of thin films of  $Ge_1Sb_2Te_4$  and  $Ge_2Sb_2Te_5$  phase-change materials,” *J. Appl. Phys.*, vol. 110, no. 1, p. 013703, Jul. 2011.
- [54] J.-W. Park, S. H. Eom, H. Lee, J.L.F. Da Silva, Y. S. Kang, T. -Y. Lee and Y. H. Khang, “Optical properties of pseudobinary  $GeTe$ ,  $Ge_2Sb_2Te_5$ ,  $GeSb_2Te_4$ ,  $GeSb_4Te_7$ , and  $Sb_2Te_3$  from ellipsometry and density functional theory,” *Phys. Rev. B*, vol. 80, no. 11, p. 115209, Sep. 2009.
- [55] J. Pries, J. C. Sehringer, S. Wei, P. Lucas, and M. Wuttig, “Glass transition of the phase change material AIST and its impact on crystallization,” *Mater. Sci. Semicond. Process.*, vol. 134, no. July, p. 105990, Nov. 2021.
- [56] T. Matsunaga, J. Akola, S. Kohara, T. Honma, K. Kobayashi, E. Ikenag, R. O. Jones, N. Yamada, M. Takata and R. Kojima, “From local structure to nanosecond recrystallization dynamics in AgInSbTe phase-change materials,” *Nat. Mater.*, vol. 10, no. 2, pp. 129–134, Feb. 2011.
- [57] H. Tashiro, M. Horigaya, Y. Kageyama, K. Ito, M. Shinotsuka, K. Tani, A. Watada, N. Yiwata, Y. Nakata and S. Emura, “Structural analysis of Ag-In-Sb-Te phase-change material,” *Japanese J. Appl. Physics, Part 1 Regul. Pap. Short Notes Rev. Pap.*, vol. 41, no. 6 A, pp. 3758–3759, Jun. 2002.
- [58] Y. Maeda, H. Andoh, I. Ikuta, and H. Minemura, “Reversible phase-change optical data storage in InSbTe alloy films,” *J. Appl. Phys.*, vol. 64, no. 4, pp. 1715–1719, Aug. 1988.
- [59] Y. Tae Kim and S.-I. Kim, “Comparison of thermal stabilities between Ge-Sb-Te and In-Sb-Te phase change materials,” *Appl. Phys. Lett.*, vol. 103, no. 12, p. 121906, Sep. 2013.

- [60] S. K. Pandey and A. Manivannan, “Sub-nanosecond threshold-switching dynamics and set process of  $\text{In}_3\text{SbTe}_2$  phase-change memory devices,” *Appl. Phys. Lett.*, vol. 108, no. 23, p. 233501, Jun. 2016.
- [61] S. Sahu, A. Manivannan, H. Shaik, and G. Mohan Rao, “Local structure of amorphous  $\text{Ag}_5\text{In}_5\text{Sb}_{60}\text{Te}_{30}$  and  $\text{In}_3\text{SbTe}_2$  phase change materials revealed by X-ray photoelectron and Raman spectroscopic studies,” *J. Appl. Phys.*, vol. 122, no. 1, p. 015305, Jul. 2017.
- [62] V. L. Deringer, W. Zhang, P. Rausch, R. Mazzarello, R. Dronskowski, and M. Wuttig, “A chemical link between Ge–Sb–Te and In–Sb–Te phase-change materials,” *J. Mater. Chem. C*, vol. 3, no. 37, pp. 9519–9523, 2015.
- [63] S. Raoux, W. Welnic, and D. Ielmini, “Phase change materials and their application to nonvolatile memories,” *Chem. Rev.*, vol. 110, no. 1, pp. 240–267, Jan. 2010.
- [64] Y.-J. Yoon, C. -K. Min, W. -C. Kim, N. -C. Park, Y. -P. Park, T. Hong and K. Lee, “Solid Immersion Lens Optical Head for High-Numerical-Aperture Cover-Layered Incident Near-Field Recording,” *Jpn. J. Appl. Phys.*, vol. 48, no. 3, p. 03A040, Mar. 2009.
- [65] M. Kuwahara, T. Nakano, J. Tominaga, M. B. Lee, and N. Atoda, “High-Speed Optical Near-Field Photolithography by Super Resolution Near-Field Structure,” *Jpn. J. Appl. Phys.*, vol. 38, no. Part 2, No. 9A/B, pp. L1079–L1081, Sep. 1999.
- [66] M. S. Arjunan, N. Saxena, A. Mondal, T. Dixit, K. N. V. D. Adarsh, and A. Manivannan, “High-Stability and Low-Noise Multilevel Switching in  $\text{In}_3\text{SbTe}_2$  Material for Phase Change Photonic Memory Applications,” *Phys. status solidi – Rapid Res. Lett.*, vol. 15, no. 3, p. 2000354, Mar. 2021.
- [67] G. W. Burr, M. J. Breitwisch, M. Franceschini, D. Garetto, K. Gopalakrishnan, B. Jackson, B. Kurdi, C. Lam, L. A. Lastras, A. Padilla, B. Rajendran, S. Raoux and R. S. Shenoy, “Phase change memory technology,” *J. Vac. Sci. Technol. B*, vol. 28, no. 2, pp. 223–262, Mar. 2010.
- [68] A. Pirovano, A. L. Lacaita, F. Pellizzer, S. A. Kostylev, A. Benvenuti, and R. Bez, “Low-field amorphous state resistance and threshold voltage drift in chalcogenide materials,” *IEEE Trans. Electron Devices*, vol. 51, no. 5, pp. 714–719, May 2004.

- [69] Z.-C. Liu and L. Wang, “Applications of Phase Change Materials in Electrical Regime From Conventional Storage Memory to Novel Neuromorphic Computing,” *IEEE Access*, vol. 8, pp. 76471–76499, 2020.
- [70] D. Kuzum, R. G. D. Jeyasingh, B. Lee, and H.-S. P. Wong, “Nanoelectronic Programmable Synapses Based on Phase Change Materials for Brain-Inspired Computing,” *Nano Lett.*, vol. 12, no. 5, pp. 2179–2186, May 2012.
- [71] M. Suri, O. Bichler, D. Querlioz, B. Traoré, O. Cueto, L. Perniola, V. Sousa, D. Vuillaume, C. Gamrat and B DeSalvo, “Physical aspects of low power synapses based on phase change memory devices,” in *Journal of Applied Physics*, 2012, vol. 112, no. 5, p. 054904.
- [72] P. Hu, T. -R. Wei, P. Qiu, Y. Cao, J. Yang, X. Shi, and L. Chen, “Largely Enhanced Seebeck Coefficient and Thermoelectric Performance by the Distortion of Electronic Density of States in  $\text{Ge}_2\text{Sb}_2\text{Te}_5$ ,” *ACS Appl. Mater. Interfaces*, vol. 11, no. 37, pp. 34046–34052, Sep. 2019.
- [73] L. Xie, Y. Chen, R. Liu, E. Song, T. Xing, T. Deng, Q. Song, J. Liu, R. Zheng, X. Gao, S. Bai and L. Chen, “Stacking faults modulation for scattering optimization in GeTe-based thermoelectric materials,” *Nano Energy*, vol. 68, no. November 2019, p. 104347, Feb. 2020.
- [74] P. Singh, A. P. Singh, N. Kanda, M. Mishra, G. Gupta, and A. Thakur, “High transmittance contrast in amorphous to hexagonal phase of  $\text{Ge}_2\text{Sb}_2\text{Te}_5$ : Reversible NIR-window,” *Appl. Phys. Lett.*, vol. 111, no. 26, p. 261102, Dec. 2017.
- [75] X. Sun, M. Ehrhardt, A. Lotnyk, P. Lorenz, E. Thelander, J. W. Gerlach, T. Smausz, U. Decker and B. Rauschenbach, “Crystallization of  $\text{Ge}_2\text{Sb}_2\text{Te}_5$  thin films by nano- and femtosecond single laser pulse irradiation,” *Sci. Rep.*, vol. 6, no. 1, p. 28246, Sep. 2016.
- [76] P. Singh, A.P. Singh, J. Sharma, A. Kumar, M. Mishra, G. Gupta, and A. Thakur, “Reduction of Rocksalt Phase in Ag-Doped  $\text{Ge}_2\text{Sb}_2\text{Te}_5$ : A Potential Material for Reversible Near-Infrared Window,” *Phys. Rev. Appl.*, vol. 10, no. 5, p. 054070, Nov. 2018.
- [77] J. Pries, S. Wei, M. Wuttig, and P. Lucas, “Switching between Crystallization from the

- Glassy and the Undercooled Liquid Phase in Phase Change Material  $\text{Ge}_2\text{Sb}_2\text{Te}_5$ ,” *Adv. Mater.*, vol. 31, no. 39, p. 1900784, Sep. 2019.
- [78] J. Akola and R. O. Jones, “Structural phase transitions on the nanoscale: The crucial pattern in the phase- change materials  $\text{Ge}_2\text{Sb}_2\text{Te}_5$  and  $\text{GeTe}$ ,” *Phys. Rev. B*, vol. 76, no. 23, p. 235201, Dec. 2007.
- [79] X. Zhou, M. Xia, F. Rao, L. Wu, X. Li, Z. Song, S. Feng, and H. Sun “Understanding Phase-Change Behaviors of Carbon-Doped  $\text{Ge}_2\text{Sb}_2\text{Te}_5$  for Phase-Change Memory Application,” *ACS Appl. Mater. Interfaces*, vol. 6, no. 16, pp. 14207–14214, Aug. 2014.
- [80] B. Zhang, X. -P. Wang, Z -J. Shen, X. -B. Li, C. -S. Wang, Y. -J. Chen, J. -X. Li, J. -X. Zhang, Z. Zhang, S. -B. Zhang and X. -D. Han, “Vacancy Structures and Melting Behavior in Rock-Salt  $\text{GeSbTe}$ ,” *Sci. Rep.*, vol. 6, no. 1, p. 25453, Jul. 2016.
- [81] Y. Zheng, Y. Wang, T. Xin, Y. Cheng, R. Huang, P. Liu, M. Luo, Z. Zhang, S. Lv, Z. Song and S. Feng, “Direct atomic identification of cation migration induced gradual cubic-to-hexagonal phase transition in  $\text{Ge}_2\text{Sb}_2\text{Te}_5$ ,” *Commun. Chem.*, vol. 2, no. 1, p. 13, Dec. 2019.
- [82] Z. Sun, J. Zhou, and R. Ahuja, “Structure of Phase Change Materials for Data Storage,” *Phys. Rev. Lett.*, vol. 96, no. 5, p. 055507, Feb. 2006.
- [83] B. J. Kooi and J. T. M. De Hosson, “Electron diffraction and high-resolution transmission electron microscopy of the high temperature crystal structures of  $\text{Ge}_x\text{Sb}_2\text{Te}_{3+x}$  ( $x=1,2,3$ ) phase change material,” *J. Appl. Phys.*, vol. 92, no. 7, pp. 3584–3590, 2002.
- [84] T. Matsunaga, N. Yamada, and Y. Kubota, “Structures of stable and metastable  $\text{Ge}_2\text{Sb}_2\text{Te}_5$  , an intermetallic compound in  $\text{GeTe}-\text{Sb}_2\text{Te}_3$  pseudobinary systems,” *Acta Crystallogr. Sect. B Struct. Sci.*, vol. 60, no. 6, pp. 685–691, Dec. 2004.
- [85] A. V. Kolobov, P. Fons, A. I. Frenkel, A. L. Ankudinov, J. Tominaga, and T. Uruga, “Understanding the phase-change mechanism of rewritable optical media,” *Nat. Mater.*, vol. 3, no. 10, pp. 703–708, Oct. 2004.
- [86] S. R. Elliott, “Electronic mechanism for resistance drift in phase-change memory

- materials: link to persistent photoconductivity,” *J. Phys. D. Appl. Phys.*, vol. 53, no. 21, p. 214002, May 2020.
- [87] W. Zhang and E. Ma, “Unveiling the structural origin to control resistance drift in phase-change memory materials,” *Mater. Today*, vol. 41, pp. 156–176, Dec. 2020.
- [88] K. Ding, J. Wang, Y. Zhou, H. Tian, L. Lu, R. Mazzarello, C. Jia, W. Zhang, F. Rao, E. Ma, “Phase-change heterostructure enables ultralow noise and drift for memory operation,” *Science*, vol. 366, no. 6462, pp. 210–215, Oct. 2019.
- [89] M. Mitra, Y. Jung, D. S. Gianola, and R. Agarwal, “Extremely low drift of resistance and threshold voltage in amorphous phase change nanowire devices,” *Appl. Phys. Lett.*, vol. 96, no. 22, p. 222111, May 2010.
- [90] F. Yang, Yue Tao, L. Zhang, J. Han, X. Cao, Z. Zhuo, Z. Zhu, W. Liu, and Y. Dai, “Ab initio study on the fast reversible phase transitions of  $\text{Ge}_2\text{Sb}_2\text{Te}_5$ ,” *J. Appl. Phys.*, vol. 130, no. 2, p. 025106, Jul. 2021.
- [91] B.-S. Lee, R. M. Shelby, S. Raoux, C. T. Retter, G. W. Burr, S. N. Bogle, K. Darmawikarta, S. G. Bishop and J. R. Abelson, “Nanoscale nuclei in phase change materials: Origin of different crystallization mechanisms of  $\text{Ge}_2\text{Sb}_2\text{Te}_5$  and  $\text{AgInSbTe}$ ,” *J. Appl. Phys.*, vol. 115, no. 6, p. 063506, Feb. 2014.
- [92] M. Luong, N. Cherkashin, B. Pecassou, C. Sabbione, F. Mazen, and A. Claverie, “Effect of Nitrogen Doping on the Crystallization Kinetics of  $\text{Ge}_2\text{Sb}_2\text{Te}_5$ ,” *Nanomaterials*, vol. 11, no. 7, p. 1729, Jun. 2021.
- [93] R. Wang, J. Shen, X. Chen, H. Wang, S. Song, and Z. Song, “High thermal stability and fast operation speed phase-change memory devices containing Hf-doped  $\text{Ge}_2\text{Sb}_2\text{Te}_5$  films,” *Mater. Lett.*, vol. 278, p. 128402, Nov. 2020.
- [94] Y. Mao, Y. Chen, Q. Zhang, R. Wang, and X. Shen, “Improvement of thermal stability and phase change behavior of  $\text{Ge}_2\text{Sb}_2\text{Te}_5$  thin films by Calcium doping,” *J. Non. Cryst. Solids*, vol. 549, no. April, p. 120338, Dec. 2020.
- [95] Y. Cheng, D. Cai, Y. Zheng, S. Yan, L. Wu, C. Li, W. Song, T. Xin, S. Lv, R. Huang, H. Lv, Z. Song and S. Feng, “Microscopic Mechanism of Carbon-Dopant Manipulating Device Performance in  $\text{CGeSbTe}$ -Based Phase Change Random Access

- Memory,” *ACS Appl. Mater. Interfaces*, vol. 12, no. 20, pp. 23051–23059, May 2020.
- [96] N. Yamada, E. Ohno, K. Nishiuchi, N. Akahira, and M. Takao, “Rapid-phase transitions of  $GeTe-Sb_2Te_3$  pseudobinary amorphous thin films for an optical disk memory,” *J. Appl. Phys.*, vol. 69, no. 5, pp. 2849–2856, Mar. 1991.
- [97] J. A. Kalb, M. Wuttig, and F. Spaepen, “Calorimetric measurements of structural relaxation and glass transition temperatures in sputtered films of amorphous Te alloys used for phase change recording,” *J. Mater. Res.*, vol. 22, no. 3, pp. 748–754, Mar. 2007.
- [98] J. H. Han, K. Jeonga, M. Ahna, D. -H. Lima, W. J. Yanga, S. J. Parka, and M. -H. Cho, “Modulation of phase change characteristics in Ag-incorporated  $Ge_2Sb_2Te_5$  owing to changes in structural distortion and bond strength,” *J. Mater. Chem. C*, vol. 5, no. 16, pp. 3973–3982, 2017.
- [99] B. Prasai, G. Chen, and D. A. Drabold, “Direct ab-initio molecular dynamic study of ultrafast phase change in Ag-alloyed  $Ge_2Sb_2Te_5$ ,” *Appl. Phys. Lett.*, vol. 102, no. 4, p. 041907, Jan. 2013.
- [100] K.-H. Song, S.-W. Kim, J.-H. Seo, and H.-Y. Lee, “Characteristics of amorphous  $Ag_{0.1}(Ge_2Sb_2Te_5)_{0.9}$  thin film and its ultrafast crystallization,” *J. Appl. Phys.*, vol. 104, no. 10, p. 103516, Nov. 2008.
- [101] Y. Kim, K. Jeong, M.-H. Cho, U. Hwang, H. S. Jeong, and K. Kim, “Changes in the electronic structures and optical band gap of  $Ge_2Sb_2Te_5$  and N-doped  $Ge_2Sb_2Te_5$  during phase transition,” *Appl. Phys. Lett.*, vol. 90, no. 17, p. 171920, Apr. 2007.
- [102] B. Liu, Z. Song, T. Zhang, J. Xia, S. Feng, and B. Chen, “Effect of N-implantation on the structural and electrical characteristics of  $Ge_2Sb_2Te_5$  phase change film,” *Thin Solid Films*, vol. 478, no. 1–2, pp. 49–55, May 2005.
- [103] Z. T. Song, D. L. Cai, X. Li, L. Wang, Y. F. Chen, H. P. Chen, Q. Wang, Y. P. Zhan and M. H. Ji, “High Endurance Phase Change Memory Chip Implemented based on Carbon-doped  $Ge_2Sb_2Te_5$  in 40 nm Node for Embedded Application,” in *2018 IEEE International Electron Devices Meeting (IEDM)*, 2018, vol. 2018-Decem, pp. 27.5.1-27.5.4.

- [104] W.-X. Song, Y. Cheng, D. Cai, Q. Tang, Z. Song, L. Wang, J. Zhao, T. Xin, and Z. -P. Liu, “Improving the performance of phase-change memory by grain refinement,” *J. Appl. Phys.*, vol. 128, no. 7, p. 075101, Aug. 2020.
- [105] V. E. Madhavan, M. Carignano, A. Kachmar, and K. S. Sangunni, “Crystallization properties of arsenic doped GST alloys,” *Sci. Rep.*, vol. 9, no. 1, p. 12985, Dec. 2019.
- [106] E. M. Vinod, K. Ramesh, R. Ganesan, and K. S. Sangunni, “Direct hexagonal transition of amorphous  $(Ge_2Sb_2Te_5)_{0.9}Se_{0.1}$  thin films,” *Appl. Phys. Lett.*, vol. 104, no. 6, p. 063505, Feb. 2014.
- [107] D. Lee, G. Kang, K. Lee, S. Yoon, J. Kim, and S. Han, “First-principles calculations on effects of Al and Ga dopants on atomic and electronic structures of amorphous  $Ge_2Sb_2Te_5$ ,” *J. Appl. Phys.*, vol. 125, no. 3, p. 035701, Jan. 2019.
- [108] T. Guo, S. Song, Z. Song, X. Ji, Y. Xue, L. Chen, Y. Cheng, B. Liu, L. Wu, M. Qi, and S. Feng, “SiC-Doped  $Ge_2Sb_2Te_5$  Phase-Change Material: A Candidate for High-Density Embedded Memory Application,” *Adv. Electron. Mater.*, vol. 4, no. 8, p. 1800083, Aug. 2018.
- [109] G. Wang, Q. Nie, X. Shen, R. P. Wang, L. Wu, J. Fu, T. Xu, and S. Dai, “Phase change behaviors of Zn-doped  $Ge_2Sb_2Te_5$  films,” *Appl. Phys. Lett.*, vol. 101, no. 5, p. 051906, Jul. 2012.
- [110] T. Gu, J. Wang, H. Liu, Z. Wang, Y. Luo, P. Liu, J. Zhong, G. Wang, “One-step phase transition and thermal stability improvement of  $Ge_2Sb_2Te_5$  films by erbium-doping,” *Vacuum*, vol. 145, pp. 258–261, Nov. 2017.
- [111] Q. Yin and L. Chen, “Enhanced optical properties of Sn-doped  $Ge_2Sb_2Te_5$  thin film with structural evolution,” *J. Alloys Compd.*, vol. 770, pp. 692–700, Jan. 2019.
- [112] Y. Chen, N. Chen, B. Chen, Q. Zhang, X. Li, Q. Deng, B. Zhang, S. Zhang, Z. Zhang, and X. Han, “Electrical properties and structural transition of  $Ge_2Sb_2Te_5$  adjusted by rare-earth element Gd for nonvolatile phase-change memory,” *J. Appl. Phys.*, vol. 124, no. 14, p. 145107, Oct. 2018.
- [113] T. Kim and S. Lee, “Evolution of Phase-Change Memory for the Storage-Class Memory and Beyond,” *IEEE Trans. Electron Devices*, vol. 67, no. 4, pp. 1394–1406,

- Apr. 2020.
- [114] W. Zhang, R. Mazzarello, M. Wuttig, and E. Ma, “Designing crystallization in phase-change materials for universal memory and neuro-inspired computing,” *Nat. Rev. Mater.*, vol. 4, no. 3, pp. 150–168, Mar. 2019.
- [115] S. Lai, “Current status of the phase change memory and its future,” in *IEEE International Electron Devices Meeting 2003*, 2003, pp. 10.1.1-10.1.4.
- [116] A. Lotnyk, I. Hilmi, M. Behrens, and B. Rauschenbach, “Temperature dependent evolution of local structure in chalcogenide-based superlattices,” *Appl. Surf. Sci.*, vol. 536, no. September 2020, p. 147959, Jan. 2021.
- [117] L. Zhou, Z. Yang, X. Wang, H. Qian, M. Xu, X. Cheng, H. Tong, and X. Miao, “Resistance Drift Suppression Utilizing  $GeTe/Sb_2Te_3$  Superlattice-Like Phase-Change Materials,” *Adv. Electron. Mater.*, vol. 6, no. 1, p. 1900781, Jan. 2020.
- [118] P. Kowalczyk, F. Hippert, N. Bernier, C. Mocuta, C. Sabbione, W. B. Pessoa, and P. Noe, “Impact of Stoichiometry on the Structure of van der Waals Layered  $GeTe/Sb_2Te_3$  Superlattices Used in Interfacial Phase-Change Memory (iPCM) Devices,” *Small*, vol. 14, no. 24, p. 1704514, Jun. 2018.
- [119] Q. Zheng, Y. Wang, and J. Zhu, “Nanoscale phase-change materials and devices,” *Journal of Physics D: Applied Physics*, vol. 50, no. 24. IOP Publishing, p. 243002, 21-Jun-2017.
- [120] R. Pandian, B. J. Kooi, J. T. M. De Hosson, and A. Pauza, “Influence of capping layers on the crystallization of doped  $Sb_xTe$  fast-growth phase-change films,” *J. Appl. Phys.*, vol. 100, no. 12, p. 123511, Dec. 2006.
- [121] R. Wang, Z. Song, W. Song, T. Xin, S. Lv, S. Song, J. Liu, “Phase-change memory based on matched Ge-Te, Sb-Te, and In-Te octahedrons: Improved electrical performances and robust thermal stability,” *InfoMat*, vol. 3, no. 9, pp. 1008–1015, Sep. 2021.



## Chapter 2

### Physical Properties of *Sm* Doped *Ge<sub>2</sub>Sb<sub>2</sub>Te<sub>5</sub>*

- **Sanjay Kumar**, Pankaj Sharma, and Vineet Sharma, “Dependence of structural cross-linking, system energy and transition temperature on coordination number for Sm doped GST,” **Results in Physics.**, vol. 13, p. 102276, Jun. 2019.
- **Sanjay Kumar** and Vineet Sharma, “Improvement in stability of GST PCMs on Sm addition for memory devices,” **Journal of Non-Crystalline Solids**, vol. 532, p. 119887, Mar. 2020.



## 2.1 Introduction

Chalcogenide glasses cover wide range of applications in electronics and optoelectronics due to their novel optical, thermal and electronic characteristics [1]. Chalcogenides have been studied immensely and find applications in optical data storage devices [2], high precision glass lenses for thermal imaging [3], IR transmitting optical fibers [4], switching [5], electrical data storage devices [6], holographic recording [7] and photonics [8]. Due to the high non-linearity of refractive index and low-loss signal transmission in terahertz frequency range, chalcogenide glasses finds them suitable candidate for the waveguides and signal processing applications [9], [10].

The requirement of large data storage and fast operation of storage devices has been increasing continuously with the advancement in information technology. The existing memory devices i.e. *SRAM* and *DRAM* consumes large amount of electrical power and are much expensive to assemble for high performance computing. The volatile nature of *SRAMs* and *DRAMs* also limits their use in the “universal memories” for performing both data storage and processing tasks by the single unit. Whereas the *NAND* and *NOR* flash memories have slower operation and cannot meet the requirements of fast data processing. The phase change memories based upon chalcogenide material have the ability for unifying the fast device operation of *SRAMs* and *DRAMs* and long term data retention (non-volatile nature) of *SSDs* for efficient computing.

Phase change (*PC*) memories are the new emerging technology which works on the principle of reversible switching among disordered (amorphous) phase and ordered (crystalline) phase. Ovshinsky [11] in very first time in 1969 put forward the idea of reversible switching between crystalline and non-crystalline phases of chalcogenide glassy alloy. The amorphous phase of phase change materials is electrically highly resistive in nature whereas its crystalline counterpart is conducting nature which is induced by heat treatment above crystallization temperature of the phase change material. The disorder-order switching provides large contrast in optical reflectivity and electrical resistivity of phase change materials [12]. The contrast in conductivity of phase change materials among amorphous and crystalline phases has been utilized in one bit storage cell of *PC* memory for information storage. The *Ge* based alloys are promising for phase change memory materials because of their higher transition temperature and large resistivity contrast. The higher contrast of resistivity between amorphous and crystalline states is advantageous for improved signal to noise ratio or *ON/OFF* ratio of *PC* memory device. The enhanced amorphous phase

stability necessitates the higher value of activation energy and crystallization temperature for long term data retention. The ternary compounds lying in the tie line between  $GeTe$  and  $Sb_2Te_3$  pseudo-binary compounds have been known to be potential materials for  $PC$  memory applications [13]. The compounds lying near the  $GeTe$  end of pseudo-binary tie line exhibit the higher transition temperature and crystallization temperature because of which they acquire higher thermal stability. While the compounds at the opposite end of the tie line rich in  $Sb$  content show lower transition temperature and higher switching speed. The appropriate proportion of both  $GeTe$  and  $Sb_2Te_3$  is required to attain both the enhanced crystallization speed and higher transition temperature for the improved performance of  $PC$  memory device.  $Ge_2Sb_2Te_5$  ( $GST$ ) exhibits the best combination of crystallization speed and thermal stability and shows the crystallization temperature of  $\sim 160^\circ\text{C}$  [14]. The pseudo-binary compounds  $GeSb_2Te_4$  and  $GeSb_4Te_7$  constitute the comparatively lower crystallization temperature of  $131^\circ\text{C}$  and  $123^\circ\text{C}$  respectively, whereas,  $GeTe$  has lower crystallization speed. The improvement of the performance of  $Ge_2Sb_2Te_5$  by doping with  $Zn$  has been reported by Wang *et al.* [14] and observed the 10 years data retention at  $88.9^\circ\text{C}$  and  $167.5^\circ\text{C}$  for undoped  $GST$  and 15%  $Zn$  doping. Modeling the performance of  $PC$  memory device by substituting the suitable impurity elements to the  $GST$  alloys has been studied extensively in literature [15]–[21]. The rare earths recently attracted the attention for improving the performance of  $GST$  because of their ability to lower the power consumption of  $PC$  memory device [22]. The rare earths exist in positively charged ionic state leading to creation of stronger bonds with constituent elements of  $GST$  which helps to control the electrical properties of  $GST$  [23]. In addition to that due to larger atomic size and vacant  $f$  shell of rare earth elements can form stronger bonds and may result the local network structure of  $GST$  for the modification of switching mechanism. The  $Er$  doping has been investigated and found suitable for enhanced crystallization temperature in  $Sb$  thin films [24]. The crystallization mechanism improvement in  $Sn_{15}Sb_{85}$  alloy by  $Sm$  doping has been reported by Hua Zou *et al.* [22]. The lower electronegativity of  $Sm$  in comparison to  $Er$  can enhance the crystallization temperature largely [22]. The enhancement of electrical properties of  $GST$  by substituting  $Gd$  has been reported by Yongjin Chen *et al.* and observed amorphous phase resistance to increase with  $Gd$  concentration [23]. In the similar study the formation of  $Gd_2Te_3$  resulting in reduction of  $Sb_2Te_3$  formation on  $Gd$  doping has been observed the origin of resistance increase. The formation of stronger bonds with rare earth  $Gd$  doping in  $GST$  increases the crystallization

activation energy from 2.24 eV to 3.98 eV with *Gd* content enhancing the amorphous phase stability.

The physical parameters and efficiency of structural modification in *GST* on addition of *Sm* has been studied in this work. The estimation of fragile or rigid network structural formation has been made using the inter-atomic bonding constraints and mean coordination number calculations. The evaluation of physical parameters such as molar volume, density, free volume ratio, compactness and mean bond energy of *Sm* added *GST* has been carried out to understand the behavior of glass transition temperature. The change in the bond fraction on *Sm* doping in *GST* and cohesive energy has been evaluated employing the chemical bond approach. The bond switching or structural relaxation mechanism of *Sm* added *GST* alloys has been discussed using the computation of lone pair electrons, metallicity, degree of covalency and structural modification efficiency.

## 2.2. Results and Discussion

### 2.2.1 Bonding Constraints and Structural Rigidity

The phase change phenomena of chalcogenide *PCMs* is the result of the deformation of random covalent network structure continuously and reduces the part of zero frequency modes on increasing the temperature of annealing. The glassy alloys exhibiting the lower value of mean coordination number display the floppy nature, whereas, the alloys containing comparatively higher value of mean coordination number show the formation of rigid constrained structural networks with lower glass formation ability [25]. The computed mean coordination number ( $Z$ ) values have been provided in the table 2.1. The calculation of  $Z$  values is essential to know the glassy behavior of alloys and estimation of glass transition temperature ( $T_g$ ) [26]. Higher the value of mean coordination number higher will be the  $T_g$  value. The mean coordination number ( $Z$ ) values have been computed employing the relation [27]

$$Z = \left[ \frac{aN_{Ge} + bN_{Sb} + cN_{Te} + dN_{Sm}}{100} \right] \quad (2.1)$$

where the respective atomic percentages for *Ge*, *Sb*, *Te* and *Sm* have been represented through  $a$ ,  $b$ ,  $c$ , and  $d$ . The coordination numbers have been respectively denoted through  $N_{Sm}$ ,  $N_{Ge}$ ,  $N_{Te}$  and  $N_{Sb}$  for *Sm*, *Ge*, *Te*, and *Sb* whose values are 4, 3, 2 and 3 [28]. The formation of cross-linked three dimensional network structures on *Sm* addition has been examined from the evaluated  $Z$  values which show an increase with *Sm* concentration in table 2.1 [29]. The glass forming ability of alloys can be physically predicted by evaluating the lone pair electrons ( $L$ ). Higher the  $L$  values, higher will be the ability of glass formation

of an alloy. The number of lone pair electrons of  $(Ge_2Sb_2Te_5)_{100-x}Sm_x$  has been evaluated by subtracting the mean coordination number ( $Z$ ) from the average value of valence electrons. The  $L$  values evaluated from  $(Ge_2Sb_2Te_5)_{100-x}Sm_x$  alloys summarised in table 2.1 show the increase with  $Sm$  content.

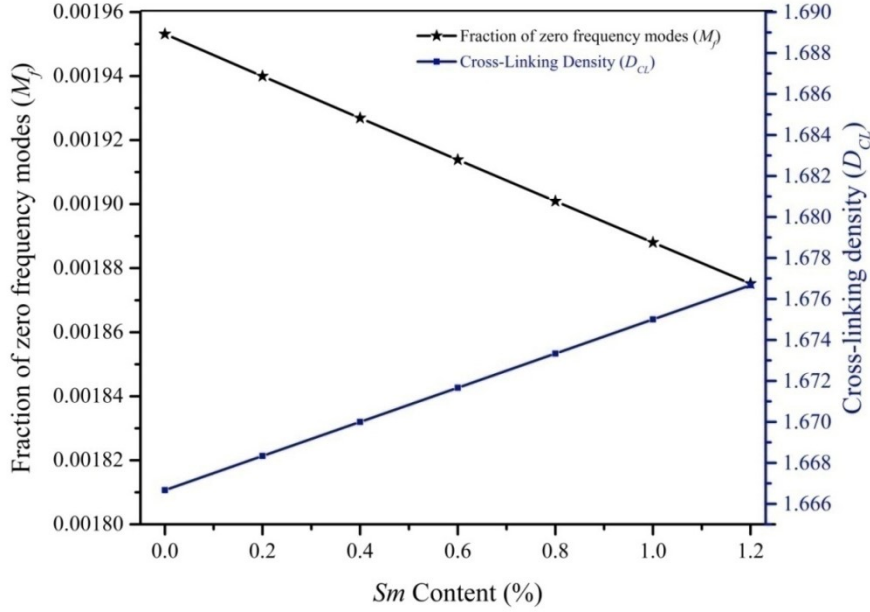


**Figure 2.1.** Plot for the crosslinking density ( $D_{CL}$ ) value and fraction of zero frequency modes ( $M_f$ ) with increasing  $Sm$  concentration.

The constraints theory on glass formation relating the inter-atomic force fields of neighboring atoms on the conditions of glass formation has been reported by Philips and Thorpe [30]. The central forces of nearest neighboring atom constrain the bond stretching and bond bending motions. The rigidity of the structural network can be explored using the evaluation of net constraints (the sum of stretching and bending constraints) also known as inter-atomic force fields per atom ( $N_{con}$ ). The  $N_{con} = N_d$  (Degrees of freedom) is the threshold value for rigidity and the network structures with  $N_{con} < N_d$  are referred as under-constrained or floppy whereas the structures with  $N_{con} > N_d$  are over-constrained or rigid. The bond bending constraint ( $N_\alpha$ ) has been evaluated using the relation  $N_\alpha = \frac{Z}{2}$  and the evaluation of bond stretching constraint ( $N_\beta$ ) has been executed using the relation  $N_\beta = 2Z - 3$ . The  $N_\alpha$ ,  $N_\beta$  and  $N_{con}$  values for  $(Ge_2Sb_2Te_5)_{100-x}Sm_x$  augment with  $Sm$  content (Table 2.1). The zero frequency modes ( $M_f$ ) fraction has been evaluated using the relation [30]  $M_f = \left[\frac{3-Z}{Z}\right]^3$  and the dependence of cross-linking density ( $D_{CL}$ ) on net constraints values follows the equation  $D_{CL} = N_{con} - 2$ . At  $Z = 2.67$ , the network structure transforms from

polymeric linear chains to rigid three dimensional cross-linked structures and is referred as chemical threshold and near the value  $Z = 3$ , the  $M_f$  value approaches toward zero [26]. The change in the  $M_f$  values with  $Sm$  addition has been displayed in figure 2.1. The experimentally observed density for  $(Ge_2Sb_2Te_5)_{100-x}Sm_x$  alloys attained least value at the chemical threshold  $Z = 2.67$ . The least value of experimentally observed density at the chemical threshold may be on account of  $Sb$  by the  $Sm$  atoms creating the  $SmTe_3$  or  $Sm_2Te_3$  structural units with the removal of  $Sb-Te$  bonds has been shown in figure 2.2. The augmentation of cross-linking with  $Sm$  concentration has been also analyzed from the obtained values of  $D_{CL}$  that enhance with  $Sm$  (Table 2.1) which are also in agreement with obtained  $M_f$  values. The  $Sm$  doping may enhance the fraction of rigid regions and reduce the floppy regions of the  $GST$  structural network.

$x$	$Z$	$N_\alpha$	$N_\beta$	$N_{con}$	$L$	$M_f$	$D_{CL}$
0	2.6670	1.3333	2.3333	3.6667	2.667	0.00195	1.667
0.2	2.6673	1.3337	2.3347	3.6683	2.671	0.00193	1.668
0.4	2.6680	1.3340	2.3360	3.6700	2.676	0.00192	1.670
0.6	2.6687	1.3343	2.3373	3.6717	2.680	0.00191	1.671
0.8	2.6693	1.3347	2.3387	3.6733	2.685	0.00190	1.673
1.0	2.6700	1.3350	2.3400	3.6750	2.690	0.00188	1.675
1.2	2.6707	1.3353	2.3413	3.6767	2.695	0.00187	1.677

**Table 2.1.** The computed values of physical parameters of  $(Ge_2Sb_2Te_5)_{100-x}Sm_x$  as a function of  $Sm$  content.

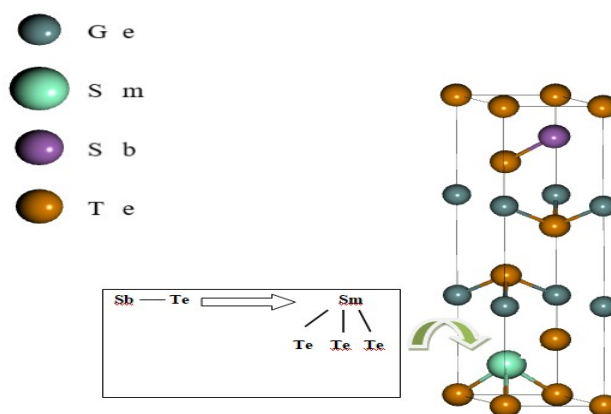


**Figure 2.2.** The substitution of few of the  $Sb$  atoms by the  $Sm$  atoms in the unit cell of  $GST$  is displayed.

### 2.2.2 Kinetics of Supercooled Liquid

Rapidly cooling the liquid to its glass transition temperature ( $T_g$ ) avoids the crystallization to take place and results the increase in viscosity and decrease in diffusion motion of molecules. The evaluation of number of bonds and average cross-linking in a unit volume is achieved employing the  $Z$  values. The strength of covalent bonds formed in a structural network is related directly to the glass transition temperature ( $T_g$ ) [31]. The breakage of bonds and the formation unsaturated ions takes place at melting temperature ( $T_m$ ). The formation of stable structural units takes place while cooling the melt below  $T_g$  through the diffusion motion of these unsaturated ions. The evaluation of physical parameters *i.e.* density ( $\rho$ ), compactness ( $\delta$ ) and molar volume ( $V_m$ ) for  $Sm$  doped  $GST$  phase change materials are helpful in understanding the effect of  $Sm$  incorporation on the glass transition behavior and thermal stability of  $GST$ . The density of materials is dependent upon the atomic arrangements and bonding in structural network. The variation in bond length and arrangement of atoms alters the material's density value and provides the assessment of the rigidity of amorphous materials. The density in case of amorphous glass forming alloys can be theoretically estimated using the empirical relation [32]

$$\rho = \sum_{i=1}^4 \left( \frac{m_i}{d_i} \right)^{-1} \quad (2.2)$$

such that,  $m_i$  represents the mass fraction of  $i^{th}$  element amongst  $Ge$ ,  $Sb$ ,  $Te$  and  $Sm$  as well as similarly  $d_i$  stands for corresponding density of element. The respective elemental density values used for the calculation of density of  $Sm$  doped  $GST$  alloys have been taken as  $5.32 \text{ g/cm}^3$ ,  $6.697 \text{ g/cm}^3$ ,  $6.24 \text{ g/cm}^3$  and  $7.52 \text{ g/cm}^3$  for  $Ge$ ,  $Sb$ ,  $Te$  and  $Sm$  [28]. The values of theoretical density for  $(Ge_2Sb_2Te_5)_{100-x}Sm_x$  alloys have been displayed in table 2.2 and shows an augmentation with the  $Sm$  incorporation which may be owing to the relatively larger values of  $Sm$  density in comparison to that of  $Ge$ ,  $Sb$  and  $Te$ . The change in density value with  $Sm$  content is the result of relative change in molecular mass and atomic packing because of the differences in atomic radii, bond lengths as well as bond angles with  $Sm$  addition. The density of alloys is related directly to their refractive index and the increase in the theoretically obtained values of density can be attributed for the enhancement in refractive index with  $Sm$  content. The density of  $(Ge_2Sb_2Te_5)_{100-x}Sm_x$  alloys has been also evaluated experimentally by utilizing the Archimedes principle and has been displayed in table 2.2. The experimentally obtained density values of  $(Ge_2Sb_2Te_5)_{100-x}Sm_x$  alloys are in close agreement with their theoretically estimated values.

The molar volume ( $V_m$ ) of glass forming alloys is also related to the glass transition temperature ( $T_g$ ). The diffusion motion of molecules or unsaturated ions on cooling below its melting temperature ( $T_m$ ) is affected by the molar volume ( $V_m$ ). Thiruvikraman reported the relation of molar volume ( $V_m$ ) with  $T_g$  [33]. The calculation of molar volume ( $V_m$ ) has been performed by utilizing the empirical relation [34], [35]

$$V_m = \sum_{i=1}^4 \left( \frac{x_i M_i}{\rho} \right) \quad (2.3)$$

where in  $x_i$  represents the fraction of  $i^{th}$  atom or structural unit present in a system, while the corresponding molecular weight or atomic weight is  $M_i$ . The obtained values of  $V_m$  for  $(Ge_2Sb_2Te_5)_{100-x}Sm_x$  alloys have been displayed in table 2.2 showing the augmentation on  $Sm$  incorporation owing to the longer covalent radius incase of  $Sm$  ( $1.98 \text{ \AA}$ ) compared to  $Ge$  ( $1.20 \text{ \AA}$ ),  $Te$  ( $1.38 \text{ \AA}$ ) and  $Sb$  ( $1.39 \text{ \AA}$ ). [36].

The theoretical molar volume ( $V_t$ ) value has been computed from the relation  $V_t = aV_a + bV_b + cV_c + dV_d$  such that  $a$ ,  $b$ ,  $c$ , and  $d$  represents atomic percentage, while  $V_a$ ,  $V_b$ ,  $V_c$  and  $V_d$  respectively represents  $Ge$ ,  $Sb$ ,  $Te$  and  $Sm$  atomic volume. Utilizing obtained  $V_t$  and  $V_m$  values, the free volume ratio ( $FVR$ ) values have been evaluated employing  $FVR = \left( \frac{V_t - V_m}{V_m} \right) \times 100$ . The reduction in the free space or voids with increase in  $Sm$  concentration in  $GST$  has been analyzed from the obtained  $FVR$  values displayed in table 2.2. The formation of rigid network structure with  $Sm$  addition can also be confirmed from the negative values of  $FVR$ . The change in molar volume is the result of alteration in inter-atomic distances on  $Sm$  addition causing variation of  $FVR$  values with  $Sm$  content.

The structural change in glassy alloys as a function of material's composition can also be examined by evaluating the physical parameter compactness ( $\delta$ ). The compactness has been evaluated using the empirical relation correlating the atomic weight, density and atomic percentage [34]

$$\delta = \sum_{i=1}^4 \left( \frac{\frac{x_i M_i}{\rho_i} - \frac{x_i M_i}{\rho}}{\frac{x_i M_i}{\rho}} \right) \quad (2.4)$$

where  $\rho_i$ ,  $x_i$ , and  $M_i$  represents respectively the density, atomic percentage and atomic weight for constituent elements  $Ge$ ,  $Sb$ ,  $Te$  and  $Sm$ . The tightly packed atomic arrangements created in  $GST$  can be inferred from the augmentation in  $\delta$  values with  $Sm$  concentration summarized in table 2.2.

The bond density created in unit volume for chalcogenide glassy alloys helps in determining the conduction band edge energy. The number of bonds formed per unit volume

( $N$ ) have been evaluated from the relation [32],  $N = Z \times \left(\frac{N_A}{V_m}\right)$  where  $N_A$  denotes the Avogadro's number. The augmentation in  $N$  values on  $Sm$  addition is shown in table 2.2, which suggests an increase in the energy of conduction band edge on  $Sm$  addition.

$x$	( $\rho$ cal.) (g/cm <sup>3</sup> )	( $\rho$ exp.) (g/cm <sup>3</sup> )	$V_m$ (cm <sup>3</sup> /mol)	$V_t$ (cm <sup>3</sup> /mol)	$FVR$	$\delta \times 10^{-5}$	$M$ (g/mol)	$N \times 10^{22}/cc$
0	6.189	6.000	18.433	18.500	-0.362	0	114.08	8.711
0.2	6.192	6.064	18.436	18.503	-0.361	0.63	114.16	8.712
0.4	6.195	6.876	18.439	18.506	-0.360	1.25	114.23	8.713
0.6	6.197	6.101	18.442	18.509	-0.359	1.87	114.30	8.714
0.8	6.200	6.425	18.445	18.512	-0.359	2.49	114.37	8.715
1.0	6.203	5.904	18.448	18.515	-0.358	3.12	114.45	8.715
1.2	6.206	6.619	18.451	18.518	-0.357	3.74	114.52	8.716

**Table 2.2.** Calculated values of density ( $\rho$  cal.), theoretical volume ( $V_t$ ), molar volume ( $V_m$ ), compactness ( $\delta$ ), molar mass ( $M$ ), free volume ratio ( $FVR$ ) and number of bonds per unit volume ( $N$ ) and experimentally obtained values of density ( $\rho$  exp.) for  $(Ge_2Sb_2Te_5)_{100-x}Sm_x$ .

### 2.2.3 Average Heat of Atomization, Cohesive Energy and Band Gap

The average heat of atomization ( $H_s$ ) may be taken as heat energy necessary to fragment a substance mole to its constituent atoms. Therefore, average heat of atomization signifies measure of alloy bond strength. The higher value of bond strength causes larger splitting of the bonding and anti-bonding orbitals leading to large band gap energy. Similarly cohesive energy ( $C.E.$ ) also signifies the average bond strength for the material. The  $H_s$  value for a binary alloy is computed using the Pauling formula [37].

$$\overline{H_s}(A - B) = \Delta H + \frac{1}{2}[(H_s^A) + (H_s^B)] \quad (2.5)$$

where  $\Delta H = a(\chi_A - \chi_B)^2$  and  $\chi_A$ ,  $\chi_B$  are electronegativities and  $H_s^A$  and  $H_s^B$  represent the heat of atomization for  $A$  and  $B$  individual constituent elements. The calculation of average heat of atomization for  $(Ge_2Sb_2Te_5)_{100-x}Sm_x$  samples has been performed by utilizing the relation [38]

$$\overline{H_s} = \left[ \frac{aH_s^{Ge} + bH_s^{Sb} + cH_s^{Te} + dH_s^{Sm}}{100} \right] \quad (2.6)$$

where  $H_s^{Ge}$ ,  $H_s^{Sb}$ ,  $H_s^{Te}$  and  $H_s^{Sm}$  represents the respective values of heat of atomization of *Ge*, *Sb*, *Te* and *Sm* with values 377 kJ/mol, 262 kJ/mol, 197 kJ/mol and 207 kJ/mol [28]. The obtained  $H_s$  values for  $(Ge_2Sb_2Te_5)_{100-x}Sm_x$  are summarized in table 2.3. The cohesive energy (*C.E.*) for *Sm* doped *GST* has been computed by adopting the chemical bond approach (*CBA*). According to *CBA*, there is preference for heteropolar bond creation over the homopolar bonds. Hence, valency requirements of cations *i.e.* *Ge*, *Sb* and *Sm* after getting fulfilled lead to the utilization of the extra *Te* in creation of *Te—Te* homopolar bonds. The bond fraction obtained using the *CBA* and the corresponding bond energy have been utilized for the calculation of cohesive energy of  $(Ge_2Sb_2Te_5)_{100-x}Sm_x$  alloys. Table 2.3 shows the calculated values of *C.E.* illustrating the enhancement in *C.E.* values on addition of *Sm*, which may be on account of the stronger heteropolar *Sm—Te* (~179.4 kJ/mol) bonds formed on *Sm* addition over the comparatively weaker *Ge—Te* (~148.5 kJ/mol) and *Sb—Te* (~132.3 kJ/mol) bonds. The impact of *Sm* addition on the average single bond energy of *GST* has been also examined by evaluating the  $H_s/Z$  ratio. The calculated values of  $H_s/Z$  ratio have been summarised in table 2.3 exhibiting the decrease in  $H_s/Z$  values on *Sm* addition owing to low heat of atomization for *Sm* and augmentation in *Z* values on addition of *Sm*. The *Sm* addition enhances the rigidity of *GST* because of the augmentation in cross-linking owing to the strong *Sm—Te* bonds creation on addition of *Sm* causing rise in the value of mean coordination number (*Z*).

The energy gap ( $E_g$ ) for  $(Ge_2Sb_2Te_5)_{100-x}Sm_x$  has been evaluated theoretically from the Shimakawa's relation [39]

$$E_g = aE_g^{Ge} + bE_g^{Sb} + cE_g^{Te} + dE_g^{Sm} \quad (2.7)$$

such that *a*, *b*, *c*, and *d*, represents the respective *Ge*, *Sb*, *Te*, and *Sm* volume fractions for  $(Ge_2Sb_2Te_5)_{100-x}Sm_x$  alloys. The volume fraction has been computed through the determination of atomic weights to density ratio of constituent elements. The  $E_g$  values obtained for  $(Ge_2Sb_2Te_5)_{100-x}Sm_x$  alloys have been tabulated in table 2.3 which enhances on addition of *Sm*. This enhancement in the value of energy gap may be on account of the lowering of the midgap non-bonding states caused by the enhanced cross-linking and creation of strong heteropolar bonds in *GST* on *Sm* addition.

#### 2.2.4 Electronegativity and Degree of Covalency

The electronegativities of elements bonded in a compound and the degree of covalency ( $C_c$ ) of alloys are related to each other. Higher the difference in the values of

electronegativity of the bonded elements lesser will be the covalency character and more the ionic character. The value of  $C_c$  for bond  $A-B$  can be mathematically expressed using the relation [40] ;  $C_c = 100 \times \exp\left(-\frac{(\chi_A - \chi_B)^2}{4}\right)$  where  $\chi_A$  and  $\chi_B$  denotes the electronegativities of  $A$  and  $B$ . The degree of covalency can be theoretically calculated using similar approach for the  $(Ge_2Sb_2Te_5)_{100-x}Sm_x$  alloys by taking the summation over the products of bond fraction and covalency character for all the bonds formed. The modified relation of the calculation of  $C_c$  values of  $(Ge_2Sb_2Te_5)_{100-x}Sm_x$  quaternary alloy is expressed as

$$C_c = \sum \alpha_k \times \exp\left[-\frac{(\chi_i - \chi_j)^2}{4}\right] \quad (2.8)$$

where  $\alpha_k$  represents the percentage of  $k^{th}$  bond and  $\chi_i$  and  $\chi_j$  are the corresponding electronegativities of bonded elements whose values are 1.17, 2.10, 2.05 and 2.01 for  $Sm$ ,  $Te$ ,  $Sb$  and  $Ge$  respectively [28]. The calculated  $C_c$  values of  $Sm$  doped  $GST$  as a function of  $Sm$  concentration have been displayed in figure 2.3 indicating an increase in  $C_c$  value with  $Sm$  incorporation. The augmentation of covalency character also signifies the reduction in ionicity with  $Sm$  addition causing the reduction in ordering of normal coordination on cooling below the melting temperature of  $Sm$  doped  $GST$  alloys [41]. The increased degree of covalency of  $GST$  on  $Sm$  addition is also beneficial for the improvement in glass forming ability of alloys.

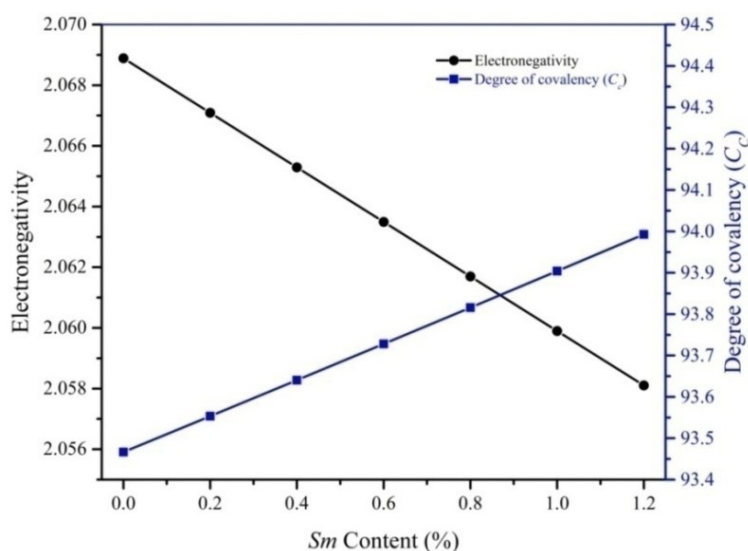


**Figure 2.3.** Degree of covalency ( $C_c$ ) and electronegativity of  $(Ge_2Sb_2Te_5)_{100-x}Sm_x$  as a function of  $Sm$  content.

$x$	$H_s$ (kJ/mol)	$H_s/Z$ (kJ/mol)	$C.E$ (kJ/mol)	$E_g$ (eV)
0	251.44	94.29	339.70	0.334
0.2	251.36	94.23	340.76	0.335
0.4	251.27	94.18	341.77	0.336
0.6	251.18	94.12	342.81	0.337
0.8	251.09	94.07	343.85	0.337
1.0	251.00	94.01	344.90	0.338
1.2	250.91	93.95	345.95	0.338

**Table 2.3.** Theoretical band gap ( $E_g$ ), cohesive energy ( $C.E$ ),  $H_s$  and  $H_s/Z$  values of  $(Ge_2Sb_2Te_5)_{100-x}Sm_x$  system.

### 2.2.5 Conduction and Valence Band Edge Energies

The estimation of conduction band edge ( $E_{CB}^0$ ) in addition to valence band edge ( $E_{VB}^0$ ) energies help us to understand the electrical conduction and optical absorption in the alloys. The values of  $E_{CB}^0$  has been evaluated utilizing the empirical relation [42]

$$E_{CB}^0 = E_e - X + 0.5E_g \quad (2.9)$$

$$X = \{x_{Ge}^a \times x_{Sb}^b \times x_{Te}^c \times x_{Sm}^d\}^{\left\{\frac{1}{a+b+c+d}\right\}}$$

$$x_{Ge} = \frac{(E_{EA}^{Ge} + E_{IE}^{Ge})}{2}$$

Similar expression can be adopted for the estimation of  $x_{Sb}$ ,  $x_{Te}$ , and  $x_{Sm}$  values, wherein  $E_{IE}^{Ge}$  and  $E_{EA}^{Ge}$  represents the the first ionization energy and electron affinity with values  $762\text{kJ/mol}$  and  $118.87\text{kJ/mol}$  respectively in case of  $Ge$  [43].  $E_e$  is energy of free electron of  $H$ -like atoms whose value is  $4.5\text{ eV}$  [43] and  $X$  represents the energy parameter for the selected materials. The  $E_{VB}^0$  values have been evaluated using conduction band-edge energy ( $E_{CB}^0$ ) and energy gap ( $E_g$ ) values. The values of band edge energies increase with  $Sm$  content in  $GST$  and have been plotted in figure 2.4. There conduction band edge shifts *w.r.t.* fermi level with  $Sm$  incorporation as indicated by enhancement of  $E_{CB}^0$ . The value of  $E_{CB}^0$  enhances with  $Sm$  addition, which may be attributed to the increase in  $E_g$  with  $Sm$  incorporation as shown in table 2.3.

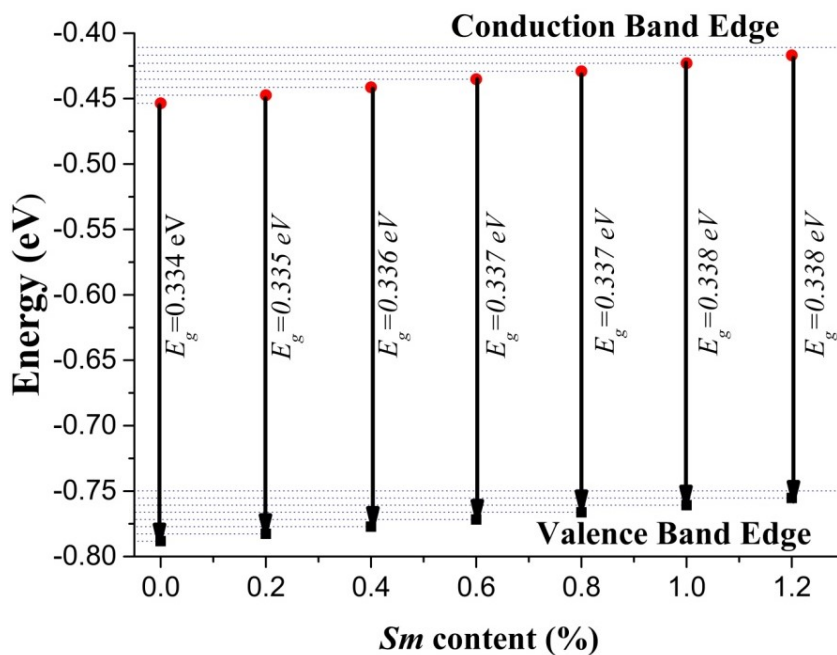


**Figure 2.4.** Variation of band edge energy values for *Sm* added *GST*.

### 2.2.6 Glass Transition Temperature

The glass transition temperature ( $T_g$ ) in glasses is based on various parameters. Glass transition is the result of continuous change in viscosity on cooling below the melting temperature without affecting the local atomic structure of materials. The viscosity changes considerably at  $T_g$  and the kinetic motion of molecules of supercooled liquid is constrained. There is correlation of  $T_g$  with mean coordination number ( $Z$ ) through Tanaka relation  $T_g = \exp(1.6Z + 2.3)$  [26]. Tanaka approach utilizes the Arrhenius viscosity relation for the estimation of  $T_g$  with the use of viscosity value  $\sim 10^{14.5}$  poise. The values of  $T_g$  obtained using Tanaka relation have been shown in table 2.4, which points to the enhancement in the  $T_g$  value on *Sm* addition. This augmentation of  $T_g$  on *Sm* incorporation improves the *GST PCMs* thermal stability. As per Tanaka approach, the values of  $T_g$  are considered nearly independent of the homopolar bond energy. However, the  $T_g$  values have also been suggested to depend on the energy of the homopolar bonds [44].

The modified Gibbs-DiMarzio equation for the estimation of glass transition temperature has been reported by Sreeram *et al.* [45] by relating the  $T_g$  through the mean coordination number ( $Z$ )

$$T_g = T_o / [1 - \beta(Z - 2)] \quad (2.10)$$

such that  $T_o$  represents the glass transition temperature for linear chains forming the system. The value of  $T_o$  has been taken to be 343 K by considering *Te* as chain forming element in

the present system under investigation and the system parameter  $\beta$  with the calculated value of 0.55 for the current system [45]. The factor  $(Z - 2)$  in equation (2.10) indicates the dependence of an increase in cross-linking on the glass transition temperature. The modified Gibbs-DiMarzio approach has been employed to evaluate  $T_g$  which shows an increase on  $Sm$  addition to  $GST$  (Table 2.4) signifying an amplification in cross-linking on  $Sm$  addition.

De Neufville and Rockstad [46] reported the expression on glass transition temperature ( $T_g$ ) relating the band gap energy ( $E_g$ ) and the mean coordination number ( $Z$ ) based on the Vogel-Fulcher viscosity relation [46].

$$T_g = T_0 + \frac{\delta(Z-2)E_g}{32.2k_B} \quad (2.11)$$

where  $T_0$  refers to the  $Te$  (chain-forming element) glass transition temperature and  $\delta$  represents the system parameter. The  $T_g$  values obtained using the above relation show an increase with  $Sm$  addition (Table 2.4) which may due to increase in the value of mean coordination number and band gap energy on addition of  $Sm$ .

The mean bond energy correlation incase of glassy alloys with  $T_g$  has been reported by Tichy and Ticha [44]. The role of type of bonding between the linear chains on the glass transition behavior has been stressed in this approach irrespective of the dependence of  $T_g$  on only the compactness of material as highlighted by De Neufville and Rockstad approach. The degree of cross-linking in the network as well as mean bond energy ( $\langle E \rangle$ ) of glass forming alloy have significant role in predicting the glass transition behavior. The validity of this approach is acceptable up to chalcogen content of 90% [44]. The chalcogen content ( $R$ ) has been computed employing the relation

$$R = \left( \frac{c \times 2}{a \times 4 + b \times 3 + d \times 3} \right) \quad (2.12)$$

where 4, 3, 2, and 3 have been assumed to be the coordination numbers respectively for  $Ge$ ,  $Sb$ ,  $Te$ , and  $Sm$  [28]. The value  $R = 1$  indicates the stoichiometric composition and  $R < 1$  suggests the deviation from stoichiometry for chalcogen poor system and  $R > 1$  for chalcogen-rich system. The values of  $R$  calculated from above relation are summarized in table 2.4. The value of  $R$  less than one for  $(Ge_2Sb_2Te_5)_{100-x}Sm_x$  illustrates this system to be chalcogen poor. The cross-linking per atom between the linear chains of chalcogen atoms ( $P_p$ ) for the system poor in chalcogen with values of  $R < 1$  has been estimated by using the expression [44].

$$P_p = \left( \frac{c \times 2}{a + b + c + d} \right) \quad (2.13)$$

For  $R < 1$ , the mean bond energies ( $\overline{E}_c$ ) for cross-linking per atom have been calculated from the equation [44]

$$\overline{E}_c = P_p E_{hb}$$

where  $E_{hb}$  represents the bond energy for heteropolar bonds which can be calculated by using the relation

$$E_{hb} = \frac{[aCN(Ge) \times E_{Ge-Te} + bC(Sb) \times E_{Sb-Te} + dCN(Sm) \times E_{Sm-Te}]}{(aCN(Ge) + bCN(Sb) + dCN(Sm))} \quad (2.14)$$

where  $CN(Ge)$ ,  $CN(Sb)$  and  $CN(Sm)$  denotes the respective coordination numbers for  $Ge$ ,  $Sb$  and  $Sm$ . The  $\overline{E}_c$  values listed in table 2.4 increase on incorporation of  $Sm$  due to the reduction in  $Ge-Te$  and  $Sb-Te$  bond fraction having bond energies  $1.54 eV$  and  $1.37 eV$  respectively and increase in the fraction of  $Sm-Te$  stronger bonds having bond energy of  $1.86 eV$ . The homopolar bond energy ( $\overline{E}_{rm}$ ) of remaining bonds formed in  $(Ge_2Sb_2Te_5)_{100-x}Sm_x$  has been estimated using the relation;

$$\overline{E}_{rm} = \frac{2\left(\left(\frac{1}{2}Z - P_p\right)E_{<>}\right)}{Z}, \text{ where } E_{<>} = \frac{E_{Te-Te} + E_{Ge-Ge} + E_{Sb-Sb}}{3}$$

and the bond energies of  $1.63 eV$ ,  $1.31 eV$  and  $1.43 eV$  for respective homopolar bonds  $Ge-Ge$ ,  $Sb-Sb$  and  $Te-Te$  have been utilized for the evaluation of  $\overline{E}_{rm}$  [47]. The sum of the bond energies for homopolar and heteropolar bonds is termed as the mean bond energy ( $\langle E \rangle$ ) expressed mathematically as [44].

$$\langle E \rangle = \overline{E}_c + \overline{E}_{rm} \quad (2.15)$$

$T_g$  is empirically related to mean bond energy  $\langle E \rangle$  as [44]

$$T_g = 311\{\langle E \rangle - 0.9\} \quad (2.16)$$

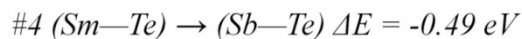
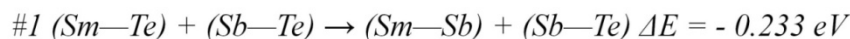
The  $Sm$  addition to  $GST$  increases the cross-linking with reduction in concentration of  $Te$  causing a rise in  $\overline{E}_{rm}$  values. The  $\langle E \rangle$  dependence on the mean coordination number and hence,  $T_g$  emphasizes the relevance of cross-linking to improve the thermal stability of  $Sm$  doped  $GST$ . The increase in mean bond energy of  $(Ge_2Sb_2Te_5)_{100-x}Sm_x$  on  $Sm$  addition is due to the augmentation in average cross-linking per atom ( $\overline{E}_c$ ) enhancing the glass transition temperature of  $GST$  on  $Sm$  incorporation as summarized in table 2.4. The different approaches adopted to evaluate the values of  $T_g$  show an augmentation on  $Sm$  incorporation to  $GST$  (Table 2.4) which highlights the enhancement of thermal stability in  $GST$  phase change material on  $Sm$  incorporation.

$x$	$Tg(Tanaka)$ (K)	$Tg(Gibbs)$ (K)	$R$	$\overline{E}_c$ (eV)	$\overline{E}_{rm}$ (eV)	$\langle E \rangle$ (eV)	$Tg(Tichy)$ (K)	$Tg(Rocksted)$ (K)
0	710.9	607.2	0.714	1.630	0.647	2.277	428.42	742.7
0.2	711.7	607.5	0.711	1.628	0.654	2.283	430.24	744.3
0.4	712.5	607.7	0.708	1.626	0.662	2.289	432.06	746.0
0.6	713.2	608.0	0.706	1.625	0.669	2.295	433.88	747.6
0.8	714.0	608.3	0.703	1.623	0.677	2.300	435.69	749.3
1.0	714.7	608.5	0.700	1.622	0.684	2.306	437.49	751.0
1.2	715.5	608.8	0.697	1.620	0.692	2.312	439.30	752.6

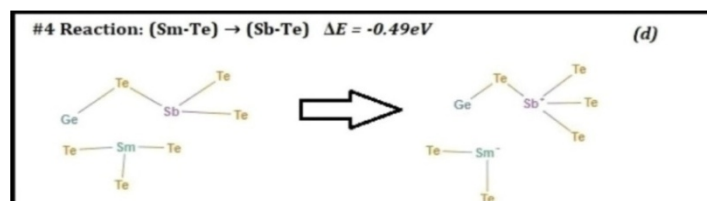
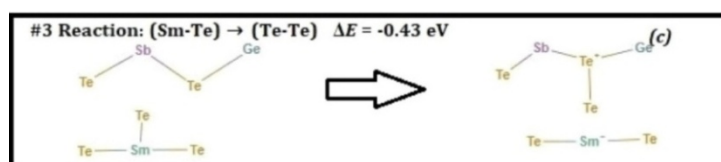
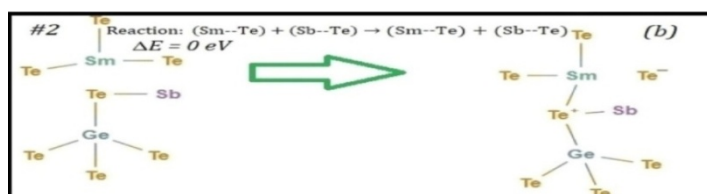
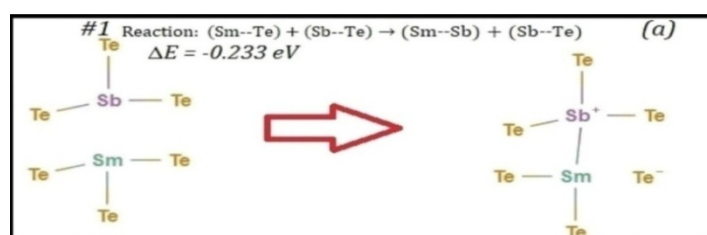
**Table 2.4.** The values of chalcogen content ( $R$ ), heteropolar and homopolar bond energies  $E_c$ ,  $E_{rm}$  and mean bond energy  $\langle E \rangle$ , glass transition temperature ( $Tg$ ) of  $(Ge_2Sb_2Te_5)_{100-x}Sm_x$  evaluated by adopting the Tanaka [26], Gibbs [45], Tichy [44] and Rockstad [46] approaches.

### 2.2.7 Bond Switching Mechanism

In chalcogenides, the optimization of physical properties is desirable to model the amorphous structures for improving the thermal stability. The properties of chalcogenide glasses can be controlled by modifying their molecular structure. The quantitative evaluation of efficiency of structural modification of glass forming alloys has been performed by utilizing its dependence upon the chemical composition and bonding nature. The modification of amorphous structures creates the charged defects or valence alternation pairs ( $VAP$ ) which affects the atomic arrangement due to the interaction with local environment [48],[49],[50]. The effect of  $Sm$  incorporation, on the bond switching mechanism and formation of  $VAPs$  in  $GST$  has been discussed in this section. The stability of charge defects created as a result of bond switching governs the feasibility of bond switching reaction [51]. The different reactions for bond switching and corresponding energy barrier values are presented in figure 2.5. The bond switching as a result of relaxation of amorphous structures leads to the creation of unusual coordinated networks. The bond switching proceeds with the creation of energetically more favorable heteropolar bonds and breaking of less favorable homopolar bonds, which, simultaneously creates the  $VAPs$  (figure 2.5(a - f)).



The barrier energy ( $\Delta E$ ) has been computed by taking the energy difference between the created bonds and broken bonds. The negative energy barrier ( $\Delta E$ ) value indicates the creation of weaker bonds on breaking of the comparatively stronger bonds [51], [52]. The supercooled melt consists of an equilibrium state among the various energetically favorable covalent bonds. The bond switching due to equilibrium between different covalent chemical bonds present in amorphous matrix leads to the formation of a metastable state.



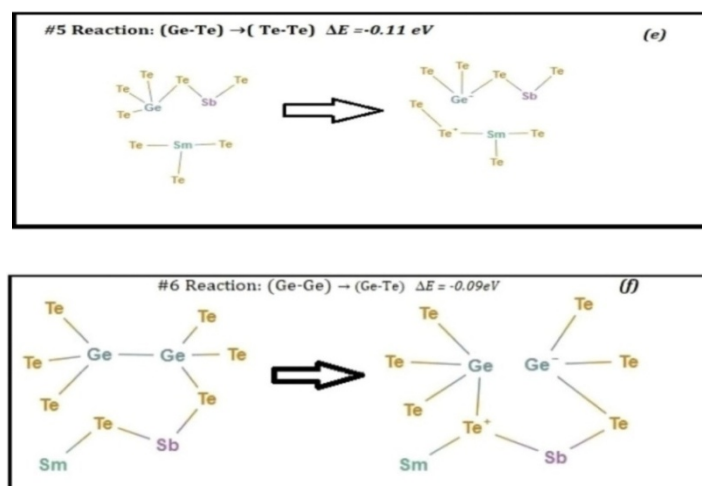


**Figure 2.5.** Some possible reactions of bond switching for  $(\text{GST})_{100-x}\text{Sm}_x$  and their corresponding barrier energies.

The left side of the reaction displays the structural units before breaking of the covalent bonds and the right side of reaction shows the new bonds created after switching. The covalently bonded chemical structures have the tendency to attain the lowest energy state in the disordered glassy solids because of which they display the continuous switching of covalent chemical bonds with the creation and destruction of heteropolar and homopolar bonds respectively.

The bond switching mechanism requires the various structural units formed during the process to acquire a state with low energy having negative energy barrier due to which the process of bond destruction and creation favors the creation of bonds that are weaker instead of stronger. The  $\text{Sm-Sb}$  formation with  $\Delta E = -0.233 \text{ eV}$  on disintegration of  $\text{Sm-Te}$  bonds creates  $\text{Sb}^+$  and  $\text{Te}^-$  charge pairs represented by the process #1 (Figure 2.5 (a)). The feasibility of the bond switching reaction #1 has been examined through the *EXAFS* and *XPS* studies on *GST* reporting the occurrence of over-coordinated *Te* and lack of the under coordinated *Te* which suggests that the process #1 is less probable [53], [54]. Similarly, the feasibility of process #2, (Figure 2.5 (b)) showing the  $\text{Sm-Te}$  bond switching among two unlike structural units creating  $\text{Te}^-$  and  $\text{Te}^+$  pairs, is also less and the same has been justified by  $\text{Te}^-$  absence observed through the *XPS* results [53]. The variation in covalency character and metallicity (discussed later) between bonds formed and broken bonds leads to the most probable bond switching reactions between the homopolar and heteropolar bonds. The creation of homopolar  $\text{Te-Te}$  bonds results in the formation of  $\text{Te}^+$  and  $\text{Sm}^-$  as a result of disintegration of  $\text{Sm-Te}$  heteropolar with a negative barrier energy of  $-0.43 \text{ eV}$  for this bond switching

reaction which has been illustrated in figure 2.5(c). This process signifies the efficiency of structural modification in amorphous *GST* on *Sm* addition. The switching among heteropolar trivalent *Sm* telluride and *Sb* telluride structural units creates under-coordinated  $Sm^-$  and over-coordinated  $Sb^+$  pairs having  $\Delta E$  value  $-0.49 eV$  (figure 2.5(d)). The creation of  $Ge^-$  and  $Te^+$  *VAPs* takes place on switching of the *Ge—Te* heteropolar bonds to homopolar *Te—Te* bonds having little  $\Delta E$  value of  $-0.11eV$  as shown in figure 2.5(e). The heteropolar *Ge—Te* and homopolar *Ge—Ge* bond switching creates  $Ge^-$  and  $Te^+$  having barrier energy  $\Delta E = -0.09 eV$ . The under-coordinated *Ge* and over-coordinated *Te* atom occurrence in the reaction indicated by figure 2.5 (f) with low value of barrier energy shows fine agreement with the *XPS* results [55],[53].

The crystallization speed of *PCMs* controls the switching speed and the performance of *PC* memory device. The *PCMs* exhibiting weak bonding strength between the constituent elements may significant raise the crystallization speed while switching incase of phase change memory devices [56]. The addition of *Sm* forms weaker bonds with other constituent elements in *GST* which may influence the structural relaxation processes in amorphous *GST* by altering the bond switching reactions due to the interaction of created charged ions with local bonding environment. The alteration in the local environment in *Sm* added *GST* may enhance the speed of crystallization.

### 2.2.8 Metallicity and Lone Pair Electrons

The operational efficiency of phase change memories depend on the crystallization and stability of structural units involved in phase transition. The theoretical investigation of *Sm* incorporated *GST* has been carried out to analyze the structural changes on *Sm* addition. The amorphous materials consist of the covalently bonded structural networks which couple between various configurations in equilibrium. The coupling of covalently bonded networks in chalcogenide glasses is on account of the lone pair electrons and determines the efficiency of structural modification. The structural modification efficiency in case of covalently bonded network enhances on number of lone pair electrons augmentation [57]. The rise in the number of lone pair electrons on *Sm* incorporation to *GST* (Table 2.1) enhances the covalent coupling and structural modification efficiency of networks. The degree of covalency and covalent coupling depends on the quantity of covalent bonds present in structural networks. The degree of covalency is related to the value of metallicity (*M*) [57], [58]  $M = (\bar{Z} - Z_{Te}) \times 10^{-2}$ , where  $Z_{Te}$  represents the valence shell electrons in *Te* and  $\bar{Z}$ , the average valence shell

electrons. Metallicity describes the degree of delocalization of electrons for chalcogenide glasses and its value increases with an increase in atomic number. The values of metallicity obtained for  $(Ge_2Sb_2Te_5)_{100-x}Sm_x$  system in table 2.5 shows a rise in  $M$  values on  $Sm$  incorporation. This rise in  $M$  values may be on account of the number of lone pair electrons augmentation on  $Sm$  addition and the constituent elements of  $GST$  having comparatively smaller size of atoms in comparison to  $Sm$ . The presence of lone pair of electrons in amorphous solids lead to charged defect states and consequently, enhances the coupling of metastable covalent networks creating different structural units. The alteration in structural networks and enhancement in covalent coupling on incorporation of  $Sm$  modifies structural relaxation in amorphous  $GST$ . The increase in the efficiency of structural modification with incorporation of  $Sm$  to  $GST$  due to rise of  $M$  may lead to the variation of electrical and optical switching behavior of  $GST$ .

$x$	$\bar{Z}$	$M$	$C_N$	$CSME$	$\Delta V_{th} \%$
0	5.333	-0.00667	1.267	1.052	5.48±0.77
0.2	5.338	-0.00661	1.210	1.104	6.08±0.90
0.4	5.344	-0.00656	1.149	1.164	6.81±1.05
0.6	5.349	-0.00651	1.118	1.199	7.24±1.14
0.8	5.355	-0.00645	1.087	1.236	7.73±1.25
1.0	5.360	-0.0064	1.021	1.318	8.87±1.51
1.2	5.365	-0.00635	0.952	1.416	10.34±1.85

**Table 2.5.** Average valence shell electrons ( $\bar{Z}$ ), metallicity ( $M$ ), covalent coupling of structural networks ( $C_N$ ),  $CSME$  and change in threshold switching voltage ( $\Delta V_{th}$ ) of  $(Ge_2Sb_2Te_5)_{100-x}Sm_x$  ( $x = 0, 0.2, 0.4, 0.6, 0.8, 1.0, 1.2$ ).

### 2.2.9 Structural Modification Efficiency

The coupling between the covalently bonded structural units simultaneously fulfills the valence of an atom and deviates from the normal valence condition of other atom. The quantitative evaluation of the structural modification efficiency of amorphous networks entails the ample understanding of covalent coupling of structural units. The correlation of covalent coupling of structural networks ( $C_N$ ) with physical parameters can be inferred from the expression [57]  $C_N = Z(I - I_c - M)/2$ , such that  $I_c = \sum_i S_i N_i$  represents the ionicity coefficient,  $S_i$  is the ionicity of the  $i^{th}$  bond evaluated by taking the electronegativity

difference of the bonded atoms and the fraction of corresponding bond is denoted by  $N_i$ . The values of  $C_N$  obtained using this relation for  $(Ge_2Sb_2Te_5)_{100-x}Sm_x$  decrease on  $Sm$  addition (Table 2.5) indicating an enhancement in structural modification. The heteropolar bond fraction formed in  $GST$  on  $Sm$  addition has been computed employing chemical bond approach and displayed in table 2.6. The bond fraction created in  $Sm$  doped  $GST$  and the corresponding bond ionicity obtained by taking the electronegativity difference of bonded atoms have been used for the estimation of coefficient of ionicity ( $I_c$ ). The  $I_c$  values in table 2.6 show an increase on  $Sm$  addition. The covalent coupling of structural networks ( $C_N$ ) and lone pair electrons dependence on the efficiency of structural modification ( $\Delta\phi$ ) has been expressed using the relation [57], [59]

$$\Delta\phi = f\left[\frac{\bar{z}-z}{z(1-I_c-M)}\right] \quad (2.17)$$

where  $f$  represents the unspecified function and factor  $\frac{\bar{z}-z}{z(1-I_c-M)}$  determines the structural modification efficiency and is known as the ‘criterion for structure modification efficiency’, *i.e.*,  $CSME$ . The  $CSME$  values for  $(Ge_2Sb_2Te_5)_{100-x}Sm_x$  in table 2.5 show an augmentation on  $Sm$  addition which can be correlated to the decrease in  $C_N$  values on  $Sm$  incorporation. The enhancement in structural modification efficiency and lone pair electrons on incorporation of  $Sm$  to  $GST$  may improve upon the possibility of having many structural configurations and may increase its glass forming ability.

$x$	<i>Ge-Te</i>	<i>Sb-Te</i>	<i>Sm-Te</i>	<i>Te-Te</i>	$I_c$
0	0.400000	0.400000	0.000000	0.200000	0.056000
0.2	0.400000	0.363265	0.048980	0.187755	0.099714
0.4	0.400000	0.325000	0.100000	0.175000	0.145250
0.6	0.400000	0.305263	0.126316	0.168421	0.168737
0.8	0.400000	0.285106	0.153191	0.161702	0.192723
1.0	0.400000	0.243478	0.208696	0.147826	0.242261
1.2	0.400000	0.200000	0.266667	0.133333	0.294000

**Table 2.6.** The fractions of bonds formed in  $Sm$  doped  $GST$  phase change materials and coefficient of ionicity ( $I_c$ ).

Hence, the transition from one structural configuration to other requires less activation energy as observed from the reduced activation energy for bond switching reaction on  $Sm$  addition to  $GST$ . This may modify the phase transition mechanism for  $GST$  and improve the phase change memory performance.

### 2.2.10 Threshold Switching Voltage

The structural changes in chalcogenide glasses determined through the evaluation of  $CSME$  affects its properties, switching characteristics and stability of various configurations. The composition of the material with large value of  $CSME$  has more possibility of structural changes and therefore, larger variations consequently bring the large spread in threshold switching voltage. The structural reconfiguration on switching at the threshold switching voltage has been correlated empirically with the  $CSME$  values and can be considered as the criterion in predicting the stability of threshold switching voltage for various compositions [57]. This relation correlating the variation of threshold switching voltage ( $\Delta V_{th}$ ) through  $CSME$  may be expressed as

$$\Delta V_{th} = \alpha \left[ \frac{\bar{Z}-Z}{Z(1-I_c)} \right]^\beta + \Delta V_0 \quad (2.18)$$

where the values of parameters  $\alpha = 4.2 - 5.5$ ,  $\beta = 1.97 - 2.23$  and  $\Delta V_0 = 1 - 2\%$ . In equation (2.18) the contribution of bond metallicity has been not taken into account, since it leads to larger dispersion in  $\Delta V_{th}$  values. Figure 2.6 displays the variation in  $\Delta V_{th}$  values as a function of  $CSME$  by taking  $M$  values also into account. The switching in  $GST$  phase change materials occur through the transition between metastable structural states from one energy minimum to another. The existence of lone pair electrons and extent of coupling of covalent bonds describes the possibility of structural transitions. The quantitative evaluation of both the lone pair electrons and covalent coupling is determined by the values of  $CSME$ . The saturated bonds in a chemical composition are indicated by  $CSME$  having the least value. But, chalcogenide glasses consist of the significant fraction of unsaturated bonds. The higher the fraction of these unsaturated bonds in chalcogenide glass compositions more will be the  $CSME$  values. The composition with comparatively higher value of  $CSME$  lead to relatively lower value of activation energy for transition among different structural configurations, hence, enhances the efficiency of transitions. These transitions can therefore, take place at a lower applied electric field or lesser irradiation. The values of  $\Delta V_{th}$  obtained for  $GST$  added with  $Sm$  increase with  $Sm$  content (Table 2.5). This shows direct dependence of the threshold

switching voltage  $\Delta V_{th}$  on  $CSME$ . The similar behavior of  $\Delta V_{th}$  and  $CSME$  values with  $Sm$  content in  $GST$  can be seen from figure 2.6. The inset of figure 2.6 displays the linear dependence of  $\Delta V_{th}$  on  $CSME$ . Therefore, the percentage variation in the value of  $\Delta V_{th}$  with  $CSME$  is vital to decide the stability of amorphous phase at high voltages and the large difference in resistivity among the amorphous and crystalline state during phase transition. The rise in the  $CSME$  values for  $GST$  on  $Sm$  incorporation lowers the  $GST$  activation energy which may be useful to improve the switching speed of phase change memories.

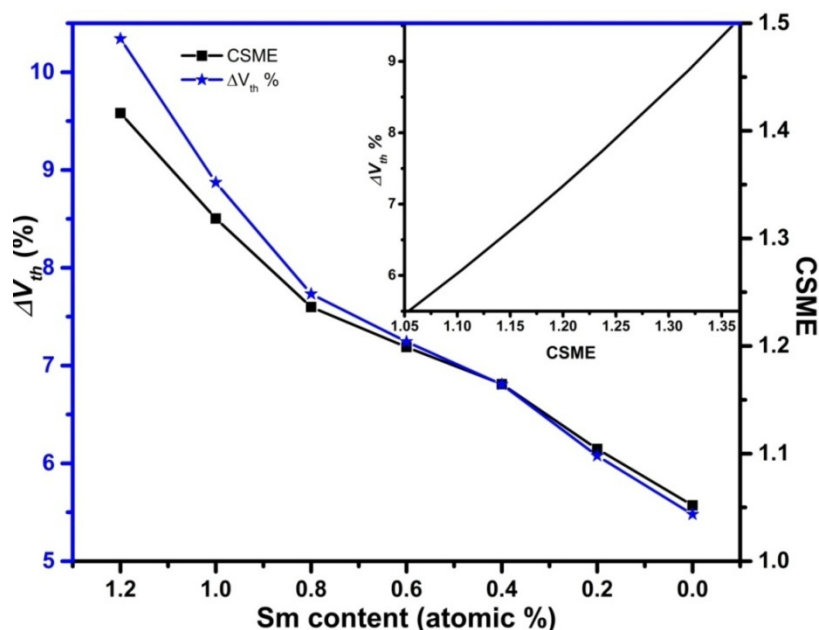


**Figure 2.6.** The variation of  $\Delta V_{th}$  and  $CSME$  with  $Sm$  content and the inset showing the linear dependence of obtained values of  $\Delta V_{th}$  with  $CSME$  for  $(Ge_2Sb_2Te_5)_{100-x}Sm_x$ .

### 2.3. Conclusion

The physical parameters of  $(Ge_2Sb_2Te_5)_{100-x}Sm_x$  ( $x = 0, 0.2, 0.4, 0.6, 0.8, 1.0, 1.2$ ) unveil the structural modifications with  $Sm$  content accompanying the change in  $T_g$ . The addition of trivalent  $Sm$  to  $Ge_2Sb_2Te_5$  increases the value of coordination number. The increase in rigidity of  $GST$  on incorporation of  $Sm$  has been analysed on the basis of augmentation of  $D_{CL}$  and reduction in  $M_f$  values. The increase in degree of covalency ( $> 93\%$ ) and band gap energy of  $GST$  on incorporation of  $Sm$  has been observed. The value of cohesive energy obtained using chemical bond approach for  $Sm$  doped  $GST$  behaves similar to the band gap. The addition of  $Sm$  affects the structural network of  $GST$  leading to an increase in the cross-linking between the linear chains and enhances the mean bond energy of structural network. The enhancement of  $T_g$  evaluated for  $Sm$  added  $GST$  is due to mean bond

energy increase with *Sm* concentration. This enhances *GST* structural modification efficiency on *Sm* incorporation. The growth in number of lone pair electrons on *Sm* addition to *GST* increases metallicity (*M*) and consequently enhances the coupling between the covalent network structures. The change in  $\Delta V_{th}$  and *CSME* values with *Sm* incorporation favors the improvement of switching speed in *GST*.

## References

- [1] G. K. Ahluwalia, *Applications of Chalcogenides: S, Se, and Te*. Cham: Springer International Publishing, 2017.
- [2] A. V Kolobov and J. Tominaga, “Chalcogenide glasses in optical recording: Recent progress,” *J. Opt. Adv. Mat.*, vol. 4, no. 3, pp. 679–686, 2002.
- [3] X. H. Zhang, Y. Guimond, and Y. Bellec, “Production of complex chalcogenide glass optics by molding for thermal imaging,” *J. Non. Cryst. Solids*, vol. 326–327, pp. 519–523, Oct. 2003.
- [4] P. Houizot, C. Boussard-Plédel, A. J. Faber, L. K. Cheng, B. Bureau, P. A. Van Nijnatten, W. L. M. Gielesen, J. Pereira do Carmo and J. Lucas, “Infrared single mode chalcogenide glass fiber for space,” *Opt. Express*, vol. 15, no. 19, p. 12529, 2007.
- [5] A. Pirovano, A. L. Lacaita, A. Benvenuti, F. Pellizzer, and R. Bez, “Electronic Switching in Phase-Change Memories,” *IEEE Trans. Electron Devices*, vol. 51, no. 3, pp. 452–459, Mar. 2004.
- [6] C. D. Wright, K. Blyuss, and P. Ashwin, “Master-equation approach to understanding multistate phase-change memories and processors,” *Appl. Phys. Lett.*, vol. 90, no. 6, p. 063113, Feb. 2007.
- [7] J. Teteris and M. Reinfeldt, “Holographic recording in amorphous chalcogenide thin films,” *J. Non. Cryst. Solids*, vol. 353, no. 13–15, pp. 1450–1453, May 2007.
- [8] M. Wuttig, H. Bhaskaran, and T. Taubner, “Phase-change materials for non-volatile photonic applications,” *Nature Photonics*, vol. 11, no. 8, pp. 465–476, 01-Aug-2017.
- [9] M. D. Pelusi, V. G. Ta’eed, L. Fu, E. Magi, M. R. E. Lamont, S. Madden, D.-Y. Choi, D. A. P. Bulla, B. Luther-Davies, and B. J. Eggleton, “Applications of Highly-Nonlinear Chalcogenide Glass Devices Tailored for High-Speed All-Optical Signal Processing,” *IEEE J. Sel. Top. Quantum Electron.*, vol. 14, no. 3, pp. 529–539, 2008.
- [10] V. A. Ryzhov and B. T. Melekh, “Optical Properties of Tellurium-Based Chalcogenide Alloys in the Far Infrared Region ( $\lambda > 30 \mu\text{m}$ ),” *Semiconductors*, vol. 52, no. 2, pp. 209–214, Feb. 2018.

- [11] S. R. Ovshinsky, “Reversible Electrical Switching Phenomena in Disordered Structures,” *Phys. Rev. Lett.*, vol. 21, no. 20, pp. 1450–1453, Nov. 1968.
- [12] C. Koch, A. L. Hansen, T. Dankwort, G. Schienke, M. Paulsen, D. Meyer, M. Wimmer, M. Wuttig, L. Kienle and W. Bensch, “Enhanced temperature stability and exceptionally high electrical contrast of selenium substituted  $\text{Ge}_2\text{Sb}_2\text{Te}_5$  phase change materials,” *RSC Adv.*, vol. 7, no. 28, pp. 17164–17172, 2017.
- [13] J. Momand, R. Wang, J. E. Boschker, M. A. Verheijen, R. Calarco, and B. J. Kooi, “Interface formation of two- and three-dimensionally bonded materials in the case of  $\text{GeTe-Sb}_2\text{Te}_3$  superlattices,” *Nanoscale*, vol. 7, no. 45, pp. 19136–19143, 2015.
- [14] G. Wang, Qihua Nie, X. Shen, R. P. Wang, L. Wu, J. Fu, T. Xu and S. Dai, “Phase change behaviors of Zn-doped  $\text{Ge}_2\text{Sb}_2\text{Te}_5$  films,” *Appl. Phys. Lett.*, vol. 101, no. 5, p. 051906, Jul. 2012.
- [15] G. Wang, X. Shen, Q. Nie, R. Wang, L. Wu, Y. Lv, F. Chen, J. Fu, S. Dai and J. Li “Improved thermal and electrical properties of Al-doped  $\text{Ge}_2\text{Sb}_2\text{Te}_5$  films for phase-change random access memory,” *J. Phys. D. Appl. Phys.*, vol. 45, no. 37, p. 375302, Sep. 2012.
- [16] M. L. Lee, K. T. Yong, C. L. Gan, L. H. Ting, S. Bin Muhamad Daud, and L. P. Shi, “Crystallization and thermal stability of Sn-doped  $\text{Ge}_2\text{Sb}_2\text{Te}_5$  phase change material,” *J. Phys. D. Appl. Phys.*, vol. 41, no. 21, p. 215402, Nov. 2008.
- [17] E. Cho, Y. Youn, and S. Han, “Enhanced amorphous stability of carbon-doped  $\text{Ge}_2\text{Sb}_2\text{Te}_5$  : Ab Initio investigation,” *Appl. Phys. Lett.*, vol. 99, no. 18, p. 183501, Oct. 2011.
- [18] Y. Lai, B. Qiao, J. Feng, Y. Ling, L. Lai, Y. Lin, T. Tang, B. Cai, and B. Chen, “Nitrogen-doped  $\text{Ge}_2\text{Sb}_2\text{Te}_5$  films for nonvolatile memory,” *J. Electron. Mater.*, vol. 34, no. 2, pp. 176–181, Feb. 2005.
- [19] Y. Hu, R. Zhang, T. Lai, X. Zhu, H. Zou, and Z. Song, “Simultaneously High Thermal Stability and Low Power Based on Ti-Doped  $\text{Ge}_2\text{Sb}_2\text{Te}_5$  Thin Films,” *ECS J. Solid State Sci. Technol.*, vol. 6, no. 12, pp. P866–P869, Dec. 2017.
- [20] A. Sherchenkov, S. Kozyukhin, A. Babich, and P. Lazarenko, “Thermal properties of

- phase change material  $\text{Ge}_2\text{Sb}_2\text{Te}_5$  doped with Bi,” *J. Non. Cryst. Solids*, vol. 377, pp. 26–29, Oct. 2013.
- [21] Y.-H. Huang and T.-E. Hsieh, “Effective thermal parameters of chalcogenide thin films and simulation of phase-change memory,” *Int. J. Therm. Sci.*, vol. 87, pp. 207–214, Jan. 2015.
- [22] H. Zou, L. Zhai, Y. Hu, X. Zhu, H. You, J. Zhang, S. Song and Z. Song, “Samarium doped  $\text{Sn}_{15}\text{Sb}_{85}$ : a promising material for phase change memory applications,” *RSC Adv.*, vol. 7, no. 88, pp. 56000–56005, 2017.
- [23] Y. Chen, N. Chen, B. Chen, Q. Zhang, X. Li, Q. Deng, B. Zhang, S. Zhang, Z. Zhang, and X. Han, “Electrical properties and structural transition of  $\text{Ge}_2\text{Sb}_2\text{Te}_5$  adjusted by rare-earth element Gd for nonvolatile phase-change memory,” *J. Appl. Phys.*, vol. 124, no. 14, p. 145107, Oct. 2018.
- [24] H. Zou, X. Zhu, Y. Hu, Y. Sui, W. Wu, J. Xue, L. Zheng and Z. Song, “Improvement of the thermal stability of Sb thin film through erbium doping,” *CrystEngComm*, vol. 18, no. 34, pp. 6365–6369, 2016.
- [25] M. F. Thorpe, “Continuous deformations in random networks,” *J. Non. Cryst. Solids*, vol. 57, no. 3, pp. 355–370, Sep. 1983.
- [26] K. Tanaka, “Glass transition of covalent glasses,” *Solid State Commun.*, vol. 54, no. 10, pp. 867–869, Jun. 1985.
- [27] J. C. Phillips, “Topology of covalent non-crystalline solids I: Short-range order in chalcogenide alloys,” *J. Non. Cryst. Solids*, vol. 34, no. 2, pp. 153–181, Oct. 1979.
- [28] A. H. Johnstone, “CRC Handbook of Chemistry and Physics-69<sup>th</sup> Edition”, Editor R. C. Weast, *J. Chem. Technol. Biotechnol.*, vol. 50, no. 2, pp. 294–295, Apr. 2007.
- [29] S. R. Alharbi, K. A. Aly, E. S. Al-Zahrani, A. Dahshan, and W. Alharbi, “Physical behavior of As-Se-Se glasses with constant coordination number ( $N_c = 2.2$ ),” *Chalcogenide Lett.*, vol. 15, no. 6, pp. 339–343, 2018.
- [30] J. C. Phillips and M. F. Thorpe, “Constraint theory, vector percolation and glass formation,” *Solid State Commun.*, vol. 53, no. 8, pp. 699–702, Feb. 1985.

- [31] L. Tichý and H. Tichá, "On the chemical threshold in chalcogenide glasses," *Mater. Lett.*, vol. 21, no. 3–4, pp. 313–319, Nov. 1994.
- [32] S. A. Fayek, M. R. Balboul, and K. H. Marzouk, "Optical, electrical and thermal studies on  $(As_2Se_3)_{3-x}(As_2Te_3)_x$  glasses," *Thin Solid Films*, vol. 515, no. 18, pp. 7281–7285, Jun. 2007.
- [33] P. K. Thiruvikraman, "Rings, chains and planes: Variation of  $T_g$  with composition in chalcogenide glasses," *Bull. Mater. Sci.*, vol. 29, no. 4, pp. 371–374, Aug. 2006.
- [34] A. Kumar and N. Mehta, "Correlation between some thermo-mechanical and physico-chemical properties in multi-component glasses of Se-Te-Sn-Cd system," *Appl. Phys. A*, vol. 123, no. 6, p. 410, Jun. 2017.
- [35] K. A. Aly, S. R. Alharbi, Y. B. Saddeek, A. M. Ali, A. Dahshan, and K. S. Shaaban, "Physical characterization of As-Se-S glasses," *Mater. Res. Express*, vol. 5, no. 6, p. 065208, Jun. 2018.
- [36] B. Cordero, V. Gomez, A. E. Platero-Prats, M. Reves, J. Echeverria, E. Cremades, F. Barragan and S. Alvarez, "Covalent radii revisited," *Dalt. Trans.*, vol. 2, no. 21, p. 2832, 2008.
- [37] L. Pauling, "X-Ray Crystallography and the Nature of the Chemical Bond," in *The Chemical Bond*, vol. 26, no. 2014, Elsevier, 1992, pp. 3–16.
- [38] V. Sadagopan and H. C. Gatos, "On the relationship of semiconductor compound properties and the average heats of atomisation," *Solid. State. Electron.*, vol. 8, no. 6, pp. 529–534, Jun. 1965.
- [39] K. Shimakawa, "On the compositional dependence of the optical gap in amorphous semiconducting alloys," *J. Non. Cryst. Solids*, vol. 43, no. 2, pp. 229–244, Mar. 1981.
- [40] V. Pamukchieva A. Szekeres, K. Todorova, M. Fabian, E. Svab, Zs. Revay, L. Szentmiklosi, "Evaluation of basic physical parameters of quaternary Ge–Sb–(S,Te) chalcogenide glasses," *J. Non. Cryst. Solids*, vol. 355, no. 50–51, pp. 2485–2490, Dec. 2009.
- [41] R. Khadour, F. Saiouf, and I. Mdawar, "Theoretical approach and physical analysis of optimized  $(Ge_{33} Te_{67})_{1-x} Sn_x$  chalcogenide glassy alloys," *Int. J. ChemTech Res.*, vol. 8,

- no. 10, pp. 200–210, 2015.
- [42] C. Xing, Y. Zhang, W. Yan, and L. Guo, “Band structure-controlled solid solution of  $\text{Cd}_{1-x}\text{Zn}_x\text{S}$  photocatalyst for hydrogen production by water splitting,” *Int. J. Hydrogen Energy*, vol. 31, no. 14, pp. 2018–2024, Nov. 2006.
- [43] I. Sharma, P. Kumar, and S. . Tripathi, “Physical and optical properties of bulk and thin films of a  $-\text{Ge}-\text{Sb}-\text{Te}$  lone-pair semiconductors,” *Phase Transitions*, vol. 90, no. 7, pp. 653–671, Jul. 2017.
- [44] L. Tichý and H. Tichá, “Covalent bond approach to the glass-transition temperature of chalcogenide glasses,” *J. Non. Cryst. Solids*, vol. 189, no. 1–2, pp. 141–146, Aug. 1995.
- [45] A. N. Sreeram, D. R. Swiler, and A. K. Varshneya, “Gibbs-DiMarzio equation to describe the glass transition temperature trends in multicomponent chalcogenide glasses,” *J. Non. Cryst. Solids*, vol. 127, no. 3, pp. 287–297, Feb. 1991.
- [46] J. C. Tauc, *Amorphous and Liquid Semiconductors*. Boston, MA: Springer US, 1974.
- [47] N. Sharma, S. Sharda, V. Sharma, and P. Sharma, “Far-infrared investigation of ternary  $\text{Ge}-\text{Se}-\text{Sb}$  and quaternary  $\text{Ge}-\text{Se}-\text{Sb}-\text{Te}$  chalcogenide glasses,” *J. Non. Cryst. Solids*, vol. 375, pp. 114–118, Sep. 2013.
- [48] A. Popov, “Two generations of phase-change memory devices: Differences and common problems,” *Phys. status solidi*, vol. 246, no. 8, pp. 1837–1840, Aug. 2009.
- [49] K. Tanaka, “Configurational and Structural Models for Photodarkening in Glassy Chalcogenides,” *Jpn. J. Appl. Phys.*, vol. 25, no. Part 1, No. 6, pp. 779–786, Jun. 1986.
- [50] M. Kastner, D. Adler, and H. Fritzsche, “Valence-Alternation Model for Localized Gap States in Lone-Pair Semiconductors,” *Phys. Rev. Lett.*, vol. 37, no. 22, pp. 1504–1507, 1976.
- [51] R. Y. A. Golovchak and O. I. Shpotyuk, “Radiation-induced bond switching in mixed  $\text{Ge}-\text{As}$  sulphide glasses,” vol. 85, no. 25, pp. 2847–2860, 2005.
- [52] M. Shpotyuk, A. Kovalskiy, R. Golovchak, and O. Shpotyuk, “Phenomenology of  $\gamma$ -irradiation-induced changes in optical properties of chalcogenide semiconductor glasses: A case study of binary arsenic sulfides,” *J. Non. Cryst. Solids*, vol. 498, pp.

- 315–322, Oct. 2018.
- [53] T. Fan, F R Liu, W. Q. Li, J. C. Guo, Y. H. Wang, N. X. Sun and F. Liu, “Study on accumulated crystallization characteristics of amorphous  $\text{Ge}_2\text{Sb}_2\text{Te}_5$  induced by multi-pulsed laser irradiations with different fluences,” *Semicond. Sci. Technol.*, vol. 33, no. 7, 2018.
- [54] P. Jövári, P. Lucas, Z. Yang, B. Bureau, Ivan Kaban, B. Beuneu and J. Bednarcik, “Short-range order in Ge - As - Te glasses,” *J. Am. Ceram. Soc.*, vol. 97, no. 5, pp. 1625–1632, 2014.
- [55] K. S. Andrikopoulos, S. N. Yannopoulos, A. V. Kolobov, P. Fons, and J. Tominaga, “Raman scattering study of GeTe and  $\text{Ge}_2\text{Sb}_2\text{Te}_5$  phase-change materials,” *J. Phys. Chem. Solids*, vol. 68, no. 5–6, pp. 1074–1078, May 2007.
- [56] W. Zhang, R. Mazzarello, M. Wuttig, and E. Ma, “Designing crystallization in phase-change materials for universal memory and neuro-inspired computing,” *Nat. Rev. Mater.*, vol. 4, no. 3, pp. 150–168, Mar. 2019.
- [57] A. I. Popov, N. I. Michalev, and V. K. Shemetova, “Structural modification of some glassy chalcogenides,” *Philos. Mag. B*, vol. 47, no. 1, pp. 73–81, Jan. 1983.
- [58] A. I. Popov, I. A. Domoryad, and N. I. Michalev, “Structural modification of arsenic chalcogenide glasses under  $\gamma$ -radiation,” *Phys. Status Solidi*, vol. 106, no. 2, pp. 333–337, Apr. 1988.
- [59] A. Popov, “Chapter 2 Atomic structure and structural modification of glass,” in *Semiconductors and Semimetals*, vol. 78, no. C, 2004, pp. 51–95.



# **Chapter 3**

## **Experimental Techniques**



### 3.1. Introduction

The glass formation is a thermodynamic process that can be described from the temperature dependence of volume change as well as enthalpy change. The cooling rate plays an important part in glass synthesis. Figure 3.1 shows the plot of volume change as a function of temperature to better understand the glass formation and to avoid crystallization. Slowly cooling the melt below the melting temperature ( $T_m$ ) results in the instant crystallization accompanied with abrupt change in the volume represented by the line  $AF$  in figure 3.1. Further cooling results in the gradual volume change with temperature due to the formation of the crystalline phase shown by the line  $FG$  in figure 3.1. Rapidly cooling below the melting temperature of solids avoids crystallization to take place. As shown in figure 3.1, continuous decrease in the temperature of supercooled liquid results in the formation of a glassy state represented by the line  $AB$ . The viscosity of supercooled liquid increases continuously and at a certain point in the temperature versus volume diagram the viscosity reaches  $\sim 10^{14.5}$  poise and displays no structural change on further cooling and approaches the glassy state. Glass formation consequently takes place with the gradual change in slope of volume vs. temperature diagram. This temperature at which slope changes is known as the glass transition temperature ( $T_g$ ). The crystallization is designated as first-order phase transition, while, on the other hand the glass formation is the second-order phase transition because of the discontinuity in specific heat capacity ( $C_p$ ) with temperature.

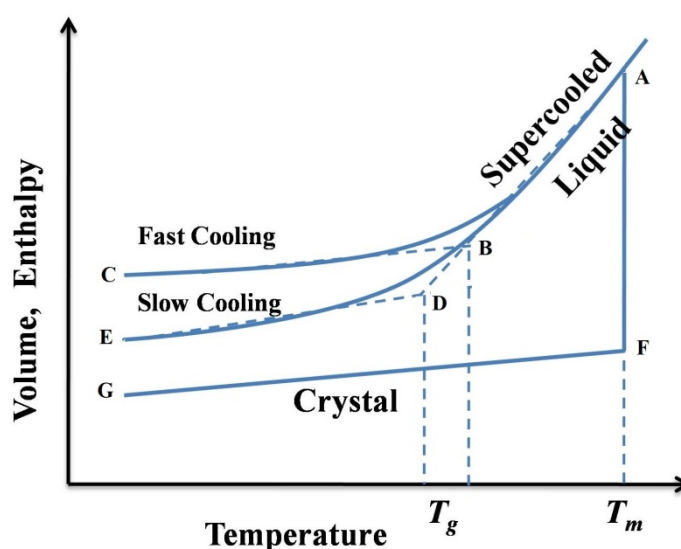


**Figure 3.1** Temperature dependence of volume and enthalpy for crystalline and glassy solids.

In addition to the thermodynamic aspects, the kinetic aspect also plays an important role in describing the glass transition temperature ( $T_g$ ). Glass transition also changes with the rate of cooling as has been illustrated in figure 3.1. The undercooled liquid displays the  $T_g$  at a lower temperature because the diffusion motion of molecules or ions in the melt has comparatively more time to adjust themselves in the metastable equilibrium state represented by the curve  $DE$ .

The tendency of glass formation for different chemical compounds varies tremendously. Glass formation of some materials is comparatively easily attainable at normal conditions, but, for certain materials very high rate of cooling of the order  $\sim 10^{10} \text{ Ks}^{-1}$  is required for glass formation which is very difficult to obtain experimentally. Different models have been adopted to correlate the glass-forming ability of alloys to their chemical bonding nature [1]–[3]. Materials exhibiting a large concentration of lone pair electrons are characterized as good glass formers [4]. The covalently bonded chalcogenide alloys containing elements of larger atomic radii have more metallic character and with the increase in the metallic character of the glass-forming alloys, their glass-forming tendency decreases considerably [4].

### 3.2. Preparation of Chalcogenide Glass

Several different techniques for the fabrication of chalcogenide glasses in bulk form and thin film have been described in the literature. Some important techniques for the synthesis of bulk alloys and deposition of thin films have been described below.

#### 3.2.1 Melt Quenching

Melt-quenching is the most convenient and widely utilized synthesis approach for chalcogenide glasses in the bulk form. This technique employs the preparation of mixture of the high purity (99.999% purity) raw material of constituent elements of glass-forming alloys in the appropriate ratio. The quartz ampoules of length  $\sim 18 \text{ cm}$  and neck thickness of 4-5 mm have been prepared using the quartz tube having the outer diameter  $\sim 10 \text{ mm}$  as depicted in figure 3.2 (a). The quartz ampoules have been cleaned using chromic acid by placing them in the chromic acid solution for 24 hours. The batch of a mixture of raw materials is placed inside the well-cleaned quartz ampoule. The ampoules containing the mixture of raw materials have been sealed at a high vacuum of order  $\sim 10^{-5} \text{ mbar}$  as has been shown in figure 3.2 (b). The sealed ampoule at a high vacuum has been shown in figure 3.2 (c).

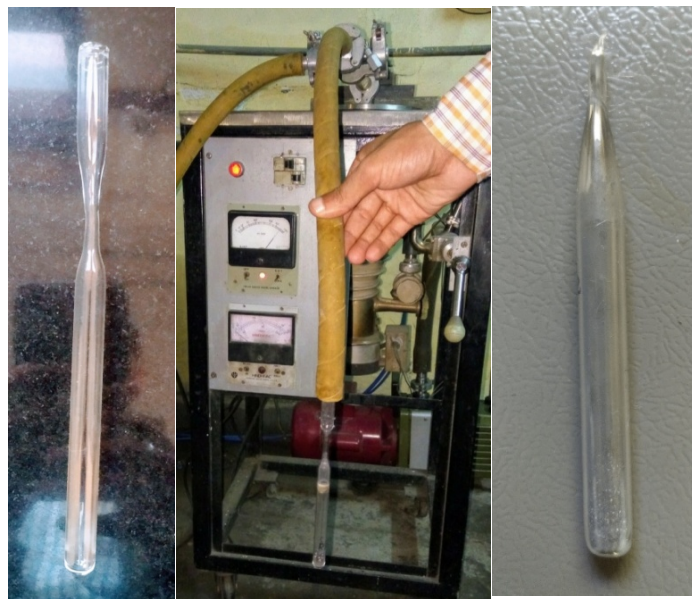


**Figure 3.2** (a) Quartz Ampoule. (b) Vacuum Sealing of Ampoule. (c) Sealed Ampoule.

Quartz ampoules sealed at high vacuum have been kept inside the muffle furnace by maintaining the multi-step heating program with a heating rate of  $2\text{-}3\text{ K/min}$ . Heating has been done up to the highest melting point of constituent elements ( $827\text{ K}$ ) in the mixture. After attaining the melting temperature the temperature of the furnace has been maintained constant for approximately  $10\text{ hours}$ . During the entire ramped heating process, continuous rocking of the ampoule has been done to maintain the homogeneity of the melt. The ampoule has been immediately dropped into the container containing ice-cold water. The rapid quenching of melt is done to avoid the crystallization and to attain the amorphous phase. The quenched ampoule has been immersed in  $\text{HF}+\text{H}_2\text{O}_2$  (1:3) solution for 48 hours. Finally, the powdered sample has been obtained by crushing the ampoule to get a solid sample ingot and subsequently using granite mortar and pestle to crush the ingot into fine powder. This method has been adopted for the synthesis of bulk alloys of  $(\text{Ge}_2\text{Sb}_2\text{Te}_5)_{100-x}\text{Sm}_x$  ( $x = 0, 0.2, 0.4, 0.6, 0.8, 1.0, 1.2$ ) because of its advantages such as wide applicability, low cost and excellent purity control *etc.*

### 3.2.2 Sol-Gel Method

This is the wet chemical route and bottom-up approach for the synthesis. This method can be successfully applied for the synthesis of glasses. Metal alkoxide precursors are used as raw materials in this method. The precursors are added into water and ethanol with continuous stirring for the complete hydrolysis to take place. The homogeneous solution

formed after hydrolysis is called sol, which further undergoes condensation reaction. Sol contains the dispersed colloidal particles in the solvent forming the heterogeneous mixture. The sol is aged subsequently for the polymerization and the formation of three-dimensional structural networks which finally leads to the formation of the gel. The gel is dried and then sintered to obtain the powder material. The samples prepared using this method are more probable to contain the residual hydroxyl group and carbon compounds in the final product which limits the use of this method.

### 3.2.3 Thermal Evaporation

This is a physical vapor deposition method for formation of the thin films. This method involves the evaporation of source materials by resistively heating the target materials in high vacuum. The technique has been utilized for deposition of  $(Ge_2Sb_2Te_5)_{100-x}Sm_x$  thin films for the current study. The deposition of evaporated material has been carried out on a pre cleaned substrate to get solid thin films. The substrates have been cleaned in soap solution and then ultrasonically agitated in distilled water, ethanol and acetone solutions subsequently before deposition. Finally, substrates have been dried using the hot acetone vapors. The evaporation of source material has been performed using the tungsten or molybdenum boats inside the vacuum chamber ( $\sim 10^{-5} mbar$ ). The Joule heating is produced in a boat by applying the electricity through the boat. The process of evaporation in the vacuum chamber has been displayed schematically in figure 3.3(a). The target material has been placed inside the boat for evaporation through the sublimation in a high vacuum and the condensation of vapors takes place onto a pre-cleaned glass substrate. This method cannot be applied for the deposition of materials with a very high melting temperature greater than the melting point of boat material. The evaporation rate and the thickness of thin films are controlled by varying the electric current across the boat and has been monitored using the digital thickness monitor (*DTM*) coupled with quartz crystal mounted at the control panel. The calibration of *DTM* has been done before deposition by pre-setting material's density (*DNT*), acoustic impedance (*ACI*) and tooling factor (*TFC*) values. Figure 3.3(b) illustrates the thermal evaporation unit *HINDHIVAV 12A4D* used for the deposition of  $(Ge_2Sb_2Te_5)_{100-x}Sm_x$  thin films. 200mg of fine powder sample has been kept inside the molybdenum boat for evaporation. The deposition rate ( $10-15 \text{ \AA/s}$ ) and the film thickness ( $\sim 1000 \text{ nm}$ ) have been maintained to ensure the good uniformity of as-deposition  $(Ge_2Sb_2Te_5)_{100-x}Sm_x$  thin films.

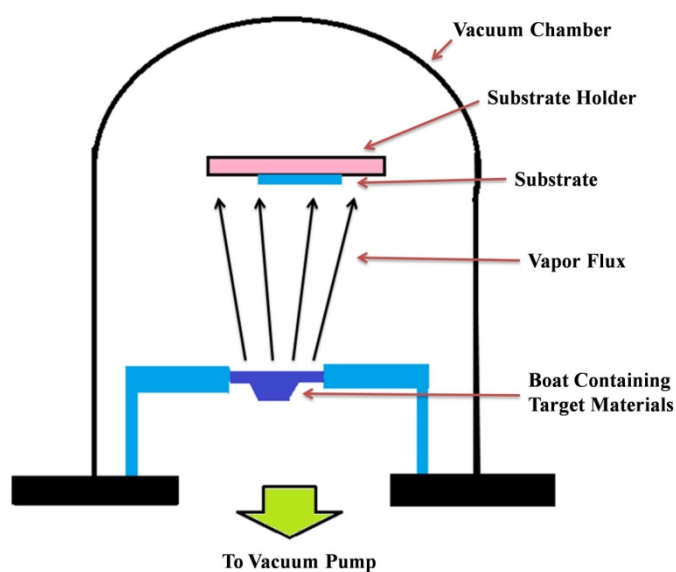


**Figure 3.3 (a)** Process of thermal evaporation. **(b)** Thermal Evaporation unit

The assembly of the rotary and diffusion pump has been attached with a vacuum chamber to create the high vacuum. This method is cost-effective and beneficial to obtain high purity thin films and offers better control over the mechanical stresses involved in the deposition of the thin films. This method is also advantageous for the deposition of multi-layers and uniform thin films and to attain a high deposition rate of  $< 50\text{\AA}/\text{s}$ .

### 3.2.4 Electron-Beam Deposition

The deposition of a thin film in this method is also carried out by the evaporation of source materials. But, in this method, the evaporation is performed using the thermionic beam of electrons which is generated from the heated filament. The beam of ejected electrons is focused on the source material placed inside the graphite crucible by using the accelerating voltage and magnetic field. The whole deposition process in this method is carried out in an evacuated chamber at a pressure of about  $10^{-5}$  mbar. The high rate of deposition  $0.1\mu\text{m}/\text{min}$  to  $100\mu\text{m}/\text{min}$  can be achieved using this method. This method allows the control over the thin film morphology and provides better thermal efficiency, less contamination and high reliability. The rate of deposition can be controlled by varying the flux and kinetic energy of the accelerated electron beam which can be monitored by quartz crystal similar to that in the thermal evaporation method. The evaporated material condenses on to a cold substrate forming the solid thin films. Figure 3.4 (a) indicates the schematic representation of the

evaporation process by focused electron beam and figure 3.4 (b) displays the picture of high voltage *dc* power supply for electron gun.

This method has several disadvantages over the other methods such as large material utilization for deposition, non-uniform deposition rate due to filament degradation, step coverage and X-ray damage.

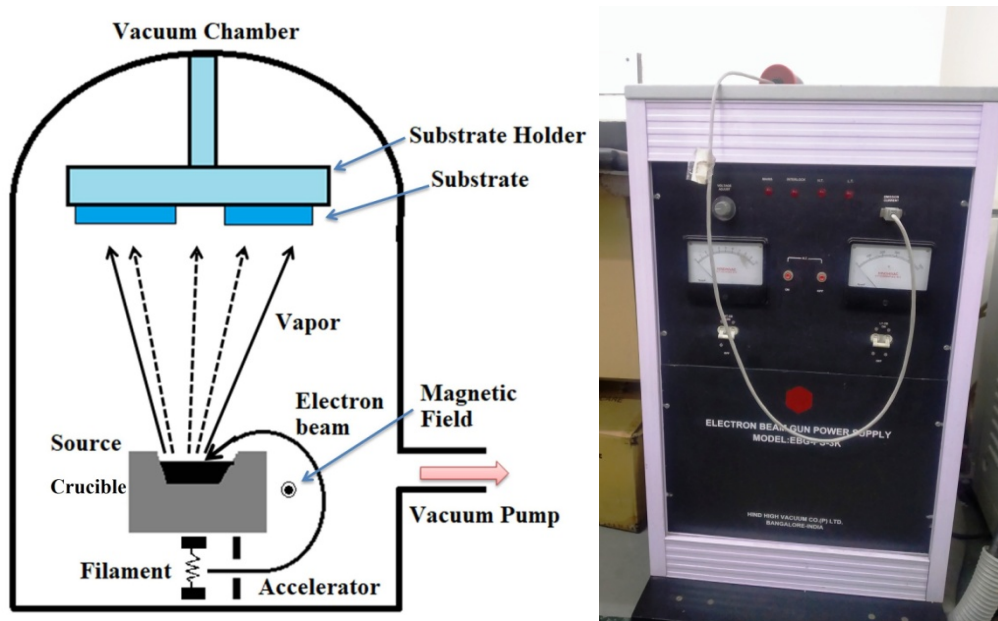


**Figure 3.4** (a) Electron beam evaporation process. (b) DC power supply for high voltage electron gun.

### 3.2.5 Flash Evaporation

Flash evaporation is also one of the techniques for thin film deposition of multi-component alloys. In this method, the *Ta* or *Ir* boats are heated to approximately  $1300\text{ }^{\circ}\text{C}$  to  $1400\text{ }^{\circ}\text{C}$  (higher than the evaporation temperature of components of alloy) for evaporation. Heated *Ta* or *Ir* boats act as an evaporator. The ultrasonically or mechanically agitated powder material is dropped over the heated evaporator to obtain the thin films. This method does not require maintaining the vapor pressure of different components of multi-component alloys and controlling the temperature of the boat. The thin films of  $\text{Bi}_2\text{Te}_3$  or compounds of the III-V group can be deposited using this method.

### 3.2.6 Pulsed Laser Deposition

The pulsed laser deposition (*PLD*) is another physical vapor deposition (*PVD*) method for thin film deposition. In this method, the high power beam of a laser pulse is focused on a target consisting of desired materials which evaporates/sublimates and is then deposited onto

the substrate. The whole evaporation process is carried out at an ultra-high vacuum of  $10^{-9}$  mbar. Moreover, the deposition can also be carried out with background gas such as oxygen for deposition of metal oxide thin films or nitrogen for deposition of nitride thin films. A high heating rate of  $10^8 K/s$  can be achieved using this method. Besides the advantage of a higher heating rate to maintain the stoichiometry of the deposited material, it also has significant drawbacks such as the films deposited using this method sometimes contain the fragments of target materials which are sputtered by the explosions induced by laser beams on the surface of target materials.

### 3.2.7 Sputtering

Sputtering is one of the commonly used technique of physical vapor deposition for the thin film deposition. Sputtering is the process of ejecting atoms from the solid target material by the bombardment of atoms, ions or molecules. The kinetic energy of the bombarded atom is transferred to the atoms on the surface of the target material due to elastic collisions and as a result the atoms on the target site are knocked out. The energy of the impinging particles (atoms or ions) largely decides the different phenomena that can take place on the surface of solids. If the energy of the bombarded particles is less than  $5eV$  it will be reflected from the surface. The surface damage or migration may take place when the energy of the particles lies in between  $5-10 eV$  and the particles with energy in between  $3$  to  $10 keV$  can cause the sputtering. The energy higher than  $10keV$  for particles results in the ion implantation. This technique is utilized for the deposition of thin films onto the substrate.

There are four basic steps of the deposition of thin films by sputtering; the first one is plasma generation and then ion bombardment followed by sputtering and subsequently the film growth. At the first stage, the inert gas is introduced in the chamber which is thereafter ionized by subjecting to the electric field between the electrodes resulting in the glow of discharge. Due to this, the free electrons created inside the chamber because of the ionization acquire kinetic energy and are accelerated towards the positively charged anode which further ionizes the neutral atoms resulting in an avalanche effect. These positively charged ions in plasma are then-accelerated towards target placed at the cathode. The bombarded positively charged ions acquire sufficient kinetic energy and impact the target resulting in momentum transfer. If the atoms on the surface attain enough energy after momentum transfer to disrupt the bonding energy, this results in ejection of the atoms, ions and electrons from the surface. The number of atoms ejected by the single positively charged ion defines the sputter efficiency of that ion and it also depends upon the angle of impact. The maximum sputter

efficiency can be achieved by maintaining the angle of impact in between  $60^{\circ}$  -  $70^{\circ}$ . The atoms sputtered from target condense at the substrate resulting in the thin film deposition.

Five different types of sputtering methods can be utilized for thin film deposition *viz.*, magnetron sputtering, *DC* sputtering, *AC* sputtering, *RF* sputtering and reactive sputtering. The *DC* voltage of  $0.5$ - $5kV$  is applied between the target and substrate to ionize the *Ar* atoms in *DC* sputtering. This method is utilized for the deposition of conducting thin films and cannot be used for the non-conducting thin films depositions. The plasma is created by both electric and magnetic fields in magnetron sputtering. The magnetic field is generated by the permanent magnet installed at the target. The argon ions get confined in the target region which does not damage the substrate and this leads to a higher deposition rate. The *ac* sputtering technique is utilized for non-conducting coating. In this case, *ac* voltage of frequency  $10$  -  $100$  *Hz* applied across the electrodes creates the plasma. *RF* sputtering method can also be used for non-conducting coating by utilizing the *ac* voltage in the radio frequency region ( $0.5$  to  $30MeV$ ). The oxide and nitride coating are often carried out using reactive sputtering by introducing oxygen or nitrogen as reactive gas.

### 3.2.8 Chemical Vapor Deposition

This is a chemical method for the deposition of thin films. In this method, the volatile precursors of the required components are transmitted to the reaction chamber in gaseous form by using the inert carrier gas. The precursors are volatile and undergo the gaseous phase reactions forming the intermediate reactant and by-product gases. The by-product gases formed inside the reaction chamber are removed with the help of carrier gas. The intermediate reactant then deposits onto the heated substrate and diffuses into the surface resulting in the formation of thin-film with nucleation and subsequent growth. The optimization of reactivity and stability of respective *CVD* precursors must be performed before deposition. Evacuation of the residual gases from the reaction chamber is an essential part of the deposition process to maintain the pressure inside the chamber. Various kinds of *CVDs viz.* low-pressure *CVD*, atmospheric pressure *CVD*, plasma-enhanced *CVD* and metal-organic *CVD* involves different deposition conditions. The reaction chamber in atmospheric pressure *CVD* is not connected to the vacuum system, whereas, in low-pressure *CVD*, the  $0.25$  torr to  $2.0$  torr vacuum and  $550^{\circ}C$  to  $600^{\circ}C$  temperature are maintained inside the chamber. The plasma-enhanced *CVD* uses the *RF* field to generate the plasma and is beneficial over the other methods to achieve higher deposition rate and to maintain low

substrate temperature. Metal-organic *CVD* is often used to deposit the thin films of *III-V* group compound semiconductors.

### 3.2.9 Spin Coating

The spin coating technique can be utilized for the depositing the chalcogenide thin films of uniform thickness ranging from few nanometer to a micrometer. In this method, the substrate mounted on a chuck is rotated at a very high speed ranging from *1000 rpm* to *8000 rpm*. The solution of coating material is made by dissolving it into a volatile solvent of appropriate viscosity and concentration. The drops of coating solution are placed on the center of the substrate placed on a rotating chuck. Due to the centrifugal force, the liquid spreads onto the substrate. The machine used for this purpose is referred to as a spin coater. The rotation of the substrate is continued till the desired thickness of the thin film is obtained. The thickness of the thin film is controlled by the angular speed, solution viscosity and concentration. Finally, the volatile solvent is evaporated to obtain the solid thin film.

### 3.3. Methods for Characterization

Experimental tools used for the examination of various properties of *Sm* doped  $Ge_2Sb_2Te_5$  phase change materials have been described in this section. X-ray diffraction (*XRD*) and energy-dispersive X-ray spectroscopy (*EDS*) have been employed respectively for investigation of prepared samples for crystal structure and elemental analysis. The chemical bonding nature of *Sm* doped  $Ge_2Sb_2Te_5$  has been analyzed with the help of X-ray photoelectron spectroscopy (*XPS*). Local structure and bonding have been explored using Raman spectroscopy and Fourier-transform infrared spectroscopy (*FTIR*). The linear and nonlinear optical behavior of *Sm* doped  $Ge_2Sb_2Te_5$  has been investigated using *UV-Vis-NIR* spectroscopy. Differential scanning calorimetry (*DSC*) has been used to examine the crystallization kinetics and thermal stability of the prepared samples.

#### 3.3.1. X-Ray Diffraction (*XRD*)

*XRD* technique has been employed to study the crystallographic information about the materials such as crystalline phase identification, unit cell parameters, crystallite size, strain, and defects *etc.* The working principle of *XRD* is based upon the constructive interference of elastically scattered monochromatic *X*-rays from the surface of material. The beam of *X*-rays is generated using the cathode ray tube and focused on the sample using the collimator as shown in figure 3.5(a). The incident *X*-ray beam interacts with the electrons present in the

sample placed on the sample holder and the diffracted beam emerges as a result of the elastic collisions. The diffracted beam follows the Bragg's equation [5]

$$n\lambda = 2d\sin\theta \quad (3.1)$$

where  $n$  is an integer and  $\theta$  is glancing angle. The incident  $X$ -ray having wavelength  $\lambda$  produces the path difference  $2d\sin\theta$  between the diffracted beams from two atomic planes with interplanar spacing  $d$ . The diffracted beam is collected by the detector at different glancing angles of the goniometer.  $Fe$ ,  $Cu$ ,  $Mo$  and  $Cr$  are some of the commonly used  $X$ -ray sources.

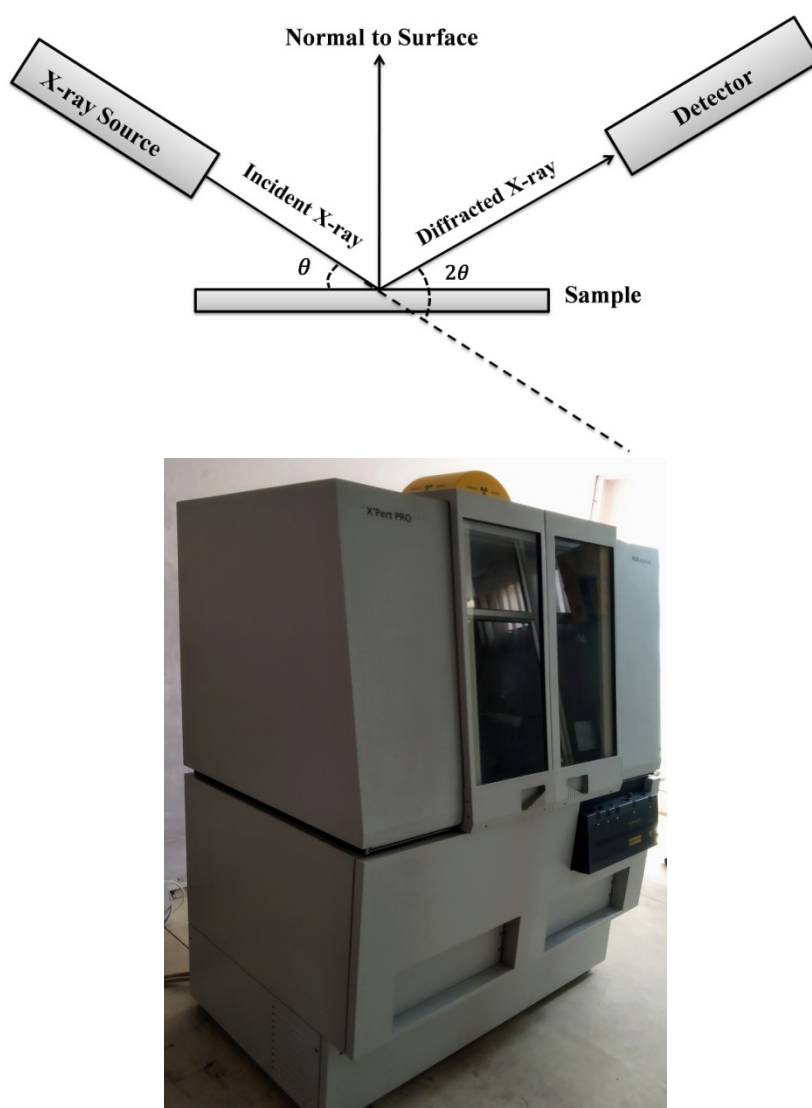


**Figure 3.5(a).** Diagrammatic representation of  $XRD$  working principle **(b).** X-ray diffractometer model PANalytical, X'Pert Pro exploited for  $XRD$  analysis.

In the current work, X-ray diffractometer PANalytical, X'Part Pro (HPU Shimla) has been used for analysis of GST added with Sm thin films while Shimadzu X-ray diffractometer model XRD 6000 (JIIT Noida) has been utilized for the investigation of powder samples. The measurement of samples has been performed by utilizing the Cu K $\alpha$  X-ray source ( $\lambda=1.54060\text{\AA}$ ) and a scan speed of 2.0 degrees/min in the  $2\theta$  range of  $20^\circ$  to  $80^\circ$  with a step size of  $0.02^\circ$ .

Following formulae have been employed to investigate the structural parameters

### (i) Crystallite Size ( $D$ ) and strain ( $\epsilon$ )

Scherrer formula relates the crystallite size with the broadening of diffraction peak ( $\beta_L$ )

$$\beta_L = \frac{K\lambda}{D_{hkl}\cos\theta} \quad (3.2)$$

where  $D_{hkl}$  represents the crystallite size and  $K$  is the shape parameter.

Williamson hall equation has been employed to calculate the strain and crystallite size

$$\beta\cos\theta = \left(\frac{K\lambda}{D}\right) + 4\epsilon\sin\theta \quad (3.3)$$

where  $\beta = \beta_L + \beta_s$  and  $\beta_s$  is strain broadening.

### 3.3.2. Energy Dispersive X-ray Spectroscopy (EDS)

Energy dispersive X-ray (EDX) or energy-dispersive X-ray spectroscopy (EDS) is the elemental analysis technique used for identifying the elements present in the prepared samples and their quantitative analysis such as elemental concentration. This technique is commonly equipped with the scanning electron microscopy (SEM) and transmission electron microscopy (TEM). The operating principle of EDS is based upon the interaction of high-energy electron beam with the sample surface. The incident primary electron beam either interacts elastically or inelastically with the sample surface. The electrons hitting the atomic nucleus are scattered elastically without loss of energy and are called backscattered electrons. The electrons passing near the positively charged nucleus results in the de-acceleration in electron velocity due to Coulombic interactions and simultaneous generation of continuum X-ray (bremsstrahlung). The primary electron beam ionizes the core-shell electrons of an atom present on the sample surface due to the inelastic collisions as illustrated in figure 3.6. The hole is created in the  $K$  shell as a result of the ejection of the electrons by the primary electron

beam. The electrons present in the higher energy states relax to fill up the hole and this results in the emission of characteristic  $X$ -rays with unique energy and wavelength for each element. The release of characteristic  $X$ -ray energy in the process of relaxation is used for the identification of elements present in a sample. The quantitative analysis can be performed by quantifying the intensities of corresponding  $X$ -rays. In figure 3.6 the notation  $K$ ,  $L$  and  $M$  refer to the atomic shells with principal quantum numbers 1, 2 and 3 respectively. The relaxation of the electrons of the  $L$  to  $K$  shell is denoted by the  $K_{\alpha}$  transition and the transition from  $M$  to  $K$  is referred to as  $K_{\beta}$  with comparatively higher energy than the former.

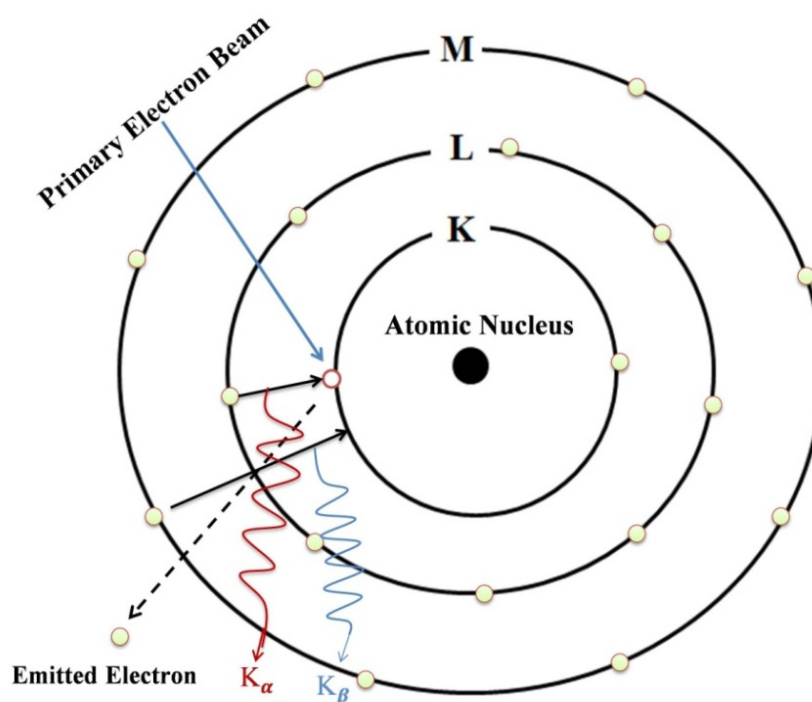


**Figure 3.6.** Working principle of *EDS* with  $X$ -ray emission.

The *EDS* instrument is composed of three main parts: detector, pre-amplifier and analyzer. The assembly of the collimator is attached for the passage of limited  $X$ -rays to reach to the detector. The energy dispersive  $X$ -ray spectrometer is utilized as a detector that detects the  $X$ -rays of all energies. The lithium drifted silicon crystal transforms the  $X$ -ray energy to a voltage signal. The voltage signal is then amplified before reaching a multichannel analyzer which converts the signal into the spectrum.

### 3.3.3. Field Emission Scanning Electron Microscopy (*FESEM*)

Scanning electron microscopy technique produces high resolution image of the sample surface. This technique uses primary beam of the focused electrons on to the sample which interacts with the atoms on the sample surface and produces various signals corresponding to the secondary electrons, back-scattered electrons, Auger electrons and generates continuum and characteristic X-rays. The secondary electrons produced from the top few nanometer layers as a result of inelastic collisions and back-scattered electrons due to the elastic collisions are used for the image processing of sample surface.

High energy beam (0.2 - 40 keV) of incident electrons is emitted thermionically from the tungsten filament and is focused by condenser lenses and further passed through the scanning coils to deflect the beam in x and y axes (Figure 3.7). The field emission electron sources are recently being used to produce the high resolution image. In these electron sources high electric field is created at the top of sharp tip to produce a fine electron beam. The secondary electrons emitted from the sample surface are collected by the secondary electron detector which are accelerated towards the scintillator and are further amplified by photomultiplier to produce two dimensional digital images.

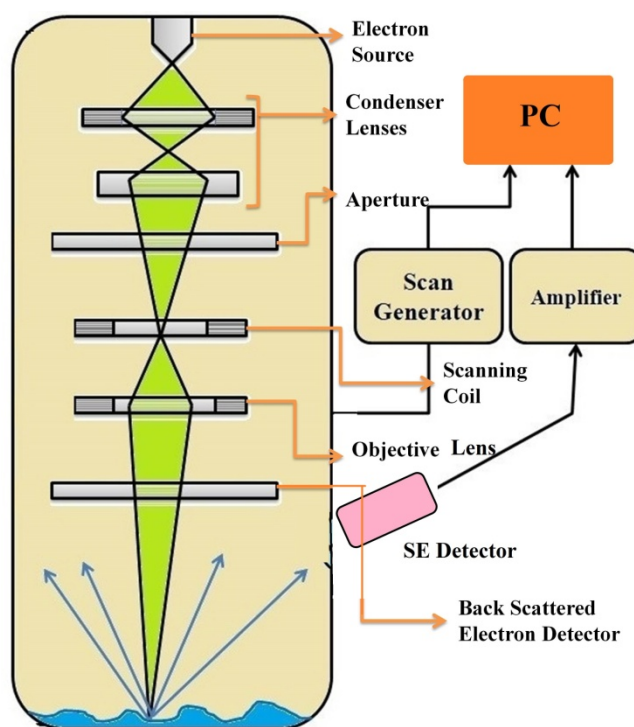


**Figure 3.7** Schematic representation of interaction of primary electron beam with matter.

### 3.3.4. X-ray Photoelectron Spectroscopy (XPS)

X-ray photoelectron spectroscopy (XPS) also called the electron spectroscopy for chemical analysis (ESCA) is one of the techniques of surface analysis used for the elemental identification, quantitative atomic composition determination and the analysis of chemical state information. A monochromatic X-ray beam is incident at sample surface in this technique, which results in the emission of photoelectrons whose energy is characteristic of the elements on the surface of the sample. The ejected electrons are collected as a function of their kinetic energy. Usually, *Mg K $\alpha$*  ( $h\nu=1253.6\text{eV}$ ) and *Al K $\alpha$*  ( $h\nu=1486.6\text{eV}$ ) are sources for X-ray employed for the chemical analysis in this technique. XPS technique is sensitive to surface contaminations with an analysis depth of 10 to 100 monolayers (1-10nm). The sensitivity of the XPS instrument for quantifying the elemental fraction is of the order of ~0.1 at%. It is difficult to detect lighter elements such as H and He using this technique. However, presence of all the elements above Li can be precisely observed using this technique with varying sensitivity of detection for each element. One of the advantages of this method is its capability to detect the contaminations on the sample surface. The contamination present on the surface of the sample can be removed before analysis by the exposure of the sample to  $Ar^+$  ions to sputter away the surface layer.

XPS was invented in the 1950s by Kai Siegbahn while he was working in Uppsala University Sweden and was awarded in 1981 with Nobel Prize for this invention [6]. The underlying operation of XPS makes use of the photoelectric effect. Incident X-ray beam ejects the core electrons from the sample surface as illustrated in figure 3.8 (a). These ejected electrons are collected as a function of their kinetic energy. The kinetic energy ( $E_k$ ) of the emitted photoelectrons is related to the electron binding energy ( $E_B$ ) and the energy of incident X-ray ( $h\nu$ ) using the relation  $E_k = h\nu - E_B - \varphi_{sp}$  where  $\varphi_{sp}$  is the spectrometer work function. The electromagnetic lenses are used to focus the emitted photoelectrons in the path of hemispherical energy analyzer to reach the electron detector. The whole analysis process in XPS has been carried out in the ultra-high vacuum. Figure 3.8 (b) shows the XPS setup model Thermo Scientific NEXSA (IIT Mandi) used for the sample analysis.

The XPS spectra of  $(Ge_2Sb_2Te_5)_{100-x}Sm_x$  thin films in current research work have been recorded in energy steps of 0.1eV and employing the *Al K $\alpha$*  X-ray source. The peak shape and peak position at different binding energies in the spectrum of the XPS core-shell give information about the hybridization and oxidation state of the constituent elements. The

integrated area under the *XPS* core-shell peak can be used to evaluate the material's composition. For the current work, this technique has been utilized to obtain the chemical information and materials composition of  $(Ge_2Sb_2Te_5)_{100-x}Sm_x$  thin films.

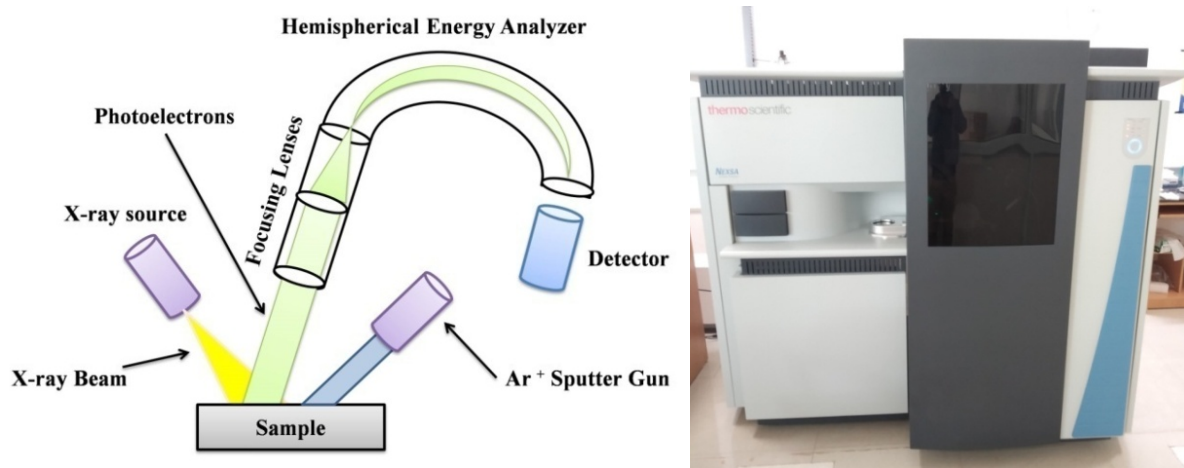


**Figure 3.8 (a).** Schematic illustration of *XPS* (b) Thermo Scientific *NEXSA XPS* setup.

### 3.3.5. Raman Spectroscopy

Raman spectroscopy technique named after the great Indian physicist sir C. V. Raman utilizes the transitions between the vibrational energy states due to the inelastic scattering of photons to obtain information about the molecular structure. In this technique, the monochromatic lasers of wavelengths in the range of ultra-violet, visible and near-infrared are used as excitation sources. The interaction of laser light with the sample surface results in the change in polarizability and creates the induced dipole moment. The light is scattered from the molecules either elastically without the loss of any energy leading to Rayleigh scattering or may scatter inelastically with energy different from the incident light and in that case it is referred to as Raman scattering. In case the energy of the scattered light is lower than the incident light, it is called Stokes shift and if the energy of the scattered light is higher energy than the incident light, it is called an anti-Stokes shift. The loss or gain in energy of Raman scattered light with vibrations provides information about the molecular structure. Figure 3.9 displays the energy level diagram involving the transition between vibrational states of molecules for Rayleigh and Raman scattered light.

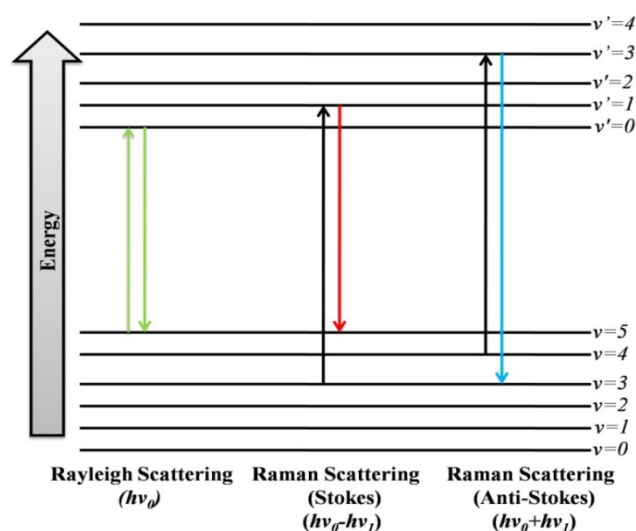


**Figure 3.9** Energy transition in Rayleigh scattering and Raman scattering

The Raman spectrometer consists of several components. The incident laser light is initially passed through the beam splitter placed at 45 degrees in the path of light. The focusing optics is attached to converge the beam of light onto the sample. The scattered light is collected in the notch filters to block the Rayleigh scattered light and permit the Raman scattered light to pass to the monochromator, where the grating is attached to split the scattered light at different frequencies. The charge-coupled device (CCD) is attached to detect the light at different frequencies which are finally processed to the interfaced computer system. Figure 3.10 shows the Raman spectrometer (model Horiba Jobin-Yvon LabRAM HR evolution) used for the present work for the structural analysis of  $Sm$  doped  $Ge_2Sb_2Te_5$  phase change materials at room temperature using  $50\times LWD$  objective ( $NA=0.5$ ) and  $785\text{ nm}$  laser with a spot diameter of  $1.9\mu\text{m}$  and  $1800\text{ grooves/mm}$  grating.



**Figure 3.10** Raman spectrometer model Horiba Jobin-Yvon LabRAM HR evolution (*IIT Mandi*) used for analysis.

### 3.3.6. Fourier-Transform Infrared Spectroscopy (*FTIR*)

Fourier-transform infrared spectroscopy (*FTIR*) is also used for the molecular structural analysis. *FTIR* is an absorption spectroscopy technique that works on the principle of absorption of incident *IR* radiation by the sample and the transmitted radiations provide information about the molecular vibrations. The fundamental difference between the *FTIR* and Raman spectroscopy is that the absorption of *IR* radiation in the sample produces the dipole moments in *FTIR* in contrast to Raman spectroscopy which is based upon the change in polarizability.

The beam of *IR* is collimated onto the Michelson interferometer where the beam splitter divides it into two parts. One half is passed on to the fixed mirror, while the other half of the beam is processed to the movable mirror. The light gets reflected from both the mirrors and combines to give constructive and destructive interference pattern. The light then passes through the sample where some of the *IR* radiation is absorbed by the sample. The transmitted light is detected and then processed to the computer system.

The vibrational properties of the *Sm* doped  $Ge_2Sb_2Te_5$  samples have been measured by using the Vertex 80 Bruker with Hyperion 3000 microscope *FTIR* (IIT Bombay) in the far-*IR* region from  $30\text{ cm}^{-1}$  to  $300\text{ cm}^{-1}$  at room temperature. The *FTIR* measurements have been performed over the pellets of as-prepared samples by using the polyethylene utilizing the hydraulic press.

### 3.3.7. *UV-Vis-NIR* Spectroscopy

*UV-Vis-NIR* spectroscopy involves the measurement of the absorption of incident light by the sample. This method is based on the linear relationship between the path length, concentration of the solute and the absorbance in accordance to Beer-Lambert law. This spectroscopy technique utilizes the light in ultraviolet, visible and near-infrared regions to analyze the solid, liquid and gaseous samples. The absorption of light excites the electrons between the bonding and anti-bonding orbitals. *UV-Vis-NIR* spectrophotometer measures the intensity of transmitted or reflected light from the sample. The intensity of light after passing through the sample with respect to the reference beam is used to evaluate the transmittance. Figure 3.11 shows the double beam spectrophotometer block diagram where a single beam split up into two beams. One half of the splitted beam is passed through the reference and the

other half is allowed to pass through the sample. The ratio of intensities of two beams is used for the measurement of transmittance.

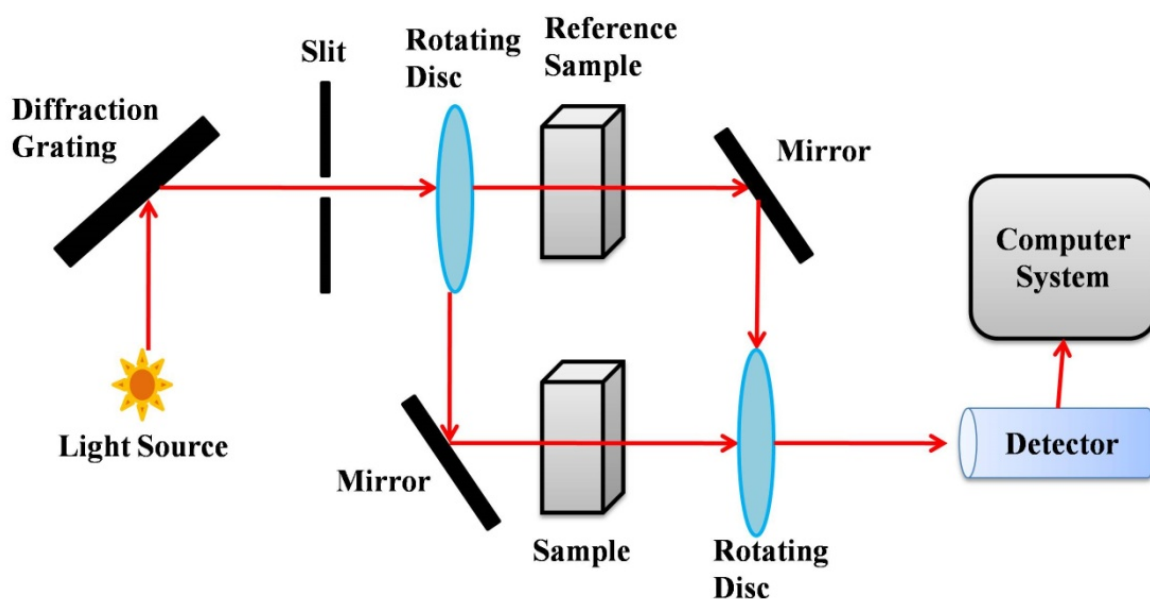


**Figure 3.11** Block diagram of *UV-Vis-NIR* spectrophotometer.

In the current work, the *UV-Vis-NIR* spectrophotometer model Perkin Elmer Lambda 750 (Figure 3.12) has been employed for the optical analysis of  $(Ge_2Sb_2Te_5)_{100-x}Sm_x$  thin films. The  $(Ge_2Sb_2Te_5)_{100-x}Sm_x$  thin films transmission spectra have been recorded in the  $600\text{ nm}$  to  $2700\text{ nm}$ . The thin films on absorbance display oscillating transmittance spectra on account of interference. The thickness of film and optical constants like index of refraction ( $n$ ), and absorption coefficient ( $\alpha$ ) have been evaluated employing Swanepoel method [7]. Figure 3.12 displays the interference fringe pattern in the transmission spectra of deposited thin films. The upper envelope ( $T_M$ ) and lower envelope ( $T_m$ ) corresponds to the transmission maximum and transmission minimum respectively. The evaluation of complex refractive index ( $n^* = n - ik$ ) for its real and imaginary parts has been performed from the fringe pattern in transparent and weak absorption area. The glass substrate refraction ( $s$ ) along with the refractive index ( $n$ ) are associated to  $T_M$  and  $T_m$  in the transparent region where  $\alpha = 0$  through the expressions [8]

$$T_M = \frac{2s}{(s^2+1)} \quad \text{and} \quad T_m = \frac{4n^2s}{n^4+n^2(s^2+1)+s^2} \quad (3.4)$$



**Figure 3.12** *UV-Vis-NIR* spectrophotometer (model Perkin Elmer Lambda 750) used to measure optical transmission.

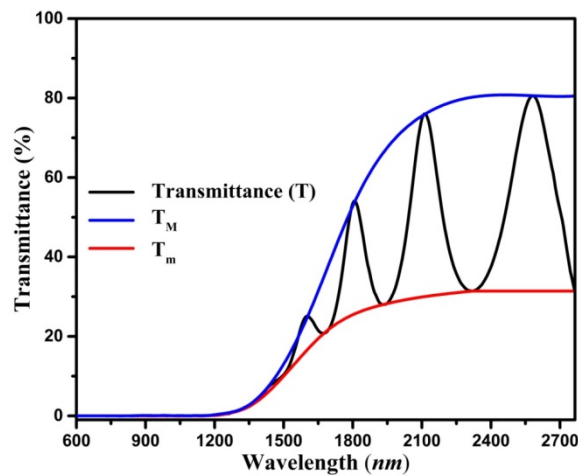


**Figure 3.13** Transmittance spectra of thin films with upper envelope ( $T_M$ ) and lower envelope ( $T_m$ ) and transmittance of a glass substrate.

The dependence of  $T_M$  and  $T_m$  on  $n$  and  $s$  in weak and medium absorption regions where  $\alpha \neq 0$  can be expressed as

$$n = [N + (N^2 - s^2)^{1/2}]^{1/2} \quad (3.5)$$

such that

$$N = 2s \left( \frac{T_M - T_m}{T_M T_m} \right) + \frac{s^2 + 1}{2}$$

The thickness of thin films ( $d$ ) can be obtained by utilizing the refractive index and wavelength values at adjacent extremes using the relation [7]

$$d = \frac{\lambda_1 \lambda_2}{2(\lambda_1 n_2 - \lambda_2 n_1)} \quad (3.6)$$

where  $n_2$  and  $n_1$  are the refractive index values corresponding to the wavelengths  $\lambda_2$  and  $\lambda_1$  respectively. The interference fringes in the transmission spectrum follow the equation

$$2nd = m\lambda \quad (3.7)$$

where  $m$  represents the order number that has integral values in case of transmission maximum and half-integral values in case of transmission minimum. Cauchy relation  $\left(n = b + \frac{a}{\lambda^2}\right)$  has been employed to evaluate the refractive index at the absorption region by extrapolating the values of  $n$  with  $\lambda$  obtained in the transparent region. The calculation of absorption coefficient ( $\alpha$ ) has been performed using the relation [9]

$$\alpha = \frac{1}{d} \ln \left[ \frac{(1-R_1)(1-R_2)(1-R_3)}{T} \right] \quad (3.8)$$

where  $R_1 = \left(\frac{n-n_0}{n+n_0}\right)^2$ ,  $R_2 = \left(\frac{n-s}{n+s}\right)^2$  and  $R_3 = \left(\frac{s-n_0}{s+n_0}\right)^2$  represent the reflection coefficients at air-film, film-substrate and substrate-air interfaces respectively. The refractive index of air ( $n_0$ ) has been taken as unity for the evaluation of  $\alpha$ . The values of  $\alpha$  have been used to obtain the extinction coefficient ( $k(\lambda)$ ) using the equation

$$k = \left(\alpha\lambda/4\pi\right) \quad (3.9)$$

The band tail extent or Urbach energy ( $E_u$ ) obey the exponential relation between  $\alpha$  and the incident photon energy  $h\nu$  for  $\alpha \leq 10^4 \text{ cm}^{-1}$  and is expressed as [10]

$$\alpha = \alpha_0 \exp\left(\frac{h\nu}{E_u}\right) \quad (3.10)$$

where  $\alpha_0$  is the pre-exponential factor. The high absorption region where  $\alpha \geq 10^4 \text{ cm}^{-1}$  has been used to obtain the value of optical band gap ( $E_g$ ) employing Tauc relation [11]

$$\alpha(h\nu) = B(h\nu - E_g)^r \quad (3.11)$$

where  $B$  is the order parameter or transition probability. The  $r = 2$  value represents the indirect allowed transitions,  $r = 1/2$  value indicates the direct allowed transition. Wemple-DiDomenico (WDD) single oscillator model correlates the refractive index dispersion to single oscillator energy ( $E_0$ ) and dispersion energy ( $E_d$ ) through the relation [12]

$$(n^2 - 1) = \frac{E_0 E_d}{(E_0^2 - E^2)} \quad (3.12)$$

where  $E$  is the energy of incident photons. The use of  $E_0$  and  $E_d$  values further facilitate the evaluation of the static refractive index ( $n_0$ ) and static dielectric constant ( $\epsilon_L$ ) using the relation [13]

$$\epsilon_L = n_0^2 = \left(1 + \frac{E_d}{E_0}\right) \quad (3.13)$$

The dielectric constant on account of the electronic contribution can be assessed using the calculation of the high-frequency dielectric constant ( $\epsilon_\infty$ ) obtained using the relation [14]

$$n^2 = \epsilon_\infty - \left(\frac{e^2}{4\pi^2\epsilon_0 c^2}\right) \left(\frac{N}{m^*}\right) \lambda^2 \quad (3.14)$$

where  $e$  represents the electronic charge,  $\epsilon_0$  is the free space permittivity while  $c$  is light velocity. The ratio  $\left(\frac{N}{m^*}\right)$  is free carrier concentration to effective mass ratio which has been used to evaluate the plasma frequency ( $\omega_{plasma}$ ) [14]

$$\omega_{plasma}^2 = \left\{ \left(\frac{e^2}{4\epsilon_0\epsilon_\infty}\right) \left(\frac{N}{m^*}\right) \right\} \quad (3.15)$$

### 3.3.8. Differential Scanning Calorimetry (DSC)

Calorimetry is used for measurement of the thermal parameters for material by correlating the enthalpy changes of different thermodynamic processes at a particular temperature. Differential scanning calorimetry (*DSC*) is one of the popular thermal analysis techniques which measure the change in physical properties of materials as a function of temperature as well as time. Heat flow as a function of temperature is analyzed in this technique to measure the material's transitions and processes involved. *DSC* can be broadly divided into two categories: heat flux *DSC* and power compensated *DSC*. In heat flux *DSC* instruments, equal heat is supplied in a linear heating rate to the reference pan and sample pan through the thermoelectric disc inside the furnace. The thermal equilibrium is maintained between the reference pan and sample pan through the heat transfer bridge between them. The amount of heat flow through the bridge between the sample pan and reference pan is measured and is recorded as a function of temperature and time. In power compensated *DSC*, reference pan as well as sample pan are placed in separate furnaces. The amount of heat supplied to the sample with respect to the reference sample to maintain the same temperature in both the furnaces is measured. The heat amount essential to raise the temperature of a material is specified by its specific heat capacity.

The thermal properties of  $(Ge_2Sb_2Te_5)_{100-x}Sm_x$  samples have been analyzed using the *DSC EXSTAR TG/DTA 6300* model in the current research work. The non-isothermal *DSC* analysis of samples has been carried out at the heating rate of  $10K/min$  and in the temperature range of  $35^\circ C$  to  $1000^\circ C$ . For *DSC* analysis, approx  $5mg$  sample has been used in an alumina pan in an inert atmosphere maintained with the flow of Argon at the rate of  $200 ml/min$ .

Following relations have been used for the analysis of thermal properties.

The dependence of crystallization fraction ( $\chi$ ) on crystallization activation energy ( $E_c$ ) has been expressed by Henderson [15], [16]

$$\frac{d[\ln(-\ln(1-\chi))]}{dT^{-1}} = -\frac{E_c}{k} - 2nT \left[ 1 - \frac{nkT}{E_c + 2nkT} \right] \quad (3.16)$$

where  $T$  is the exothermic peak temperature,  $k$  is the Boltzmann constant and  $n$  is the Avrami exponent. The dependence of Avrami exponent ( $n$ ) on  $E_c$  can be expressed through the relation [15], [16]

$$\ln\left(\frac{d\chi}{dt}\right) = \ln\left(nK_0^{\frac{1}{n}}f(\chi)\right) - \frac{E_c}{nkT} \quad (3.17)$$

where  $K_0$  is constant whereas  $f(\chi) = (1 - \chi)[-\ln(1 - \chi)]^{(n-1)/n}$

Matusita's equation presents the dependence of and heating rate ( $\alpha$ ), crystallization fraction ( $\chi$ ) on  $E_c$  [17].

$$\ln[-\ln(1 - \chi)] = -n\ln(\alpha) - 1.052m \left(\frac{E_c}{RT}\right) + const. \quad (3.18)$$

where  $m$  describes the crystal growth kinetics of materials.

### 3.3.9. Electrical Measurements

Electrical measurements of  $(Ge_2Sb_2Te_5)_{100-x}Sm_x$  thin films have been performed at room temperature using the Keithley 6487 electrometer. Two probe method has been adopted to measure the resistivity of amorphous  $(Ge_2Sb_2Te_5)_{100-x}Sm_x$  phase change materials. The voltage source of  $500V$  and digital pico-ammeter with a maximum current limit of  $2.5mA$  has been used for current-voltage ( $I-V$ ) measurements of  $(Ge_2Sb_2Te_5)_{100-x}Sm_x$  thin films. The  $I-V$  measurements have been carried out for *GST* thin films added with *Sm* in  $0-100V$  voltage range in steps of  $0.5V$ . Figure 3.14 shows the electrometer (Keithley 6487) used for the  $I-V$  studies of prepared  $(Ge_2Sb_2Te_5)_{100-x}Sm_x$  thin films. The coplanar geometry has been adopted

for  $I$ - $V$  measurements of thin films as has been shown in figure 3.15. The high purity silver paste has been used to make the electrodes on thin films and the distance between two electrodes has been maintained  $2\text{mm}$ . The temperature dependent electrical measurements of  $(\text{Ge}_2\text{Sb}_2\text{Te}_5)_{100-x}\text{Sm}_x$  thin films have also been performed in coplanar geometry from  $20^\circ\text{C}$  to  $200^\circ\text{C}$  using Keithley electrometer (model No: 2611) with maximum current limit of  $100\text{mA}$ .



**Figure 3.14** Keithley 6487 electrometer used for the electrical measurements of prepared samples.

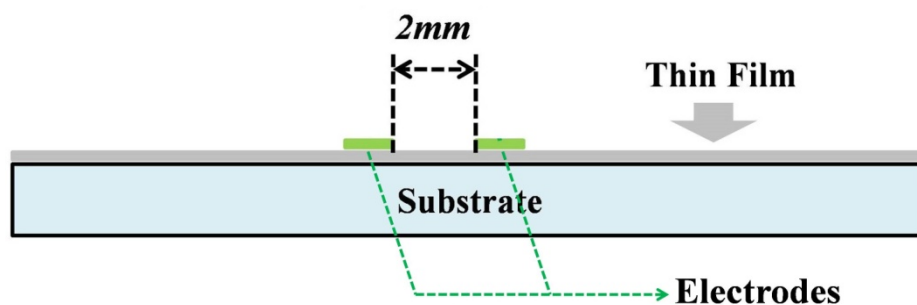


**Figure 3.15** Schematic representation of co-planar geometry for the measurements of electrical properties of thin films.

## References

- [1] A. Hrubý, “Evaluation of glass-forming tendency by means of DTA,” *Czechoslov. J. Phys.*, vol. 22, no. 11, pp. 1187–1193, Nov. 1972.
- [2] T. A. Vilgis, “Strong and fragile glasses: A powerful classification and its consequences,” *Phys. Rev. B*, vol. 47, no. 5, pp. 2882–2885, Feb. 1993.
- [3] M. Saad and M. Poulain, “Glass Forming Ability Criterion,” *Mater. Sci. Forum*, vol. 19–20, pp. 11–18, Jan. 1987.
- [4] A. V. Kolobov, Y. Saito, P. Fons, and M. Krbal, “Structural Metastability in Chalcogenide Semiconductors: The Role of Chemical Bonding,” *Phys. status solidi*, vol. 257, no. 11, p. 2000138, Nov. 2020.
- [5] B. D. Cullity, *Elements of X-ray Diffraction*, 2nd ed. Phillippines, 1978.
- [6] K. Siegbahn and K. Edvarson, “ $\beta$ -Ray spectroscopy in the precision range of 1 : 105,” *Nucl. Phys.*, vol. 1, no. 8, pp. 137–159, Jan. 1956.
- [7] R. Swanepoel, “Determination of the thickness and optical constants of amorphous silicon,” *J. Phys. E.*, vol. 16, no. 12, pp. 1214–1222, Dec. 1983.
- [8] R. Swanepoel, “Determination of surface roughness and optical constants of inhomogeneous amorphous silicon films,” *J. Phys. E.*, vol. 17, no. 10, pp. 896–903, Oct. 1984.
- [9] A. Ganjoo and R. Golovchak, “Computer program PARAV for calculating optical constants of thin films and bulk materials: Case study of amorphous semiconductors,” *J. Optoelectron. Adv. Mater.*, vol. 10, no. 6, pp. 1328–1332, 2008.
- [10] F. Rao, Z. Song, Y. Cheng, M. Xia, K. Ren, L. Wu, B. Liu and S. Feng “Investigation of changes in band gap and density of localized states on phase transition for  $\text{Ge}_2\text{Sb}_2\text{Te}_5$  and  $\text{Si}_{3.5}\text{Sb}_2\text{Te}_3$  materials,” *Acta Mater.*, vol. 60, no. 1, pp. 323–328, Jan. 2012.
- [11] J. Tauc, R. Grigorovici, and A. Vancu, “Optical Properties and Electronic Structure of Amorphous Germanium,” *Phys. status solidi*, vol. 15, no. 2, pp. 627–637, 1966.
- [12] S. H. Wemple, “Refractive-Index Behavior of Amorphous Semiconductors and

- Glasses,” *Phys. Rev. B*, vol. 7, no. 8, pp. 3767–3777, Apr. 1973.
- [13] S. H. Wemple and M. DiDomenico, “Behavior of the Electronic Dielectric Constant in Covalent and Ionic Materials,” *Phys. Rev. B*, vol. 3, no. 4, pp. 1338–1351, Feb. 1971.
- [14] A. S. Hassanien and I. Sharma, “Optical properties of quaternary a-Ge<sub>15-x</sub>Sb<sub>x</sub>Se<sub>50</sub>Te<sub>35</sub> thermally evaporated thin-films: refractive index dispersion and single oscillator parameters,” *Optik (Stuttg.)*, vol. 200, no. July 2019, p. 163415, Jan. 2020.
- [15] D. W. Henderson, “Experimental analysis of non-isothermal transformations involving nucleation and growth,” *J. Therm. Anal.*, vol. 15, no. 2, pp. 325–331, Apr. 1979.
- [16] D. W. Henderson, “Thermal analysis of non-isothermal crystallization kinetics in glass forming liquids,” *J. Non. Cryst. Solids*, vol. 30, no. 3, pp. 301–315, Jan. 1979.
- [17] K. Matusita, T. Komatsu, and R. Yokota, “Kinetics of non-isothermal crystallization process and activation energy for crystal growth in amorphous materials,” *J. Mater. Sci.*, vol. 19, no. 1, pp. 291–296, Jan. 1984.



## Chapter 4

# Structural Investigation of $(Ge_2Sb_2Te_5)_{100-x}Sm_x$ Bulk Alloys and Thin Films

- **Sanjay Kumar** and Vineet Sharma, “Structural transition on doping rare earth *Sm* to  $Ge_2Sb_2Te_5$  phase change material,” **Journal of Alloys and Compounds**, vol. 877, p. 160246, May 2021.
- **Sanjay Kumar** and Vineet Sharma, “Improvement in thermal stability and crystallization mechanism of *Sm* doped  $Ge_2Sb_2Te_5$  thin films for phase change memory applications,” **Journal of Alloys and Compounds**, vol. 893, p. 162316, Feb. 2022.



#### 4.1. Introduction

Next-generation memory technology utilizes  $Ge_2Sb_2Te_5$  (*GST*) phase change material to be a leading contender for applications in memory devices [1]–[3]. The main concept for storage of data in phase change (*PC*) memories is based upon switching between the non-crystalline (disordered) and crystalline (ordered) phases of *GST* repeatedly. The amorphous phase of *GST* can be transformed to *fcc* crystalline phase, which can be further transformed to the hexagonal phase on annealing.

The phase change mechanism of *GST* is explained by utilizing the umbrella-flip model for the amorphous to *fcc* phase transformation. According to this model, the amorphous to rocksalt cubic phase transition of *GST* is the result of modification in the *Ge* atom local structure from tetrahedral configuration to octahedral configurations. The *Te* atoms occupy the *4a* anionic sites of rocksalt cubic crystal structure of *GST* whereas *Ge*, *Sb* atoms along with 20% vacant sites take the positions at the *4b* cationic sites [4]. The annealing above *fcc* crystallization temperature, results in *GST* making a transition to the hexagonal phase. The *fcc* → hexagonal phase transition leads to the occupation of vacant sites by *Te* atoms and creating *Te–Te* bonds. The transformation of *fcc* to hexagonal phase induces the shear strain on square rings of *Ge–Te–Sb–Te*- and consequently transforms them to the shape of rhombus and also alters the bonding environment of *Sb* [5]. The phase transition of *GST* plays vital part to affect storage devices performance by inducing a change in local structure. The crystallization speed and thermal stability enhancement in *GST* is required for improved device performance.

The *GST* phase change material use in commercial device applications is also limited on account of resistance drift in the amorphous state with device aging. Understanding the relaxation mechanism of amorphous structures is imperative to improve the resistance drift of *GST* for faster device operation [6]. Amorphous *GST* matrix constitutes the large fraction of homopolar *Sb–Sb*, *Ge–Sb* and *Ge–Ge* “wrong bonds” contained in *Ge* tetrahedra and executes the  $\beta$ -relaxations causing the resistance drift in less constrained regions [1]. The suppression of  $\beta$ -relaxation by adding suitable impurity elements into *GST* can be implemented to diminish resistance drift. In amorphous *GST*  $1/3^{rd}$  of *Ge* atoms have been observed to be present in the tetrahedral geometry which comprises of the *Ge–Sb*, *Sb–Sb* and *Ge–Ge* bonds exhibiting the aging effects [6]. Reducing the fraction of tetrahedral *Ge* by substituting *Sn* in *GeTe* has been observed as the key for reducing the resistance drift

coefficient and mid-gap charged states [7]. Doping *GST* with a suitable impurity element with non-metallic, metallic, and semiconducting nature has been reported in the literature for improving its applicability in storage devices [8]–[14]. The rare earths possess interesting bond formation capabilities with *GST* because of their comparatively lower electronegativity than *Ge*, *Sb* and *Te*, forming stronger heteropolar bonds and rigid network structure in *GST* [15]. Rare earths also have a bigger atomic radius and own unique luminescence, electrochemical and magnetic properties. The crystallization mechanism and thermal stability improvement in *GST* by substituting rare earths has been reported in numerous studies [15], [16].

This chapter reports the impact of *Sm* doping on structural features of *GST*. X-Ray Diffraction (*XRD*) measurements for  $(Ge_2Sb_2Te_5)_{100-x}Sm_x$  bulk alloys prepared by melt-quenching have been performed for the investigation of crystal structure. *XRD* spectra of as-prepared samples reveal the nano-crystalline nature. The *XRD* spectra of  $(Ge_2Sb_2Te_5)_{100-x}Sm_x$  bulk alloys have been used for crystal structure analysis. The phase quantification in *XRD* spectra of *Sm* added *GST* bulk alloys has been performed through the Rietveld refinement analysis. The evaluation of lattice parameters for  $(Ge_2Sb_2Te_5)_{100-x}Sm_x$  bulk alloys has been carried out. The chemical analysis of *Sm* added *GST* has been performed using *FTIR* and Raman spectroscopy to analyze the consequences of addition of *Sm* to *GST* for switching mechanism. The  $(Ge_2Sb_2Te_5)_{100-x}Sm_x$  alloy thin films have been deposited by employing the thermal evaporation method. The confirmation of the amorphous nature of the  $(Ge_2Sb_2Te_5)_{100-x}Sm_x$  thin films has been done through the *XRD* spectra. The nature of chemical bonding in  $(Ge_2Sb_2Te_5)_{100-x}Sm_x$  thin films has been investigated employing X-Ray Photoelectron Spectroscopy (*XPS*). The core-level *XPS* spectra of *Ge 3d*, *Sb 3d*, *Te 3d* and *Sm 3d* have been used for the compositional analysis and to investigate the effect of *Sm* content in thin films of  $(Ge_2Sb_2Te_5)_{100-x}Sm_x$  for *PC* memory applications.

## 4.2. Experimental Details

### 4.2.1. Sample Preparation

The preparation of  $(Ge_2Sb_2Te_5)_{100-x}Sm_x$  ( $x = 0, 0.2, 0.4, 0.6, 0.8, 1.0, 1.2$ ) alloys has been carried out using the melt-quenching method described in section 3.2.1. The powder samples of  $(Ge_2Sb_2Te_5)_{100-x}Sm_x$  obtained by crushing solid ingot employing the granite

mortar and pestle have been used for the deposition of  $(Ge_2Sb_2Te_5)_{100-x}Sm_x$  thin films using the thermal evaporation unit (*HINDHIVAC 12A4D*) with more details in section 3.2.3.

#### 4.2.2. Characterization Details

Shimadzu (*XRD-6000*) X-Ray Diffractometer has been employed to obtain the structural information of  $(Ge_2Sb_2Te_5)_{100-x}Sm_x$  bulk alloys prepared through melt-quenching. *XRD* measurements of  $(Ge_2Sb_2Te_5)_{100-x}Sm_x$  alloys have been performed at room temperature in Bragg-Brentano geometry employing *Cu K $\alpha$*  as source of *X*-rays. FullProf Suite software has been used to carry out Rietveld refinement for phase quantification of *Sm* doped *GST* alloys. Raman spectroscopic analysis of  $(Ge_2Sb_2Te_5)_{100-x}Sm_x$  alloys have been performed using Horiba Jobin-Yvon LabRAM HR evolution spectrometer using laser excitation at the wavelength *785nm*. The Raman spectra of *Sm* doped *GST* alloys have been analyzed in the range  $20\text{ cm}^{-1}$  to  $400\text{ cm}^{-1}$  by means of the diffraction grating with grooves density of *1800 grooves/mm*. *FTIR* measurements have been performed employing Bruker Vertex 80 along with Hyperion 3000 microscope to analyze the crystallinity and overall insight of molecular structures of  $(Ge_2Sb_2Te_5)_{100-x}Sm_x$  alloys. The thin films of  $(Ge_2Sb_2Te_5)_{100-x}Sm_x$  deposited through the vacuum evaporation technique has been examined for the confirmation of amorphous nature utilizing the *X*-ray diffractometer (*XRD*, *PANalytical*, *X'Pert*). The X-Ray Photoelectron Spectroscopy (*XPS*) (model Thermo Scientific *NEXSA*) equipped with a monochromatic *Al K $\alpha$*  *X*-ray source has been employed to examine the chemical compositions and bonding nature in thin films of *Sm* incorporated *GST*. *Ar*<sup>+</sup> ion sputtering on surface of thin films has been carried out to remove surface contaminations with an exposure time of the *20s*.

### 4.3. Results and Discussion

#### 4.3.1 Characterization of $(Ge_2Sb_2Te_5)_{100-x}Sm_x$ Bulk alloys

As-prepared bulk alloys of  $(Ge_2Sb_2Te_5)_{100-x}Sm_x$  have been studied using *XRD* for obtaining information about crystal structure. The phase quantification and lattice parameter evaluation has been executed through the Rietveld refinement of nano-crystalline *XRD* spectra for  $(Ge_2Sb_2Te_5)_{100-x}Sm_x$  alloys. Raman spectroscopy and *FTIR* spectroscopy has been employed to examine the impact of *Sm* doping on local structures of *GST*.

### 4.3.1.1 X-Ray Diffraction (XRD) and Rietveld Refinement Analysis

Figure 4.1 illustrates the XRD spectra for bulk alloys of  $(Ge_2Sb_2Te_5)_{100-x}Sm_x$  ( $x = 0, 0.2, 0.4, 0.6, 0.8, 1.0, 1.2$ ). The diffraction pattern reveals the nano-crystalline character of as-prepared samples. The presence of diffraction peaks in as-prepared samples (Figure 4.1) is due to the formation of nano-crystallites formed during melt-quenching as a consequence of the poor glass-forming ability of GST. This is because of the high rigidity and large value of average coordination of GST at the chemical threshold of 2.67 [17]. The small crystal nuclei formed through the melt-quenching process initiate the crystallization in GST phase change materials.

The Rietveld refinement has been performed for the quantification of crystalline phase present in as-quenched samples utilizing FullProf Suite software. The diffraction peaks (111), (200), (220), (311), (222), (400), (420) and (422) present in the  $(Ge_2Sb_2Te_5)_{100-x}Sm_x$  XRD spectra correspond to  $Fm-3m$  space group with rock salt FCC crystal structure having Te atoms and Ge, Sb and 20% of vacant sites occupying the anionic sites 4a and cationic sites 4b respectively. Apart from the presence of peaks of  $Fm-3m$  space group the additional peaks (102), (103), (014), (106), (112) and (009) has been also identified in the  $(Ge_2Sb_2Te_5)_{100-x}Sm_x$  XRD spectra which have been identified with the ( $P-3m1$ ) hexagonal phase major peaks. The appearance of peaks of  $Fm-3m$  and  $P-3m1$  space groups in  $(Ge_2Sb_2Te_5)_{100-x}Sm_x$  alloys XRD spectra signify the existence of multiple phases in as-prepared samples. The presence of any other phase on Sm incorporation in the  $(Ge_2Sb_2Te_5)_{100-x}Sm_x$  XRD spectra has not been observed in figure 4.1. The shift in the most dominant peak  $(103)_{HEX}$  of the hexagonal phase for  $(Ge_2Sb_2Te_5)_{100-x}Sm_x$  has been analyzed with Sm content and displayed through the inset of figure 4.1. The shift of (103) peak toward lower  $2\theta$  value with Sm content can also be established from an increase in the  $d_{103}$ -spacing with Sm addition as shown in figure 4.2. However, no remarkable shift of the main prominent peak  $(200)_{FCC}$  for the FCC phase on Sm addition has been found. The fractional change in fcc and hexagonal phase in GST doped with Sm can be examined through the evaluation of peak intensity ratio ( $I_{103/200}$ ) of  $(103)_{HEX}$  and  $(200)_{FCC}$  peaks with Sm content (Table 4.1). The ratio increases with Sm addition till  $x = 0.4$  indicating comparatively larger fraction of the hexagonal phase as compared to the FCC phase. On addition of Sm beyond  $x = 0.4$  the  $(200)_{FCC}$  peak intensity dominates over  $(103)_{HEX}$  peak.

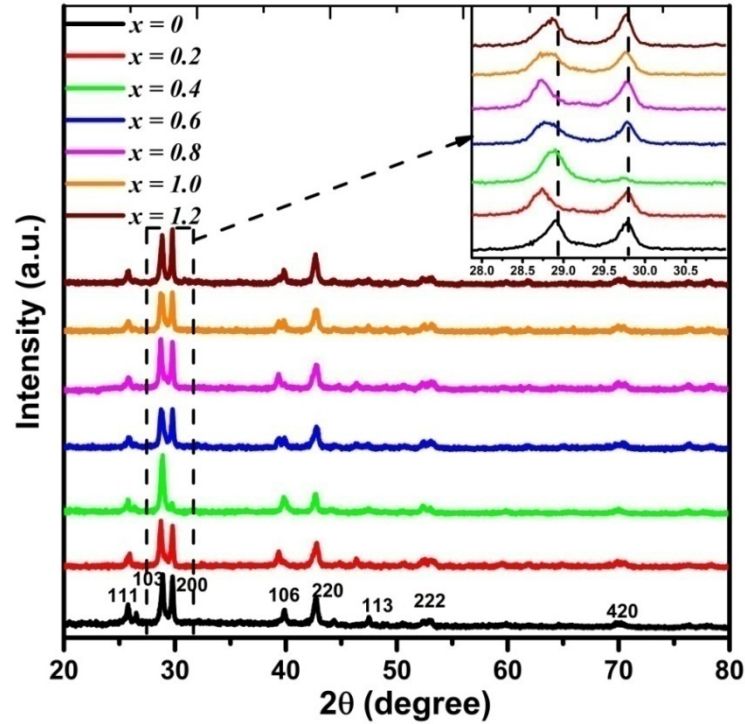


Figure 4.1. XRD spectra of  $(Ge_2Sb_2Te_5)_{100-x}Sm_x$  alloys.

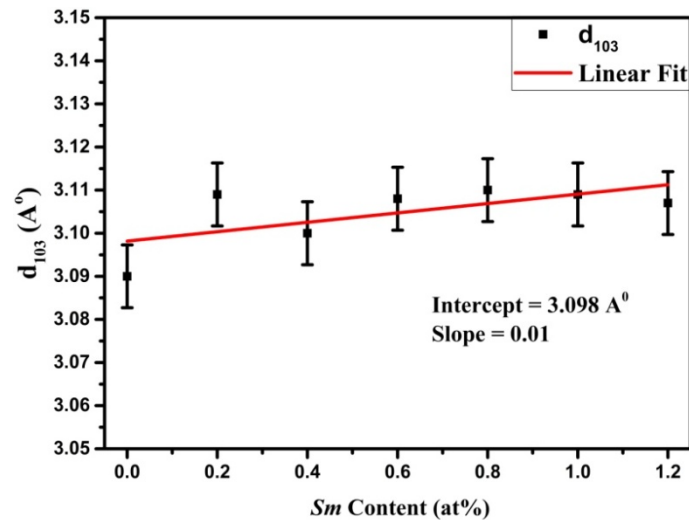


Figure 4.2. Plot of  $d_{103}$ -spacing of  $(Ge_2Sb_2Te_5)_{100-x}Sm_x$  alloys with  $Sm$  content.

The  $W$ - $H$  plot has been employed to calculate the crystallite size and value of strain for  $Sm$  doped  $GST$ . The Scherrer equation (3.2) uses the dependence of crystallite size on size broadening ( $\beta_L$ ). The collective effect of size broadening ( $\beta_L$ ) and strain broadening ( $\beta_s$ ) can be studied using the  $W$ - $H$  method. The equation (3.3) expresses the linear dependence of line broadening on crystallite size ( $D_{hkl}$ ) and the value of strain ( $\epsilon$ ). The evaluation of crystallite size ( $D_{hkl}$ ) and values of strain for  $(Ge_2Sb_2Te_5)_{100-x}Sm_x$  alloys has been carried out

employing the  $\beta\cos\theta$  vs  $4\sin\theta$  plot's linear fitting. The intercept on the y-axis provides the crystallite size ( $D_{hkl}$ ) whereas the value of strain is obtained through the slope of the straight line using equation (3.3).

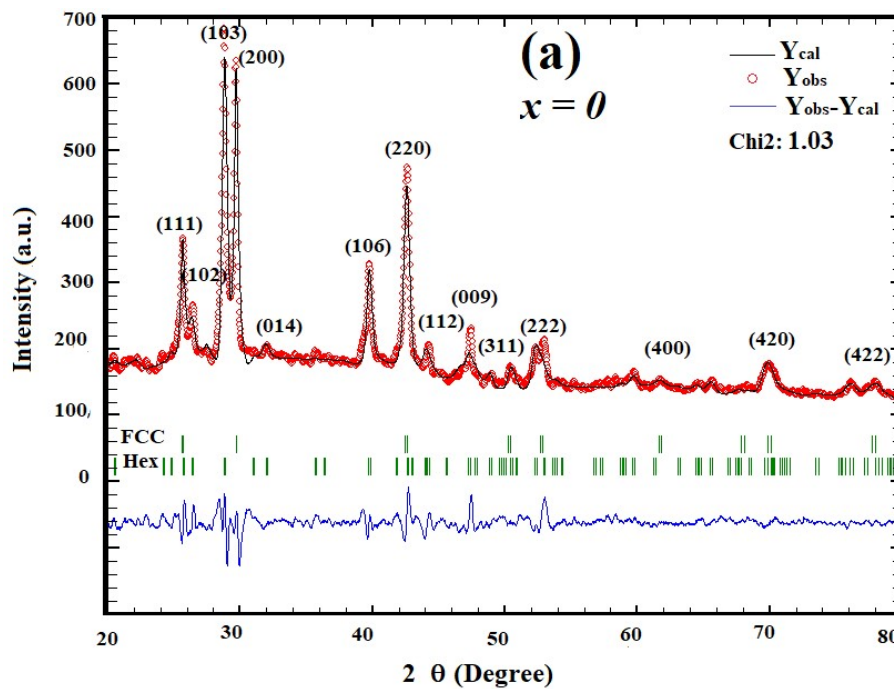
The decrease in  $d_{106}$  values up to addition of  $x = 0.4$  Sm and rise in  $d_{106}$  value for  $x > 0.4$  Sm concentration have been summarized in table 4.1. The Scherrer formula has been utilized to obtain the value of  $D_{106}$  crystallite size which shows the decrease with Sm concentration up to  $x = 0.4$  (Table 4.1). The  $D_{106}$  values increases beyond  $x > 0.4$  at% Sm content. The values of strain and crystallite size obtained from the  $W-H$  plot have been presented in table 4.1 which shows increment in crystallite size and strain values till  $x = 0.4$  at% Sm and reduction beyond addition of  $x > 0.4$  at% Sm. The decline in  $D_{106}$  values and increase in crystallite size computed from  $W-H$  equation (3.3) up to addition of  $x = 0.4$  at% Sm can be described through the obtained values of strain which also show an increase till addition of  $x = 0.4$  at% Sm. The reduction in the value of strain for  $x > 0.4$  at % is on account of decline in crystallite size computed through  $W-H$  plot.

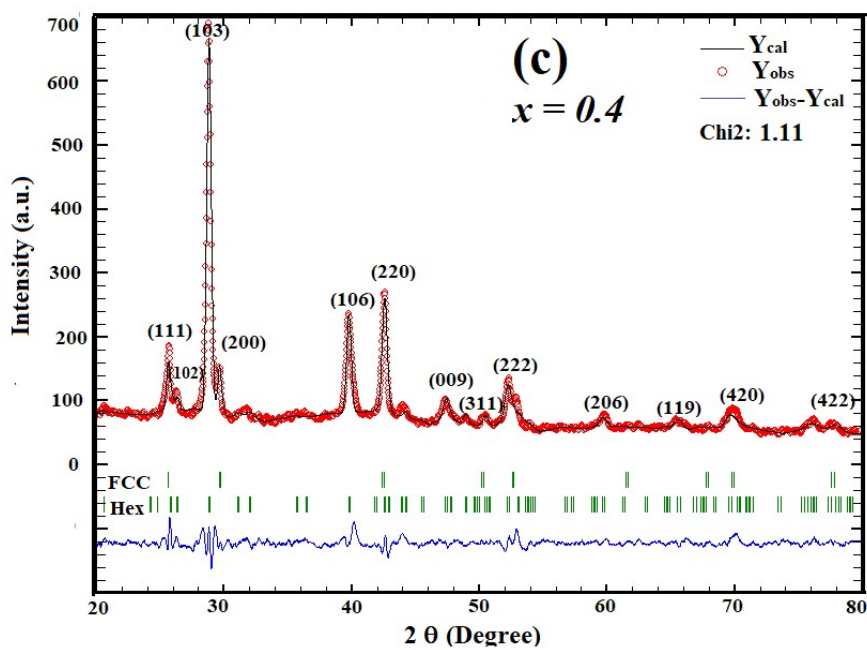
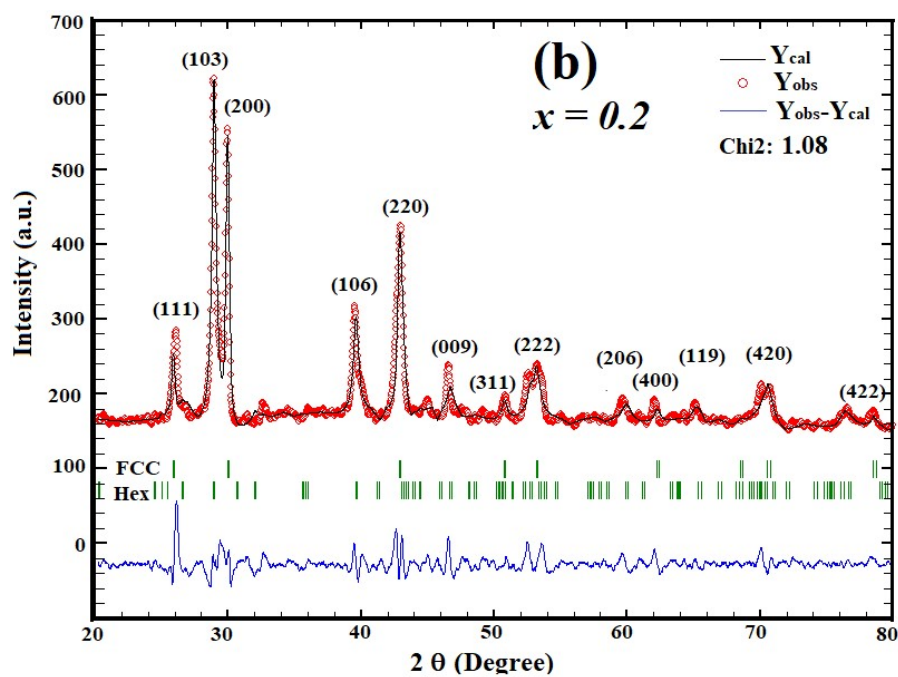
$x$	<b>d-spacing</b>	<b>Crystallite Size</b>		<b>Strain (<math>\epsilon</math>)</b>	<b>I<sub>103/200</sub></b>
	<b><math>d_{106}</math> (Å)</b>	<b>Scherrer <math>D_{106}</math> (nm)</b>	<b>W-H plot (nm)</b>		
0	2.294	28.84	40.16	0.00232	1.03
0.2	2.289	26.36	54.35	0.00649	1.13
0.4	2.261	20.88	67.11	0.00962	5.62
0.6	2.261	24.65	41.67	0.00692	1.01
0.8	2.262	24.85	34.84	0.00163	1.00
1.0	2.263	25.48	30.58	0.0011	0.95
1.2	2.265	30.17	28.82	-0.0144	0.93

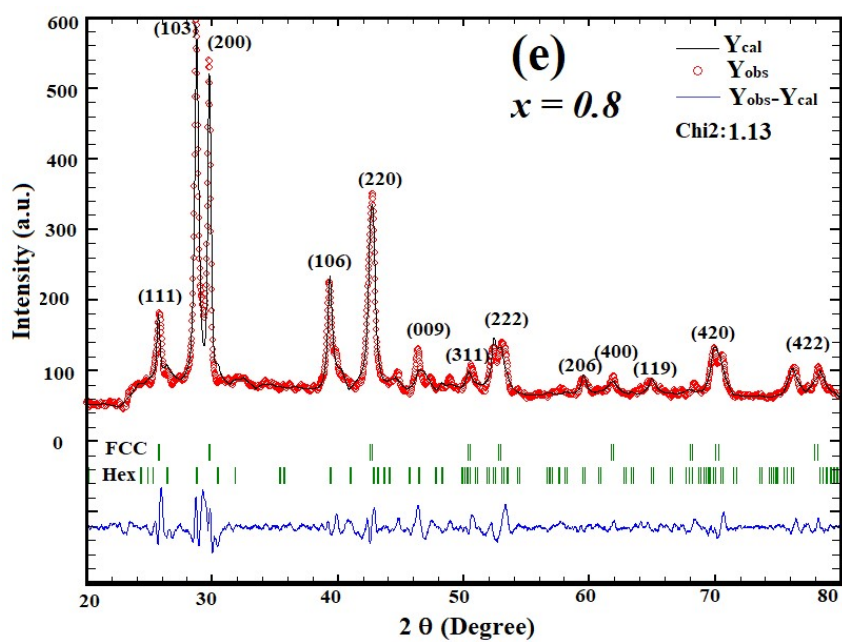
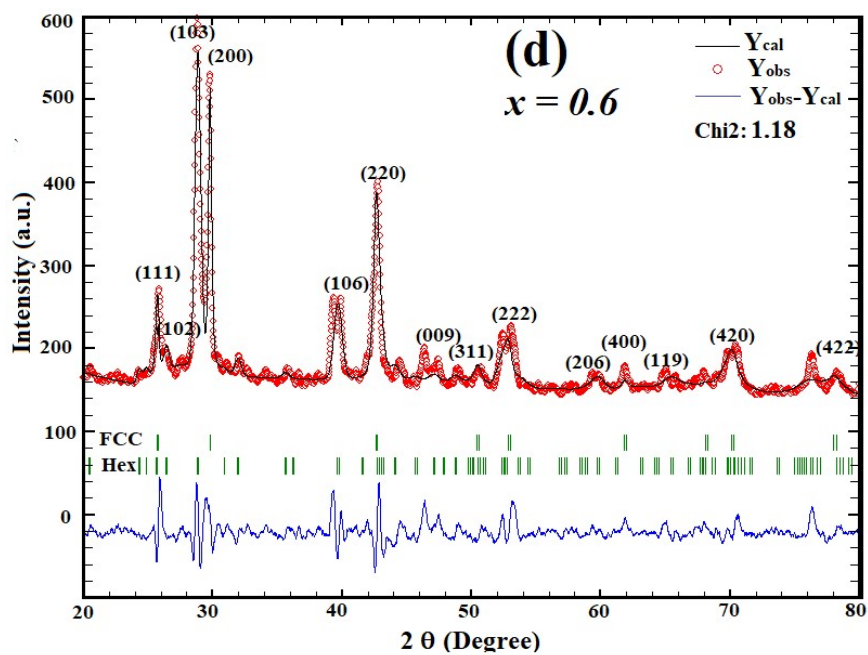
**Table 4.1.** The values of  $d_{106}$ -spacing,  $D_{hkl}$  and  $\epsilon$  for  $(Ge_2Sb_2Te_5)_{100-x}Sm_x$  alloys.

The FullProf Suite software has been employed for Rietveld refinement of XRD spectra of  $(Ge_2Sb_2Te_5)_{100-x}Sm_x$  alloys for the quantitative phase analysis and lattice parameter evaluation. The better profile intensity, correct peak position evaluation and consideration of preferred orientation are the main requirements for the evaluation of lattice parameters and quantitative analysis of the phase. The information about the atomic position, site occupancy, isotropic/anisotropic displacement and lattice parameters has been initially acquired

employing the crystallographic information file (*CIF*). The *CIF* file of *GST* phase change material has been received through the crystallography open database (*COD*). The *CIF* file of rocksalt cubic crystal structure with space group symmetry *Fm-3m* having *COD ID* 4340361 and for hexagonal phase, the space group *P-3m1* have *COD ID* 7215138 have been used for the Rietveld refinement of *XRD* data of  $(Ge_2Sb_2Te_5)_{100-x}Sm_x$  alloys. The pseudo-Voigt peak shape function has been chosen for the evaluation of *FWHM* parameters. The calculated patterns shown in figure 4.3 (a-g) for  $(Ge_2Sb_2Te_5)_{100-x}Sm_x$  ( $x = 0, 0.2, 0.4, 0.6, 0.8, 1.0, 1.2$ ) show a good fitting. The values for  $\chi^2$  and goodness of fit calculated using  $(Ge_2Sb_2Te_5)_{100-x}Sm_x$  refined patterns lie close to 1 indicating a good level of accuracy. The obtained values of unit cell parameters have been listed in table 4.2 which are in agreement with results reported earlier on *GST* [18]. The little variation among the calculated and observed profiles in *XRD* patterns of  $(Ge_2Sb_2Te_5)_{100-x}Sm_x$  can be narrated through the smooth  $Y_{obs}-Y_{cal}$  profiles shown in figure 4.3 (a-g) and from the lower values of the Bragg  $R$  factor ( $R_B$ ) and  $R_F$  factor.







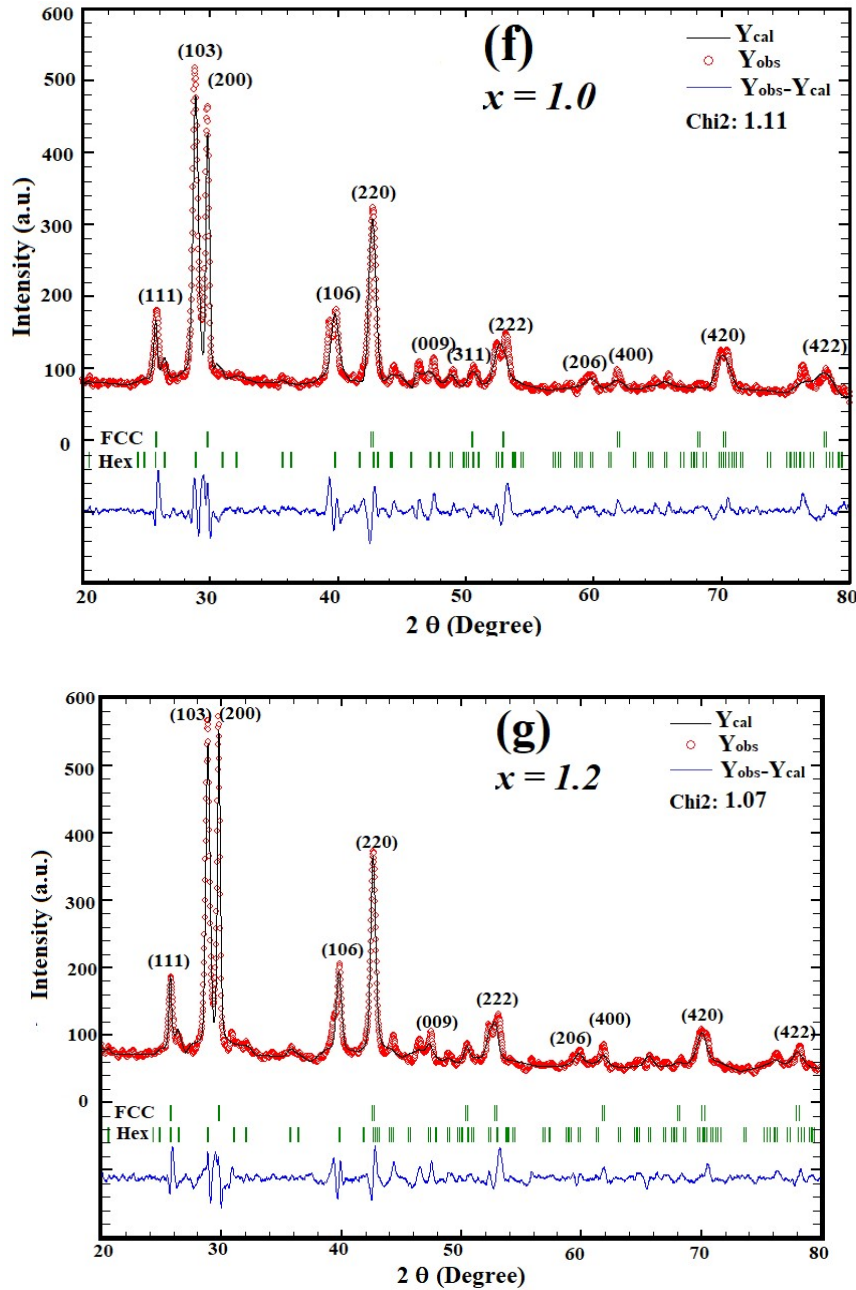


**Figure 4.3 (a-g).**  $(Ge_2Sb_2Te_5)_{100-x}Sm_x$  ( $x = 0, 0.2, 0.4, 0.6, 0.8, 1.0, 1.2$ ) rietveld refinement for XRD patterns.

The *fcc* phase emerges as a result of the growth of square rings of *Ge-Te-Sb-Te* in (200) crystallographic orientation and forming the layer of vacancies. Similarly, formation of the hexagonal phase is because of the growth of the rhombus of *Ge-Te-Sb-Te* in (103) orientation. The transformation from rocksalt *fcc* crystal structure to hexagonal changes the dihedral angle of four-membered rings *Ge-Te-Sb-Te* and bond lengths *Ge-Te* and *Sb-Te* and simultaneously creates *Te-Te* bonds on *Te* atoms replacing the vacancies [5]. The fraction of hexagonal and *fcc* phase present in as-prepared  $(Ge_2Sb_2Te_5)_{100-x}Sm_x$  alloys has

been analyzed using the Rietveld refinement which has been observed to augment for  $x = 0.4at\%$   $Sm$  addition (Table 4.2). The decrease in  $fcc$  phase fraction with doping of  $Sm$  concentration up to  $x = 0.4at\%$  can be due to the removal of vacancy concentration on  $Sm$  incorporation. The vacancies are crucial in transformation to the  $GST$  hexagonal phase. The most dominant (103) peak shift observed with  $Sm$  incorporation in hexagonal phase is on account of  $Sm$  having larger atomic radius in comparison to that of  $Ge$ ,  $Sb$  and  $Te$  atoms. The reduction in hexagonal phase fraction for  $Sm$ ,  $x > 0.4$  incorporation is consequence of larger  $Sm$  atomic size inducing the grain refinement [19]. Similar grain refinement has also been reported for the  $Y$  doped  $Sb_2Te_3$  [19]. Because of the different  $Sb-Te$  and  $Sm-Te$  bond lengths and bond angles there is lattice twisting and retardation of propagation of crystal plane, which may induce the grain refinement in  $GST$ .

$x$	FCC Phase				Hexagonal Phase				
	$a$ (Å)	$R_B$	$R_F$	Phase Fraction (%)	$a$ (Å)	$c$ (Å)	$R_B$	$R_F$	Phase Fraction (%)
0	6.096	5.10	3.45	50.87	4.229	17.372	8.95	11.60	49.13
0.2	6.009	6.16	4.03	30.44	4.218	17.417	10.40	13.40	69.56
0.4	6.026	8.60	7.48	24.00	4.245	17.266	9.61	12.70	76.00
0.6	5.997	5.98	4.68	28.70	4.228	17.374	7.68	8.79	71.30
0.8	6.003	4.83	3.31	36.24	4.224	17.608	6.69	10.40	63.76
1.0	5.998	7.97	7.49	40.51	4.229	17.372	7.49	8.47	59.49
1.2	6.003	7.40	4.77	41.10	4.236	17.293	9.11	15.80	58.90

**Table 4.2.** The lattice parameters along with phase fractions of  $fcc$  and hexagonal phases for  $(Ge_2Sb_2Te_5)_{100-x}Sm_x$  alloys.

#### 4.3.1.2 Raman Analysis

Figure 4.4 shows the Raman spectra of bulk alloys for  $(Ge_2Sb_2Te_5)_{100-x}Sm_x$  ( $x = 0, 0.2, 0.4, 0.6, 0.8, 1.0, 1.2$ ) illustrating vibrational bands at  $262\text{ cm}^{-1}$ ,  $190-210\text{ cm}^{-1}$ ,  $160\text{ cm}^{-1}$ ,  $136\text{ cm}^{-1}$ ,  $120\text{ cm}^{-1}$ ,  $105\text{ cm}^{-1}$ ,  $90\text{ cm}^{-1}$ ,  $62\text{ cm}^{-1}$  and  $56\text{ cm}^{-1}$ . The vibrational bands that are most prominent have been analyzed near  $160\text{ cm}^{-1}$  and  $120\text{ cm}^{-1}$  whose appearance in  $GST$  is still debated in the literature [16], [20], [21]. M. Riccardo [20] proposed the  $160\text{ cm}^{-1}$  and  $120\text{ cm}^{-1}$  vibrational bands on account of octahedral  $Ge$  vibrations.  $Ge$  has been found to exist

in both tetrahedral as well as octahedral geometry in the amorphous *GST* containing 1/3 fraction in tetrahedral and 2/3 fraction in octahedral geometry [22]. The *Ge* atoms fraction presence in tetrahedral geometry in the amorphous *GST* matrix can produce sufficient optical reflectivity as well as electrical resistivity contrast on phase transition. The tetrahedral *Ge* switches to octahedral geometry on *fcc* crystallization amorphous *GST* [23]. Some reports linked the origin of  $120\text{ cm}^{-1}$  peak for the  $\nu_1(A_1)$  stretching mode of corner-sharing tetrahedra of  $GeTe_{4-n}Ge_n$  ( $n=1, 2$ ) whereas peak near  $160\text{ cm}^{-1}$  for the *Sb-Sb* bond vibration and  $A_{1g}(2)$  mode of  $SbTe_3$  pyramidal structure [16], [21], [24]. The weak features near  $56\text{ cm}^{-1}$  in the Raman spectra of *Sm* doped *GST* are due to the disorder effects of amorphous materials causing the breakdown of selection rule for transitions and has been also known as “boson peak”. The peak near  $62\text{ cm}^{-1}$  and shoulder at  $75\text{ cm}^{-1}$  have been allocated to bending mode  $\nu_4(F_2)$  of  $GeTe_{4-n}Ge_n$  ( $n=1, 2$ ) and bending mode  $\nu_2(E)$  of  $GeTe_4$  respectively [25]. The appearance of the vibrational band about  $90\text{ cm}^{-1}$  in Raman spectra is the consequence of threefold coordinated *Te* atoms present in a defective octahedral geometry. The anti-symmetric stretching mode  $\nu_3(F_2)$  of  $GeTe_4$  as well as *Sm-Te*, *Sb-Te* bond stretching collectively cause the weak features from  $190\text{ cm}^{-1}$  to  $210\text{ cm}^{-1}$  [21], [26], [27]. The symmetric stretching  $\nu_1(A_1)$  mode of  $GeTe_4$  corner or edge-sharing tetrahedra shows the peak about  $105\text{ cm}^{-1}$ . The  $\nu_1(A_1)$  symmetric vibration of *Ge* rich  $GeGe_4$  or  $GeTeGe_3$  tetrahedra exhibits its signature at  $262\text{ cm}^{-1}$  in the Raman spectra of *Sm* incorporated *GST*. The presence of a vibrational band with center about  $135\text{ cm}^{-1}$  has been attributed to the symmetric stretching mode  $\nu_1(A_1)$  of  $GeTe_{4-n}Ge_n$  ( $n=0,1, 2$ ) tetrahedra. The emergence of Raman bands about  $120\text{ cm}^{-1}$  and  $160\text{ cm}^{-1}$  is most likely owing to the atoms of *Ge* in defective octahedral geometry. The *fcc* crystal structure of *GST* shows the defective octahedral geometry of *Ge* atoms. The *Ge* defective octahedral geometry predominating over tetrahedral geometry can also be confirmed from the presence of rocksalt *fcc* phase of *GST* in the *XRD* results. However, the significant fraction of tetrahedral structures of  $GeTe_{4-n}Ge_n$  ( $n=1, 2$ ) in the amorphous matrix of *GST* cannot be denied. The  $A_{1g}(2)$  vibrational mode of  $Sb_2Te_3$  pyramidal structures at  $\sim 160\text{ cm}^{-1}$  has been observed to shift with *Sm* concentration (Figure 4.4) [28]. The  $A_{1g}(2)$  mode has been observed to be shifted along the lower wavenumber upto  $x=0.4$  *Sm* addition which may be consequence of higher atomic mass *Sm* replacing one of the *Sb* atoms.

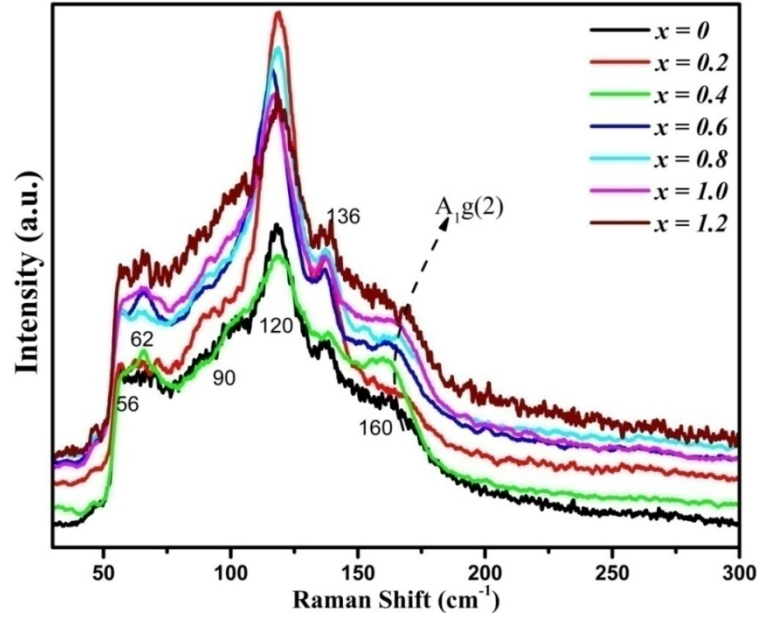


**Figure 4.4.** Raman spectra of  $(Ge_2Sb_2Te_5)_{100-x}Sm_x$  alloys.

The substitution of  $Sm$  in  $Te_2Sb-SbTe_2$  pyramidal structure may also bring up the change in  $fcc$  and hexagonal phase fraction. The local structure about  $Sb$  in the rocksalt  $fcc$  phase considerably differs from the hexagonal phase whereas no significant alteration in local structure of  $Ge$  occurs on  $fcc$  to the hexagonal phase transition. The  $A_{1g}(2)$  mode slight shift of  $Sb_2Te_3$  pyramidal structure toward higher frequency has been observed on enhancing the  $Sm$  concentration  $x > 0.4 at\%$ . This shift towards higher frequency side can also be due to the creation of  $(SbTe)Sm-Sb(SbTe)$  and  $(SbTe)Sm-Sb(Te_2)$  structures preferred over the  $Te_2Sm-SbTe_2$  at the higher  $Sm$  concentration. The lower bond formation energy for  $Sm-Sb$  compared to  $Sm-Te$  displays the negative barrier of energy for bond switching which alters the bond formation probability discussed extensively in section 2.3.7. The change in crystallinity content with  $Sm$  concentration up to  $x = 0.4 at\%$  can also be inferred from the modification in  $120 cm^{-1}$  peak intensity and corresponding  $FWHM$  with  $Sm$  content. The Raman spectra peak fitting for  $(Ge_2Sb_2Te_5)_{100-x}Sm_x$  alloys has been performed by Gaussian function for evaluation of peak area (Figure 4.5(a-g)). The peak area ratio for various vibrational bands computed for  $(Ge_2Sb_2Te_5)_{100-x}Sm_x$  alloys have been listed in table 4.3. The ratio of  $Ge$  octahedral to  $A_{1g}(2)$  mode of  $SbTe_3$  pyramidal structure peak areas has been labeled as  $A_2/B_1$  in table 4.3. The computed values of  $A_2/B_1$  enhance till  $x = 0.4 Sm$  incorporation and then decreases. Table 4.3 displays the obtained values of  $A_1/A_2$  ratio exhibiting the increase in octahedral  $Ge$  fraction compared to tetrahedral with  $Sm$  addition till  $x = 0.4 at\%$ . Moreover, the alteration in  $A_2/B_1$  and  $A_1/A_2$  values with  $Sm$  concentration is due

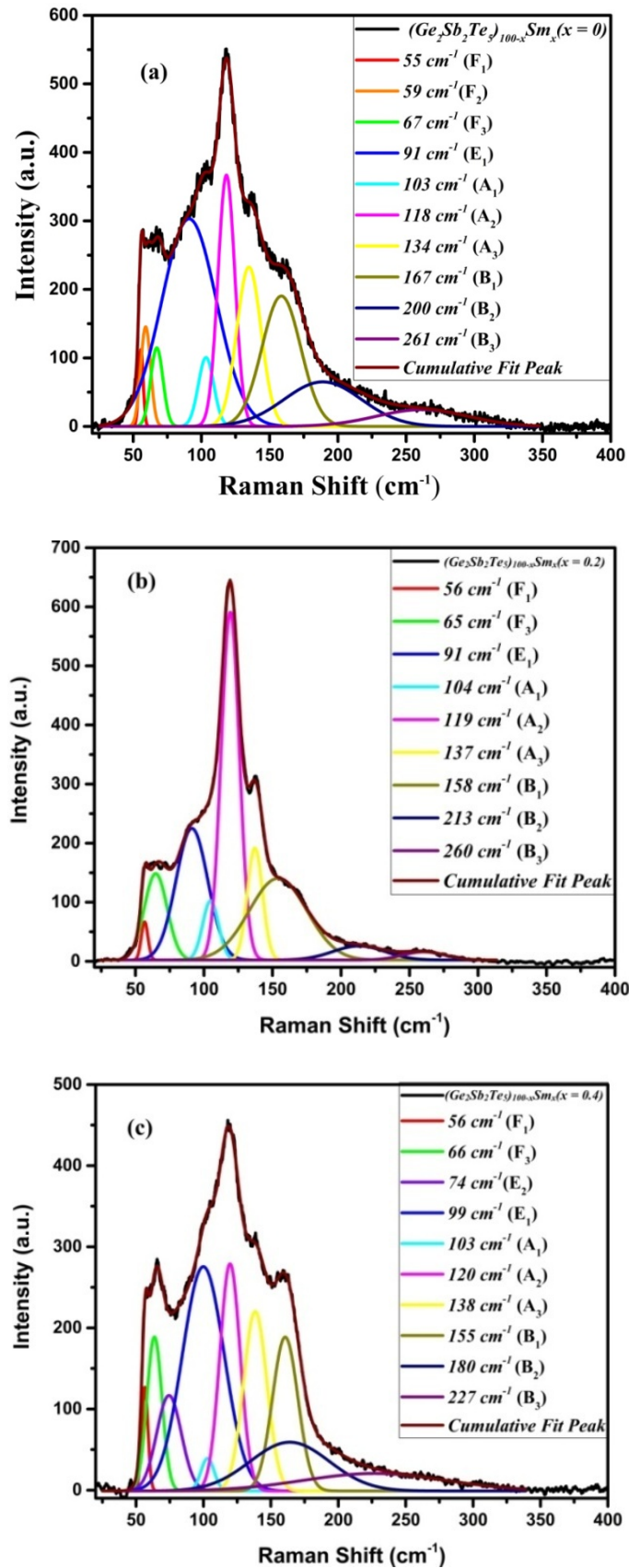
to the fractional change in *Ge* octahedral structure. The variation in  $B_2/A_2$  peak area ratio computed for  $(Ge_2Sb_2Te_5)_{100-x}Sm_x$  shows concurrence with tetrahedral to octahedral fraction  $A_1/A_2$ . The octahedral *Ge* fraction rises compared to tetrahedral *Ge* as well as pyramidal  $Sb_2Te_3$  structures on enhancing the *Sm* to  $x = 0.4$  at%, whereas, octahedral *Ge* structure decreases for *Sm* addition  $x > 0.4$  at%.

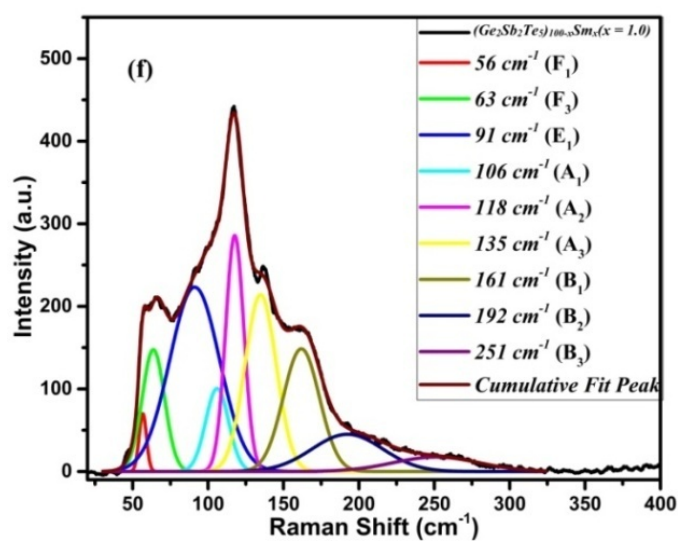
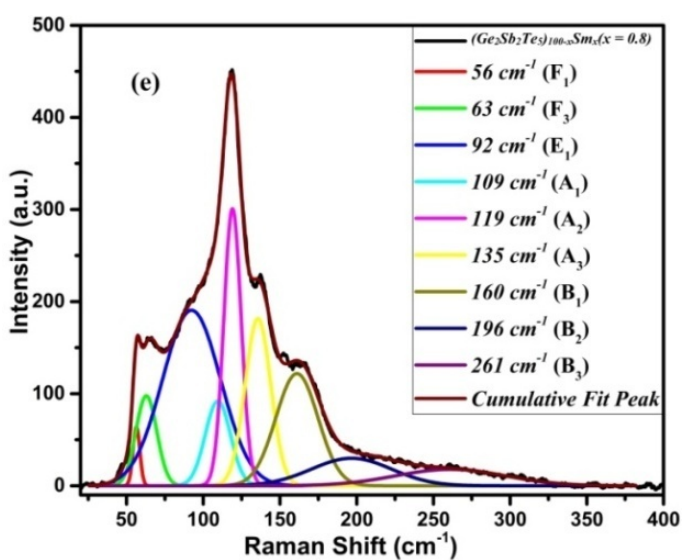
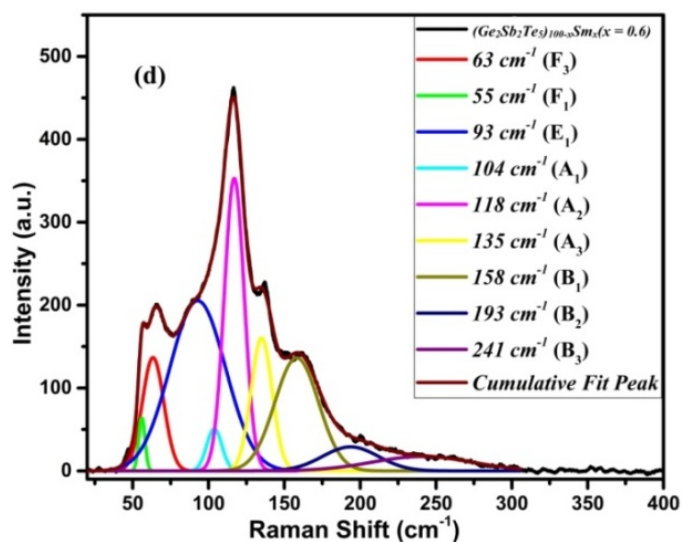
<i>x</i>	Peak Position		Peak Area Ratio		
	$A_2$	$B_1$	$A_2/B_1$	$A_1/A_2$	$B_2/A_2$
0	118.40	167.76	1.08	0.26	1.27
0.2	119.41	158.26	1.12	0.15	0.84
0.4	119.98	155.50	1.18	0.09	0.12
0.6	118.85	158.90	1.17	0.11	0.23
0.8	119.12	160.83	1.01	0.44	0.45
1.0	118.63	161.00	0.98	0.45	0.61
1.2	119.40	162.41	0.97	1.13	1.42

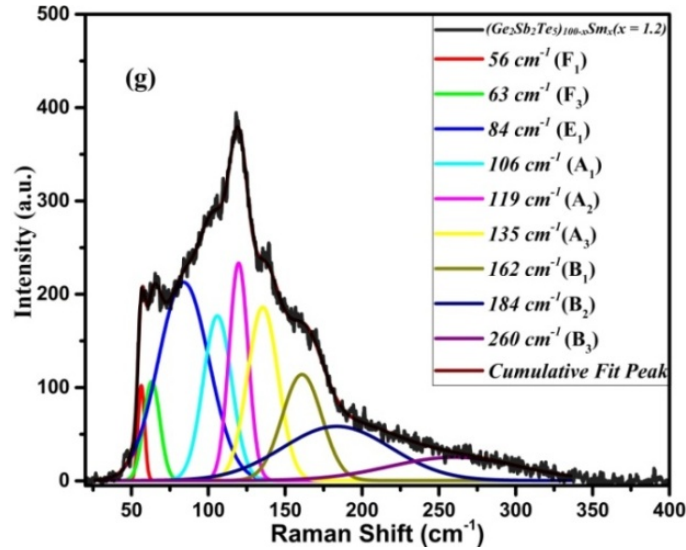
**Table 4.3.** The ratios for peak area and Raman shift of  $(Ge_2Sb_2Te_5)_{100-x}Sm_x$  alloys.

Figure 4.5(a-g) shows the Raman spectra peak fitting for  $(Ge_2Sb_2Te_5)_{100-x}Sm_x$  alloys and vibrational mode shifting for  $SbTe_3$  pyramidal structure labeled  $B_1$ . The redshift of the vibrational frequency of pyramidal structures and increase in hexagonal phase spacing  $d_{103}$  is owing to the bigger atomic size *Sm* replacing *Ge*, *Sb* and *Te*. The replacement of constituents of *GST* by the *Sm* atom may also lead to the reduction of vacancy concentration and formation of *Sm—Te* bonds with  $SbTe_3$  pyramidal structures causing the reduction of *fcc* phase fraction up to  $x = 0.4$  at%. The enhancement of octahedral *Ge* fraction compared to *Ge* in tetrahedral geometry till addition of  $x = 0.4$  at% *Sm* can be correlated to the rise in crystallinity. The reduction in the tetrahedral *Ge* fraction till *Sm* addition of  $x = 0.4$  at% can also be viewed in terms of the decline in homopolar bonds fraction of *Ge—Ge*, *Ge—Sb* and *Sb—Sb* bonds as these bonds are mainly exist in a tetrahedral geometry. The decline in tetrahedral geometry for  $x > 0.4$  at% owes it to the larger size *Sm* atoms inducing grain refinement because of the earlier discussed reasons. The concentration of localized charged defects reduces till *Sm* addition of  $x = 0.4$  owing to the *Sm* atoms replacing the *Te*, *Sb*, *Ge*, and vacancies. A decline in density of localized states on *Sm* addition can be due to the rise in

average coordination and a decrease in non-bonding electrons with  $Sm$  content results in the alteration in the band structure.







**Figure 4.5(a-g).** Raman active modes Gaussian peak fitting for *Sm* added *GST*.

#### 4.3.1.3 FTIR Measurements

Figure 4.6 shows the *FTIR* transmission spectra for  $(Ge_2Sb_2Te_5)_{100-x}Sm_x$  ( $x = 0, 0.2, 0.4, 0.6, 0.8, 1.0, 1.2$ ) alloys measured from  $30\text{ cm}^{-1}$  to  $300\text{ cm}^{-1}$ . *FTIR* spectroscopy and Raman spectroscopy collectively offer the insight into molecular and vibrational behavior of amorphous solids. The fundamental difference between *FTIR* and Raman spectroscopy is the different selection rules for vibrational transitions in both techniques. Raman spectroscopy measures the change in polarizability whereas *FTIR* measures the dipole moment. This fundamental difference between both the techniques results in dissimilar magnitudes of modes of vibrations in the *FTIR* and Raman spectra. The glasses exhibit the breakdown of the selection rule for vibrational transitions due to the disorder whose presence in as-prepared  $(Ge_2Sb_2Te_5)_{100-x}Sm_x$  alloys can be evidenced from the emergence of a wide absorption band ranging from  $38\text{ cm}^{-1}$  -  $55\text{ cm}^{-1}$  [29], [30]. The existence of shoulder of  $(Ge_2Sb_2Te_5)_{100-x}Sm_x$  in the *FTIR* transmission spectra near  $63\text{ cm}^{-1}$  has been associated with the vibration of  $Sb_2Te_3$  in  $A_u(1)$  IR active mode. Similarly, the presence of IR absorption band ranging  $75\text{ cm}^{-1}$  -  $88\text{ cm}^{-1}$  can be either on account of the vibration of *GeTe* tetrahedral in  $T_{1u}$  mode or due to the  $E_u(2)$  IR active of  $Sb_2Te_3$  [28], [30]. The  $E_u(3)$  vibrational mode of the  $Sb_2Te_3$  pyramidal structure shows the wide  $91\text{ cm}^{-1}$  -  $100\text{ cm}^{-1}$  peak [28]. The peaks in the *FTIR* transmission spectra in the range  $106\text{ cm}^{-1}$  -  $113\text{ cm}^{-1}$  along with  $145\text{ cm}^{-1}$  -  $163\text{ cm}^{-1}$  corresponds to  $A_{2u}(2)$  and  $A_{2u}(3)$  IR modes of  $Sb_2Te_3$  respectively [28]. The occurrence of homopolar wrong bonds *Ge—Sb* and *Sb—Sb* in amorphous matrix of *Sm* added *GST* alloys has been linked with the appearance of peaks from  $160\text{ cm}^{-1}$  -  $194\text{ cm}^{-1}$  [31], [32]. The

heteropolar  $Ge-Te$  and  $Sm-Te$  bonds display features near  $212\text{ cm}^{-1}$  and  $217\text{ cm}^{-1}$  respectively [26], [32]. The signature of  $Ge-Ge$  homopolar bonds contained in  $GeGe_4$  or  $GeTeGe_3$  can be confirmed from the appearance of peaks in  $225\text{ cm}^{-1} - 300\text{ cm}^{-1}$  range.

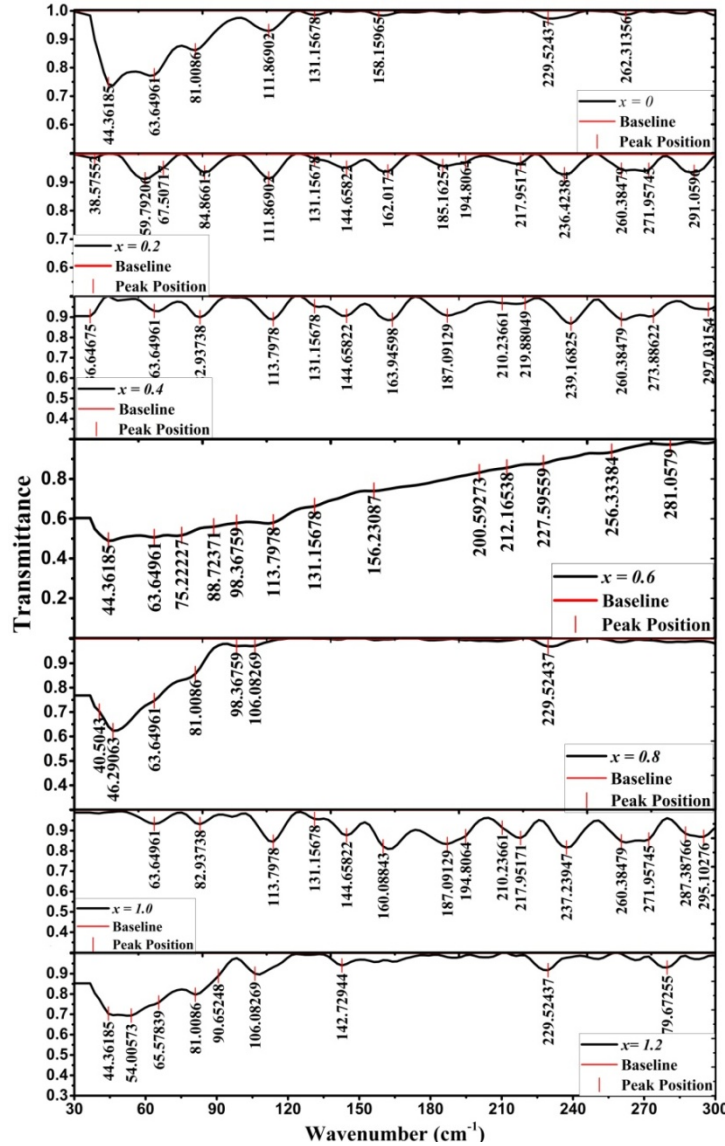


**Figure 4.6.**  $(Ge_2Sb_2Te_5)_{100-x}Sm_x$  ( $x = 0, 0.2, 0.4, 0.6, 0.8, 1.0, 1.2$ ) FTIR transmission spectra in *Far-IR* wavelength range.

The  $(Ge_2Sb_2Te_5)_{100-x}Sm_x$  alloys FTIR transmittance spectra illustrated in figure 4.6 presents the wide absorption band in the range of lower wavenumber which indicates the short-range order and presence of ionic impurities in amorphous regions causing the large dipole moment. The occurrence of the free carrier in amorphous materials can be described through the appearance of peaks towards higher frequencies above  $150\text{ cm}^{-1}$  whose amplitude tells about its concentrations [30]. From figure 4.6, it can be inferred that with rise in

concentration to  $x = 0.4$  Sm in GST the vibrational modes or phonon modes at low-frequency gets suppressed, whereas, there is an enhancement in the amplitude of phonon modes at higher frequencies, which can be owing to rise in crystallinity content and hence, the free carrier concentration. The appearance of mixed phonon modes for  $x > 0.4$  Sm incorporation to GST can be because of vacancy defects and disorder inclusion on further increase in Sm concentration causing space group symmetry breakdown.

### 4.3.2 Characterization of $(Ge_2Sb_2Te_5)_{100-x}Sm_x$ Thin Films

The characterizations for thin films of  $(Ge_2Sb_2Te_5)_{100-x}Sm_x$  deposited by means of thermal evaporation have been performed employing XRD and XPS measurements. The nature of as-prepared thin films has been investigated along with the confirmation study of the stoichiometry and bonding nature in them.

#### 4.3.2.1 Thin Film XRD

The structural analysis of thin films of  $(Ge_2Sb_2Te_5)_{100-x}Sm_x$  ( $x = 0, 0.2, 0.4, 0.6, 0.8, 1.0, 1.2$ ) deposited using the thermal vapor deposition has been performed using X-ray diffractometer (PANalytical, X'pert Pro). The XRD measurements in as-deposited thin films of  $(Ge_2Sb_2Te_5)_{100-x}Sm_x$  have been carried out in Bragg-Brentano geometry by utilizing the source  $Cu K_\alpha$  for X-rays. Figure 4.7 presents the XRD spectra of as-deposited thin films not having any sharp diffraction peaks which suggest the  $(Ge_2Sb_2Te_5)_{100-x}Sm_x$  thin films to be of amorphous nature.

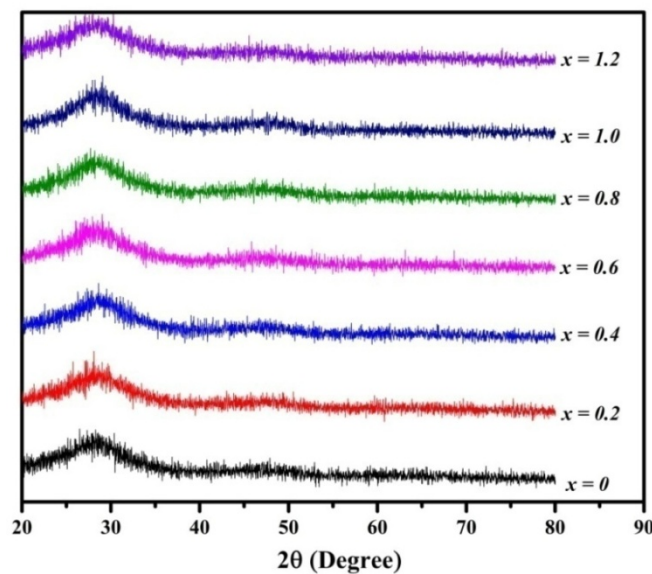


**Figure 4.7.** The XRD spectra for  $(Ge_2Sb_2Te_5)_{100-x}Sm_x$  thin films.

### 4.3.2.2 X-Ray Photoelectron Spectroscopy (XPS)

The analysis of as-deposited thin films surface of  $(Ge_2Sb_2Te_5)_{100-x}Sm_x$  ( $x = 0, 0.2, 0.4, 0.6, 0.8, 1.0, 1.2$ ) has been performed using XPS to investigate the effect of *Sm* addition on the nature of chemical bonding in *GST*. Figure 4.8(a) illustrates the XPS core-level spectra for *Te 3d* of as-prepared *Sm* added *GST* thin films. The *Te 3d*<sub>5/2</sub> and *Te 3d*<sub>3/2</sub> binding energies for bonds *Te*—*X*, where *X* = *Sb*, *Te*, *Ge* respectively at 573.7 eV and 584.1 eV with 10.4 eV energy for spin-orbit splitting have been analyzed for the undoped *GST* sample [33]. The surface contamination owing to oxygen for undoped thin films of *GST* can be ascertained through the presence of *Te 3d*<sub>5/2</sub> and *Te 3d*<sub>3/2</sub> peaks at the higher binding energies 577.2 eV and 587.5 eV respectively on account of creation of *Te*—*O* bonds [33]. The shift in *Te 3d*<sub>5/2</sub> and *Te 3d*<sub>3/2</sub> binding energies with *Sm* concentration towards lower energies can be noticed from figure 4.8(a). The *Te 3d* binding energy chemical shift of 1.4 eV for thin film  $x = 1.2$  at% towards lower energy confirms the creation of *Sm*—*Te*. The *Sb 3d* XPS core-level spectra displayed in figure 4.8(b) also implies the redshift of binding energy with *Sm* content. The peak position of *Sb 3d*<sub>5/2</sub> and *Sb 3d*<sub>3/2</sub> at respectively 528.8 eV and 538.2 eV have been identified due to *Sb*—*X* bonds (*X* = *Sm*, *Te*, *Sb*) for undoped *GST* [33] which have been observed to be shifted to 527.9 eV and 537.3 eV for 1.2 at% *Sm* content confirming the *Sb*—*Sm* bond formation.

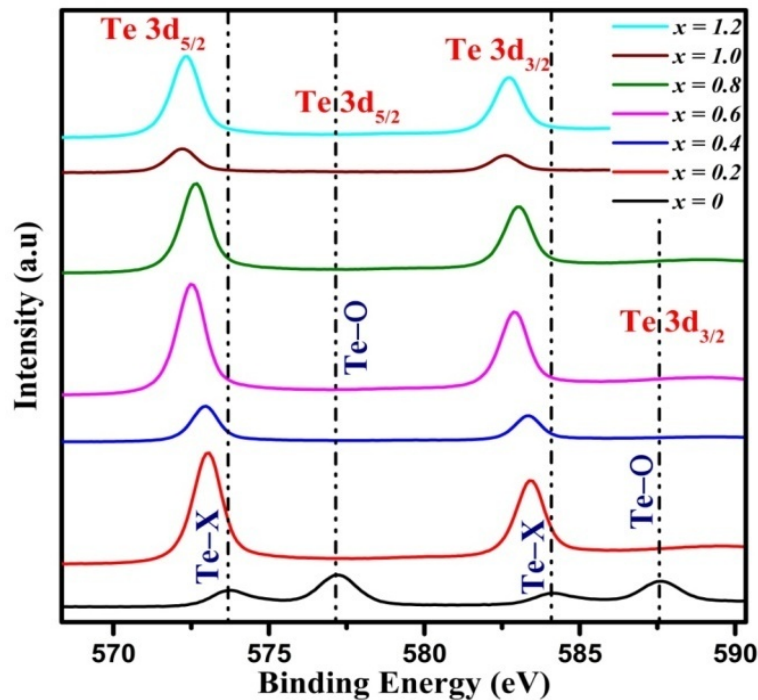


**Figure 4.8 (a).** *Te 3d* XPS spectra for thin films of  $(Ge_2Sb_2Te_5)_{100-x}Sm_x$ .

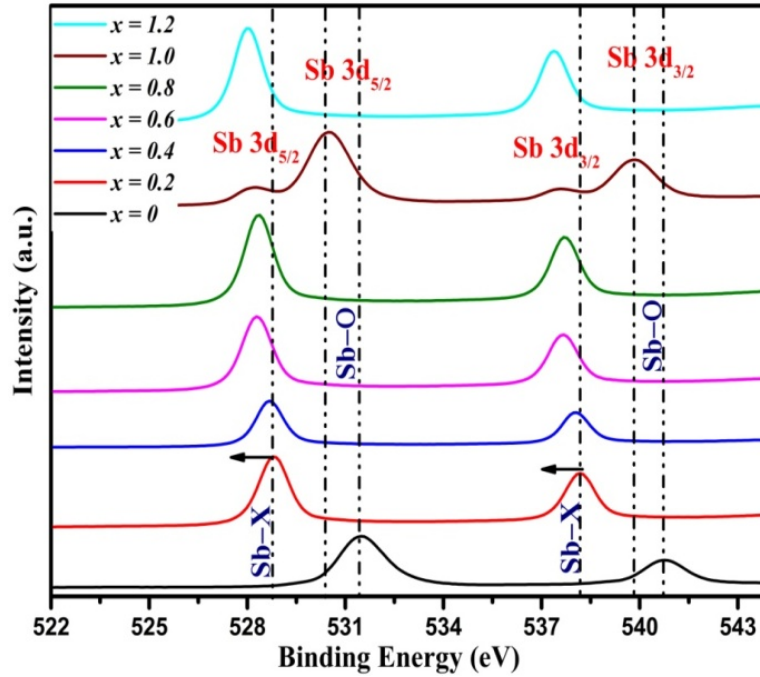


**Figure 4.8(b).** *Sb 3d* XPS spectra of  $(\text{Ge}_2\text{Sb}_2\text{Te}_5)_{100-x}\text{Sm}_x$  thin films.

The oxidation on thin-film surfaces for  $x = 0, 1.0$  can be inferred from the appearance of *Sb 3d* peaks at higher binding energy in both the samples due to the creation of *Sb—O* bonds. The *Sb 3d*<sub>5/2</sub> and *Sb 3d*<sub>3/2</sub> states binding energies have been detected at respective binding energies for  $x = 0$  at  $531.4 \text{ eV}$  and  $540.8 \text{ eV}$  and respective binding energies for  $x = 1.0$  % at  $530.5 \text{ eV}$  and  $539.9 \text{ eV}$  indicating presence of oxygen due to surface contaminations. The *Ge 3d*, *Sb 4d* and *Te 4d* XPS core-level spectra have been presented for *GST* thin films added with *Sm* in figure 4.9(a). The *Ge 3d* peak in undoped sample  $x = 0$  has been identified at  $31.1 \text{ eV}$  for *Ge—Te* bond. The redshift for *Ge 3d* binding energy with *Sm* concentration can be found in figure 4.9(a). The *Ge 3d* binding energy for  $x = 1.2 \text{ at\%}$  thin films has been detected at  $29.69 \text{ eV}$  and found to be redshifted by  $1.4 \text{ eV}$  compared to undoped  $x = 0$  *GST* sample. The *3d* peaks for *Te*, *Sb* and *Ge* shift on adding *Sm*, which clearly indicate the bond formation with *Sm* atoms in *GST* thin films. The observed XPS shift in the core level spectra toward the lower binding energy side is due to *Sm* having comparatively lesser electronegativity ( $1.17$ ) than *Te* ( $2.1$ ), *Sb* ( $2.05$ ) and *Ge* ( $2.01$ ). The contamination on surface of thin-films for *Sm* addition  $x = 0, 1.0$  has also been confirmed from *GeO*<sub>2</sub> creation having respective binding energies  $33.45 \text{ eV}$  and  $32.17 \text{ eV}$  for *Ge 3d*. Figure 4.9(a) also depicts the existence of doublet peaks allocated to *Sb 4d*<sub>5/2</sub> and *Sb 4d*<sub>3/2</sub> peaks of *Sb*<sub>2</sub>*Te*<sub>3</sub> structural units. The binding energy ranges from  $32.86 \text{ eV}$  to  $32.02 \text{ eV}$  for *Sb 4d*<sub>5/2</sub> and for *Sb 4d*<sub>3/2</sub>, it ranges between  $34.14 \text{ eV}$  to  $33.03 \text{ eV}$  for *Sb 4d*<sub>3/2</sub> in *GST* thin

films incorporated with *Sm*. The  $Sb_2O_3$  creation on the thin film surface for *Sm* concentration  $x = 0$  and  $x = 1.0\%$  can be inferred from the comparatively higher binding energies  $Sb\ 4d_{5/2}$  and  $Sb\ 4d_{3/2}$  in respective thin films. The peak positions at  $35.5\ eV$  and  $36.38\ eV$  in the undoped thin film sample  $x = 0$  and for  $x = 1.0\%$  thin film at  $34.6\ eV$  and  $35.5\ eV$  have been identified for  $Sb\ 4d_{5/2}$  and  $Sb\ 4d_{3/2}$  states respectively containing  $Sb_2O_3$ . The figure 4.9(a) depicts the appearance of  $Te\ 4d_{5/2}$  and  $Te\ 4d_{3/2}$  peaks in the range  $39.9\ eV$  to  $41.5\ eV$  besides  $Ge\ 3d$  and  $Sb\ 4d$  peaks. Figure 4.9(b) displays the  $Sm\ 3d$  core-level spectra for  $(Ge_2Sb_2Te_5)_{100-x}Sm_x$  thin films indicating the peaks for  $Sm\ 3d_{5/2}$  and  $Sm\ 3d_{3/2}$ . The occurrence of *Sm* in oxidation state +3 can be identified from the  $Sm\ 3d_{5/2}$  peak appearance in the range of binding energy  $1087.8\text{--}1089.4\ eV$  ( $1084.1\ eV$  standard value) and for  $Sm\ 3d_{3/2}$  from  $1107.3\text{--}1114.1\ eV$  ( $1111.1\ eV$  standard value) in  $(Ge_2Sb_2Te_5)_{100-x}Sm_x$  thin films [34].

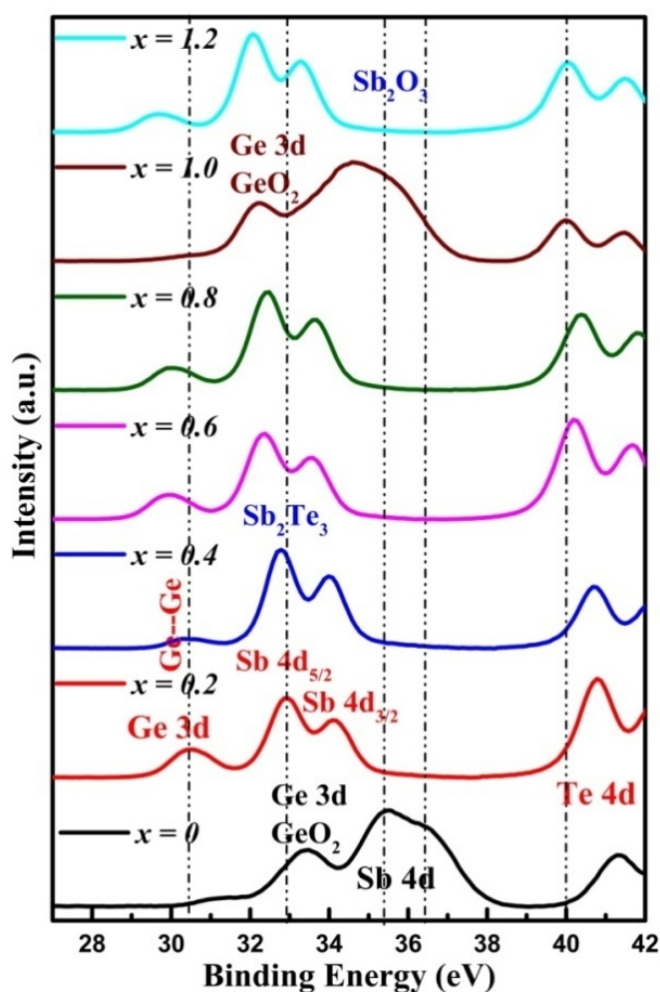


**Figure 4.9(a).** XPS spectra for  $Ge\ 3d$ ,  $Sb\ 4d$  along with  $Te\ 4d$  in thin films of  $(Ge_2Sb_2Te_5)_{100-x}Sm_x$ .

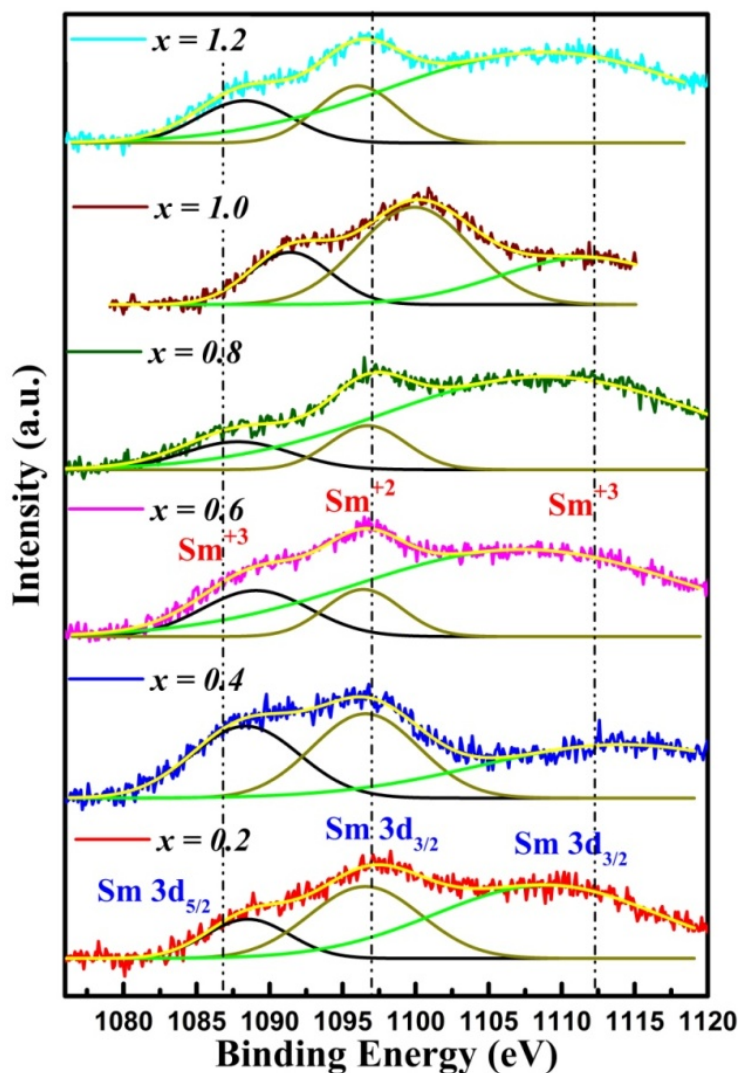


**Figure 4.9(b).** XPS spectra of *Sm* 3*d* core-level in thin films of  $(Ge_2Sb_2Te_5)_{100-x}Sm_x$ .

The  $Sm^{+2}$  oxidation state occurrence has been also observed for *Sm* added *GST* thin films besides +3 oxidation state. The *Sm* 3*d* XPS core-level spectra indicated in figure 4.9(b) manifests the presence of the oxidation state  $Sm^{+2}$  from the detected peak for *Sm* 3*d*<sub>3/2</sub> ranging from 1096.1-1096.7 eV in *Sm* added *GST* thin films [33]. The quantitative evaluation of elemental fraction of *Sm*, *Sb*, *Ge* and *Te* has been carried out through the area ratio of peaks in spectra of XPS core-level for *Sm* incorporated *GST* as-deposited thin films. It can be ascertained from table 4.4, that the evaluated values of atomic percentage obtained through XPS spectra are close to the stoichiometry of as-prepared thin films. Furthermore, the compositional analysis of thin films of *Sm* added *GST* has been also performed using EDAX measurements which have been discussed in section 5.3.1.

$x$	Measured Atomic Percentage				Calculated Atomic Percentage			
	<i>Ge</i> (at%)	<i>Sb</i> (at%)	<i>Te</i> (at%)	<i>Sm</i> (at%)	<i>Ge</i> (at%)	<i>Sb</i> (at%)	<i>Te</i> (at%)	<i>Sm</i> (at%)
0	22.03	23.51	54.46	0	22.22	22.22	55.56	0
0.2	22.85	22.71	54.21	0.23	22.17	22.17	55.44	0.2
0.4	22.42	21.29	55.78	0.50	22.13	22.13	55.33	0.4
0.6	21.47	22.51	55.34	0.67	22.08	22.08	55.22	0.6
0.8	21.82	22.88	54.42	0.86	22.04	22.04	55.11	0.8
1.0	21.75	21.92	55.25	1.08	22.00	22.00	55.00	1.0
1.2	21.58	21.99	55.18	1.23	21.95	21.95	54.89	1.2

**Table 4.4.**  $(Ge_2Sb_2Te_5)_{100-x}Sm_x$  thin films compositions observed employing XPS measurements and corresponding stoichiometric compositions.

#### 4.4 Conclusion

The as-prepared  $(Ge_2Sb_2Te_5)_{100-x}Sm_x$  bulk alloys have been investigated by performing measurements employing XRD that identify the presence of *fcc* and hexagonal phases in varying proportion. The addition of *Sm* induces the change in  $d_{103}$  spacing of the hexagonal phase of *GST* because of the shift of  $(103)$  diffraction peak towards the lower  $2\theta$  direction with *Sm* content. The substitution of *Sm* atoms in vacancy sites of *GST* results in the enhancement of tensile strain with *Sm* concentration up to  $x = 0.4$  at % and consequently boosts the hexagonal phase fraction. Furthermore, *Sm* addition also augments the crystallite size as inferred from the *W-H* plot till addition of  $x = 0.4\%$  *Sm*. The hexagonal phase fraction is suppressed for higher *Sm* incorporation  $x > 0.4\%$  because of grain refinement induced by *Sm* atoms, which simultaneously lowers the tensile strain and average crystallite size. The alteration in the *Sb* local environment on incorporation of *Sm* has been observed from the Raman shift of *SbTe<sub>3</sub>* pyramidal structure consequently, whereas, the change in hexagonal phase fraction with incorporation of *Sm* has been verified through the analysis employing Rietveld refinement. The analysis of XPS for *Sm* incorporated *GST* as-deposited thin films reveals the core-level spectra chemical shift for *Te 3d*, *Sb 3d* and *Ge 3d* confirming the formation of *Sb—Sm*, *Sm—Te* as well as *Ge—Sm* bonds on *Sm* incorporation to *GST*. The *Sm* oxidation states +2 and +3 presence has been confirmed through the *Sm 3d* core-level spectra

of  $(Ge_2Sb_2Te_5)_{100-x}Sm_x$  thin films. The  $Sm$  addition has been observed to reduce the  $Ge-Ge$  and  $Sb-Ge$  bond fraction lowering the  $\beta$ -relaxation in  $GST$  and resulting in the creation of heteropolar  $Sm-Te$  bonds. Reduction in  $\beta$ -relaxation on  $Sm$  addition may be advantageous to improve the resistance drift issue of  $GST$ . The  $Sm$  doping can be advantageous in  $GST$  in view of enhanced hexagonal phase fraction with  $Sm$  addition which offers an opportunity to utilize the  $fcc$  to hexagonal transformation for faster  $PC$  memory storage.

## References

- [1] W. Zhang and E. Ma, “Unveiling the structural origin to control resistance drift in phase-change memory materials,” *Mater. Today*, vol. 41, pp. 156–176, Dec. 2020.
- [2] M. Wuttig, H. Bhaskaran, and T. Taubner, “Phase-change materials for non-volatile photonic applications,” *Nature Photonics*, vol. 11, no. 8. pp. 465–476, 01-Aug-2017.
- [3] N. Youngblood, C. Rios, E. Gemo, J. Feldmann, Z. Cheng, A. Baldycheva, W. H.P Pernice, C. David Wright, and H. Bhaskaran, “Tunable Volatility of  $\text{Ge}_2\text{Sb}_2\text{Te}_5$  in Integrated Photonics,” *Adv. Funct. Mater.*, vol. 29, no. 11, p. 1807571, Mar. 2019.
- [4] X. Yu and J. Robertson, “Modeling of switching mechanism in GeSbTe chalcogenide superlattices,” *Sci. Rep.*, vol. 5, no. 1, p. 12612, Oct. 2015.
- [5] W. Zhang, H. S. Jeong, and S. A. Song, “Martensitic transformation in  $\text{Ge}_2\text{Sb}_2\text{Te}_5$  alloy,” *Adv. Eng. Mater.*, vol. 10, no. 1–2, pp. 67–72, 2008.
- [6] S. R. Elliott, “Electronic mechanism for resistance drift in phase-change memory materials: link to persistent photoconductivity,” *J. Phys. D. Appl. Phys.*, vol. 53, p. 214002, 2020.
- [7] J. Luckas, A. Piarristeguy, G. Bruns, P. Jost, S. Grothe, R. M. Schmidt, C. Longeaud, and M. Wuttig, “Stoichiometry dependence of resistance drift phenomena in amorphous GeSnTe phase-change alloys,” *J. Appl. Phys.*, vol. 113, no. 2, p. 023704, Jan. 2013.
- [8] G. Wang, X. Shen, Qihua Nie, R. Wang, L. Wu, Y. Lv, F. Chen, J. Fu, S. Dai and J. Li, “Improved thermal and electrical properties of Al-doped  $\text{Ge}_2\text{Sb}_2\text{Te}_5$  films for phase-change random access memory,” *J. Phys. D. Appl. Phys.*, vol. 45, no. 37, p. 375302, Sep. 2012.
- [9] M. L. Lee, K. T. Yong, C. L. Gan, L. H. Ting, S. Bin Muhamad Daud, and L. P. Shi, “Crystallization and thermal stability of Sn-doped  $\text{Ge}_2\text{Sb}_2\text{Te}_5$  phase change material,” *J. Phys. D. Appl. Phys.*, vol. 41, no. 21, p. 215402, Nov. 2008.
- [10] E. Cho, Y. Youn, and S. Han, “Enhanced amorphous stability of carbon-doped  $\text{Ge}_2\text{Sb}_2\text{Te}_5$  : Ab Initio investigation,” *Appl. Phys. Lett.*, vol. 99, no. 18, p. 183501, Oct.

- 2011.
- [11] Y. Lai, B. Qiao, J. Feng, Y. Ling, L. Lai, Y. Lin, T. Tang, B. Cai, and B. Chen, “Nitrogen-doped  $\text{Ge}_2\text{Sb}_2\text{Te}_5$  films for nonvolatile memory,” *J. Electron. Mater.*, vol. 34, no. 2, pp. 176–181, Feb. 2005.
- [12] Y. Hu, R. Zhang, T. Lai, X. Zhu, H. Zou, and Z. Song, “Simultaneously High Thermal Stability and Low Power Based on Ti-Doped  $\text{Ge}_2\text{Sb}_2\text{Te}_5$  Thin Films,” *ECS J. Solid State Sci. Technol.*, vol. 6, no. 12, pp. P866–P869, Dec. 2017.
- [13] A. Sherchenkov, S. Kozyukhin, A. Babich, and P. Lazarenko, “Thermal properties of phase change material  $\text{Ge}_2\text{Sb}_2\text{Te}_5$  doped with Bi,” *J. Non. Cryst. Solids*, vol. 377, pp. 26–29, Oct. 2013.
- [14] Y.-H. Huang and T.-E. Hsieh, “Effective thermal parameters of chalcogenide thin films and simulation of phase-change memory,” *Int. J. Therm. Sci.*, vol. 87, pp. 207–214, Jan. 2015.
- [15] Y. Chen, B. Chen, Q. Zhang, X. Li, Q. Deng, B. Zhang, S. Zhang, Z. Zhang, and X. Han, “Electrical properties and structural transition of  $\text{Ge}_2\text{Sb}_2\text{Te}_5$  adjusted by rare-earth element Gd for nonvolatile phase-change memory,” *J. Appl. Phys.*, vol. 124, no. 14, p. 145107, Oct. 2018.
- [16] T. Gu, J. Wang, H. Liu, Z. Wang, Y. Luo, P. Liu, J. Zhong and G. Wang, “One-step phase transition and thermal stability improvement of  $\text{Ge}_2\text{Sb}_2\text{Te}_5$  films by erbium-doping,” *Vacuum*, vol. 145, pp. 258–261, Nov. 2017.
- [17] S. Wei, G. J. Coleman, P. Lucas, and C. A. Angell, “Glass Transitions , Semiconductor-Metal Transitions , and Fragilities in Ge - V - Te ( V = As , Sb ) Liquid Alloys : The Difference One Element Can Make,” *Phys. Rev. Appl.*, vol. 7, no. 034035, pp. 1–10, 2017.
- [18] Z. Sun, J. Zhou, and R. Ahuja, “Structure of Phase Change Materials for Data Storage,” *Phys. Rev. Lett.*, vol. 96, no. 5, p. 055507, Feb. 2006.
- [19] B. Liu, W. Liu, Z. Li, K. Li, L. Wu, J. Zhou, Z. Song, and Z. Sun, “Y-Doped  $\text{Sb}_2\text{Te}_3$  Phase-Change Materials: Toward a Universal Memory,” *ACS Appl. Mater. Interfaces*, vol. 12, no. 18, pp. 20672–20679, 2020.

- 
- [20] R. Mazzarello, S. Caravati, S. Angioletti-Uberti, M. Bernasconi, and M. Parrinello, “Signature of tetrahedral Ge in the Raman spectrum of amorphous phase-change materials,” *Phys. Rev. Lett.*, vol. 104, no. 8, p. 085503, 2010.
- [21] K. S. Andrikopoulos, S. N. Yannopoulos, A. V. Kolobov, P. Fons, and J. Tominaga, “Raman scattering study of GeTe and Ge<sub>2</sub>Sb<sub>2</sub>Te<sub>5</sub> phase-change materials,” *J. Phys. Chem. Solids*, vol. 68, no. 5–6, pp. 1074–1078, May 2007.
- [22] S. Caravati, M. Bernasconi, T. D. Kühne, M. Krack, and M. Parrinello, “Coexistence of tetrahedral- and octahedral-like sites in amorphous phase change materials,” *Appl. Phys. Lett.*, vol. 91, no. 17, p. 171906, 2007.
- [23] W. Welnic, S. Botti, L. Reining, and M. Wuttig, “Origin of the optical contrast in phase-change materials,” *Phys. Rev. Lett.*, vol. 98, no. 23, p. 236403, 2007.
- [24] X. Zhou, M. Xia, F. Rao, L. Wu, X. Li, Z. Song, S. Feng, and H. Sun, “Understanding Phase-Change Behaviors of Carbon-Doped Ge<sub>2</sub>Sb<sub>2</sub>Te<sub>5</sub> for Phase-Change Memory Application,” *ACS Appl. Mater. Interfaces*, vol. 6, no. 16, pp. 14207–14214, Aug. 2014.
- [25] K. S. Andrikopoulos, S. N. Yannopoulos, G. A. Voyiatzis, A. V. Kolobov, M. Ribes, and J. Tominaga, “Raman scattering study of the a-GeTe structure and possible mechanism for the amorphous to crystal transition,” *J. Phys. Condens. Matter*, vol. 18, no. 3, pp. 965–979, 2006.
- [26] R. I. Alekberov, S. I. Mekhtiyeva, G. A. Isayeva, and A. I. Isayev, “Raman scattering in As-Se-S and As-Se-Te Chalcogenide vitreous semiconductors,” *Semiconductors*, vol. 48, no. 6, pp. 800–803, 2014.
- [27] E. M. Vinod, K. Ramesh, and K. S. Sangunni, “Structural transition and enhanced phase transition properties of Se doped Ge<sub>2</sub>Sb<sub>2</sub>Te<sub>5</sub> alloys,” *Sci. Rep.*, vol. 5, no. 8050, pp. 1–7, 2015.
- [28] G. C. Sosso, S. Caravati, and M. Bernasconi, “Vibrational properties of crystalline Sb<sub>2</sub>Te<sub>3</sub> from first principles,” *J. Phys. Condens. Matter*, vol. 21, no. 9, p. 095410, 2009.
- [29] T. S. Grigera, V. Martín-Mayor, G. Parisi, and P. Verrocchio, “Phonon interpretation

- of the ‘boson peak’ in supercooled liquids,” *Nature*, vol. 422, no. 6929, pp. 289–292, 2003.
- [30] V. Bragaglia, K. Holldack, J. E. Boschker, F. Arciprete, E. Zallo, T. Flissikowski and R. Calarco, “Far-Infrared and Raman Spectroscopy Investigation of Phonon Modes in Amorphous and Crystalline Epitaxial GeTe-Sb<sub>2</sub>Te<sub>3</sub> Alloys,” *Sci. Rep.*, vol. 6, no. 28560, pp. 1–7, 2016.
- [31] S. Sharda, N. Sharma, P. Sharma, and V. Sharma, “Finger prints of chemical bonds in Sb-Se-Ge and Sb-Se-Ge-In glasses: A Far-IR study,” *J. Non. Cryst. Solids*, vol. 362, no. 1, pp. 136–139, 2013.
- [32] N. Sharma, S. Sharda, V. Sharma, and P. Sharma, “Far-infrared investigation of ternary Ge-Se-Sb and quaternary Ge-Se-Sb-Te chalcogenide glasses,” *J. Non. Cryst. Solids*, vol. 375, pp. 114–118, Sep. 2013.
- [33] J. Chastain and J. Roger C. King, *Handbook of X-ray Photoelectron Spectroscopy*. USA: Perkin-Elmer, 1992.
- [34] S. Stojadinović and R. Vasilić, “Orange–red photoluminescence of Nb<sub>2</sub>O<sub>5</sub>:Eu<sub>3+</sub>, Sm<sub>3+</sub> coatings formed by plasma electrolytic oxidation of niobium,” *J. Alloys Compd.*, vol. 685, no. July, pp. 881–889, Nov. 2016.



## Chapter 5

### Optical Properties of $(Ge_2Sb_2Te_5)_{100-x}Sm_x$ Thin Films

- **Sanjay Kumar** and Vineet Sharma, “Effect of local structure on the optical and dielectric behaviour of Sm doped GeSbTe phase change material,” **Optical Materials.**, vol. 115, p. 111057, May 2021.



### 5.1. Introduction

The technological and fundamental aspects of phase change (*PC*) materials based upon chalcogenide glasses have attracted the attention of the scientific community immensely. Compositionally variable optical bandgap and transparency in the mid-infrared wavelength region are the fundamental characteristics of chalcogenide *PC* materials. Their technological importance includes applications in *RF* switches, optical memory, *PC*-memory, neuromorphic computing, photonics, holographic imaging, thermoelectrics [1]–[7], *etc.*

The *PC* materials lying on the tie line between (*GeTe*) and (*Sb<sub>2</sub>Te<sub>3</sub>*) has been chosen to be prospective materials for electrical and optical storage applications due to their high optical non-linearity and difference in electrical and optical properties in crystalline and amorphous states [8], [9]. Among various *PC* materials, *Ge<sub>2</sub>Sb<sub>2</sub>Te<sub>5</sub>* (*GST*) is the most studied and novel alloy for memory storage [10][7]. The compositionally tunable optical property of *PC* material is beneficial to improve the performance of storage devices by alloying with impurity elements. The reflectivity of thin films of *GST* is largely based upon the optical parameters *viz.* extinction coefficient (*k*), refractive index (*n*), *etc.* Furthermore, optical studies of *GST* thin film provide information on the band structure and electronic transport properties.

The *Ge* atoms are coordinated tetrahedrally in amorphous *GST* which transforms to defective octahedral structure in the corresponding crystalline state [11]. The amorphous phase of *GST* obeys the  $\delta$ -*N* rule for coordination and has mostly the heteropolar bonds *viz.* *Sb—Te* and *Ge—Te*. The crystalline phase of *GST* comprise of over-coordinated networks and results in the violation of  $\delta$ -*N* rules. The crystallization of *GST* leads to the redshift in the optical absorption spectrum because of the alteration of the bonding environment and variation in the dielectric constant [12]. The value of the dielectric constant is comparatively higher for the crystalline state than the amorphous [13]. The presence of vacancy defects in amorphous *GST* also results in the modification of optical properties. The amorphous structures undergo relaxation with aging and result in the removal of localized defect density, thus, augmenting the activation energy for conduction [14]. The crystallization introduces compressive mechanical stress and, therefore, manifests the 6.5% higher density of crystalline phase of *GST* compared to the amorphous phase [15].

The rare earth elements recently attained enormous attention for doping *PC* materials to improve the device performance [16][17]. Doping *GST* with the rare earth element can

significantly improve the optical and electrical conduction mechanism [18]. Rare earth doping can also result in the modification of structural relaxation and crystallization mechanism of *GST* on account of their lower electronegativity, bigger atomic size and occurrence in the positively charged ionic state. Improving the performance of *PC* memory has been investigated by modeling the switching speed and thermal stability by substituting *GST* with rare earths viz. *Gd* [18], *Er* [19], *Yb* [20] and *Ce* [21] etc.

The current research work highlights the analysis of optical behavior in  $(GST)_{100-x}Sm_x$  thin films prepared using thermal evaporation method. The doping effect of *Sm*, a rare earth element, on the optical gap and dielectric properties of *GST* has been examined. Furthermore, the electron conduction mechanism and corresponding activation energy have been correlated to the optical parameters. The investigation of optical behavior of  $(GST)_{100-x}Sm_x$  thin films also helps to understand its electron transport properties. The Urbach energy of  $(GST)_{100-x}Sm_x$  thin films have been examined to probe doping effect of *Sm* on the degree of band tailing. The dispersion parameters and non-linear index of refraction have been calculated to explore the effect of light on materials structure. The real as well as imaginary dielectric constants, volume energy loss function (*VELF*), surface energy loss function (*SELF*) as well as optical conductivity for  $(GST)_{100-x}Sm_x$  thin films are also evaluated.

### 5.2. Experimental Details

The process of melt quenching described in section 3.2.1 has been employed for the synthesis of bulk alloys of  $(GST)_{100-x}Sm_x$  ( $x = 0, 0.2, 0.4, 0.6, 0.8, 1.0, 1.2$ ). The as-prepared powder material of  $(GST)_{100-x}Sm_x$  alloys has been used for thin film deposition making use of thermal evaporation technique described in section 3.2.3.

The compositional analysis of  $(GST)_{100-x}Sm_x$  thin films has been carried out by means of the energy dispersive *X-Ray (EDX)* having an attachment for field emission scanning electron microscopy (*FESEM, Hitachi SU-8010*). The elemental distribution and surface morphology of as-deposited  $(GST)_{100-x}Sm_x$  ( $x = 1.2$ ) thin film has been investigated using *FESEM* elemental mapping and imaging to ensure surface homogeneity for elemental distribution. The uniformity of elemental distribution along thin films surface has been also analyzed using *EDX* measurements at different locations. The transmittance spectra measured from *Lambda 750, Perkin Elmer, UV-Vis-NIR* spectrophotometer have been used to investigate optical properties of  $(GST)_{100-x}Sm_x$  thin films.

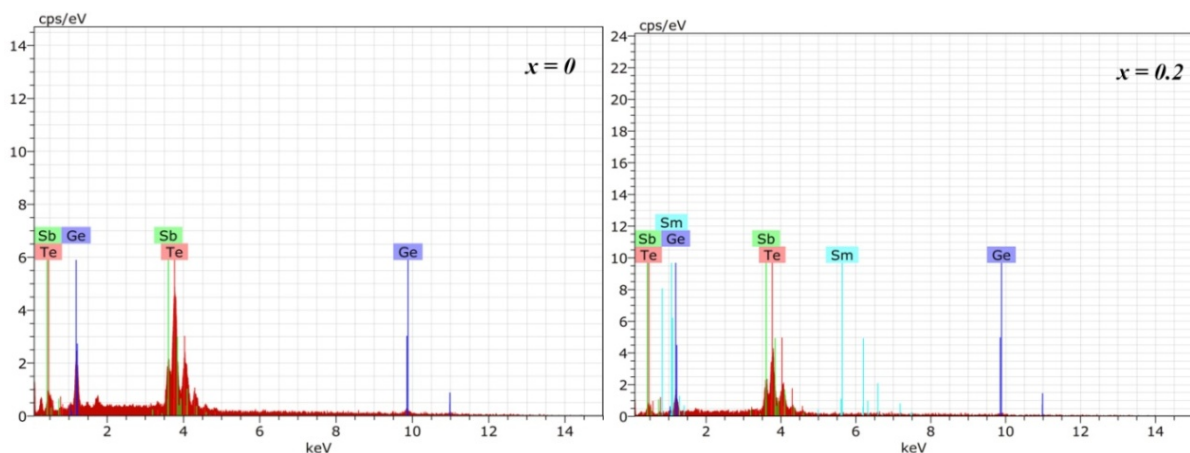
### 5.3. Results and Discussion

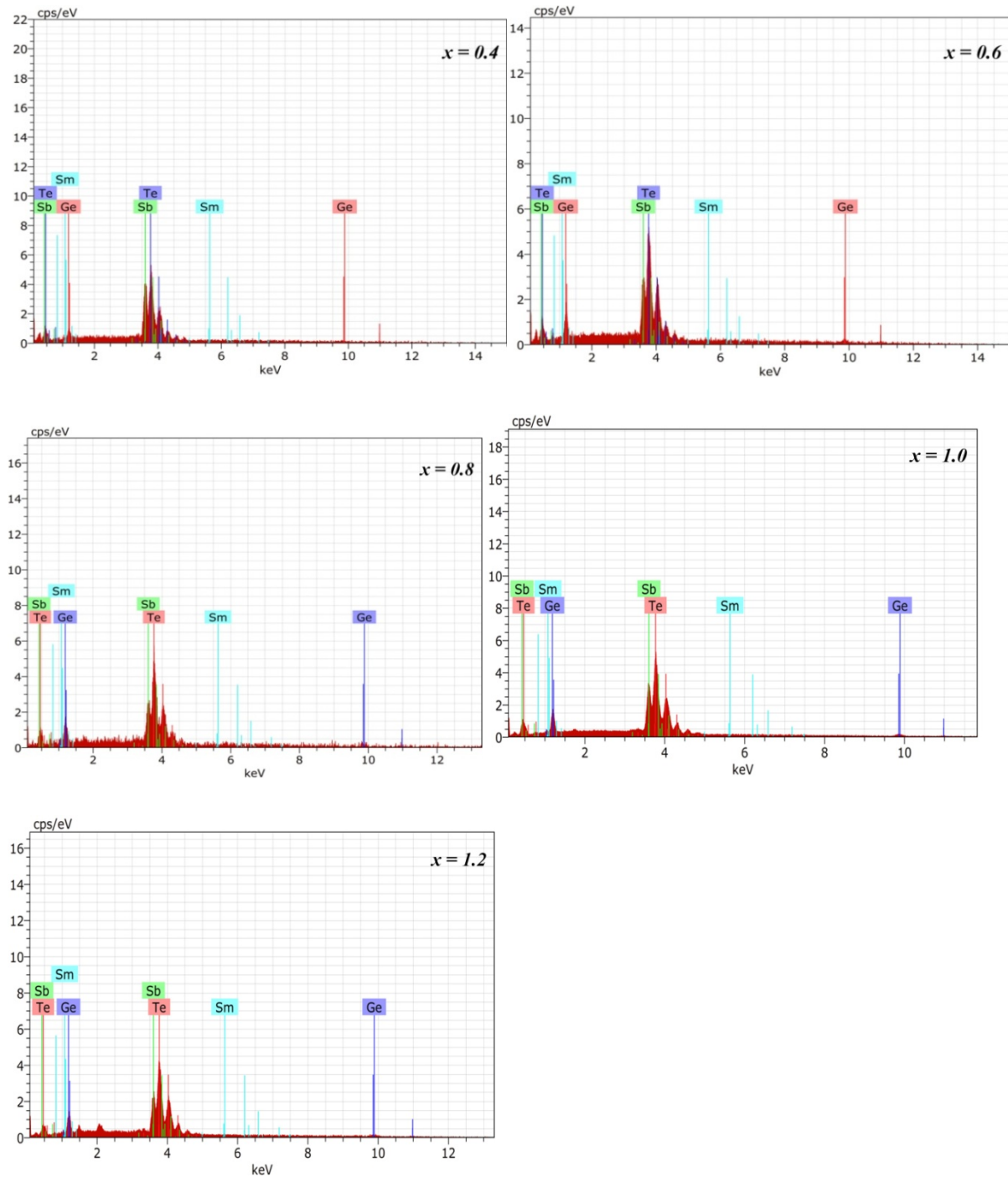
#### 5.3.1 Compositional Analysis

The presence of comprising elements in  $(GST)_{100-x}Sm_x$  alloy thin films has been examined from corresponding *EDX* spectra (Figure 5.1). The elements *Ge*, *Sb*, *Te* and *Sm* fraction in the  $(GST)_{100-x}Sm_x$  thin films computed by performing the *EDX* measurements at various locations on thin films surface indicate uniform elemental distribution. The evaluation of atomic fraction has been performed by averaging the values at different locations. The measured atomic fractions of all the samples have been observed to be in agreement with the stoichiometry and have been displayed for the samples  $x = 0$  and  $x = 0.8\%$  in table 5.1. The analysis of composition for  $(GST)_{100-x}Sm_x$  thin films have been also carried out using *XPS* measurements discussed in section 4.3.2.2.

	$Ge_2Sb_2Te_5 (x = 0)$			$(Ge_2Sb_2Te_5)_{99.20}Sm_{0.8} (x = 0.8)$		
	Measured		Calculated	Measured		Calculated
	Weight Percent (%)	Atomic Percent (%)	Atomic Percent (%)	Weight Percent (%)	Atomic Percent (%)	Atomic Percent (%)
<i>Te</i>	62.56	55.78	55.56	61.09	54.76	55.11
<i>Sb</i>	22.83	21.34	22.22	23.84	22.39	22.04
<i>Ge</i>	14.61	22.88	22.22	13.99	22.03	22.04
<i>Sm</i>	-	-	-	1.08	0.82	0.80
<b>Total</b>	100	100	100	100	100	100

**Table 5.1.**  $(Ge_2Sb_2Te_5)_{100-x}Sm_x$  ( $x = 0, 0.8$ ) thin film's compositional analysis.

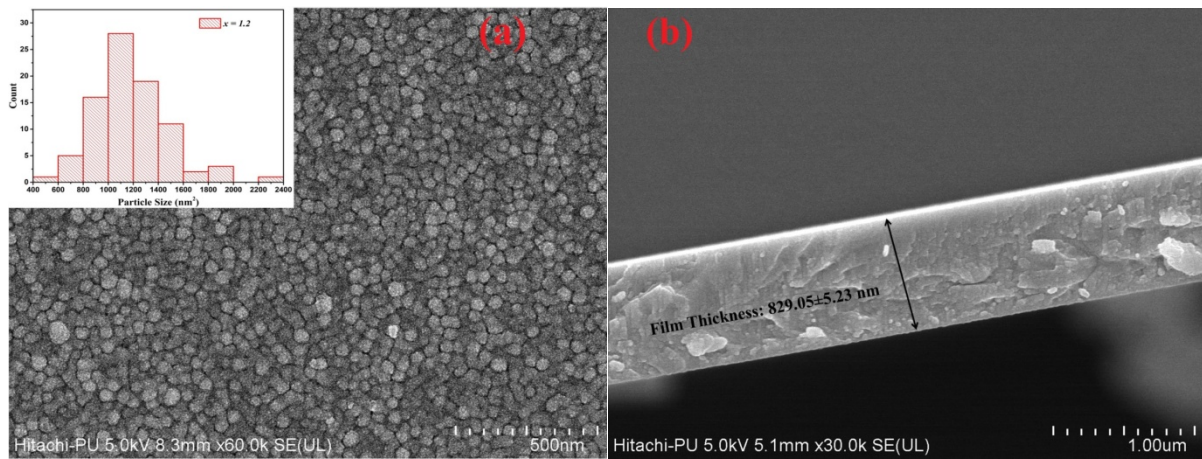




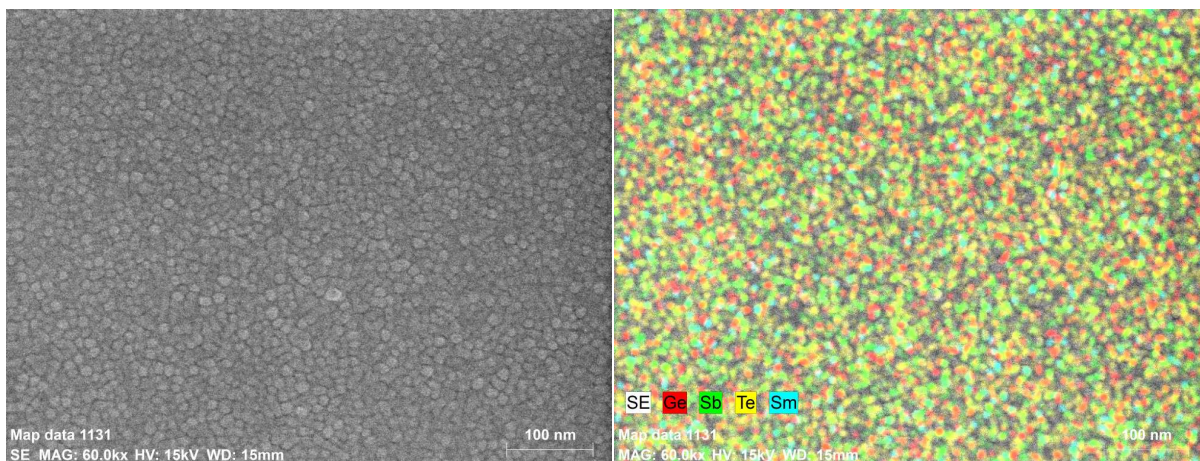
**Figure 5.1.** EDX spectra of  $(Ge_2Sb_2Te_5)_{100-x}Sm_x$  thin films.

The topography and elemental distribution analysis of surface of thin film  $(Ge_2Sb_2Te_5)_{100-x}Sm_x$  ( $x = 1.2$ ) have been performed using the FESEM measurements. The FESEM top view image of thin films of  $(Ge_2Sb_2Te_5)_{100-x}Sm_x$  ( $x = 1.2$ ) has been presented in figure 5.2(a) showing the smooth crack-free and uniform surface morphology. The particle

size of  $x = 1.2$  thin film sample has been analyzed to be in  $475 \text{ nm}^2 - 2200 \text{ nm}^2$  range with  $1170.87 \text{ nm}^2$  mean value. The inset of figure 5.2(a) displays histogram of particle size exhibiting Gaussian distribution. The *FESEM* image of the film has been also taken along the interfacial cross-section illustrating the appearance of void free texture (Figure 5.2(b)). The thickness of  $x = 1.2$  thin film measured from the cross-sectional image has been observed to be  $829.05 \pm 5.23 \text{ nm}$ . Figure 5.3 shows the elemental mapping images of *FESEM* for the thin film sample  $x = 1.2 \text{ at\% Sm}$ . The images show that the elements are distributed uniformly along the thin film surface.



**Figure 5.2(a).** *FESEM* top-view image of  $(\text{Ge}_2\text{Sb}_2\text{Te}_5)_{100-x}\text{Sm}_x$  ( $x = 1.2$ ) and inset displays histogram of particle size. **(b)** Thickness of  $(\text{Ge}_2\text{Sb}_2\text{Te}_5)_{100-x}\text{Sm}_x$  ( $x = 1.2$ ) thin film measured using *FESEM* cross section image.



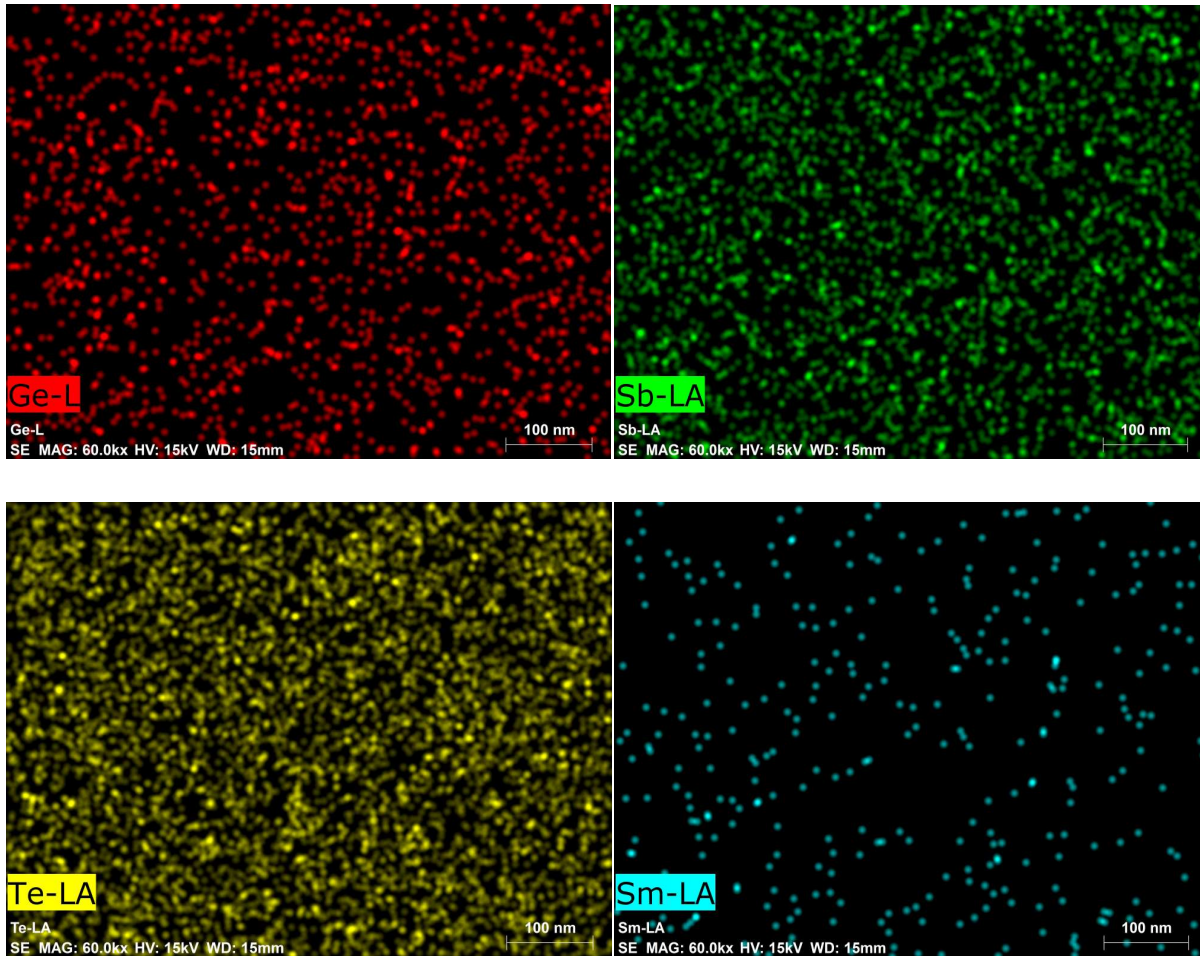


**Figure 5.3.** FESEM mapping of thin film of  $(Ge_2Sb_2Te_5)_{100-x}Sm_x$  ( $x = 1.2$ ).

### 5.3.2 Linear refractive index ( $n$ ) and optical absorption coefficient ( $\alpha$ )

The transmittance spectra of thin films of  $(Ge_2Sb_2Te_5)_{100-x}Sm_x$  have been illustrated in figure 5.4 exhibiting the oscillating curves. The beams of light reflected multiple times from the interface between the film-air, film-substrate and substrate-air produce interference pattern due to the path difference resulting in the oscillating curve. The appearance of fringe patterns of  $(Ge_2Sb_2Te_5)_{100-x}Sm_x$  thin films displayed in figure 5.4 indicates the uniform thickness in thin films of as-deposited  $(Ge_2Sb_2Te_5)_{100-x}Sm_x$ . The effect of local structure modification in  $Sm$  doped  $GST$  for optical properties has been investigated with respect to compositional dependence. The transmittance spectra of  $(Ge_2Sb_2Te_5)_{100-x}Sm_x$  thin films displayed in figure 5.4 shows the absorption edge redshift with  $Sm$  incorporation. The interference fringe pattern of transmittance spectra of  $Sm$  doped  $GST$  has been utilized to evaluate the refractive index ( $n$ ) along with optical extinction coefficient ( $k$ ) by making use of the Swanepoel approach [22]. *PARAV* software has been employed to evaluate the optical

constants by fitting the envelope functions [23]. The detailed procedure for the evaluation of optical constants by utilizing this approach has been briefly outlined in section 3.3.6.

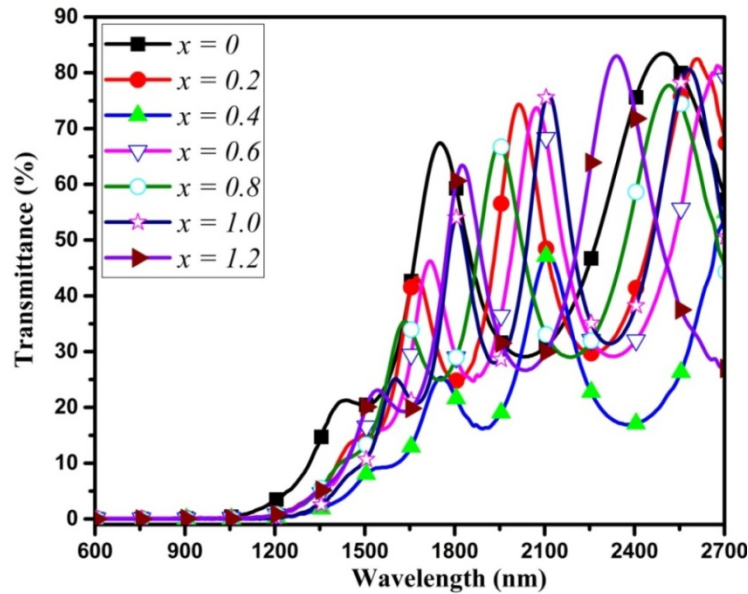


**Figure 5.4.** The transmittance spectra of  $(Ge_2Sb_2Te_5)_{100-x}Sm_x$  thin films.

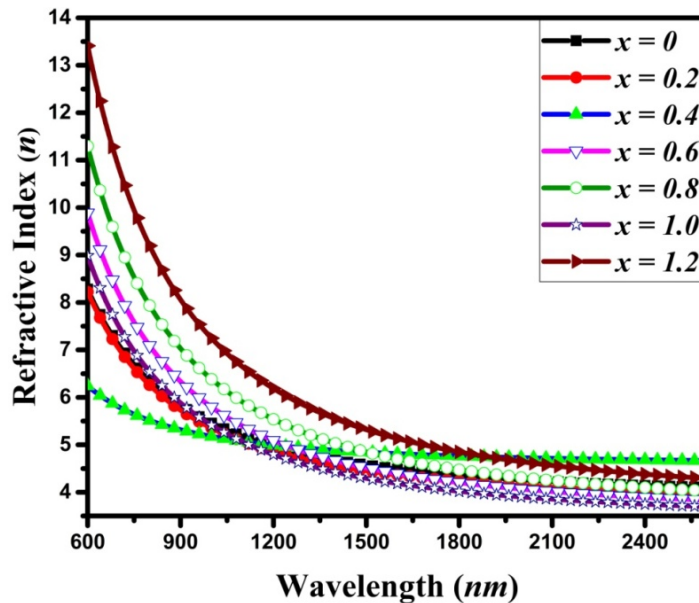


**Figure 5.5.** The linear index of refraction for  $(Ge_2Sb_2Te_5)_{100-x}Sm_x$  thin films.

The  $(Ge_2Sb_2Te_5)_{100-x}Sm_x$  thin film thickness ( $d$ ) values have been obtained by utilizing equation (3.6). The obtained values of  $d$  have been further employed for the calculation of refractive index ( $n$ ) by using equation (3.7). The linear interpolation of calculated  $n$  values at transparent and low absorption regions using the Cauchy dispersion relation  $\left(n = b + \frac{a}{\lambda^2}\right)$

has been employed to obtain  $n$  values in the strong absorption domain. The obtained  $n$  values of  $(Ge_2Sb_2Te_5)_{100-x}Sm_x$  thin films show normal dispersion with wavelength as shown in figure 5.5. The computed refractive index values for thin films of  $GST$  added with  $Sm$  exhibit maximum value for composition with  $Sm$  concentration  $x = 0.4$  at% followed by a decrease (Figure 5.5). The augmentation in  $n$  values analyzed at lower  $Sm$  concentration upto  $x = 0.4$  at% is on account of the increase in free electrons and unsaturated defects on  $Sm$  doping. Whereas the decrease in refractive index value on further increase in  $Sm$  concentration can be due to homopolar  $Sm-Sm$  bond creation. The equation (3.8) has been employed to evaluate the optical absorption coefficient ( $\alpha$ ) values of  $(Ge_2Sb_2Te_5)_{100-x}Sm_x$  thin film by utilizing the refraction coefficients at different interfaces [23].

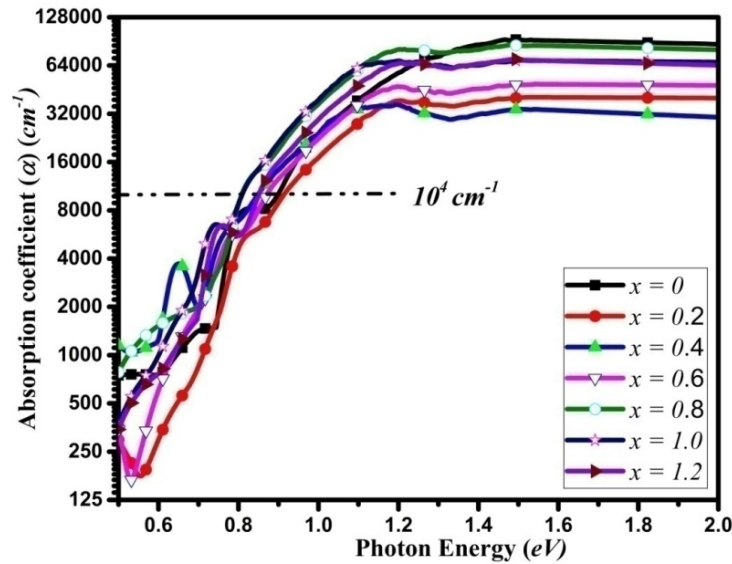


**Figure 5.6.** The plot of optical absorption coefficient ( $\alpha$ ) against photon energy ( $h\nu$ ) for  $(Ge_2Sb_2Te_5)_{100-x}Sm_x$  thin films.

Figure 5.6 presents  $\alpha$  vs  $h\nu$  plot of  $(Ge_2Sb_2Te_5)_{100-x}Sm_x$  thin films demonstrating the redshift on addition of  $Sm$ . The value of optical absorption coefficient ( $\alpha$ ) is used to compute the optical extinction coefficient ( $k(\lambda)$ ) by using the equation (3.9). The redshift of absorption edge can be also inferred from the shift of  $\alpha$  values with  $Sm$  content in the high absorption region ( $>10^4$   $cm^{-1}$ ) shown in figure 5.6. The comparatively larger shift of absorption edge for thin film having  $x = 0.4$  at%  $Sm$  can owing to the structural transitions on incorporation of  $Sm$  which has been also confirmed through the transmission spectra (Figure 5.4). The redshift observed for the absorption edge of  $(Ge_2Sb_2Te_5)_{100-x}Sm_x$  transmission spectra with  $Sm$  concentration can be correlated with the decrease in band gap value on  $Sm$  addition.

Furthermore, *Sm* addition also affects the interference fringe amplitude of  $(Ge_2Sb_2Te_5)_{100-x}Sm_x$  thin films which are due to the modification in the linear refractive index (*n*) with *Sm* content. The addition of *Sm* may also cause the modification of the local structure of *GST* leading to the disorder or defect creation which is reflected from the exponential or band tailing of the optical absorption spectrum. The Urbach energy ( $E_u$ ) computed employing the relation (3.10) has been utilized to assess the degree of band tailing in  $(Ge_2Sb_2Te_5)_{100-x}Sm_x$  thin films [24].

The  $E_u$  values of  $(Ge_2Sb_2Te_5)_{100-x}Sm_x$  thin films have been evaluated from  $\ln(\alpha)$  vs  $h\nu$  plot with slope  $1/E_u$  and intercept  $\ln(\alpha_0)$  according to equation (3.10). Table 5.2 summarizes the calculated values of  $E_u$  for thin films of *GST* added with *Sm* exhibiting an early decrease on *Sm* incorporation and followed by an increase for  $x > 0.4$  at%. For sample  $x = 0.4$  the presence of strong effects of interference near the absorption edge rules out the precise evaluation of  $E_u$ . The decrease in  $E_u$  value on *Sm* incorporation can be caused by strong heteropolar *Sm—Te* (~1.86 eV), *Ge—Sm* (~ 1.66 eV) and *Sm—Sb* (~1.63 eV) bonds creation. The rise in non-bonding electron concentration with *Sm* addition can be correlated with the localized state density. Furthermore, the enhancement in  $E_u$  values observed for  $x > 0.4$  at% *Sm* concentration may be the consequence of creation of *Sm—Sm* (~ 0.56 eV) homopolar bonds.

<i>x</i>	<i>d</i> (nm)	Tauc $E_g$ (eV)	$B^{1/2}$ ( $cm \cdot eV$ ) <sup>-1/2</sup>	$E_u$ (meV)	$E_d$	$E_o$	$E_g$ (eV) WDD	$N_c$
0	938.48	0.75	505.6	104.66	23.17	1.59	0.79	3.26
0.2	901.75	0.74	524.38	87.50	21.22	1.57	0.78	2.98
0.4	1047.67	0.73	613.00	.....	21.11	1.43	0.72	2.96
0.6	926.32	0.72	576.12	77.16	17.46	1.39	0.69	2.45
0.8	908.85	0.71	556.28	93.93	17.36	1.37	0.68	2.44
1.0	1158.93	0.70	543.32	98.98	17.27	1.35	0.67	2.43
1.2	928.67	0.68	534.94	118.6	17.18	1.32	0.66	2.41

**Table 5.2.** Thickness of thin film (*d*), optical band gap ( $E_g$ ) evaluated employing the Tauc and WDD methods, Urbach energy or tailing width ( $E_u$ ), dispersion energy ( $E_d$ ), single oscillator energy ( $E_o$ ), ordered parameter ( $B^{1/2}$ ) and cation coordination ( $N_c$ ) for  $(Ge_2Sb_2Te_5)_{100-x}Sm_x$  thin films.

### 5.3.3 Optical Gap ( $E_g$ ) and Optical Dispersion

The as-deposited thin films of  $(Ge_2Sb_2Te_5)_{100-x}Sm_x$  shows the three main absorption regions *viz.* low absorption region, exponential edge region ( $\alpha \leq 10^4 \text{ cm}^{-1}$ ) as well as high absorption region ( $\alpha \geq 10^4 \text{ cm}^{-1}$ ) which can be observed from the calculated absorption coefficient ( $\alpha$ ) displayed in figure 5.6. The absorption region has been utilized for the evaluation of optical gap ( $E_g$ ) by employing the Tauc method expressed in equation (3.11) [25]. The indirect bandgap in thin films of  $(Ge_2Sb_2Te_5)_{100-x}Sm_x$  have been estimated through the linear dependence of  $(\alpha h\nu)^{1/2}$  on photon energy ( $h\nu$ ) above  $\alpha \geq 10^4 \text{ cm}^{-1}$ . The  $E_g$  values of  $(Ge_2Sb_2Te_5)_{100-x}Sm_x$  have been evaluated by plotting  $(\alpha h\nu)^{1/2}$  vs  $(h\nu)$  followed by its linear fitting in the high absorption region. Figure 5.7 shows the Tauc plot with the extrapolation of linear fit in absorption region to zero value on the  $(\alpha h\nu)^{1/2}$  axis which provides the bandgap of  $(Ge_2Sb_2Te_5)_{100-x}Sm_x$  thin films. The obtained  $E_g$  values for  $(Ge_2Sb_2Te_5)_{100-x}Sm_x$  thin films have been summarized in table 5.2. The calculated  $E_g$  values of  $(Ge_2Sb_2Te_5)_{100-x}Sm_x$  show the redshift with  $Sm$  content. The slope of the linear fit of Tauc plot provides information about the order parameter ( $B^{1/2}$ ) and obtained values of  $B^{1/2}$  for thin films of  $GST$  incorporated with  $Sm$  are displayed in table 5.2. The values of  $B^{1/2}$  for thin films of  $(Ge_2Sb_2Te_5)_{100-x}Sm_x$  increase upto addition of  $x = 0.4 \text{ at}\%$   $Sm$  which may be on account of a decrease in the fraction of weak bonds with creation of strong  $Sm-Te$  bonds causing the reduction in disorder. Furthermore,  $Sm$  addition to  $GST$  inserts the charged  $C_1^-$  and  $P_2^-$  defects, which may result in the variation in density of localized states. The reduction of order parameter  $B^{1/2}$  at higher  $Sm$  content  $x > 0.4 \text{ at}\%$  can be due to the possibility of  $Sm-Sm$  bond formation resulting in disorder effects. The  $E_g$  value declines with  $Sm$  concentration which can be due to increase in both the band tailing width and localized state density up to addition of  $x = 0.4\%$   $Sm$ .

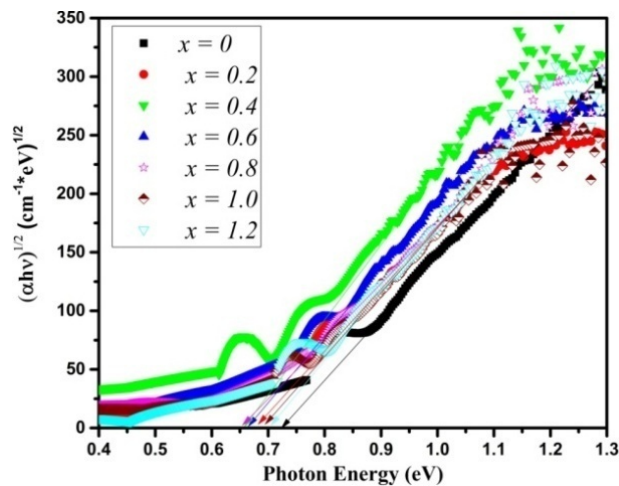


**Figure 5.7.** Tauc plots for  $(Ge_2Sb_2Te_5)_{100-x}Sm_x$  thin films.

The single oscillator expression (3.12) utilizes the refractive index values to estimate the dispersion parameters by using the Wemple-DiDomenico (*WDD*) model [26]. The dispersion energy ( $E_d$ ) as well as single oscillator energy ( $E_0$ ) for as-deposited  $(Ge_2Sb_2Te_5)_{100-x}Sm_x$  thin films have been evaluated. The dispersion energy obey the empirical relation  $E_d = \beta N_c Z_a N_e$  where  $\beta = 0.37 \pm 0.04$  eV for covalent solids and  $\beta = 0.26 \pm 0.03$  eV for ionic solids [27]. The values of  $E_d$  obtained using the *WDD* method have been used in this empirical relation for the calculation of cation coordination ( $N_c$ ) neighbouring anions and substituting the values of formal chemical valency ( $Z_a$ ) and total valence electrons per anion ( $N_e$ ). The evaluation of  $E_d$  and  $E_0$  values of  $(Ge_2Sb_2Te_5)_{100-x}Sm_x$  thin films has been performed by linear fitting the  $1/(n^2 - 1)$  vs  $(hv)^2$  plot with slope of  $\left(\frac{1}{E_0 E_d}\right)$  and intercept  $(E_0 / E_d)$  according to the equation (3.12).

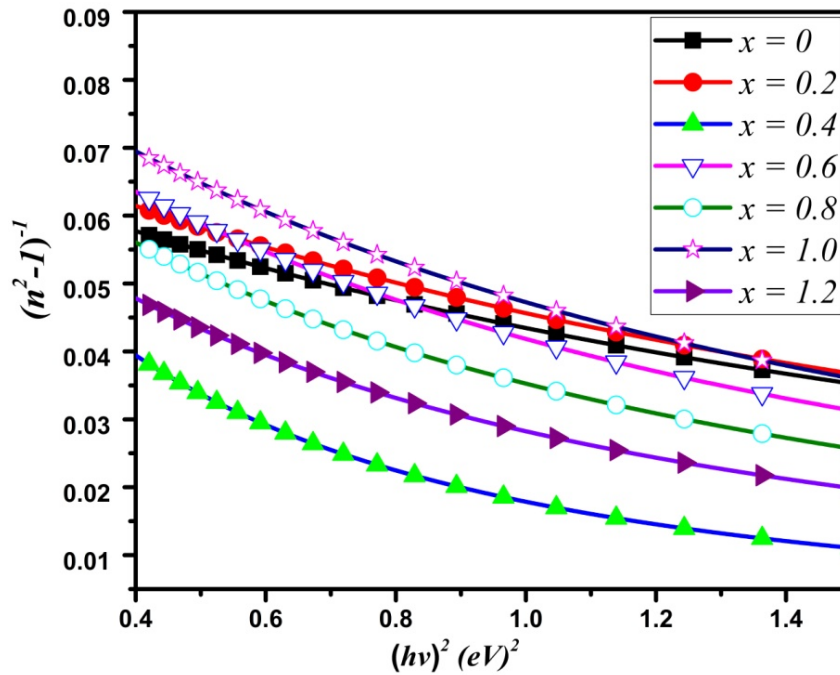


**Figure 5.8.**  $(n^2-1)^{-1}$  vs  $(hv)^2$  plot for  $(Ge_2Sb_2Te_5)_{100-x}Sm_x$  thin films.

Table 5.2 summarises the obtained  $E_0$  and  $E_d$  values exhibiting the decline on addition of *Sm*. The reduction in the dispersion energy with *Sm* addition to *GST* may be due to void formation and decrease in packing density. The cation coordination ( $N_c$ ) values obtained using the above empirical relation illustrates the decrease in its values with *Sm* content on account of its dependence on dispersion energy. The change in structural network and bonding in amorphous *GST* on *Sm* addition can be correlated to the variation in cation coordination. The comparatively larger atomic size of *Sm* may change the local structure of

cations (*Ge* in the present case) and subsequently the void formation leading to decrease in  $N_c$  values. The variation in the values of  $E_0$  agrees with the change in Tauc gap with *Sm* concentration as summarized in table 5.2. The higher  $E_0$  value signifies the higher bond strengths of chemical bonds formed in the samples. The values of static refractive index ( $n_0$ ) and static dielectric constant ( $\epsilon_L$ ) also known as zero frequency dielectric constant have been evaluated by utilizing the obtained values of  $E_0$  and  $E_d$  parameters employing the equation (3.13) [27]. The estimation of static parameters helps to explore the polarizability of materials and excludes the exciton generation effect and the loss associated with it. The small change in the values of  $n_0$  and  $\epsilon_L$  upto addition of  $x = 0.4$  at% *Sm* because of the collective effect of polarizability of bond for stronger *Sm—Te* bond and high atomic polarizability as a result of large ionic radius of *Sm*. Furthermore, as has been already described the creation of weak *Sm—Sm* bond at higher *Sm* concentration  $x > 0.4$  at% changes the polarizability and subsequently alters the values of  $n_0$  and  $\epsilon_L$  with *Sm* content.

The evaluation of  $M_{-1}$  and  $M_{-3}$ , the negative momentum coefficients, in the electronic domain of the  $\epsilon_2$  spectrum is performed employing the correlation with  $E_0$  and  $E_d$  through the expressions  $E_0^2 = \frac{M_{-1}}{M_{-3}}$  and  $E_d^2 = \frac{M_{-1}^3}{M_{-3}}$ . The  $M_{-3}$  values are related to dispersion of real component of dielectric constant near the band edge, while,  $M_{-1}$  values signify the real component dielectric constant magnitude underneath optical absorption edge. The obtained  $M_{-1}$  and  $M_{-3}$  values show the movement of the  $\epsilon_2$  spectrum along the lower energy on *Sm* addition to *GST*, which reveals compositional dependence of the distribution of free charges (Table 5.3). The change in  $M_{-1}$  and  $M_{-3}$  magnitudes varies in agreement with disorder effects induced on *Sm* addition to *GST* estimated through Tauc parameters [28].

The refractive index dispersion provides the electronic contribution of dielectric constant through the evaluation of high-frequency dielectric constant ( $\epsilon_\infty$ ) by utilizing the relation (3.14) [29]. The estimation of the values of  $\epsilon_\infty$  has been performed by utilizing the plot between  $n^2$  and  $\lambda^2$  and employing the linear fitting in the transparent region (Figure 5.9). The linear fitted curves intersect at  $\lambda^2 = 0$  axis which provides  $\epsilon_\infty$  value. The slope of the linear fitted curve corresponds to  $-\left(\frac{e^2}{4\pi^2\epsilon_0 c^2}\right)\left(\frac{N}{m^*}\right)$  where charge on electron is  $e$ , free space permittivity ( $\epsilon_0$ ), the light velocity ( $c$ ) whereas  $\left(\frac{N}{m^*}\right)$  represents the ratio of free carrier

concentration to effective mass. Table 5.3 summarizes the obtained  $\left(\frac{N}{m^*}\right)$  and  $\epsilon_{\infty}$  values of  $(Ge_2Sb_2Te_5)_{100-x}Sm_x$  thin films illustrating the decrease with  $Sm$  concentration.

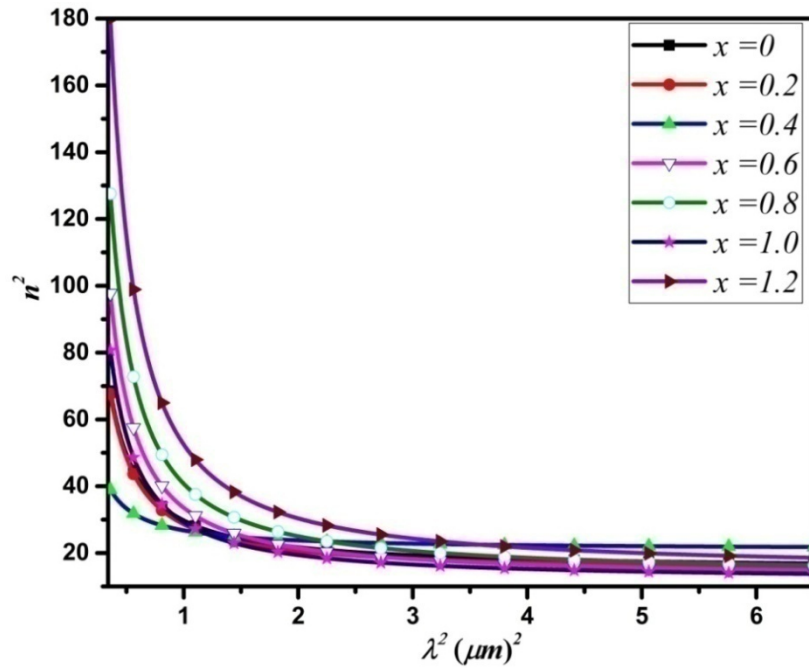


Figure 5.9.  $n^2$  vs  $\lambda^2$  plot for  $(Ge_2Sb_2Te_5)_{100-x}Sm_x$  thin films.

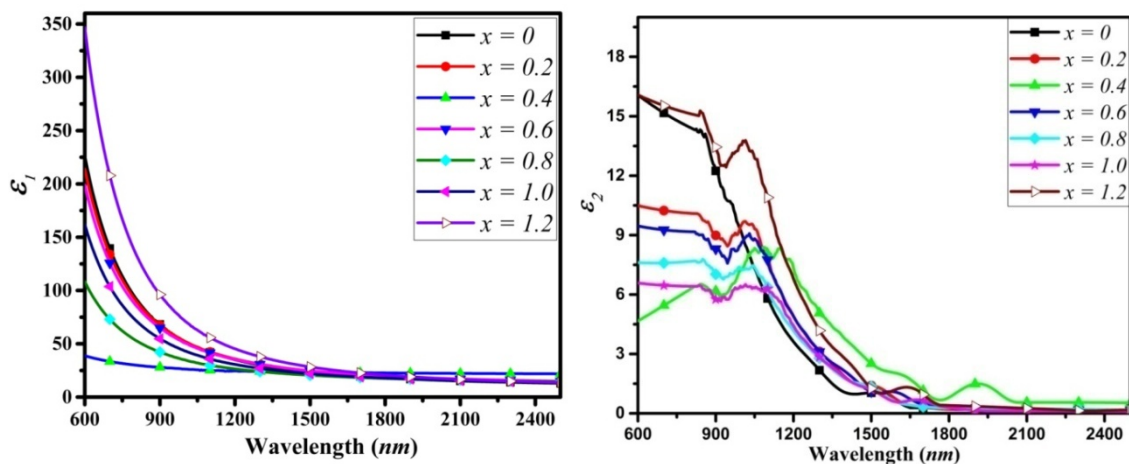
$x$	$\epsilon_{\infty}$	$N/m^*$ ( $g^{-1}cm^{-3}$ ) $\times 10^{47}$	$M_{-3}$	$M_{-1}$	$n_0$	$\epsilon_L$	$\omega_{Plasma}^2$ $\times 10^{28}$ Hz
0	19.78	4.39	5.67	14.49	3.94	1.98	1.61
0.2	18.72	4.33	5.47	13.51	3.81	1.95	1.67
0.4	18.03	4.23	7.13	14.70	3.96	1.99	1.69
0.6	17.71	4.08	6.40	12.50	3.67	1.92	1.67
0.8	17.20	4.02	6.73	12.66	3.69	1.92	1.69
1.0	16.98	3.91	7.07	12.82	3.72	1.93	1.67
1.2	16.48	3.82	7.42	12.98	3.74	1.93	1.68

Table 5.3. The value of parameters viz. high-frequency dielectric constant ( $\epsilon_{\infty}$ ),  $N/m^*$  ratio,  $M_{-3}$  and  $M_{-1}$  negative momentum coefficients, static refractive index ( $n_0$ ), static dielectric constant ( $\epsilon_L$ ) and plasma frequency ( $\omega_{Plasma}^2$ ) for  $Sm$  doped  $GST$ .

The equation (3.15) employs the obtained  $\left(\frac{N}{m^*}\right)$  value of  $(Ge_2Sb_2Te_5)_{100-x}Sm_x$  thin films to evaluate the plasma frequency ( $\omega_{plasma}^2$ ) [29]. The calculated  $\omega_{plasma}^2$  values of  $Sm$  doped  $GST$  shows the variation in the range  $1.6 \times 10^{28} Hz - 1.7 \times 10^{28} Hz$  on addition of  $Sm$  and have been shown in table 5.3.

### 5.3.4 Real and Imaginary Dielectric Constants, Energy Loss Functions and Optical Conductivity.

The evaluation of complex dielectric constant is important for the fabrication of optoelectronic devices, since it provides knowledge of electronic structure of the interacting medium. The complex dielectric constant ( $\epsilon^* = \epsilon_1 + i\epsilon_2$ ) is the sum of  $\epsilon_1$  and  $\epsilon_2$  that are respectively its real and imaginary part. The values of  $\epsilon_1$  and  $\epsilon_2$  for  $(Ge_2Sb_2Te_5)_{100-x}Sm_x$  thin films have been computed by using the relations  $\epsilon_1 = n^2 - k^2$  and  $\epsilon_2 = 2nk$ . The real part of dielectric constant  $\epsilon_1$  signifies the polarizability of the medium and is related to the material's ability to store energy and  $\epsilon_2$  represents the damping or dissipation or absorption of electromagnetic waves while propagating in the absorbing medium. Figure 5.10 (a) and (b) shows the dependence respectively of obtained  $\epsilon_1$  and  $\epsilon_2$  values on wavelength for thin films of  $(Ge_2Sb_2Te_5)_{100-x}Sm_x$ . The  $\epsilon_1(\lambda)$  plot of  $(Ge_2Sb_2Te_5)_{100-x}Sm_x$  thin films shows no significant change in its values below the band edge energy, but, increases in the absorption region. The observed  $\epsilon_2$  values below the band edge energy for  $(Ge_2Sb_2Te_5)_{100-x}Sm_x$  thin films are found to be less than unity and are higher above the bandgap energy. The shift in absorption edge with  $Sm$  concentration can be examined from the  $\epsilon_2$  spectra.



**Figure 5.10 (a).** The plots of wavelength versus  $\epsilon_1$  (b) and  $\epsilon_2$  for  $(Ge_2Sb_2Te_5)_{100-x}Sm_x$  thin films.

The electromagnetic waves dissipate while passing through the dielectric materials leading to dielectric loss computed using loss tangent  $\tan \delta = \frac{\epsilon_2}{\epsilon_1}$ . Figure 5.11 shows the  $\tan \delta$  versus wavelength plot of  $(Ge_2Sb_2Te_5)_{100-x}Sm_x$  thin films. The peak observed at around 1000 nm to 1100 nm in the  $\tan \delta$  plot signifies the maximum absorption in *GST* thin films incorporated with *Sm*. There is  $\tan \delta$  peak shift of  $(Ge_2Sb_2Te_5)_{100-x}Sm_x$  thin films on adding *Sm* following the variation of the optical gap.

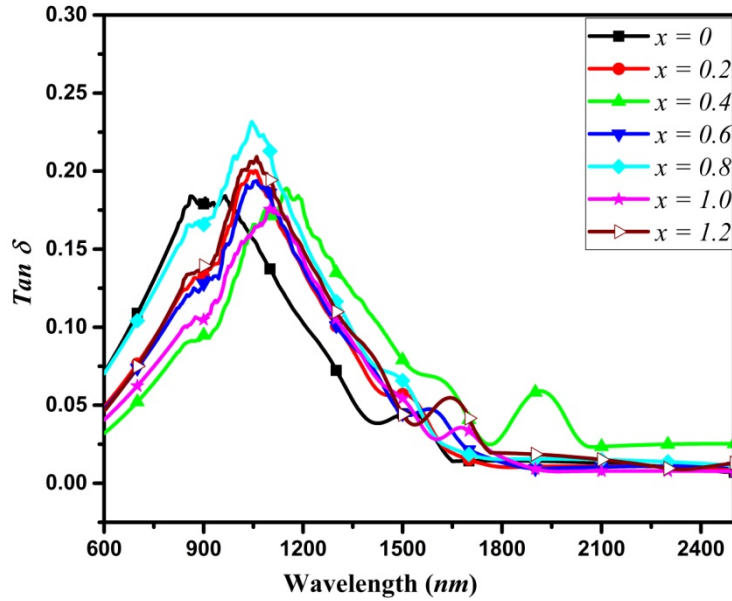


**Figure 5.11.** Wavelength dependence of dielectric loss of  $(Ge_2Sb_2Te_5)_{100-x}Sm_x$  thin films.

The bulk and surface electrons excitation probability of *GST* added with *Sm* has been assessed by computing the bulk energy loss function (*BELF*) and surface energy loss function (*SELF*) respectively. *SELF* corresponds to the imaginary part of  $-1/(1 + \epsilon)$  which has been calculated by using the relation [30],  $Im\{-1/[1 + \epsilon]\} = \left\{ \frac{\epsilon_2}{[(1 + \epsilon_1)^2 + \epsilon_2^2]} \right\}$ . Similarly the *BELF* correspond to the imaginary part of inverse of complex dielectric function and follows the relation [30]  $Im\{-1/\epsilon\} = \left\{ \frac{\epsilon_2}{[\epsilon_1^2 + \epsilon_2^2]} \right\}$ . The *SELF* and *BELF* plots as wavelength function for  $(Ge_2Sb_2Te_5)_{100-x}Sm_x$  have been displayed in figure 5.12 (a) and 5.12 (b) respectively. The most prominent intense peak in the spectra of both *SELF* and *BELF* in *Sm* doped *GST* describes the excitation energy of surface and bulk plasmon respectively. The position of peak in undoped *GST* sample spectra for *SELF* and *BELF* is observed respectively at 1026 nm and 1018.9 nm. The difference in the electron density between the surface and

bulk electrons leads to the lower energy of surface plasmon compared to bulk plasmon which has been reflected from the plasmon peak positions in the spectra of both *SELF* and *BELF* of *Sm* doped *GST*. The slight shoulder observed besides the surface plasmon peak in the spectra of *SELF* can be on account of the film substrate interface plasmon. Furthermore, the strong effects of interference for peak in the absorption region are observed in spectra of both *SELF* and *BELF* above wavelength *1800 nm*. The position of plasmon peak in the spectra of both *SELF* and *BELF* shifts towards the higher wavelength with *Sm* concentration.

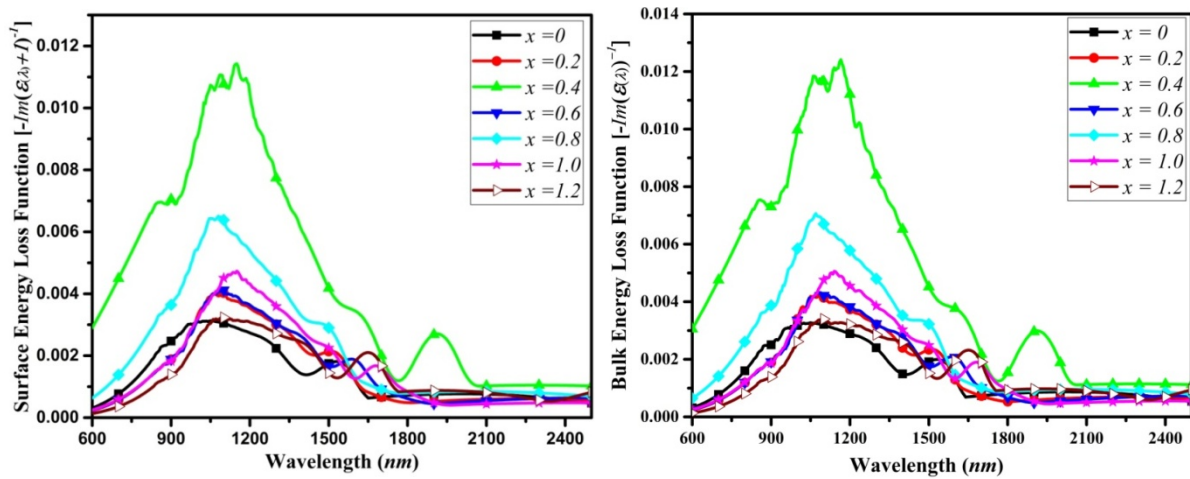


**Figure 5.12.** (a) *SELF*, Surface energy loss function (b) *BELF*, Bulk energy loss function for thin films of  $(Ge_2Sb_2Te_5)_{100-x}Sm_x$ .

The relation  $\sigma = \left(\frac{\alpha nc}{4\pi}\right)$  provides the correlation of optical conductivity ( $\sigma$ ) with the refractive index ( $n$ ) and absorption coefficient ( $\alpha$ ), where  $c$  represents the light velocity, [31]. Optical conductivity simply signifies the frequency dependent optical transitions of dielectric materials. Figure 5.13 shows the wavelength dependent optical response of  $(Ge_2Sb_2Te_5)_{100-x}Sm_x$  thin films which displays the strong absorption in the lower wavelength region. Moreover, the obtained value of  $\sigma$  shows sharp increase near the band edge and varies in accordance with absorption coefficient  $\alpha$  on *Sm* addition to *GST*. The optical conductivity of amorphous *GST* significantly differs from the corresponding crystalline phase because of the contrast in the optical gap. The evaluation of optical conductivity can be advantageous for *PC* memory applications to attain better signal-to-noise contrast. The incident light dissipates while propagation and the dissipation factor rises largely with an increase in photon energy, which can be inferred from figure 5.13. Comparatively lower dissipation for  $x = 0.4$  thin-film sample indicates that it can be advantageous for improved device performance.

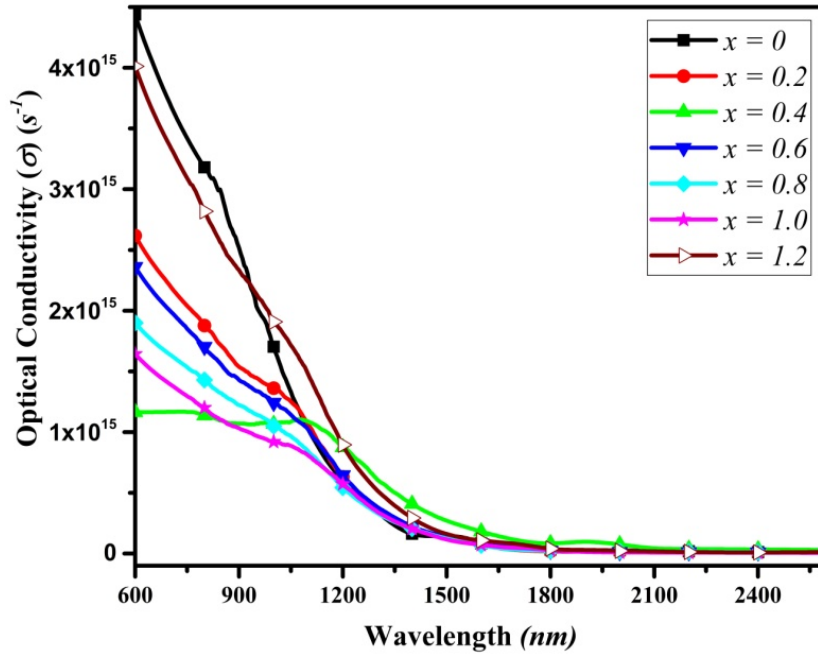


Figure 5.13. A plot of  $\sigma$  vs  $\lambda$  for  $(Ge_2Sb_2Te_5)_{100-x}Sm_x$  thin films.

### 5.3.5 Optical Non-linear Parameters

Polarizability ( $P$ ) can be expressed as a linear function of optical susceptibility ( $\chi$ ) and electric field ( $E$ ) as  $P = \chi^{(1)}E + \chi^{(2)}E^2 + \chi^{(3)}E^3$  where  $\chi^{(1)}(h\nu \rightarrow 0) = \frac{E_d}{4\pi E_0}$  is referred to as the linear optical susceptibility,  $\chi^{(2)}$  refers to the second-order non-linear susceptibility [29] and similarly  $\chi^{(3)}(h\nu \rightarrow 0) = 6.82 \times 10^{-15} \left(\frac{E_d}{E_0}\right)^4 esu = C [(n_0^2 - 1)/4\pi]^4$  and is known as third-order non-linear susceptibility. The  $\chi^{(2)}$  term vanishes for optically isotropic glassy materials. The third-order optical susceptibility ( $\chi^{(3)}$ ) specifies the optical excitations in longer wavelength regions due to the induced dipole moment. The covalent materials possess the  $\chi^{(3)}$  value in between  $10^{-9} esu$  to  $10^{-10} esu$  and lies in the range of  $10^{-14} esu$  to  $10^{-15} esu$  ionic materials. The interaction of incident light with energy lower than the bandgap value on thin films surface leads to the rearrangement of local structures. The evaluation of  $\chi^{(3)}$  value can be beneficial to understand the effect of exposure of light on material structures. Table 5.4 summarizes the obtained  $\chi^{(3)}$  values for  $(Ge_2Sb_2Te_5)_{100-x}Sm_x$  thin films which confirm the covalent nature of thin films of GST incorporated with Sm. The  $\chi^{(3)}$  values of Sm doped GST follows the change in  $\epsilon_L$  values with Sm concentration. The third-order non-

linear optical susceptibility shows dependence on non-linear refractive index ( $n_2$ ) and its value for  $(Ge_2Sb_2Te_5)_{100-x}Sm_x$  thin films has been obtained by using the expression [29]

$$n_2 = \frac{12\pi\chi^{(3)}}{n_0}$$

The variation in obtained values of  $n_2$  with  $Sm$  content follows the change in linear refractive index (Table 5.4). The  $n_2$  values are related to the polarizability in accordance with the Lorentz-Lorenz relation.

The optical electronegativity ( $\eta_{opt}$ ) of  $Sm$  doped  $GST$  thin films can be evaluated by utilizing the correlation [29]  $\eta_{opt} = \left(\frac{C}{n_0}\right)^{1/4}$  such that constant  $C$  has value 25.54. The obtained  $\eta_{opt}$  values for  $(Ge_2Sb_2Te_5)_{100-x}Sm_x$  thin films have been observed to be almost constant on addition of  $Sm$  and have been summarised in table 5.4.

$x$	$\chi^{(1)}$ ( $h\nu \rightarrow 0$ )	$\chi^{(3)} \times 10^{-10}$ ( $h\nu \rightarrow 0$ ) <i>esu</i>	$n_2 \times 10^{-9}$ ( $h\nu \rightarrow 0$ ) <i>esu</i>	$\eta_{opt}$ ( $h\nu \rightarrow 0$ )
0	1.15	3.01	2.88	1.59
0.2	1.07	2.27	2.25	1.61
0.4	1.17	3.19	3.03	1.59
0.6	0.99	1.66	1.71	1.62
0.8	1.00	1.75	1.78	1.62
1.0	1.02	1.84	1.87	1.62
1.2	1.03	1.94	1.95	1.62

**Table 5.4.** Linear optical susceptibility ( $\chi^{(1)}$ ), non-linear refractive index ( $n_2$ ), 3<sup>rd</sup> order non-linear susceptibility ( $\chi^{(3)}$ ), as well as optical electronegativity ( $\eta_{opt}$ ) for  $(Ge_2Sb_2Te_5)_{100-x}Sm_x$  thin films.

In summary,  $(Ge_2Sb_2Te_5)_{100-x}Sm_x$  thin films show depletion of band tailing width and simultaneous enhancement in localized state density upto addition of  $x = 0.4$  at%  $Sm$  which may be owing to the stronger heteropolar  $Sm-Te$  bond creation and change in concentration of charged defects. Moreover, the creation of homopolar  $Sm-Sm$  bonds has been analyzed for incorporation of higher  $Sm$  concentration  $x > 0.4$  at% leading to the enhancement in

width of band tailing states due to the disorder effects causing the lowering of  $E_g$  value. The lower optical gap and hence lower crystallization activation energy is advantageous for *PC* memory applications due to the improvement in switching speed.

The incorporation of *Sm* upto addition of  $x = 0.4 \text{ at\% Sm}$  alters the polarizability owing to the polar *Sm—Te* covalent bond creation and for addition of higher *Sm* concentration,  $x > 0.4 \text{ at\%}$  creates non-polar *Sm—Sm* bonds. This consequently changing the value of dielectric parameters. Furthermore, *Sm* doping affects the local bonding arrangement of *GST* which leads to the variation in non-linear refractive index and static refractive index with *Sm* content. The coordination number of cations in *GST* significantly affects the switching in *PC* materials. Moreover, *Sm* doping can be beneficial for improvement in the performance of *GST* on account of modification in local structure which has been corroborated through the variation in dispersion energy and non-linear parameters with *Sm* content.

### 5.4 Conclusion

The optical behavior of as-deposited  $(\text{Ge}_2\text{Sb}_2\text{Te}_5)_{100-x}\text{Sm}_x$  thin films have been studied and the effect of *Sm* addition has been analyzed. The value of optical gap ( $E_g$ ) for  $(\text{Ge}_2\text{Sb}_2\text{Te}_5)_{100-x}\text{Sm}_x$  thin films has been observed to decrease with *Sm* concentration from  $0.75 \text{ eV}$  to  $0.68 \text{ eV}$  on addition of  $x = 1.2 \text{ at\% Sm}$ . The calculated values of order parameter ( $B^{1/2}$ ) and Urbach energy vary inversely with each other on addition of *Sm*. The *Sm* doping enhances the conductivity of *GST* which has been corroborated from the lowering of optical gap ( $E_g$ ) and enhancement in band tailing extent on *Sm* addition. The reduction in the values of  $\epsilon_\infty$  and  $N/m^*$  ratio for  $(\text{Ge}_2\text{Sb}_2\text{Te}_5)_{100-x}\text{Sm}_x$  thin films with *Sm* concentration indicates the local structure alteration and modification in polarizability. Moreover, modification in values of non-linear parameters on *Sm* addition also supports local bonding network alteration. The  $\chi^{(3)}$  values of *Sm* doped *GST* signifies the creation of *Sm—Sm* bonds for incorporation of higher concentration of *Sm* to *GST* with simultaneous creation of charged defects  $C_1^-$  and  $P_2^-$  which may improve *GST* switching performance.

## References

- [1] P. Hu, T. -R. Wei, P. Qiu, Y. Cao, J. Yang, X. Shi, and L. Chen, “Largely Enhanced Seebeck Coefficient and Thermoelectric Performance by the Distortion of Electronic Density of States in  $\text{Ge}_2\text{Sb}_2\text{Te}_5$ ,” *ACS Appl. Mater. Interfaces*, vol. 11, no. 37, pp. 34046–34052, Sep. 2019.
- [2] T. Singh and R. R. Mansour, “Chalcogenide Phase Change Material GeTe Based Inline RF SPST Series and Shunt Switches,” in *2018 IEEE MTT-S International Microwave Workshop Series on Advanced Materials and Processes for RF and THz Applications, IMWS-AMP 2018*, 2018, pp. 1–3.
- [3] B. J. Eggleton, B. Luther-davies, and K. Richardson, “Chalcogenide photonics,” *Nat. Photonics*, vol. 5, no. 3, pp. 141–148, 2011.
- [4] X. Yu and J. Robertson, “Modeling of switching mechanism in GeSbTe chalcogenide superlattices,” *Sci. Rep.*, vol. 5, no. 1, p. 12612, Oct. 2015.
- [5] W. Zhang, R. Mazzarello, M. Wuttig, and E. Ma, “Designing crystallization in phase-change materials for universal memory and neuro-inspired computing,” *Nat. Rev. Mater.*, vol. 4, no. 3, pp. 150–168, Mar. 2019.
- [6] S.-Y. Lee, Y. -H. Kim, S. -M. Cho, G. H. Kim, T. -Y. Kim, H. Ryu, H. N. Kim, H. B. Kang, C. -Y. Hwang and C. -S. Hwang, “Holographic image generation with a thin-film resonance caused by chalcogenide phase-change material,” *Sci. Rep.*, vol. 7, no. 1, p. 41152, Mar. 2017.
- [7] M. Wuttig, H. Bhaskaran, and T. Taubner, “Phase-change materials for non-volatile photonic applications,” *Nature Photonics*, vol. 11, no. 8. pp. 465–476, 01-Aug-2017.
- [8] P. Singh, P. Sharma, V. Sharma, and A. Thakur, “Linear and non-linear optical properties of Ag-doped  $\text{Ge}_2\text{Sb}_2\text{Te}_5$  thin films estimated by single transmission spectra,” *Semicond. Sci. Technol.*, vol. 32, no. 4, p. 045015, Apr. 2017.
- [9] S. Liu, J. Wei, and F. Gan, “Optical nonlinear absorption characteristics of crystalline  $\text{Ge}_2\text{Sb}_2\text{Te}_5$  thin films,” *J. Appl. Phys.*, vol. 110, no. 3, p. 033503, Aug. 2011.
- [10] J. Sun, S. Mukhopadhyay, A. Subedi, T. Siegrist, and D. J. Singh, “Transport properties of cubic crystalline  $\text{Ge}_2\text{Sb}_2\text{Te}_5$ : A potential low-temperature thermoelectric

- material,” *Appl. Phys. Lett.*, vol. 106, no. 12, p. 123907, Mar. 2015.
- [11] K. V. Mitrofanov, A. V. Kolobov, P. Fons, X. Wang, J. Tominaga, Y. Tamenori, T. Uruga, N. Ciocchini, and D. Ielmini, “Ge L 3 -edge x-ray absorption near-edge structure study of structural changes accompanying conductivity drift in the amorphous phase of  $\text{Ge}_2\text{Sb}_2\text{Te}_5$ ,” *J. Appl. Phys.*, vol. 115, no. 17, p. 173501, May 2014.
- [12] W.-X. Song, Z.-P. Liu, and L.-M. Liu, “Inherent Simple Cubic Lattice Being Responsible for Ultrafast Solid-Phase Change of  $\text{Ge}_2\text{Sb}_2\text{Te}_5$ ,” *J. Phys. Chem. Lett.*, vol. 8, no. 12, pp. 2560–2564, Jun. 2017.
- [13] C. Chen, P. Jost, H. Volker, M. Kaminski, M. Wirtsohn, U. Engelmann, K. Kruger, F. Schlich, C. Schlockermann, R. P. S. M. Lobo, and M. Wuttig, “Dielectric properties of amorphous phase-change materials,” *Phys. Rev. B*, vol. 95, no. 9, p. 094111, Mar. 2017.
- [14] T. A. Miller, M. Rudé, V. Pruneri, and S. Wall, “Ultrafast optical response of the amorphous and crystalline states of the phase change material  $\text{Ge}_2\text{Sb}_2\text{Te}_5$ ,” *Phys. Rev. B*, vol. 94, no. 2, p. 024301, Jul. 2016.
- [15] W. K. Njoroge, H.-W. Wöltgens, and M. Wuttig, “Density changes upon crystallization of  $\text{Ge}_2\text{Sb}_{2.04}\text{Te}_{4.74}$  films,” *J. Vac. Sci. Technol. A Vacuum, Surfaces, Film.*, vol. 20, no. 1, pp. 230–233, Jan. 2002.
- [16] H. Zou, Y. Hu, X. Zhu, and Z. Song, “Simultaneously high thermal stability and ultrafast phase change speed based on samarium-doped antimony thin films,” *RSC Adv.*, vol. 7, no. 49, pp. 31110–31114, 2017.
- [17] H. Zou, L. Zhai, Y. Hu, X. Zhu, H. You, J. Zhang, S. Song and Z. Song, “Samarium doped  $\text{Sn}_{15}\text{Sb}_{85}$ : A promising material for phase change memory applications,” *RSC Adv.*, vol. 7, no. 88, pp. 56000–56005, 2017.
- [18] Y. Chen, N. Chen, B. Chen, Q. Zhang, X. Li, Q. Deng, B. Zhang, S. Zhang, Z. Zhang, and X. Han, “Electrical properties and structural transition of  $\text{Ge}_2\text{Sb}_2\text{Te}_5$  adjusted by rare-earth element Gd for nonvolatile phase-change memory,” *J. Appl. Phys.*, vol. 124, no. 14, p. 145107, Oct. 2018.

- [19] H. Zou, X. Zhu, Y. Hu, Y. Sui, Y. Sun, J. Zhang, L. Zheng, and Z. Song, “Simultaneous thermal stability and phase change speed improvement of  $\text{Sn}_{15}\text{Sb}_{85}$  thin film through erbium doping,” *J. Appl. Phys.*, vol. 120, no. 24, p. 245303, Dec. 2016.
- [20] Z. Li, C. Si, J. Zhou, H. Xu, and Z. Sun, “Yttrium-Doped  $\text{Sb}_2\text{Te}_3$ : A Promising Material for Phase-Change Memory,” *ACS Appl. Mater. Interfaces*, vol. 8, no. 39, pp. 26126–26134, 2016.
- [21] Y. J. Huang, M. C. Tsai, C. H. Wang, and T. E. Hsieh, “Characterizations and thermal stability improvement of phase-change memory device containing Ce-doped  $\text{GeSbTe}$  films,” *Thin Solid Films*, vol. 520, no. 9, pp. 3692–3696, 2012.
- [22] R. Swanepoel, “Determination of surface roughness and optical constants of inhomogeneous amorphous silicon films,” *J. Phys. E.*, vol. 17, no. 10, pp. 896–903, Oct. 1984.
- [23] A. Ganjoo and R. Golovchak, “Computer program PARAV for calculating optical constants of thin films and bulk materials: Case study of amorphous semiconductors,” *J. Optoelectron. Adv. Mater.*, vol. 10, no. 6, pp. 1328–1332, 2008.
- [24] F. Rao, Z. Song, Y. Cheng, M. Xia, K. Ren, L. Wu, B. Liu, S. Feng, “Investigation of changes in band gap and density of localized states on phase transition for  $\text{Ge}_2\text{Sb}_2\text{Te}_5$  and  $\text{Si}_{3.5}\text{Sb}_2\text{Te}_3$  materials,” *Acta Mater.*, vol. 60, no. 1, pp. 323–328, Jan. 2012.
- [25] J. Tauc, R. Grigorovici, and A. Vancu, “Optical Properties and Electronic Structure of Amorphous Germanium,” *Phys. status solidi*, vol. 15, no. 2, pp. 627–637, 1966.
- [26] S. H. Wemple, “Refractive-Index Behavior of Amorphous Semiconductors and Glasses,” *Phys. Rev. B*, vol. 7, no. 8, pp. 3767–3777, Apr. 1973.
- [27] S. H. Wemple and M. DiDomenico, “Behavior of the Electronic Dielectric Constant in Covalent and Ionic Materials,” *Phys. Rev. B*, vol. 3, no. 4, pp. 1338–1351, Feb. 1971.
- [28] S. H. Wemple, J. D. Gabbe, and G. D. Boyd, “Refractive-index behavior of ternary chalcopyrite semiconductors,” *J. Appl. Phys.*, vol. 46, no. 8, pp. 3597–3605, 1975.
- [29] A. S. Hassanien and I. Sharma, “Optical properties of quaternary  $\text{a-Ge}_{15-x}\text{Sb}_x\text{Se}_{50}\text{Te}_{35}$  thermally evaporated thin-films: refractive index dispersion and single oscillator parameters,” *Optik (Stuttg.)*, vol. 200, no. July 2019, p. 163415, Jan. 2020.

- [30] G. L. Tan, L. K. Denoyer, R. H. French, M. J. Guittet, and M. Gautier-Soyer, “Kramers-Kronig transform for the surface energy loss function,” *J. Electron Spectros. Relat. Phenomena*, vol. 142, no. 2, pp. 97–103, 2005.
- [31] W. G. Spitzer and H. Y. Fan, “Determination of Optical Constants and Carrier Effective Mass of Semiconductors,” *Phys. Rev.*, vol. 106, no. 5, pp. 882–890, Jun. 1957.



**Chapter 6**  
**Thermal and Electrical**  
**Properties of  $(Ge_2Sb_2Te_5)_{100-x}Sm_x$**   
**Thin Films**

- **Sanjay Kumar** and Vineet Sharma, “Improvement in thermal stability and crystallization mechanism of *Sm* doped  $Ge_2Sb_2Te_5$  thin films for phase change memory applications,” **Journal of Alloys and Compounds**, vol. 893, p. 162316, Feb. 2022.



## 6.1 Introduction

The 21<sup>st</sup>-century era is mainly focused on the development of artificial intelligence (AI) applications which entails the requirement of efficient computing devices that can perform rapid data processing and large storage capacity [1]. Current computing algorithms based upon von Neumann and existing storage devices cannot fulfill such demands. The futuristic memory devices based upon neuro-inspired computing are capable to mimic the activity of the human brain and are considered as the preferred choice for next-generation memories [2]. Many memory technologies are under active research and development and among them the phase change (PC) memories are the most mature and have already been launched in the market and are known as 3D X-Point storage class memories. Chalcogenide PC memories can unify gap of performance among DRAMs and SSDs. The use of PC non-volatile memories can be advantageous to overcome the drawbacks of the existing computing approach [2].

$Ge_2Sb_2Te_5$  (GST) acts as the programmable material in PC non-volatile memories and has been considered as the backbone of next-generation memory. The amorphous GST transforms to the crystalline state on heating over glass transition temperature ( $T_g$ ) and is referred to as SET (writing) operation. The operation RESET (erasing) in PC memory is realized by heating up to the melting temperature ( $T_m$ ) of GST followed by rapid quenching leading to formation of the amorphous phase. GST undergoes the two-stage crystallization, the first step includes the amorphous to fcc phase transformation accompanying the change in Ge local environment [3]. In the second stage, there is transition of fcc to hexagonal phase through the completion of vacancy layer by Te atoms and subsequently forming the Te—Te bonds which alters the Sb atom local environment [4].

The resistance drift issue of amorphous GST limits the switching speed of storage devices due to the presence of Ge rich tetrahedral  $GeTe_{4-x}Ge_x$  ( $x = 1, 2$ ) structures containing Sb—Sb, Ge—Ge and Ge—Sb homopolar bonds [5]. GST is also considered to be a candidate material for thermoelectric applications besides their use in storage devices [6].

The crystallization mechanism of GST must be explored for the improvement in PC memory device performance. The crystallization of GST plays a significant role in PC memory device performance and is related directly to the thermal parameters viz. peak crystallization ( $T_p$ ) and melting temperature ( $T_m$ ). Different methods for the investigation of crystallization kinetics of GST have been employed such as temperature-dependent sheet

resistance measurements, differential scanning calorimetry (*DSC*), laser irradiation, *etc.* [7]–[9]. Hudgens and Johnson [10] theoretically overestimated the value of  $T_g$  for *GST* at  $\sim 350^\circ\text{C}$  which is experimentally observed to be below  $150^\circ\text{C}$  [11]. The *DSC* analysis of *GST* has been reported by J. Kalb *et al.* [11] and claimed the glass transition temperature ( $T_g$ ) to merge at  $101^\circ\text{C}$  with crystallization onset ( $T_c$ ). Though, the authors modified this result in the later stage in another article and reported the separate signals for  $T_g$  and  $T_c$  [7]. Lankhorst [12] analyzed the value of  $T_g$  for *GST* at  $111^\circ\text{C}$  temperature which is close to Kalb's observation. The low reduced glass transition temperature ( $T_{rg}$ ) along with rapid crystallization ability causes marginal glass-forming ability in *GST* [11].

This chapter includes the measurements and analysis of differential scanning calorimetry (*DSC*) in non-isothermal conditions, temperature dependent current-voltage (*I-V*) and *XRD* studies of  $(\text{Ge}_2\text{Sb}_2\text{Te}_5)_{100-x}\text{Sm}_x$  thin films. The *DSC* measurements have been used to study the outcome of *Sm* incorporation on *GST* for crystallization kinetics. The thermal parameters of *GST* added with *Sm* *viz.*  $T_c$ ,  $T_p$ ,  $T_m$  *etc.* have been computed to investigate the structural rigidity. Henderson's and Matusita's methods have been adopted to estimate the Avrami exponent ( $n$ ) and crystallization activation energy ( $E_c$ ) of *Sm* doped *GST*. The temperature dependent current-voltage (*I-V*) measurements of  $(\text{Ge}_2\text{Sb}_2\text{Te}_5)_{100-x}\text{Sm}_x$  thin films have been performed for the analysis of electrical resistivity of as-deposited thin films.

## 6.2 Experimental Section

The synthesis of  $(\text{Ge}_2\text{Sb}_2\text{Te}_5)_{100-x}\text{Sm}_x$  ( $x = 0, 0.2, 0.4, 0.6, 0.8, 1.0, 1.2$ ) bulk alloys have been carried out employing the melt-quenching. The *HINDHIVAC 12A4D* thermal evaporation unit has been utilized for the deposition of thin films of  $(\text{Ge}_2\text{Sb}_2\text{Te}_5)_{100-x}\text{Sm}_x$  using thermal evaporation by making use of the as-prepared powder sample for evaporation. The detailed procedure for the synthesis of *Sm* incorporated *GST* samples has been described in section 5.2. The curves obtained from *DSC* instrument (*EXSTAR TG/DTA 6300*) have been used for the analysis of crystallization kinetics of as-deposited  $(\text{Ge}_2\text{Sb}_2\text{Te}_5)_{100-x}\text{Sm}_x$  thin film. The *DSC* measurements have been performed in a non-isothermal environment at  $10\text{K}/\text{min}$  steady heating rate. The  $200\text{ ml}/\text{min}$  flow of argon gas has been maintained throughout the *DSC* measurements to ensure the inert atmosphere. The non-isothermal *DSC* characterization has been performed by using  $5.0\text{mg}$  powder sample obtained by scratching the as-deposited thin films. The alumina powder has been used as a reference sample and the alumina pan as a sample holder. The current-voltage characteristics of as-deposited  $(\text{Ge}_2\text{Sb}_2\text{Te}_5)_{100-x}\text{Sm}_x$  thin

films have been carried out using Keithley 2611 electrometer with temperature. The  $(Ge_2Sb_2Te_5)_{100-x}Sm_x$  thin films have been annealed at temperatures  $50^\circ C$ ,  $160^\circ C$  and  $250^\circ C$  for an hour in vacuum ( $10^{-3}$  mbar). X-ray diffractometer (Panalytical X'Pert Pro) has been used to study the change in structure of these vacuum annealed thin films of  $(Ge_2Sb_2Te_5)_{100-x}Sm_x$ .

## 6.3 Results and Discussion

### 6.3.1 DSC Analysis

The non-isothermal *DSC* curves obtained at a steady heating rate of  $10K/min$  have been employed to study the crystallization in thin films of  $(Ge_2Sb_2Te_5)_{100-x}Sm_x$ . The compositional dependence of crystallization temperature of *GST* with varying *Sm* concentration has been investigated. Figure 6.1 shows the *DSC* curves of as-deposited  $(Ge_2Sb_2Te_5)_{100-x}Sm_x$  thin films exhibiting the appearance of melting temperature ( $T_m$ ) and peak crystallization temperature. The *DSC* curves display the exothermic peaks at the temperature of about  $150^\circ C$  which has been assigned to the *fcc* crystallization of *GST*. Apart from that, an additional exothermic peak has been also observed in *DSC* curves of *GST* added with *Sm* in the temperature range  $235^\circ C - 240^\circ C$  ascribed for the hexagonal crystallization of *GST* and corresponding peak crystallization temperature has been marked  $T_{p2}$  in figure 6.1. The crystallization in various *Sm* doped *GST* compositions can be analysed from the various thermal parameters *viz.*  $T_c$ , *fcc* peak crystallization temperature ( $T_{p1}$ ), hexagonal phase peak crystallization temperature ( $T_{p2}$ ) along with melting temperature ( $T_m$ ) and their values are tabulated in table 6.1.

$x$	$T_c$ (K)	$T_{p1}$ (K)	$T_m$ (K)
0	419.29	423.03	879.13
0.2	421.93	433.57	881.23
0.4	419.57	432.53	872.25
0.6	419.53	436.01	877.73
0.8	413.63	432.31	879.53
1.0	424.43	427.31	880.36
1.2	411.73	421.07	879.55

**Table 6.1.** Onset and peak crystallization temperature and  $T_m$  values for  $(Ge_2Sb_2Te_5)_{100-x}Sm_x$  thin films.

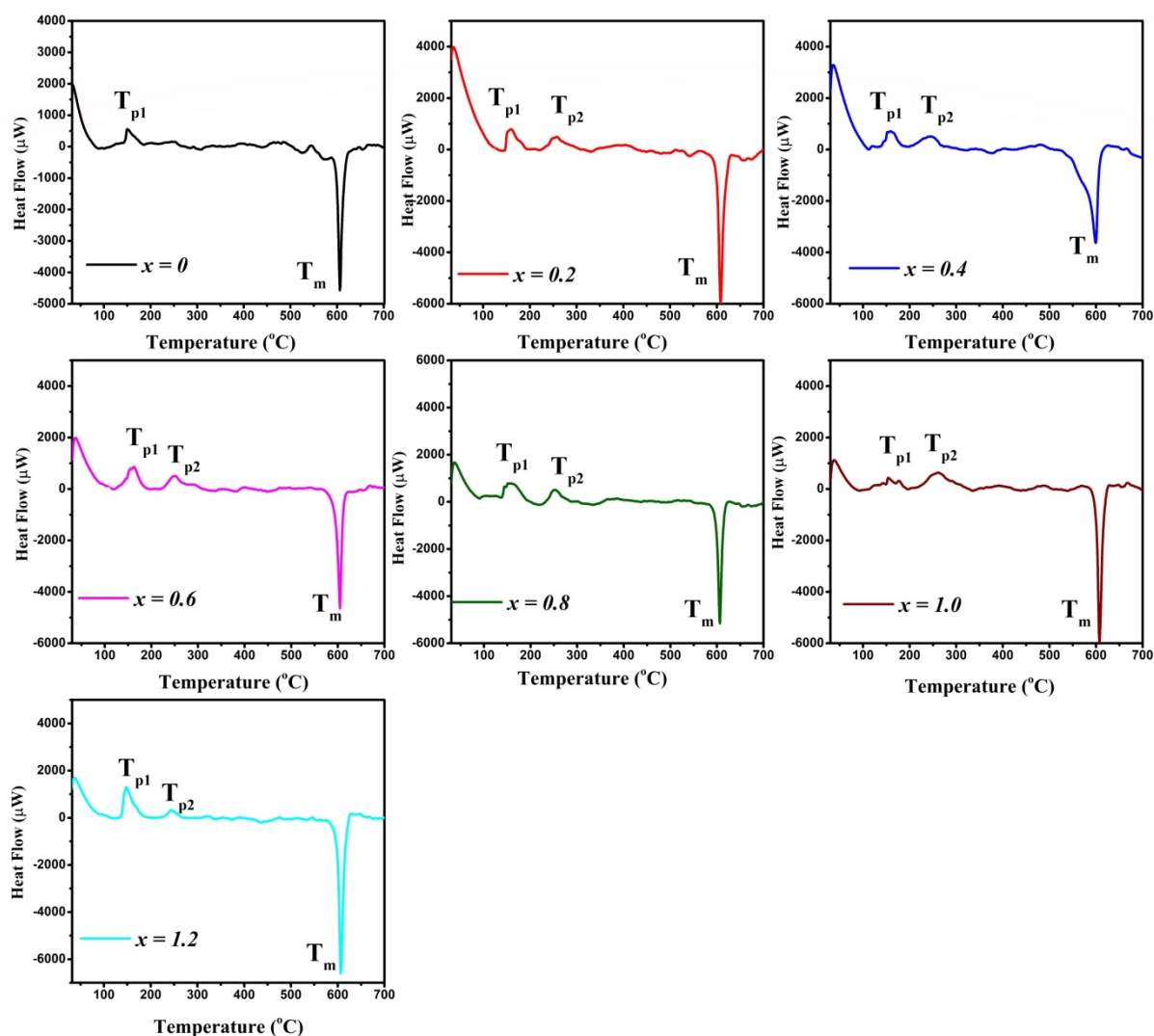


**Figure 6.1.** DSC thermogram of  $(Ge_2Sb_2Te_5)_{100-x}Sm_x$  thin films obtained at  $10K/min$  linear heating rate.

### 6.3.2 Crystallization

The approach of Johnson-Mehl-Avrami (*JMA*) has been adopted to analyse the crystallization kinetics of  $(Ge_2Sb_2Te_5)_{100-x}Sm_x$  samples in a non-isothermal conditions. The *JMA* approach was initially developed for the analysis of crystallization mechanism in isothermal conditions which involves the dependence of time on the crystallization fraction ( $\chi$ ). The applicability of the *JMA* approach has been also extended for the non-isothermal conditions in some of the reports only for “isokinetic” transformations, *i.e.*, which means nucleation ought to take place at the beginning of crystallization transformation reaction and must have zero nucleation rate during the growth process [13]–[15]. The *JMA* based analysis methods for the investigation of non-isothermal crystallization kinetics demands ample

insight on nucleation and growth processes involved in the crystallization for a system to ensure the validity of this analysis method. The kinetics of crystallization for  $Ge_2Sb_2Te_5$  has been explored extensively in the literature [16]–[18]. However, it has been reported that there is significant difference in mechanism of crystallization for  $GST$  between the samples synthesized employing melt-quench and thermal evaporation methods. [19]. The crystallization initiates through the nuclei acted upon by square rings of  $-Te-Sb-Te-Ge-$  in  $GST$  thin films. The relevance of the methods utilized for thermal analysis of mechanism of crystallization in  $GST$  thin films has been examined and the impact of  $Sm$  doping has been investigated.

### 6.3.2.1 Henderson's Method

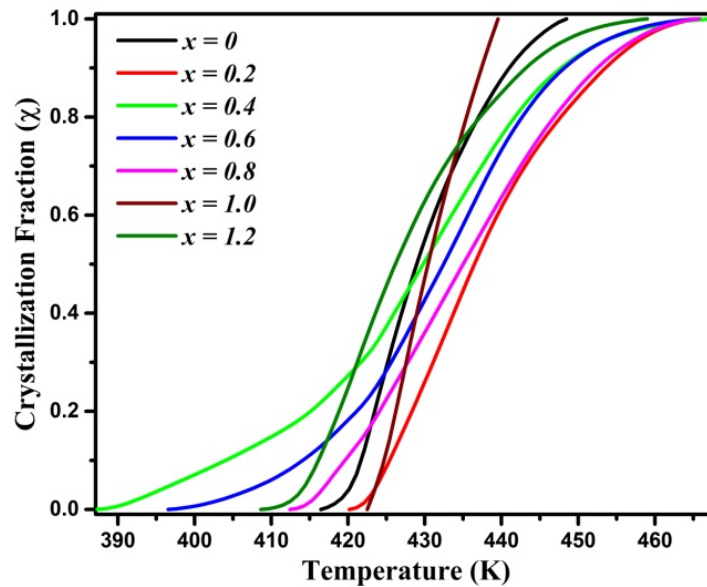
Henderson's method extends the rate equation for  $JMA$  transformation to analyze the kinetics of non-isothermal crystallization process [14], [15]. This method has limited applicability. Figure 6.1 shows the  $DSC$  curves of  $(Ge_2Sb_2Te_5)_{100-x}Sm_x$  samples obtained at  $10K/min$  heating rate in non-isothermal conditions. The crystallization activation energy ( $E_c$ ) of  $GST$  added with  $Sm$  has been evaluated employing equation (3.16) showing the dependence of  $E_c$  on crystallization fraction ( $\chi$ ).

$x$	<i>Handerson's Method</i>			<i>Matusita's Method</i>			<i>Avg.</i> $E_{c1}(eV)$
	$E_{c1}(eV)$	$E_{c1}/n_1 (eV)$	$n_1$	$mE_{c1}(eV)$	$m$	$E_{c1} (eV)$	
0	2.43	2.14	1.14	2.31	1	2.31	2.37
0.2	2.19	2.09	1.05	2.08	1	2.08	2.13
0.4	1.12	1.02	1.10	1.06	1	1.06	1.09
0.6	1.58	1.24	1.27	1.50	1	1.50	1.54
0.8	1.68	1.56	1.07	1.60	1	1.60	1.64
1.0	2.07	2.63	0.78	1.97	1	1.97	2.02
1.2	2.08	1.96	1.06	1.98	1	1.98	2.03

**Table 6.2.** The activation energy for  $fcc$  crystallization in  $(Ge_2Sb_2Te_5)_{100-x}Sm_x$  samples.

The calculation of crystallization fraction ( $\chi$ ) from the exothermic peak of  $DSC$  curves of  $(Ge_2Sb_2Te_5)_{100-x}Sm_x$  samples has been performed using the relation  $\chi = A/A_T$  where  $A$  refers

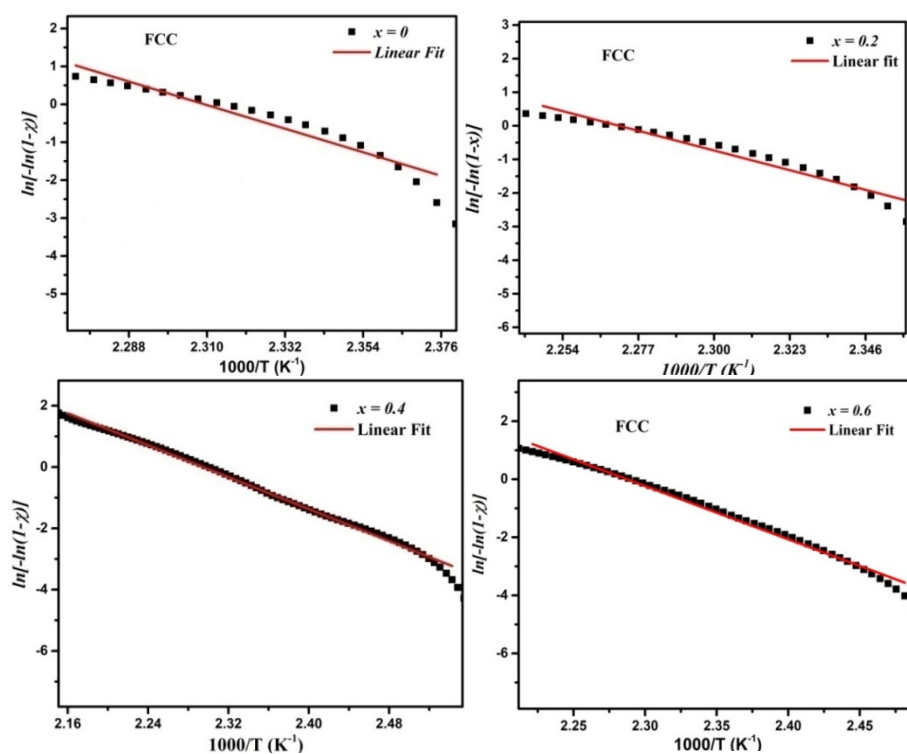
to the partial peak area and  $A_T$  is total area of exothermic peak. Figure 6.2 illustrates the crystallization fraction ( $\chi$ ) of the *fcc* phase with temperature for  $(Ge_2Sb_2Te_5)_{100-x}Sm_x$  samples. The equation (3.16) has been employed for the computation of *fcc* phase crystallization activation energy ( $E_{c1}$ ) and  $2^{nd}$  term in the right side has been neglected in comparison to the first term in this equation. The  $\ln(-\ln(1 - \chi))$  vs  $1000/T$  plots for  $(Ge_2Sb_2Te_5)_{100-x}Sm_x$  samples have been used to evaluate the  $E_{c1}$  value by utilizing the slope of linear fit (Figure 6.3). The values obtained for  $E_{c1}$  for  $(Ge_2Sb_2Te_5)_{100-x}Sm_x$  samples have been summarised in table 6.2. These  $E_{c1}$  values obtained for *GST* have been found to be in agreement with the earlier reports [20]. The obtained values of  $E_{c1}$  decrease to minimum for  $x = 0.4$  composition and then increases. The crystallization to hexagonal phase ( $E_{c2}$ ) activation energy attained adopting similar process have been presented in table 6.3 which indicates an enhancement in  $E_{c2}$  values with *Sm* concentration in *GST*.



**Figure 6.2.** The crystallization fraction ( $\chi$ ) of *fcc* phase of  $(Ge_2Sb_2Te_5)_{100-x}Sm_x$  phase change materials.

$x$	<i>Henderson's Method</i>			<i>Matusita's Method</i>			Avg. $E_{c2}$ (eV)	$T_{p2}$ (K)
	$E_{c2}$ (eV)	$\frac{E_{c2}}{n_2}$ (eV)	$n_2$	$mE_{c2}$ (eV)	$m$	$E_{c2}$ (eV)		
0.2	1.69	1.62	1.04	1.61	1	1.61	1.65	527.66
0.4	1.92	1.57	1.22	1.82	1	1.82	1.87	514.67
0.6	2.62	2.36	1.11	2.49	1	2.49	2.55	521.14
0.8	2.72	2.18	1.25	2.59	1	2.59	2.65	526.33
1.0	2.76	1.41	1.96	2.63	1	2.63	2.69	532.75
1.2	2.84	2.33	1.22	2.70	1	2.70	2.77	515.94

**Table 6.3.** The evaluated values of parameters of  $(Ge_2Sb_2Te_5)_{100-x}Sm_x$  for the estimation of hexagonal phase crystallization kinetics.



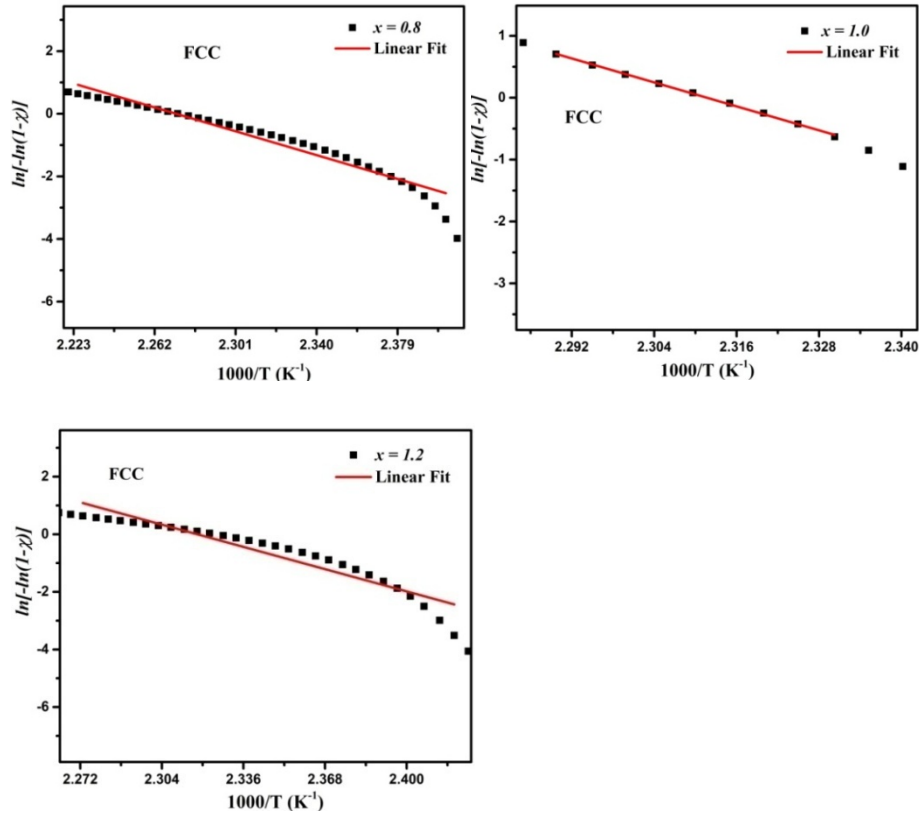


**Figure 6.3.** The  $\ln(\ln(1-\chi)^{-1})$  vs  $1000/T$  plots of  $(Ge_2Sb_2Te_5)_{100-x}Sm_x$  for *fcc* crystallization.

Equation (3.17) expresses the dependence of crystallization fraction ( $\chi$ ) on Avrami exponent ( $n$ ) and crystallization activation energy. Using equation (3.17) the linear fit obtained for  $\ln\left(\frac{d\chi}{dt}\right)$  vs  $1000/T$  plots have been employed to compute the slope  $-\frac{E_c}{n}$ . The contribution of  $I^{st}$  term containing  $f(\chi)$ , an implicit function of temperature in equation (3.17), has been ignored owing to the exponential term. The values of slope obtained using the linear fitting of  $\ln\left(\frac{d\chi}{dt}\right)$  vs  $1000/T$  plots have been used for the evaluation of Avrami exponent by substituting the  $E_c$  value calculated through equation (3.16). The Avrami exponent for *fcc* crystallization ( $n_1$ ) and hexagonal crystallization ( $n_2$ ) for  $(Ge_2Sb_2Te_5)_{100-x}Sm_x$  phase change materials have been computed. Figure 6.4 illustrates the  $\ln\left(\frac{d\chi}{dt}\right)$  vs  $1000/T$  plots for *fcc* crystallization used for the evaluation of  $n_1$  for  $(Ge_2Sb_2Te_5)_{100-x}Sm_x$  samples. The nucleation and growth mechanism of  $(Ge_2Sb_2Te_5)_{100-x}Sm_x$  samples can be described using the Avrami exponent. Table 6.2 summarizes the obtained  $n_1$  values for *GST* samples added with *Sm* lying close to 1, which signifies the nucleation by means of one-dimensional growth in sample from surface to inside [21]. The attained  $n_1$  values have been observed in accord with earlier reports [22]. Similarly,  $n_2$  values for *GST* thin film samples incorporated with *Sm* for

hexagonal crystallization have been obtained. The calculated  $n_2$  values have been presented in table 6.3. The  $n_2$  values also lie close to 1 which indicates an alike mechanism of nucleation and growth in case of hexagonal crystallization in the samples.

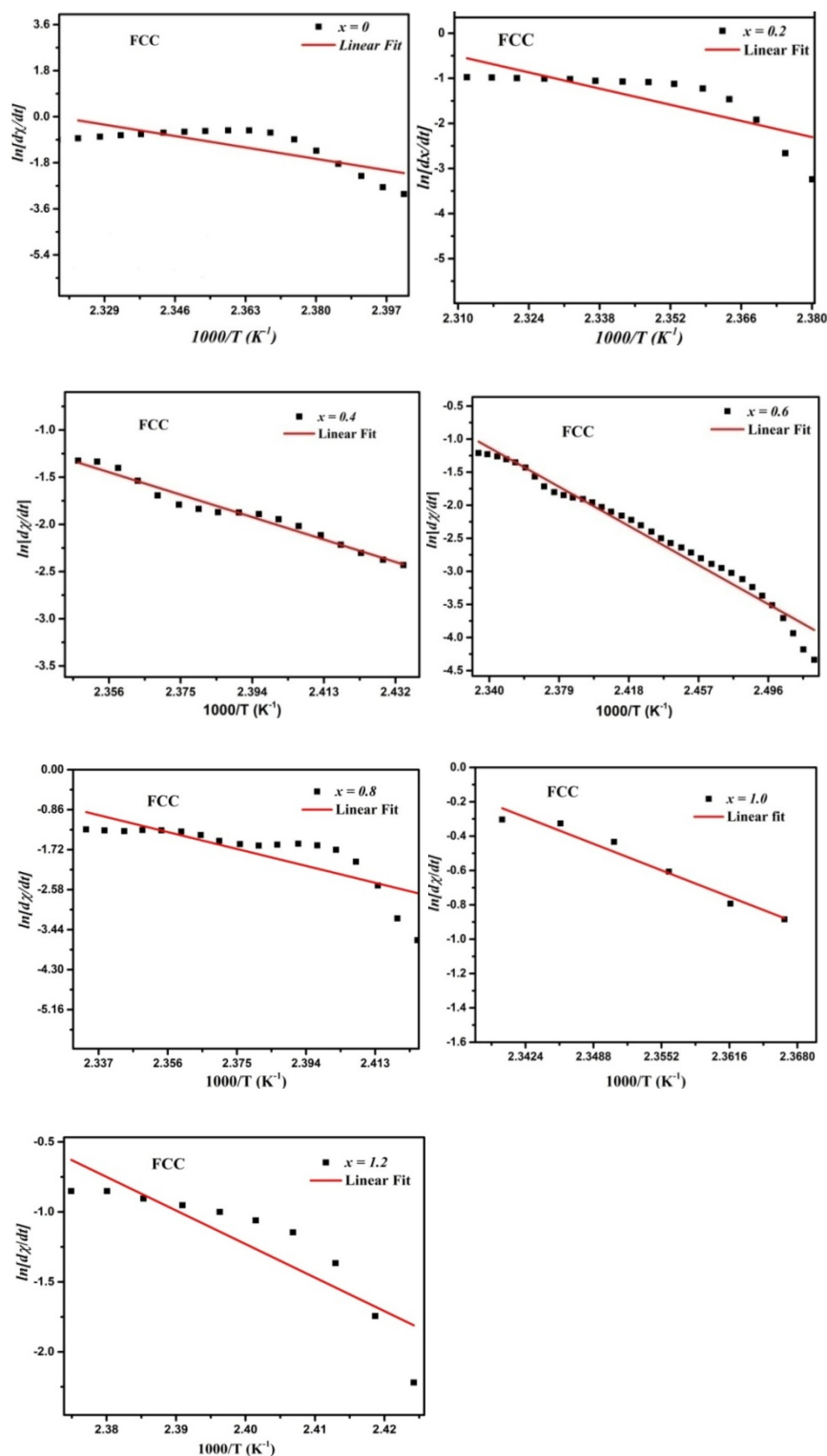


Figure 6.4. The  $\ln(dx/dt)$  vs.  $1000/T$  plots of  $(Ge_2Sb_2Te_5)_{100-x}Sm_x$  for fcc crystallization.

### 6.3.2.2 Matusita's Method

Matusita's method has been used to analyze non-isothermal crystallization kinetics for  $(Ge_2Sb_2Te_5)_{100-x}Sm_x$  samples using the constant heating rate ( $\alpha$ ) [23]. K. Matusita and S. Sakka described the nucleation and growth mechanism of glasses and derived the equation (3.18) exhibiting the dependence of heating rate ( $\alpha$ ), crystallization fraction ( $\chi$ ) and crystallization activation energy ( $E_c$ ) [13], [21]. The dimensionality of crystal growth and nucleation process has been described through the values of constant parameter  $m$ . The melt-quenched systems that contain no nuclei have been represented by  $m = n - 1$  where  $n$  represents the Avrami exponent. Whereas, the glassy systems comprising of large number of nuclei correspond to the value  $m = n$ . The nucleation and growth behavior of systems must be explored before the analysis of crystallization activation energy ( $E_c$ ). The three-dimensional crystal growth is signified by  $m = 3$  and  $m = 2$  stands for the growth of crystals in two-dimensions. The value of  $m = 1$  manifests the surface to inside growth in one dimension. The  $E_c$  value of  $(Ge_2Sb_2Te_5)_{100-x}Sm_x$  samples has been obtained by utilizing equation (3.18). Figure 6.3 displays the  $\ln[-\ln(1 - \chi)]$  vs  $1000/T$  plots for  $(Ge_2Sb_2Te_5)_{100-x}Sm_x$  PC materials with the slope of  $(mE_c)$  according to equation (3.18). The dominant surface nucleation and crystal growth in one dimension in thin films of GST added with Sm have been substantiated on the basis of obtained Avrami exponents  $n_1$  and  $n_2$  values lying close to 1. For the studied  $(Ge_2Sb_2Te_5)_{100-x}Sm_x$  samples,  $m$  value has been assumed to be 1. The obtained  $E_{c1}$  values for as-prepared samples using both the methods proposed by Henderson and Matusita show similar trends with addition of Sm to GST and agree with each other (Table 6.2). The value of  $E_{c2}$  has been also evaluated using equation (3.18) and summarized in table 6.3. The obtained values of  $E_{c2}$  enhance with the Sm concentration in GST.

The crystallization mechanism of  $(Ge_2Sb_2Te_5)_{100-x}Sm_x$  samples has been investigated using the DSC measurements and has been analyzed. The incorporation of Sm enhances the value of  $E_{c2}$ , the crystallization to hexagonal phase activation energy, of GST and reduces the value of  $E_{c1}$ , the activation energy for fcc phase, to minimum incase of  $x = 0.4$  addition of Sm to GST. It can be inferred from the decrease in  $E_{c1}$  values and increase in  $E_{c2}$  values till Sm addition  $x = 0.4$  at% to GST that Sm atoms may suppress the fcc phase and prefer to form a hexagonal structural network. Moreover, Sm doping to GST provides the benefit of using the fcc to hexagonal transition mechanism for enhancing the characteristics in PC memories.

### 6.4 Current-Voltage ( $I$ - $V$ ) Characteristics

Figure 6.5 shows the current-voltage ( $I$ - $V$ ) characteristics of as-deposited  $(Ge_2Sb_2Te_5)_{100-x}Sm_x$  thin films. The electrical measurements of these films have been performed at room temperature in planer geometry in the voltage range of  $0$ - $80V$  with a step size of  $0.5V$ . The high purity silver paste has been used to make electrodes on thin films. The  $2mm$  gap has been maintained between the electrodes for the electrical measurements. The electrical resistivity ( $\rho_e$ ) of  $(Ge_2Sb_2Te_5)_{100-x}Sm_x$  thin films has been evaluated using the relation  $\rho_e = R \frac{A}{l}$  where  $R$  stands for resistance,  $A$  represents cross-section area and separation between electrodes is  $l$ . The electrical resistivity of as-prepared thin films of  $GST$  added with  $Sm$  in the range  $0$ - $80V$  has been indicated in figure 6.6. The effect of increase in  $Sm$  concentration in as-deposited thin films on electrical resistivity has been studied. The current-voltage linear behavior in  $(Ge_2Sb_2Te_5)_{100-x}Sm_x$  thin films suggests the ohmic nature.

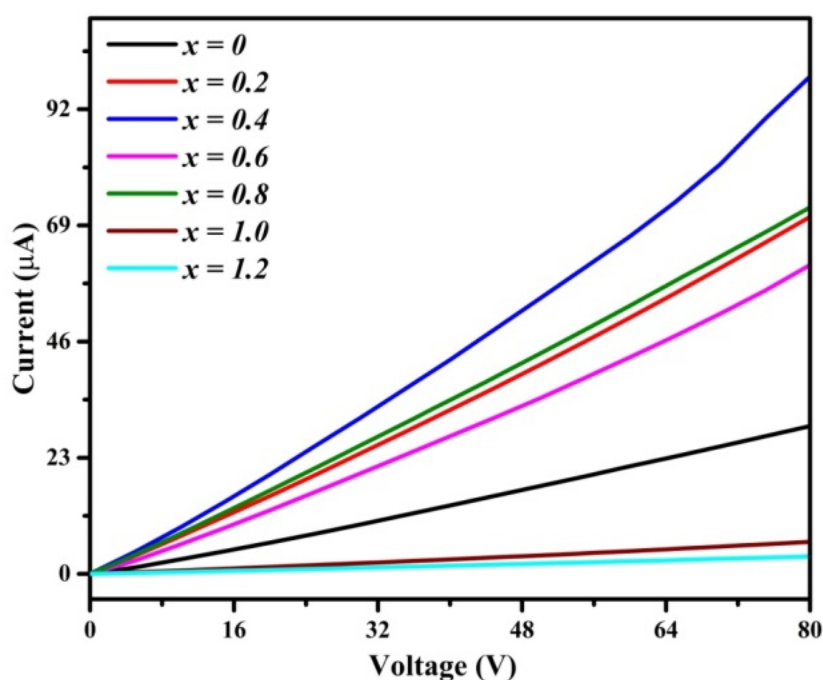


**Figure 6.5.**  $I$ - $V$  characteristics of  $(Ge_2Sb_2Te_5)_{100-x}Sm_x$  thin films.

The value of  $\rho_e$  for undoped  $GST$  has been observed to be of the order of  $2.5 \times 10^3 \Omega\text{-cm}$  at room temperature. The electrical resistivity decreases to minimum for  $Sm$  addition  $x = 0.4$  to  $GST$ . The addition of more  $Sm$  enhances the electrical resistivity from  $1.0 \times 10^3 \Omega\text{-cm}$  for  $x = 0.4 \text{ at\%}$  to  $1.8 \times 10^4 \Omega\text{-cm}$  for  $x = 1.2 \text{ at\%}$ . The reduction in resistivity for addition of  $Sm$  upto  $x = 0.4$  may be due to an increase in the free carrier concentration and

increase in the mobility resulting in augmentation of hopping conduction. This reduction in resistivity can also be correlated with the decline in defect concentration, and increase in ordered parameter  $B^{1/2}$  value to maximum for  $x = 0.4at\%$   $Sm$  content which has already been discussed in section 5.3.3. The charged defects ( $C_3^+$ ,  $C_1^-$ ) formed owing to the lone pair electrons in amorphous materials also known as valence alternation pairs ( $VAPs$ ) play significant role in electrical conduction. The enhancement in resistivity on more  $Sm$  addition, *i.e.*, for  $x > 0.4$  may be on account of reduction in mobility due to an increase in disorder with  $Sm$  content leading to minimum  $B^{1/2}$  value of  $534.94 \text{ cm}^{-1/2} * eV^{-1/2}$  and  $N/m^*$  value of  $3.82 \times 10^{47} \text{ g}^{-1} \text{ cm}^{-3}$  for  $x = 1.2\%$  (Table 5.2).

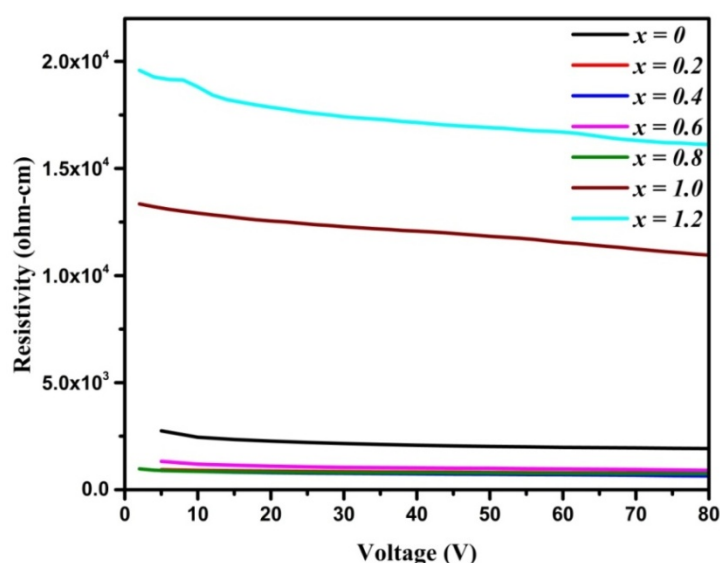
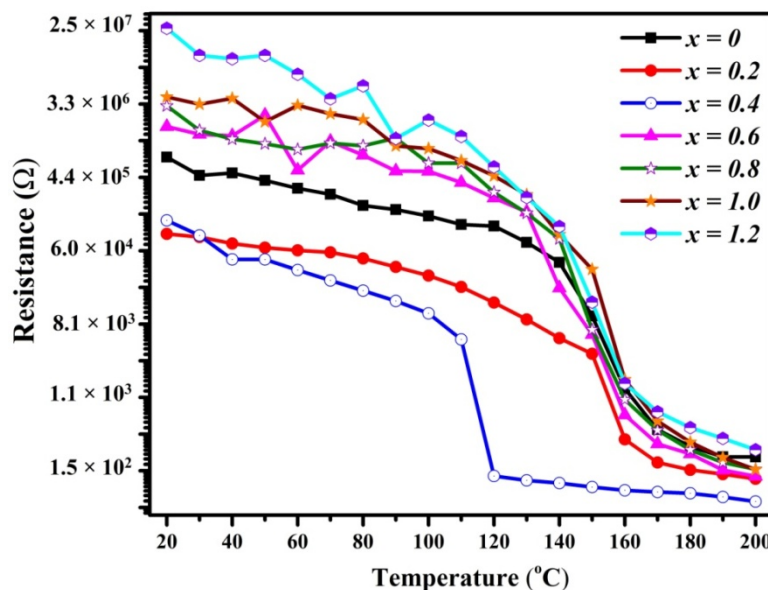


**Figure 6.6.** Electrical resistivity of  $(Ge_2Sb_2Te_5)_{100-x}Sm_x$  thin films.

### 6.5 Temperature – Resistance ( $R-T$ ) Measurements

The resistance versus temperature ( $R-T$ ) measurements of  $(Ge_2Sb_2Te_5)_{100-x}Sm_x$  thin films have been performed in planar geometry at constant heating rate of  $10 \text{ }^\circ\text{C}/\text{min}$  from  $20 \text{ }^\circ\text{C}$  to  $200 \text{ }^\circ\text{C}$  using Keithley 2611 electrometer.

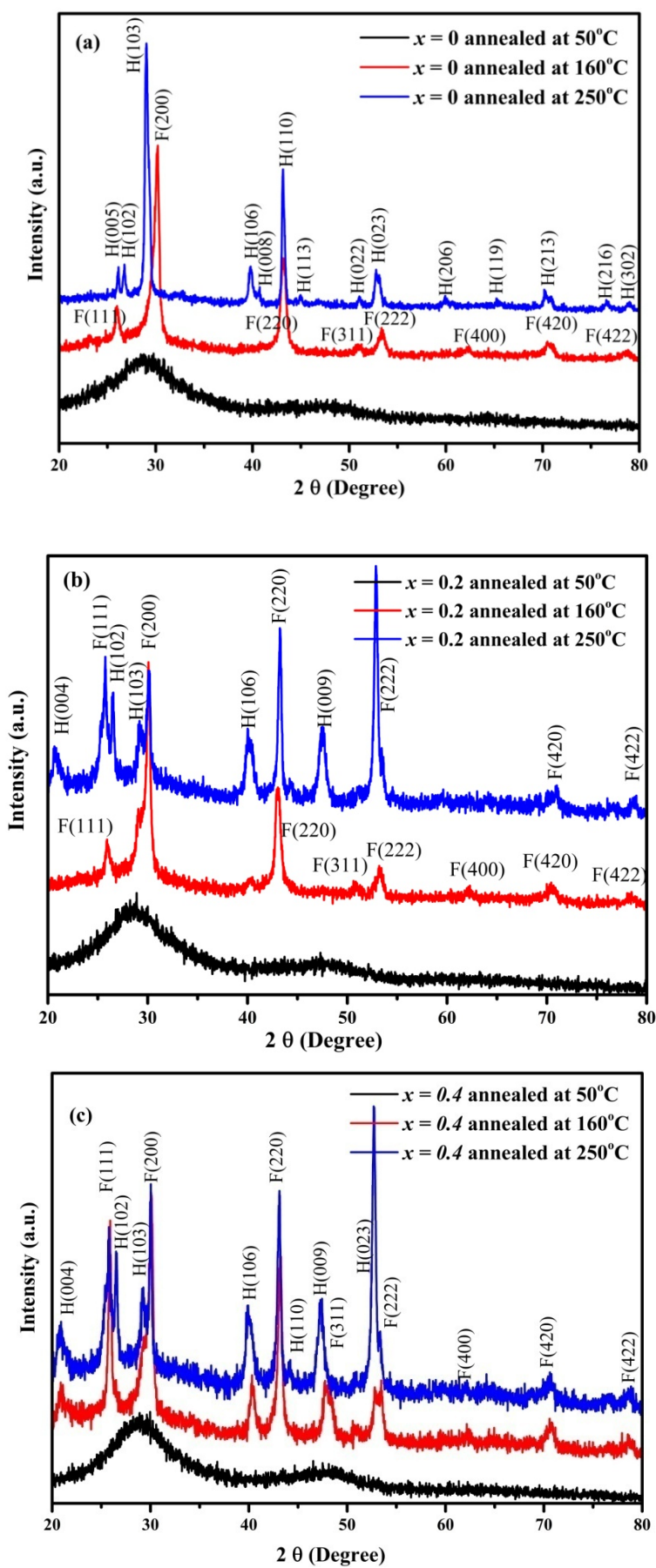
Figure 6.7 shows the temperature dependent electrical resistance of  $(Ge_2Sb_2Te_5)_{100-x}Sm_x$  thin films illustrating the sharp drop in electrical resistance at crystallization temperature ( $T_c$ ). The  $T_c$  value decreases from about  $160^\circ\text{C}$  to  $120 \text{ }^\circ\text{C}$  for  $0.4\%$   $Sm$  addition and increases on further addition of  $Sm$  concentration above  $x > 0.4\%$ . The improvement in the resistance contrast between amorphous and crystalline phase of  $(Ge_2Sb_2Te_5)_{100-x}Sm_x$  has been observed above the  $x = 0.4\%$   $Sm$  content which may be advantageous for better signal to noise ratio of memory device. The decrease in the crystallization temperature of  $GST$  till  $x = 0.4\%$   $Sm$  content may be due to increase in the rigidity of the structural network.

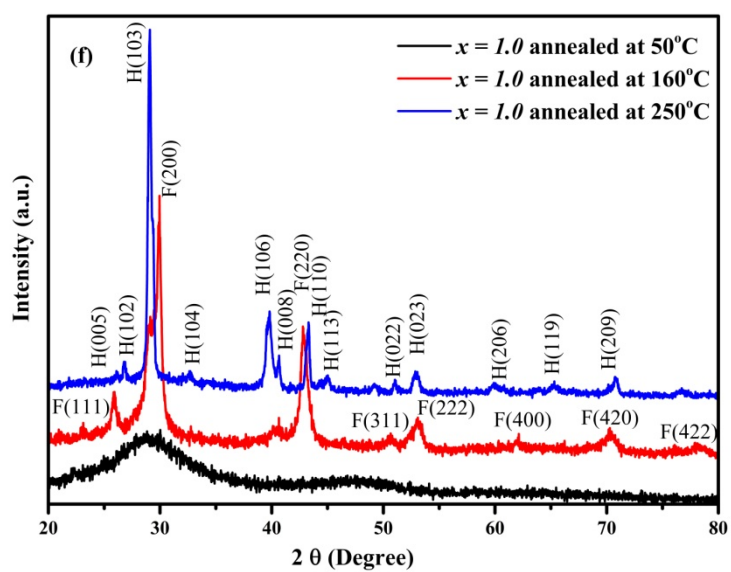
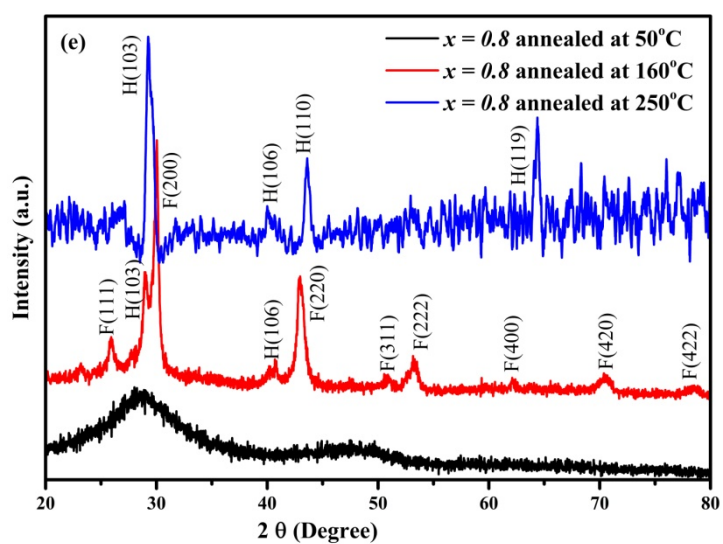
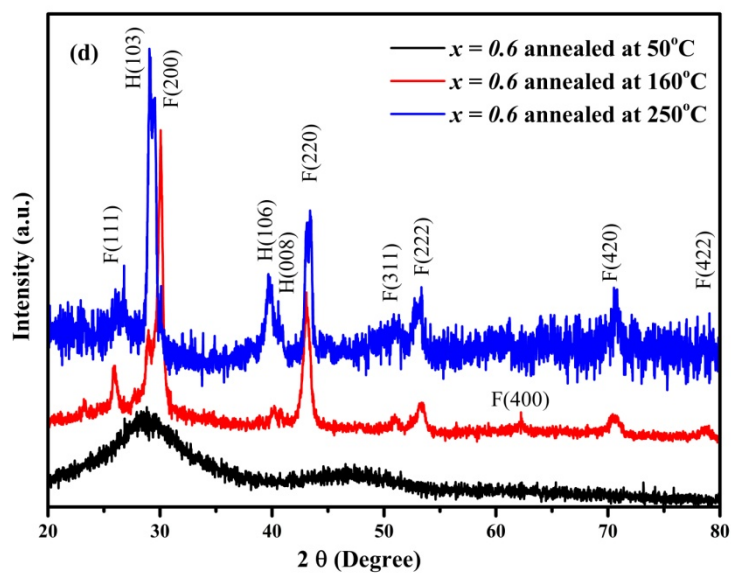


**Figure 6.7.** Temperature dependent electrical resistance of  $(Ge_2Sb_2Te_5)_{100-x}Sm_x$  thin films.

### 6.6 Temperature Dependent XRD Studies

Figure 6.8(a-g) shows the *XRD* patterns of  $(Ge_2Sb_2Te_5)_{100-x}Sm_x$  thin films annealed at temperatures  $50^\circ C$ ,  $160^\circ C$  and  $250^\circ C$  in vacuum. The *XRD* patterns of  $(Ge_2Sb_2Te_5)_{100-x}Sm_x$  thin films annealed at  $50^\circ C$  temperature show the absence of diffraction peaks which indicates the amorphous nature. Furthermore,  $(Ge_2Sb_2Te_5)_{100-x}Sm_x$  thin films annealed at  $160^\circ C$  temperature illustrates the presence of sharp diffraction peaks near  $\sim 25.8^\circ$ ,  $29.9^\circ$ ,  $42.9^\circ$ ,  $50.7^\circ$ ,  $53.4^\circ$ ,  $62.3^\circ$ ,  $70.6^\circ$  and  $78.7^\circ$  which have been indexed for  $(111)$ ,  $(200)$ ,  $(220)$ ,  $(311)$ ,  $(222)$ ,  $(400)$ ,  $(420)$  and  $(422)$  respectively for rocksalt cubic ( $Fm-3m$ ) crystal structure of *GST* (*ICDD* card number: *01-078-3710*). The presence of sharp diffraction pattern of rocksalt cubic phase in the thin films annealed at  $160^\circ C$  temperature signify the amorphous to *fcc* phase transition in  $(Ge_2Sb_2Te_5)_{100-x}Sm_x$  thin films. However, the presence of additional peaks at  $\sim 29^\circ$  and  $\sim 39.8^\circ$  in the *Sm* doped *GST* thin films annealed at  $160^\circ C$  has been also observed which corresponds to the  $(103)$  and  $(106)$  planes of the hexagonal phase. In addition, on annealing the thin films at  $250^\circ C$ , new diffraction peaks have been observed which correspond to the  $(004)$ ,  $(005)$ ,  $(102)$ ,  $(103)$ ,  $(106)$ ,  $(008)$ ,  $(110)$ ,  $(009)$ ,  $(113)$ ,  $(022)$ ,  $(023)$ ,  $(206)$ ,  $(119)$ ,  $(209)$ ,  $(213)$ ,  $(216)$  and  $(302)$  for hexagonal phase ( $P-3m1$ ) (*ICDD* card number: *04-006-9784*). There is appearance of hexagonal phase in pure *GST* thin film sample and mixed *fcc* and hexagonal phases in *Sm* doped *GST* samples annealed at  $250^\circ C$ , which indicates the *fcc* to hexagonal transition at this temperature.





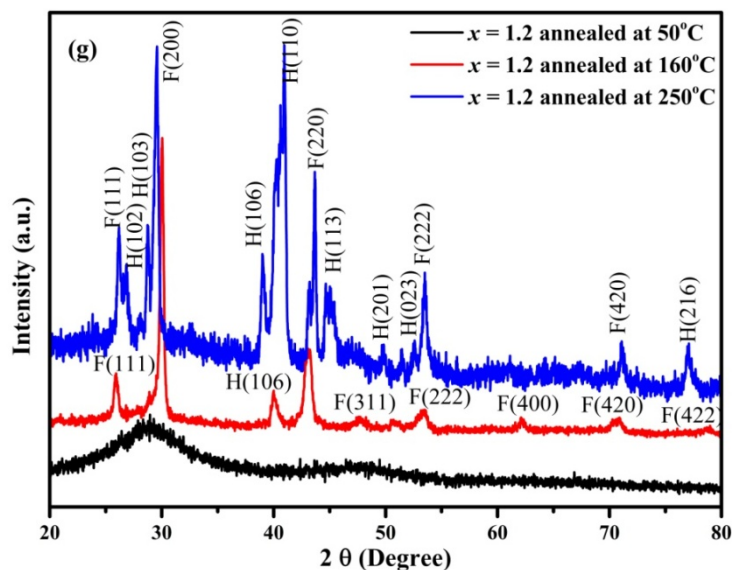


**Figure 6.8.** XRD patterns of  $(Ge_2Sb_2Te_5)_{100-x}Sm_x$  thin films annealed at  $50^\circ C$ ,  $160^\circ C$  and  $250^\circ C$  temperature.

### 6.7 Conclusions

The non-isothermal DSC curves of as-deposited  $(Ge_2Sb_2Te_5)_{100-x}Sm_x$  samples obtained at  $10K/min$  heating rate display two exothermic peaks at  $\sim 150^\circ C$  and  $\sim 235^\circ C$  which have been identified for the respective transitions of amorphous GST to fcc phase and  $fcc \rightarrow$  hexagonal. The  $E_{c1}$  value computed using the two methods, Henderson's and Matusita's methods, decreases to minimum for Sm addition  $x = 0.4 at\%$  to GST and then rises. Furthermore, the obtained  $E_{c2}$  value rises with Sm incorporation to GST. The crystallization in thin films of GST incorporated with Sm takes place because of nucleation on surface and surface to inside growth in one-dimension corroborated through the obtained  $n_1$  and  $n_2$  values lying close to 1. The electrical resistivity ( $\rho_e$ ) of  $(Ge_2Sb_2Te_5)_{100-x}Sm_x$  thin films investigated at room temperature decreases upto Sm addition  $x = 0.4at\%$  to GST and rises further at higher Sm concentration. There is prominent electrical resistance contrast between amorphous and crystalline phase of GST. There is increase in crystallization temperature for samples with Sm content  $x > 0.4\%$  as observed from the  $R-T$  measurements. The appearance of amorphous phase on annealing the thin films at  $50^\circ C$  and fcc phase on annealing the thin films at  $160^\circ C$  points towards the amorphous to fcc phase transition, while the presence of hexagonal phase in the XRD spectra of  $(Ge_2Sb_2Te_5)_{100-x}Sm_x$  thin films annealed at higher temperature of  $250^\circ C$  indicates the fcc to hexagonal transition.

## References

- [1] W. Zhang, R. Mazzarello, and E. Ma, “Phase-change materials in electronics and photonics,” *MRS Bull.*, vol. 44, no. 09, pp. 686–690, Sep. 2019.
- [2] Q. Wang, G. Niu, W. Ren, R. Wang, X. Chen, X. Li, Z.-G. Ye, Y. -H. Xie, S. Song and Z. Song, “Phase Change Random Access Memory for Neuro-Inspired Computing,” *Adv. Electron. Mater.*, vol. 7, no. 6, p. 2001241, Jun. 2021.
- [3] A. V. Kolobov, P. Fons, A. I. Frenkel, A. L. Ankudinov, J. Tominaga, and T. Uruga, “Understanding the phase-change mechanism of rewritable optical media,” *Nat. Mater.*, vol. 3, no. 10, pp. 703–708, Oct. 2004.
- [4] W. Zhang, H. S. Jeong, and S. A. Song, “Martensitic transformation in  $\text{Ge}_2\text{Sb}_2\text{Te}_5$  alloy,” *Adv. Eng. Mater.*, vol. 10, no. 1–2, pp. 67–72, 2008.
- [5] W. Zhang and E. Ma, “Unveiling the structural origin to control resistance drift in phase-change memory materials,” *Mater. Today*, vol. 41, pp. 156–176, Dec. 2020.
- [6] P. Hu, T. -R. Wei, P. Qiu, Y. Cao, J. Yang, X. Shi and L. Chen, “Largely Enhanced Seebeck Coefficient and Thermoelectric Performance by the Distortion of Electronic Density of States in  $\text{Ge}_2\text{Sb}_2\text{Te}_5$ ,” *ACS Appl. Mater. Interfaces*, vol. 11, no. 37, pp. 34046–34052, Sep. 2019.
- [7] J. A. Kalb, M. Wuttig, and F. Spaepen, “Calorimetric measurements of structural relaxation and glass transition temperatures in sputtered films of amorphous Te alloys used for phase change recording,” *J. Mater. Res.*, vol. 22, no. 3, pp. 748–754, Mar. 2007.
- [8] Y. Mao, Y. Chen, Q. Zhang, R. Wang, and X. Shen, “Improvement of thermal stability and phase change behavior of  $\text{Ge}_2\text{Sb}_2\text{Te}_5$  thin films by Calcium doping,” *J. Non. Cryst. Solids*, vol. 549, no. April, p. 120338, Dec. 2020.
- [9] X. Sun, M. Ehrhardt, A. Lotnyk, P. Lorenz, E. Thelander, J. W. Gerlach, T. Smausz, U. Decker and B. Rauschenbach, “Crystallization of  $\text{Ge}_2\text{Sb}_2\text{Te}_5$  thin films by nano- and femtosecond single laser pulse irradiation,” *Sci. Rep.*, vol. 6, no. 1, p. 28246, Sep. 2016.
- [10] S. Hudgens and B. Johnson, “Overview of Phase-Change Chalcogenide Nonvolatile

- Memory Technology,” *MRS Bull.*, vol. 29, no. 11, pp. 829–832, Nov. 2004.
- [11] J. Kalb, F. Spaepen, and M. Wuttig, “Calorimetric measurements of phase transformations in thin films of amorphous Te alloys used for optical data storage,” *J. Appl. Phys.*, vol. 93, no. 5, pp. 2389–2393, Mar. 2003.
- [12] M. H. . Lankhorst, “Modelling glass transition temperatures of chalcogenide glasses. Applied to phase-change optical recording materials,” *J. Non. Cryst. Solids*, vol. 297, no. 2–3, pp. 210–219, Feb. 2002.
- [13] K. Matusita, T. Komatsu, and R. Yokota, “Kinetics of non-isothermal crystallization process and activation energy for crystal growth in amorphous materials,” *J. Mater. Sci.*, vol. 19, no. 1, pp. 291–296, Jan. 1984.
- [14] D. W. Henderson, “Experimental analysis of non-isothermal transformations involving nucleation and growth,” *J. Therm. Anal.*, vol. 15, no. 2, pp. 325–331, Apr. 1979.
- [15] D. W. Henderson, “Thermal analysis of non-isothermal crystallization kinetics in glass forming liquids,” *J. Non. Cryst. Solids*, vol. 30, no. 3, pp. 301–315, Jan. 1979.
- [16] J. Kalb, F. Spaepen, and M. Wuttig, “Atomic force microscopy measurements of crystal nucleation and growth rates in thin films of amorphous Te alloys,” *Appl. Phys. Lett.*, vol. 84, no. 25, pp. 5240–5242, Jun. 2004.
- [17] J. A. Kalb, C. Y. Wen, F. Spaepen, H. Dieker, and M. Wuttig, “Crystal morphology and nucleation in thin films of amorphous Te alloys used for phase change recording,” *J. Appl. Phys.*, vol. 98, no. 5, p. 054902, Sep. 2005.
- [18] Q. M. Lu and M. Libera, “Microstructural measurements of amorphous GeTe crystallization by hot-stage optical microscopy,” *J. Appl. Phys.*, vol. 77, no. 2, pp. 517–521, Jan. 1995.
- [19] H.-Y. Cheng, S. Raoux, and Y.-C. Chen, “The impact of film thickness and melt-quenched phase on the phase transition characteristics of  $\text{Ge}_2\text{Sb}_2\text{Te}_5$ ,” *J. Appl. Phys.*, vol. 107, no. 7, p. 074308, Apr. 2010.
- [20] Y. Chen, N. Chen, B. Chen, Q. Zhang, X. Li, Q. Deng, B. Zhang, S. Zhang, Z. Zhang and X. Han, “Electrical properties and structural transition of  $\text{Ge}_2\text{Sb}_2\text{Te}_5$  adjusted by rare-earth element Gd for nonvolatile phase-change memory,” *J. Appl.*

*Phys.*, vol. 124, no. 14, p. 145107, Oct. 2018.

- [21] K. Matusita and S. Sakka, “Kinetic Study on Non-Isothermal Crystallization of Glass by Thermal Analysis,” *Bull. Inst. Chem. Res. Kyoto Univ.*, vol. 59, no. 3, pp. 159–171, Feb. 1981.
- [22] X. Wei, T. Luping, T. Chong, Z. Rong, and H. Koon, “Thickness Dependent Nano-Crystallization in  $\text{Ge}_2\text{Sb}_2\text{Te}_5$  Films and Its Effect on Devices,” *Jpn. J. Appl. Phys.*, vol. 46, no. 4B, pp. 2211–2214, Apr. 2007.
- [23] K. Matusita and S. Sakka, “Kinetic study of crystallization of glass by differential thermal analysis—criterion on application of Kissinger plot,” *J. Non. Cryst. Solids*, vol. 38–39, pp. 741–746, May 1980.



## **Summary & Conclusions**



The  $Ge_2Sb_2Te_5$  (*GST*) is a contender material for phase change memory applications. *GST* can be transformed repeatedly and rapidly between amorphous, rocksalt cubic and hexagonal phases. The different phases of *GST* distinguish among themselves by the scale of their optical reflectivity and electrical resistivity in the corresponding states. The rocksalt cubic structure of *GST* consists of *Te* atoms inhabiting the *4a* anionic sites and *Ge*, *Sb* atoms along with 20% vacant sites inhabiting the *4b* cationic sites. The annealing of *GST* above *fcc* crystallization temperature results in the transformation to the hexagonal phase. This transformation to hexagonal phase involves the *Te* atoms replacing the vacancy sites and simultaneous creation of *Te—Te* bonds. The switching mechanism of *GST* has been analyzed theoretically for the rare earth element *Sm* incorporation in *GST* to improve phase-change memory device performance.

The melt-quench technique has been used for the synthesis of  $(Ge_2Sb_2Te_5)_{100-x}Sm_x$  ( $x = 0, 0.2, 0.4, 0.6, 0.8, 1.0, 1.2$ ) bulk alloys. The thermal evaporation route has been adopted to deposit the  $(Ge_2Sb_2Te_5)_{100-x}Sm_x$  thin films on well cleaned glass substrates. The theoretical study of physical parameters has been carried out for the effect of *Sm* incorporation on *GST* in  $(Ge_2Sb_2Te_5)_{100-x}Sm_x$  samples and modification in local structure of *GST*. The increase in rigidity of *GST* with *Sm* content has been ascribed to the rise in average coordination number enhancing the structural network cross-linking. The theoretically computed mean bond energy of  $(Ge_2Sb_2Te_5)_{100-x}Sm_x$  samples increases with *Sm* content. The empirical correlations between the glass transition temperature ( $T_g$ ), mean bond energy and other physical parameters have been used to predict the  $T_g$  value of *Sm* doped *GST* samples, which shows an increase with *Sm* concentration. This enhances the efficiency of structural modification for *GST* added with *Sm*. The calculated values of average lone pair electrons, metallicity ( $M$ ) have been used to estimate the structural modification efficiency and coupling of covalent structures of *Sm* doped *GST*.

The structural investigation of  $(Ge_2Sb_2Te_5)_{100-x}Sm_x$  alloys using the *XRD* and Rietveld analysis shows the presence of mixed amorphous, *fcc* and hexagonal phase fractions in as-prepared samples. The appearance of nano-crystallites in as-prepared alloys has been analyzed from the diffraction peaks due to the limited glass-forming ability of *GST*. The most prominent peak in *XRD* spectra (*103*) corresponding to *GST* hexagonal phase with *Sm* concentration which indicates the effect of incorporation of *Sm* to *GST* in the hexagonal environment. Furthermore, *XRD* spectra Rietveld refinement indicates that *Sm* doping also

results in the change in the fraction of *fcc* and hexagonal phases. The *Sm* doping also augments the crystallite size up to addition of  $x = 0.4\%$  *Sm* to *GST*. The Raman analysis of as-prepared  $(Ge_2Sb_2Te_5)_{100-x}Sm_x$  alloys indicate the alteration in the *Sb* local structure on *Sm* incorporation inferred from the shift in frequency of vibrational mode of *SbTe*<sub>3</sub> pyramidal structure. The absence of prominent peaks observed from the *XRD* spectra of thin films of *GST* added with *Sm* indicate the amorphous nature of films. The creation of *Sb—Sm*, *Sm—Te* and *Ge—Sm* bonds on *Sm* addition to *GST* and occurrence of *Sm* in +2 and +3 oxidation states in thin film samples of  $(Ge_2Sb_2Te_5)_{100-x}Sm_x$  have been confirmed through *XPS* spectra.

The optical properties of as-deposited thin films of  $(Ge_2Sb_2Te_5)_{100-x}Sm_x$  have been probed making use of *UV-Vis-NIR* spectroscopy. The optical band gap ( $E_g$ ) of as-prepared *GST* thin films incorporated with *Sm* decreases from 0.75 eV to 0.68 eV on *Sm* addition. The *Sm* addition induces the disorder in *GST* and alters the band tailing width. There is an increase in ordering upto addition of  $x = 0.4at\%$  *Sm* to *GST* due to the formation of rigid structures and decline in homopolar wrong bond creation. The dispersion energy ( $E_d$ ), static refractive index ( $n_0$ ), plasma frequency ( $\omega_{plasma}^2$ ) and dielectric parameters of  $(Ge_2Sb_2Te_5)_{100-x}Sm_x$  show the impact of *Sm* concentration and changes in the structural modification and polarizability are also observed. The value of third order optical non-linear susceptibility ( $\chi^{(3)}$ ) for thin films of *GST* added with *Sm* indicates the covalent bonding nature. The obtained values of the non-linear refractive index ( $n_2$ ) also show dependence on *Sm* concentration owing to the modification of local structure on addition of *Sm* to *GST*.

The *Sm* addition to *GST* also affects the mechanism of crystallization, as inferred from the analysis of non-isothermal measurements from *DSC* at 10K/min heating rate. The crystallization to *fcc* phase and hexagonal phase has been correlated through the appearance of exothermic peaks at respectively about ~150 °C and ~235 °C in *DSC* thermogram. The activation energy for crystallization ( $E_{c1}$ ) analyzed from the *DSC* curves of as-deposited thin films decrease upto addition of  $x = 0.4at\%$  *Sm* followed by an increase. The transition to hexagonal phase ( $E_{c2}$ ) crystallization activation energy value rises with *Sm* content. There is induction of crystallization in thin films of *Sm* added *GST* due to the nucleation at surface with surface to inside growth process in one-dimension as assessed from the obtained Avrami exponent values. The resistivity of  $(Ge_2Sb_2Te_5)_{100-x}Sm_x$  thin films at room temperature decreases till *Sm* addition  $x = 0.4at\%$  to *GST* and then increases. The sharp drop in electrical

resistance of  $(Ge_2Sb_2Te_5)_{100-x}Sm_x$  thin films near  $\sim 160^\circ C$  because of *fcc* crystallization has been observed from the *R-T* measurements. The transition from amorphous to *fcc* and then to the hexagonal phase of *Sm* doped *GST* thin films has been confirmed through the presence of amorphous, *fcc* and hexagonal phase observed in the *XRD* spectra of thin films annealed in vacuum at  $50^\circ C$ ,  $160^\circ C$  and  $250^\circ C$  respectively. The reduced optical gap, improved optical non-linearity, reduced value of crystallization activation energy, comparatively higher thermal stability and much higher conductivity for  $x = 0.4\%$  *Sm* is beneficial for improved switching performance of phase-change memory.